Electron acceleration and betatron radiation driven by laser wakefield inside dielectric capillary tubes

Jinchuan Ju

Thèse présentée pour obtenir le grade de

DOCTEUR DE L'UNIVERSITE PARIS-SUD

École doctorale Ondes et Matière

Spécialité : Physique des Plasmas

par

Jinchuan JU

Electron acceleration and betatron radiation driven by laser wakefield inside dielectric capillary tubes

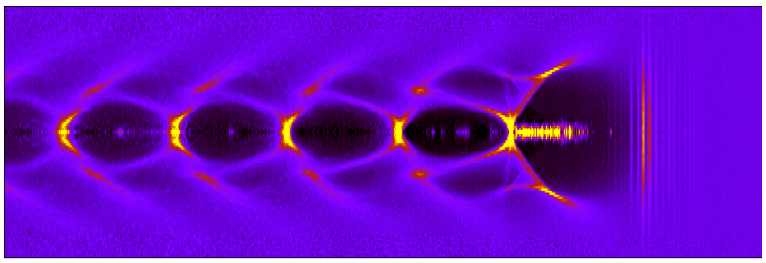

Soutenue le 27 juin 2013 devant le jury composé de :

M. Nikolay ANDREEV	Russian Academy of Sciences	Rapporteur
M. Simon HOOKER	University of Oxford	Rapporteur
M^{me} Brigitte CROS	Université Paris-Sud	Directrice de thèse
M. Pascal MONOT	CEA Saclay	Examinateur
M. Patrick PUZO	Université Paris-Sud	Président
M. Claes-Göran WAHLSTRÖM	Lund University	Invité

The thesis was prepared at the
Laboratoire de Physique des Gaz et des Plasmas (LPGP),
Bâtiment 210, Université Paris-Sud 11,
91405, Orsay CEDEX,
France.

人之为学有难易乎？学之，则难者亦易矣；不学，则易者亦难矣。

——清•彭端淑《为学》

To the memory of my grandparents
To my families
To Yan and Ruoxi

Acknowledgements

I can not imagine how the thesis would be fulfilled without the help and support of my friends, families, and most importantly advisor. Taking this opportunity, I would like to acknowledge all of them.

First I express the sincerest appreciations to my thesis advisor: Brigitte Cros. It is her who gave me the chance to do my PhD study in such an interesting frontier field. Thank you Brigitte for your consistent encouragements, supports, and guidance during the four years. I also want to acknowledge Gilles Maynard, the director of the laboratory, for his concerns on my study and stay at LPGP. Many thanks go to Hugo Ferrari at CONICET in Argentina for performing the PIC simulations and answering my "endless" questions. I appreciate Olivier Dadoun at LAL for helping us to do the GEANT modelings.

I am grateful to the present and former members in our laboratory for their invaluable assistance. Special appreciation goes to Yohann Ayoul who taught me many techniques of capillary alignment, although communication was quite difficult between us at that time. Thanks Bhooshan Paradkar for many interesting discussions and helpful comments on the thesis writing. I would also like to thank Michel Fleury, Caroline Boisse-Laporte, Joël Baudet, Jean-Claude Largon, Olivier Antonin, and ... for their warm help to the experiments at LPGP. I wish to thank the adminstration staff, Nicolas Dessaints, Thierry Devillers, Sophie Granon, and Marie-Claude Richard for their kind helps. I am specially indebted to Nicolas for his generous help for my personal business.

It is my pleasure to study and often have lunch together with Frédéric Desforges, Chengfei Jin, Jean-Sebastien Mace, Katell Gadonna, Ismaël Guesmi, Franck Duré, Lise Caillault, and ..., even though I still do not understand what they talk during the lunch. Special thanks go to Chengfei who helped me to survive when I just arrived without speaking French at all.

The thesis was in collaboration with several different groups, which provided me various experiences. Great appreciations are given to the members at the Lund Laser Centre in Sweden: Martin Hansson, Lovisa Senje, Kristoffer Svensson, Franck Wojda, Matthias Burza, Guillaume Genoud, Olle Lundh, Anders Persson, and Claes-Göran Wahlström. Thank again Claes-Göran for his wonderful organization of the experiment and providing such a comfortable working environment. Many thanks go to Andreas Döpp and Frédéric Desforges who assisted me carrying out the experiments at the LLC. I would like to thank Sandrine Dobosz Dufrénoy in PHI for her kind helps during the experiment performed at CEA Sacaly and the experiment at the LLC.

My sincere gratitude gives Prof. Huihuang Zhong, my principal supervisor at the National University of Defense Technology in China for his supports and confidence. Meanwhile, I would greatly acknowledge Prof. Ting Shu who encouraged and helped me to study abroad. Furthermore, I would like to express my appreciations to all other members of "206" for their concerns and helps. My classmates did me a lot of favors during my study abroad. Thank you very much!

I appreciate the jury committee: Prof. Nikolay Andreev, Prof. Simon Hooker, Dr. Pascal Monot, Prof. Patrick Puzo, and Prof. Claes-Göran Wahlström for reviewing the manuscript, giving helpful comments and suggestions to improve it.

I heartily acknowledge the supports from Triangle de la Physique, LaserLab Europe, and the Chinese Scholarship Council (CSC).

I am very lucky to make many new friends here: Wang Dongfang, Zhang Xiaohong, Ma Jingyi, He Jibo, Ye Shixin, Jean, Liu Yi, Zhang Yang, and .... It is so nice to meet you guys. Thanks Dongfang for giving me the bike that I ride everyday.

完成博士学业之际，我深深地思念远在家乡的父母，感谢他们多年来对我的养育、关爱和鼓励。前几日适逢父亲甲子生辰，这里将我的博士论文送给他作为迟到的生日礼物。同时，感谢岳父母对我学业、生活的理解和支持。感谢伯父母长期以来对我学习工作的关爱和鼓励，感谢所有家人对我的关心和帮助！

I am deeply indebted to my gorgeous and beautiful wife, Yan. She loses a lot to support my study abroad. Thank you for your understanding, patience, and for giving us such a lovely daughter, Ruoxi. I will always love you!

La France est romantique, mais l'apprentissage du français n'est pas romantique du tout. C'est vraiment un défi pour moi d'apprendre le français. Je remercie Brigitte d'avoir fait beaucoup de répétitions pour mes présentations en français, et avoir patiemment corrigé mes fautes de grammaire. Je tiens également à remercier Thierry, avec qui j'ai eu de très bons échanges en français et en anglais.

Au revoir à cette ville romantique et à mes amis d'ici. Vous allez me manquer!

Abstract

This dissertation addresses electron acceleration and the associated betatron X-ray radiation generated by laser wakefield inside dielectric capillary tubes. Focusing the state-of-the-art multi-terawatt laser pulses, high peak intensity, of the order of 10^{18} W/cm^2, can be achieved in the focal plane, where a plasma bubble free of electron is formed just behind the laser. Owing to space charge separation ultrahigh electric fields, of the order of 100 GV/m, occur inside the plasma bubble, providing the possibility to accelerate electrons up to GeV-class over merely a centimeter-scale distance. Furthermore, ultra-short synchrotron-like X-ray radiation, known as betatron radiation, is produced simultaneously when the accelerated electrons are transversely wiggled by the radial electric field inside the plasma bubble. This thesis reports experimental results on the generation and optimization of electron and X-ray beams, particularly when a capillary tube is used to collect the energy of laser halos in the focal plane to facilitate the laser keeping self-focused over a long distance.

The spatial distribution of gas along the axis of capillary tubes in the stationary state was obtained by numerical fluid simulations, which demonstrate a stable, uniformly distributed gas medium is established between the two capillary slits. The temporal process of gas filling into capillary tubes was characterized using a method based on a Mach-Zehnder interferometer, which suggests in our gas filling arrangement the shortest valve opening duration of 27 ms should be used for hydrogen gas in order to minimize gas leakage into the vacuum target chamber.

Employing the 40 fs, 16 TW Ti:sapphire laser at the Lund Laser Centre (LLC) in Sweden, either peaked or widely-spread accelerated electron spectra with a typical beam charge of tens of pC were measured with a maximum energy up to 300 MeV in 10 mm long capillary tubes. Meanwhile, betatron X-ray radiation consisting of 1-10 keV photons was measured with a peak brightness of the order of $\sim 10^{21}$ photons/s/mm^2/mrad^2/0.1%BW, which is around 30 times higher than that in the case of a 2 mm gas jet without external optical guiding. When the laser pointing fluctuation is compensated, reproducible electron beams are obtained with fluctuations of only $\sim$ 1 mrad RMS in beam pointing, a few percent in electron energy, and around 20% RMS in beam charge. Moreover, betatron radiation is able to provide the diagnostics about electron acceleration process and average number of betatron oscillations fulfilled by electrons inside the plasma bubble. The typical X-ray source size (waist of Gaussian distribution at $1/e^2$ intensity) is quantified to be ~ 2.5 μm using Fresnel diffraction induced by a razor blade, which furthermore yields the corresponding normalized RMS emittance of electron beam $\epsilon_n^{\perp} \simeq 0.83\pi$ mm mrad. Three dimensional particle-in-cell (PIC) modelings are in good agreement with the experimental findings. The PIC simulations also indicate the generated electron bunches (or X-ray bursts) have pulse durations as short as $\sim$ 10 fs.

Résumé

Cette thèse porte sur le rayonnement X bêtatron généré par des électrons accélérés par sillage laser plasma dans des tubes capillaires diélectriques. En l'état actuel de la technologie des impulsions laser multi-térawatts, on peut produire des faisceaux ayant une intensité crête élevée, de l'ordre de 10^{18} W/cm^2 dans le plan focal. Une telle impulsion laser se propageant au sein d'un gaz sous-dense conduit à des phénomènes d'interaction laser-plasma non-linéaires, tels que la création d'une bulle plasma, i.e. une bulle ne contenant aucun électron, suivant le laser. La séparation spatiale des charges en résultant crée des champs électriques très élevés au sein de la bulle, de l'ordre de 100 GV/m, ce qui offre la possibilité d'accélérer des électrons jusqu'au GeV après seulement quelques centimètres d'interaction. En outre, un rayonnement synchrotron ultra-bref, appelé rayonnement bêtatron, est produit lors de l'accélération des électrons puisque ces derniers, soumis au champ électrique radial de la bulle plasma, ont une trajectoire oscillante. Cette thèse présente des résultats expérimentaux sur la génération et l'optimisation de faisceaux d'électrons et de leur rayonnement X, en particulier lorsque le tube capillaire est utilisé pour recueillir l'énergie du halo laser dans le plan focal facilitant l'autofocalisation du laser sur de longues distances.

La répartition spatiale du gaz, à l'état stationnaire, le long de l'axe du tube capillaire a été déterminée grâce à des simulations numériques d'écoulement de gaz. Elles démontrent qu'un gaz stable et uniformément distribué remplit le capillaire entre ces deux fentes. La dynamique de remplissage du tube capillaire par le gaz est caractérisée par une méthode basée sur un interféromètre de Mach-Zehnder. Elle suggère, pour notre dispositif expérimental, de minimiser les fuites de gaz vers l'enceinte en choisissant un temps d'ouverture de valve de 27 ms lorsque du dihydrogène est utilisé.

Des faisceaux d'électrons de quelques dizaines de picocoulomb, avec une énergie maximale allant jusqu'à 300 MeV, et dont le spectre est soit piqué à haute énergie soit exponentiellement décroissant, ont été produits dans des tubes capillaires de 10 mm de long avec l'installation laser du Lund Laser Centre (LLC, en Suède) par une impulsion laser de 40 fs d'un 16 TW Ti: Saphir. Un rayonnement bêtatron a également été mesuré, il se compose de photons X dont l'énergie est comprise entre 1 et 10 keV et atteint une luminosité maximale d'environ 10^{21} photons/s/mm^2/mrad^2/0.1%BW. Cela équivaut à environ 30 fois l'intensité des faisceaux générés dans le cas des jets de gaz de longueur 2 mm ne disposant pas de guidage optique externe. La compensation des fluctuations de pointé laser permet de minimiser les fluctuations des propriétés du faisceau d'électrons. On obtient des faisceaux d'électrons dont les fluctuations tir-a-tir sont de ~ 1 mrad en pointé, de quelques pourcents en énergie et d'environ 20% RMS en charge. De plus, il a été montré que le rayonnement bêtatron pouvait être utilisé pour caractériser le processus d'accélération des électrons en caractérisant le nombre moyen d'oscillations bêtatron effectuées par les électrons à l'intérieur de la bulle plasma. La taille typique des sources de rayonnement X (dimension pour laquelle l'intensité gaussienne est égale à $1/e^2$ de la valeur crête) est

estimée à ~ 2.5 μm en utilisant un modèle de diffraction de Fresnel induite par une lame de rasoir. Cela correspond à une émittance RMS normalisée pour le faisceau d'électrons d'environ 0.83π mm mrad. Des simulations tridimensionnelles *particle-in-cell* (PIC) ont été effectuées et confirment les résultats expérimentaux. Elles indiquent également que les paquets d'électrons générés ainsi que les flashs X directionnels sont ultra-brefs : ~ 10 fs.

Role of author

- Theoretical work
  The author numerically calculated the equations to discuss the mechanism of laser wakefield electron acceleration, as well as the spectral and spatial features of the betatron radiation generated by electron oscillation in a plasma column.

- Determination of gas density
  The author carried out the modelling of gas flow in the capillary tubes using the code FLUENT, implemented the experimental setup, measured temporal evolution of gas density in experiments after determining the most adequate method, analyzed the data and wrote a paper.

- Experiments at the Lund Laser Centre (LLC)
  The author prepared the capillary targets, the gas filling system, and the motorized controlling system. During the two campaigns at the LLC, the author was responsible for designing the experimental setup, operating the day-to-day data acquisition, together with the electron and X-ray diagnostics. The author analyzed the data of the electrons and X-rays, and wrote the publications.

- Numerical modellings
  The particle-in-cell (PIC) simulations were carried out by Hugo Ferrari who modified the code CALDER-CIRC during his postdoc at LPGP, while Olivier Dadoun from the Laboratoire de l'Accelérateur Linéaire performed the GEANT4 modellings. The author collaborated with them on data analysis and interpreting the results.

Contents

Chapter 1

Introduction

1.1 Conventional accelerator and synchrotron radiation

Accelerators are devices which accelerate charged particles to energies from MeV to TeV-scale. Nowadays accelerators play important roles in the development of science and technology. On one hand, the produced high energy charged particles have led to remarkable progress in investigations concerning fundamental particle physics and quantum physics. Therefore, ongoing research with accelerators operating at the energy frontier are strongly chased by physicists driven by their thirst to explore unknown knowledge. Taking opportunity of these "super" accelerators, physicists hope to address the most fundamental questions: the deep structure of space and time, how the universe started and evolves, and many interesting issues in the domains of quantum mechanism and general relativity. It may bring new transformations of our understandings about the universe and human being. On the other hand, 99% accelerators in operation are actually related to societal applications, for example, medical science, biology, fusion research, cancer therapy, and so forth [1].

Looking at the Lorentz force, one can easily find that only the electric field does work on charged particles while the magnetic field bends the trajectory. The first demonstration of the concept of accelerator was based on high DC electrostatic field, typical of which is the well known Van de Graaff accelerator [2]. Unfortunately, above a few MeVs the use of electrostatic fields for accelerator is limited by a major engineering difficulty, the breakdown of insulator subjected to high voltage. In order to circumvent this difficulty, new mechanisms of acceleration were proposed employing radio frequency (RF) electric field, with which much higher accelerating field can be applied before breakdown occurs [3]. Most of the currently existing GeV-class high energy accelerators therefore utilize RF fields. Typically they are composed by a series of RF cavities to accelerate charged particles periodically, as illustrated in Figure 1.1(a). However again, the acceleration gradient is still limited to less than $\sim$ 50 MV/m by cavity breakdown [3]. Therefore, accelerators with huge dimensions are built worldwide to produce charged particles with energy up to GeV, or even to TeV range. As an example, the Stanford Linear Accelerator (USA) is capable of accelerating electrons to 50 GeV over a 3 km long tunnel, as depicted in Figure 1.1(b). Moreover, to be compact, the RF cavities are circularly arranged, while using the magnetic field to rotate the charged particles, forming an accelerator called synchrotron. The world's largest and highest-energy synchrotron accelerator: the Large Hadron Collider (LHC) locates at the border between France and Switzerland built by the European Organization for Nuclear Research (CERN), will be able to boost protons to the unprecedented energy as high as 7 TeV within a 27 km ring.

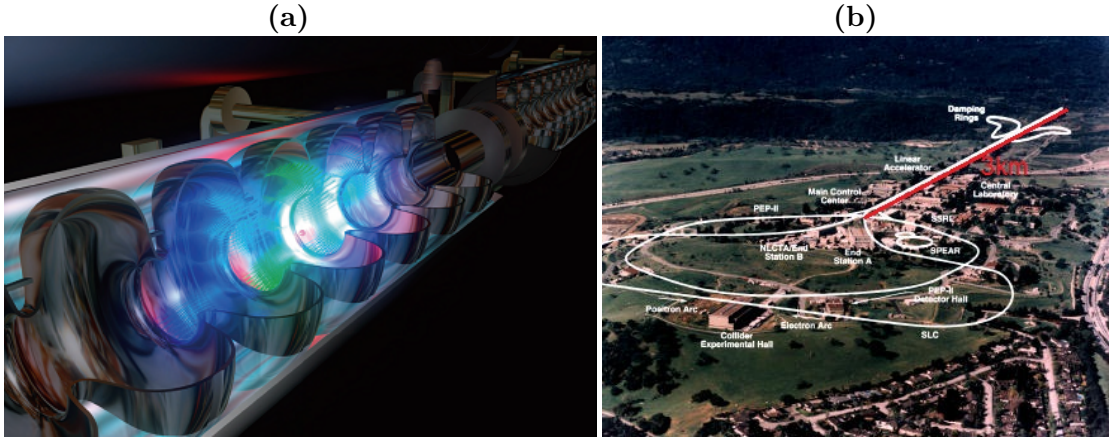

Figure 1.1: *(a) Schematic of electron acceleration by electric field inside RF cavities of conventional accelerators. (b) Aerial view of SLAC (built in Stanford, the USA) where the linac accelerates electrons to 50 GeV over 3 km. Images reproduced from the websites of DESY and SLAC.*

In a synchrotron, high energy electrons are maintained by a large storage ring which normally consists of several sections. In the so-called "beamline" section, the electrons are bent by magnetic fields to produce electromagnetic radiation, losing energy, while in the acceleration section, RF electric fields replenish them to high energy again. Therefore, the electrons can be effectively used for a long time (typically several hours). In the third generation synchrotron light sources, special insertion devices composed by hundreds of periodic magnets (called "wiggler" or "undulator") are used to enforce the flux of emission. Therefore, it is not surprising that synchrotron light sources have large dimensions as well. For example, the Soleil synchrotron facility located in the plateau of Saclay near Paris employs a 350 m circumference ring to store and boost electrons to 3 GeV. One of the three largest third generation synchrotron sources is the European Synchrotron Radiation Facility (ESRF) built in Grenoble (France), where 6 GeV electrons run in a 844 m circumference ring, as shown in Figure 1.2. The synchrotron radiation holds attractive properties [4]: high brightness ($\sim 10^{21}$ photons/s/mm^2/mrad^2/0.1%BW), high repetition rates (kHz to MHz), wide tunability in photon energy (1-20 keV), short pulse duration (tens of ps), and so on. The synchrotron lights bring renaissance of X-ray and benefit lots of multidisciplinary fields: material sciences, condensed matter physics, biological and medicine, to name a few.

Nowadays the ongoing fourth generation synchrotron sources, namely X-ray Free Electron Lasers [5], aim to produce ultrabright, coherent, time-structured hard X-ray pulses for extremely demanding and also probably yet-to-be-conceived experiments. In this new regime, a low-emittance relativistic electron bunch passes through a sufficiently long undulator, where beam-wave interaction entails X-rays generated by the mechanism of self amplified spontaneous emission (SASE) as what happens in a conventional laser [6]. The Linac Coherent Light Source built at the SLAC (USA) produced the first lasing of the fourth generation synchrotron source with X-ray wavelength as low as 1.5 Å and unprecedented peak brightness of the order of 10^{32} photons/s/mm^2/mrad^2/0.1%BW [7]. Other future facilities under construction are: the European X-ray Laser Project (XFEL) housed at the Deutsches Elektronen-Synchrotron (DESY) in Hamburg (Germany), Spring-8 (SCSS) in Japan, and the Fourth Generation Light Source (4GLS) at Daresbury Laboratory in the UK. Those remarkable advances in synchrotron sources will open many new avenues

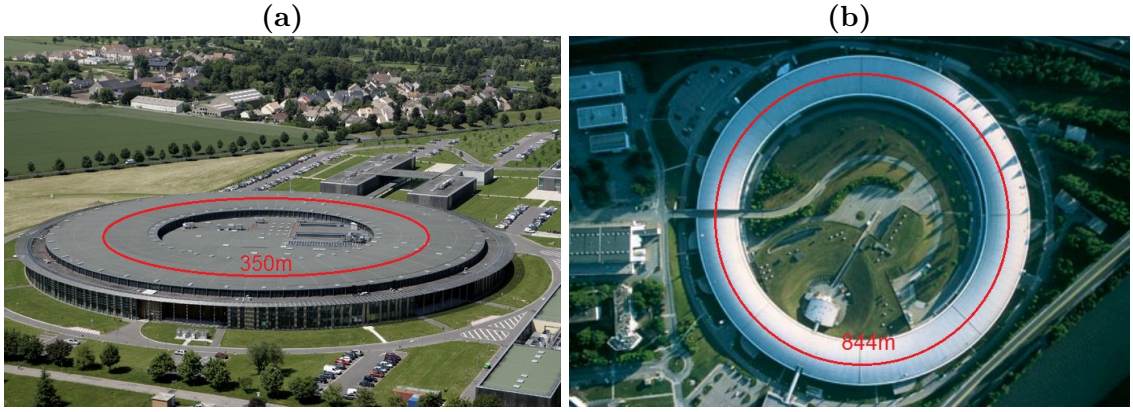

Figure 1.2: *Aerial photographs of (a) Soleil synchrotron light source (Plateau of Saclay, France) which boosts electrons to 3 GeV in a 350 m circumference ring. (b) European Synchrotron Radiation Facility (Grenoble, France) using 6 GeV electrons stored by a ring with perimeter of 844 m. Images reproduced from the websites of Soleil and ESRF.*

for scientific research which can not be realized before.

One coin has two sides. While the huge synchrotron accelerators offer plenty of new opportunities, they become extremely expensive. Such large facilities are usually funded by several countries under international projects. To have an idea: the budget of the European XFEL project is 1.1 billion Euros shared by 13 nations [8]. In long terms, if we expect charged particles with even higher energy in future, the size and cost of accelerator would become prohibitive. In this context, physicists started to think about the question: is there an alternative scheme to achieve energy frontier particles while significantly reducing the sizes of the present RF accelerators and particularly their costs?

1.2 Plasma-based acceleration and betatron X-ray radiation

The energy gained by a charged particle in an accelerator is determined by the product of accelerating gradient and distance. In order to reduce the accelerator size, the accelerating gradient has to be increased. In order to overcome the limitation on accelerating gradient by electrical breakdown in RF cavity, Tajima and Dawson first proposed to accelerate electrons via plasma wave in 1979 [9]. The concept relies on the use of the ultrahigh electric filed associated with charge separation in plasma. Electric fields of the order of ~ 100 GV/m can be sustained in an underdense plasma [10], which is three to four orders of magnitude higher than that in the conventional RF accelerators.

Generally, the current plasma-based accelerators may be classified into two kinds according to the mechanism of plasma wave generation. When the plasma wave is excited by charged particle bunch(es) (electrons, or protons), it is called plasma wakefield acceleration (PWFA) [11, 12, 13, 14, 15, 16, 17], while it is referred to as laser wakefield acceleration (LWFA) if the plasma wave is driven by a laser pulse [9, 18, 19, 20, 21, 22].

In the PWFA, the Coulomb force due to the space charge effect of the driving beam sets up a plasma wave which accelerates either an externally injected "witness" bunch or part of the driving bunch itself. The basic concept of PWFA was introduced by Chen *et al* in 1985 [11], and it was further developed to 2D nonlinear regime by Rosenzweig *et al* in 1991 [13]. It was also Rosenzweig and coworkers who for the first time tested the physics of PWFA, where an accelerating field around ~ 1 MV/m was observed with a 21 MeV, $\sim 2-3$ nC electron bunch [12]. More recently, spectacular work was carried out at the

SLAC (USA), where the energy of some electrons at the tail part of the driving bunch (43 GeV) was doubled to 85 GeV over a 85 cm long plasma medium [15]. The inferred peak accelerating gradient reached $\sim$ 52 GV/m. Even though the final electron bunch energy is dominated by an exponential distribution, it is still impressive that one meter long plasma gives the same energy gain as a 3 km long RF tunnel does.

Recently, the generation of plasma wave by proton beams was examined in simulation [16, 23]. The authors demonstrate this scheme of proton-driven PWFA is capable of scaling the energy gain of electrons up to the TeV range, which would be a significant step forward towards the energy frontier of particle physics [24]. Notwithstanding, the main drawback of PWFA is that PWFA relies on conventional RF accelerator, which contradicts the ultimate motivation of developing plasma-based accelerators.

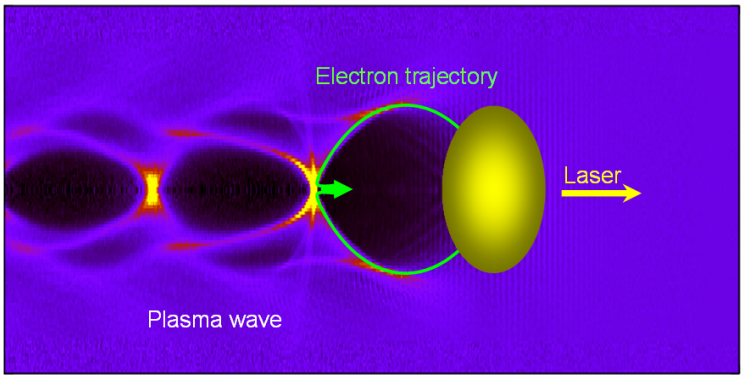

Figure 1.3: *Schematic of laser wakefield acceleration in the bubble regime. See more details in Chapter 2.*

In LWFA, plasma wave is excited by laser pulse. The ponderomotive force [25] associated with an intense laser pulse creates a plasma wave which can accelerate either externally injected or self-trapped plasma electrons to relativistic energy. In their pioneering work [9], Tajima and Dawson proposed the scheme of plasma beat-wave acceleration (PBWA) as an alternative to LWFA, since intense, ultrashort laser pulses were not available in 1979. In PBWA, two long laser pulses copropagate and excite a plasma wave, where the beat frequency of the two laser drivers roughly matches the plasma frequency. Observation of plasma wave generation and electron acceleration in PBWA were demonstrated by several groups[26, 27, 28, 29]. In those proof-of-principle experiments, the laser-driven plasma waves accelerated electrons provided by external sources, because the plasma wave is too weak to trap electrons from the background plasma. For example in Ref. [28], Everett *et al* injected a 2 MeV electron bunch into a plasma wave, and observed electron acceleration with maximum energy gain of 28 MeV.

The emergence of short (<1 ps) ultraintense (>10^{18} W/cm^2) laser beams, based on the chirped pulse amplification (CPA) technology [30], stimulated laser-plasma accelerator research to a new regime: self-modulated LWFA. As indicated by the name, in self-modulated LWFA the laser pulse that propagates in a plasma experiences nonlinear instability, which eventually modulates the driving laser into a train of resonant oscillations. The length of the laser oscillation equals plasma wavelength, so the modulated laser excites a large amplitude plasma wave [31]. The self-modulated LWFA was extensively investigated worldwide [32, 33, 34]. Particularly, in the experiments in Refs. [32, 33], the accelerated electrons were trapped by the plasma waves from the background plasma but not provided by external electron sources. The self-trapping happened when the

plasma waves were driven to the threshold of wavebreaking. This finding was a significant progress for LWFA, because it means LWFA does not necessarily rely on external injection of electrons. Hence, the experimental setup could be greatly simplified. Nevertheless, the obtained electron energy spectrum was still Maxwellian-like with only a low number electrons extending to high energy.

Subsequently, the developments in laser technology have made intense, ultrashort pulsed laser (tens of femtoseconds, 10^{19} W/cm^2) readily available [35]. Along with deeper understandings of the mechanism of LWFA in terms of simulation [36] and experiment [10], a breakthrough in LWFA was achieved in 2004 when Mangles *et al* [37], Geddes *et al* [38], and Faure *et al* [39] for the first time obtained spectrally peaked[1] electron bunches in experiment. By matching the laser duration and plasma wavelength operating in the so-called "bubble" (or "blowout") regime, these three groups produced ∼100 pC electrons at an energy of ∼100 MeV with energy spread of only a few percent. Due to the great importance of spectrally peaked electrons for applications, this success is often viewed as a milestone of the LWFA development. In 2006, the electron energy was boosted to ∼ 1 GeV by guiding the laser pulse over a 3 cm long plasma channel [40].

Meanwhile new techniques were developed to improve the quality of electron bunch. Employing a sophisticated laser colliding method, Faure *et al* achieved stable and energy tunable relativistic electrons [41]. Staged acceleration which separates the processes of electron injection and acceleration provides more tunability and controllability over the produced electrons [42, 43, 44]. Novel plasma targets boomed the development of LWFA as well. Adopting a gas-cell, Osterhoff *et al* generated stable high energy electrons [45]. Lately, Genoud *et al* demonstrated that dielectric capillary tube is able to assist laser guiding over a longer distance than in a gas-cell [46, 47], which is beneficial for generating higher energy electrons and more intense X-rays [48].

Diagnostics of the plasma wave and the electrons bunch also made tremendous progresses [49, 50, 51, 52]. Especially, two important parameters about the electrons, bunch length and transverse emittance, have been finely characterized. In Refs. [51, 52], the authors reported that the accelerated electron bunches were as short as a few femtoseconds, while the measurements in Refs. [53, 54] show that the relativistic electrons possess normalized emittance as low as $\leq 1\pi$ mm mrad. Those high quality electrons are of great interest for many scientific applications, such as the generation of ultrashort light pulses. In the proof-of-principle experiment, the electrons obtained from a LWFA were sent to an external undulator to generate visible to soft X-ray synchrotron radiations [55, 56]. The observed X-ray peak brightness was of the order of $10^{16} - 10^{17}$ photons/s/mm^2/mrad^2/0.1%BW.

Also in 2004, a breakthrough was achieved in ultrashort X-ray generation. Rousse *et al* produced an X-ray pulse based on LWFA but not using an external wiggler [57]. In this scheme, the radial eclectic field inside the plasma bubble forces the electrons to oscillate transversely when they are accelerated. This oscillation, known as "betatron oscillation", produces an X-ray beam. The plasma cavity itself plays the role of accelerator and wiggler together. This approach attracted a lot of interest, not only because it simplifies the means of X-ray generation, but also because the produced X-rays hold striking properties: ultrashort pulse duration in femtosecond scale and perfect synchronization to the pump laser. More recently, performing in the highly nonlinear bubble regime ∼10 keV X-ray photons with peak brightness of 10^{22} photons/s/mm^2/mrad^2/0.1%BW were achieved in experiment by Kneip and coworkers [58]. The photon energy was later extended to the

[1] We do not use the word "quasi-monoenergetic", as it is not clearly defined in the LWFA community. Instead, "spectrally peaked" is used to describe the electron beam displaying a clear peak in the spectrum, for which the energy spread around the peak energy can be defined.

gamma-ray range by Cipiccia *et al* through enhancing the betatron oscillation amplitude with laser electron modulation [59]. Furthermore, when a gas-cell or capillary tube is used, betatron X-ray radiation offers an approach to visualize the process of electron trapping and acceleration inside the plasma bubble [46, 60].

1.3 Objective and outline of the thesis

The objective of this work is to investigate laser wakefield acceleration of electrons and the associated betatron X-ray radiation driven by a guided laser in dielectric capillary tubes. While many laboratories around the world are pursuing higher and higher electron energy using increasing laser power, our main goal is to improve the performances of LWFA by utilizing capillary tubes.

The use of capillary tube in LWFA has been studied for more than a decade in our group: Interaction et Transport de Faisceaux Intenses dans les Plasmas (ITFIP) at the Laboratory of Physique des Gaz et des Plasmas (LPGP). In previous work [61, 62], a $\sim 10^{16}$ W/cm^2 laser pulse was guided by capillary tubes over 100 Rayleigh lengths, and the diagnostic of linear plasma waves driven by $\sim 10^{17}$ W/cm^2 laser pulses in centimeter-scale long capillary tubes was demonstrated. This thesis is especially devoted to exploring the highly nonlinear bubble regime of laser-plasma interaction in capillary tubes with laser intensity in the range of $\sim 10^{18} - 10^{19}$ W/cm^2.

During the PhD study, many efforts were spent on designing a new system to control gas filling into capillary tubes, and spatially and temporally characterizing gas density evolution in capillary tubes in experiment and fluid simulation. This work was done at LPGP. Two campaigns were performed at the Lund Laser Centre (LLC) in Sweden, where the contributions of capillary tube to laser guiding, electron acceleration, X-ray generation, beam stability, and the associated diagnostics were examined. The results obtained from those experiments are discussed in this manuscript.

The thesis is organized as follows. **Chapter 2** presents the main physics relevant to laser wakefield acceleration of electrons, while the theories and calculations associated with betatron X-ray radiation are given in **Chapter 3**. In **Chapter 4**, we show the numerical and experimental characterizations of capillary tube in terms of laser guiding and determination of gas density inside the capillary tubes. **Chapter 5** introduces the multi-terawatt laser facility at the LLC, and discusses the diagnostic methods conducted to measure the data. The observed electrons, X-rays, and their stability are demonstrated in **Chapter 6**. Finally, **Chapter 7** summarizes the work presented in this manuscript.

Chapter 2

Laser wakefield acceleration

When an ultrashort intense laser pulse propagates in an underdense plasma, the associated ponderomotive force drives a plasma wave, which is able to trap and accelerate some background electrons to ultrarelativistic energy. In this chapter, we present theoretical work associated with the key issues of laser wakefield acceleration, including plasma wave generation, nonlinear laser propagation, electron trapping, beam loading, and so forth. We also introduce the 3D nonlinear bubble regime and the related phenomenological scaling laws.

2.1 Laser electron interaction

2.1.1 Laser

Laser wakefield acceleration (LWFA) [9] employs powerful ultrashort laser pulses at the forefront of laser research and development, and LWFA has progressed significantly since the implement of the CPA technology [30]. The electromagnetic field of laser is described by Maxwell's equations (See Appendix A.1). The laser pulse is usually modeled by Gaussian functions in space and time as a good approximation of experimental profiles. The electric field $\mathbf{E}$[1] of such a bi-Gaussian laser beam propagates in vacuum along the z axis is given by

$$\begin{aligned}\mathbf{E}(r,z,t) =& E_L \frac{w_0}{w(z)} \exp\left[-\frac{r^2}{w^2(z)}\right] \exp\left[-2\ln(2)\frac{(z-ct)^2}{c^2\tau_0^2}\right] \\ & \times \Re\left\{\exp\left[i\omega_0 t - ik_0 z - ik_0\frac{r^2}{2R(z)} + i\psi_g(z)\right]\mathbf{e}_\perp\right\},\end{aligned} \tag{2.1}$$

where E_L is the amplitude of the electric field, w_0 is the waist of the laser transverse size in the focal plane ($z = 0$), c denotes the speed of light in vacuum, and τ_0 is the full width at half maximum (FWHM) pulse duration. $k_0 = 2\pi/\lambda_0$ and $\omega_0 = ck_0$ represent the wavenumber and angular frequency[2] of a laser light with wavelength λ_0. The unit vector $\mathbf{e}_\perp$ indicates the polarization of the laser. For a laser linearly polarized in the x direction: $\mathbf{e}_\perp = \mathbf{e}_x$; while for circular one: $\mathbf{e}_\perp = 1/\sqrt{2}(\mathbf{e}_x \pm i\mathbf{e}_y)$. In this thesis, we only consider the case of linear polarization.

The propagation of the Gaussian laser pulse is fully characterized by the beam waist $w(z)$, the radius of curvature of the wavefront $R(z)$, and the Gouy phase term $\psi_g(z)$.

[1] The bold symbols are vectors.

[2] Note the difference in writing between laser beam waist w_0 and angular frequency ω_0.

These parameters evolve along the z axis as

$$\begin{aligned} w(z) &= w_0\sqrt{1+\left(\frac{z}{z_R}\right)^2}, \\ R(z) &= z\left[1+\left(\frac{z}{z_R}\right)^2\right], \\ \psi_g(z) &= \arctan\left(\frac{z}{z_R}\right), \end{aligned} \tag{2.2}$$

where $z_R = \pi w_0^2/\lambda_0$ is the Rayleigh length which represents the length over which the laser transverse area is doubled due to diffraction. The beam divergence in the far-field ($z \gg z_R$) is given by $\theta_L \simeq \lambda_0/\pi w_0$, as illustrated in Figure 2.1.

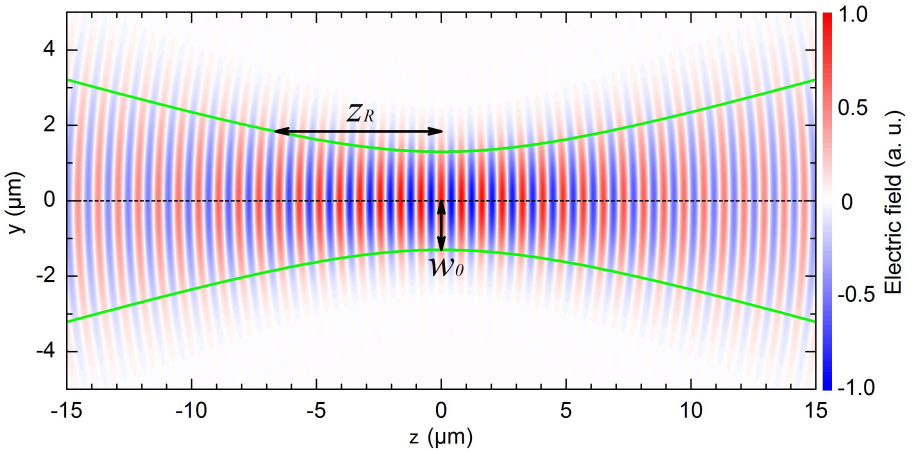

Figure 2.1: *Propagation of a Gaussian beam with $w_0 = 1.3$ μm in vacuum at $z = 0$. The laser wavelength is 0.8 μm, corresponding to the Rayleigh length $z_R \simeq 6.6$ μm.*

In some cases, it is convenient to describe the electromagnetic fields $\mathbf{E}$ and $\mathbf{B}$ in terms of the scalar potential Φ and the vector potential $\mathbf{A}$ to be

$$\begin{aligned} \mathbf{E} &= -\nabla\Phi - \frac{\partial \mathbf{A}}{\partial t}, \\ \mathbf{B} &= \nabla \times \mathbf{A}. \end{aligned} \tag{2.3}$$

Since the potentials defined by the above equations are not unique, the Coulomb gauge $\nabla \cdot \mathbf{A} = 0$ is often adopted to close the equations. Especially in vacuum $\Phi = 0$, both the fields $\mathbf{E}$ and $\mathbf{B}$ depend only on the vector potential $\mathbf{A}$.

In experiment, we usually measure the laser energy $\mathcal{E}_L$ and pulse duration τ_0. The laser power is calculated by

$$P = 2\sqrt{\frac{\ln(2)}{\pi}}\frac{\mathcal{E}_L}{\tau_0} \simeq \frac{\mathcal{E}_L}{\tau_0}. \tag{2.4}$$

The corresponding peak laser intensity in the focal plane is

$$I_0 = \frac{2P}{\pi w_0^2} \simeq \frac{2\mathcal{E}_L}{\pi \tau_0 w_0^2}. \tag{2.5}$$

Through Equation 2.5, one can assess the peak amplitude of the laser electric field via the definition of laser intensity

$$I_L = c^2\varepsilon_0\langle \mathbf{E} \times \mathbf{B}\rangle = \frac{c\varepsilon_0}{2}|\mathbf{E}|^2, \tag{2.6}$$

where $\varepsilon_0 = 8.85 \times 10^{-12}$ F/m is the permittivity of free space.

2.1.2 Electron motion in the laser field

In order to study the collective phenomena in relativistic laser-plasma interaction, a good starting point is the specific trajectory of a single electron with charge $-e$ and mass m_e in the laser electromagnetic field. The motion of an electron in the fields $\mathbf{E}$ and $\mathbf{B}$ is described by the Lorentz equation

$$\frac{d\mathbf{p}}{dt} = -e(\mathbf{E} + \mathbf{v} \times \mathbf{B}), \tag{2.7}$$

where $\mathbf{p} = \gamma m_e \mathbf{v}$ is the electron momentum, $\gamma = (1-\beta^2)^{-1/2}$ is the relativistic factor, and $\beta = v/c$ denotes the normalized velocity. We first consider the simplest case: the laser is a plane electromagnetic wave polarized along the x axis and propagating along the z axis as $\mathbf{E}(z) = E_L \cos(k_0 z - \omega_0 t)\mathbf{e}_x$. Very often, the electric field is written in the form of the vector potential by using Equation 2.3: $\mathbf{A}(z) = A_0 \sin(k_0 z - \omega_0 t)\mathbf{e}_x$ with $A_0 = E_L/\omega_0$. Taking into account the amplitude relationship of $|\mathbf{B}| = \frac{1}{c}|\mathbf{E}|$, the second term on the right side of Equation 2.7 can be neglected in the nonrelativistic regime when $\beta \ll 1$. Then Equation 2.7 is simplified to

$$\frac{d\mathbf{p}}{dt} \simeq -e\mathbf{E} = e\frac{\partial \mathbf{A}}{\partial t}. \tag{2.8}$$

Therefore an electron, initially at rest at $z = 0$, oscillates in the direction of the electric field with velocity of

$$\beta = -\frac{eA_0}{mc}\sin(\omega_0 t) \equiv -a_0 \sin(\omega_0 t), \tag{2.9}$$

where $a_0 = eA_0/mc = eE_L/mc\omega_0$ is the normalized vector potential (or laser strength). It is obvious to find from Equation 2.9 that once the laser has passed by the electron, the electron will go back to rest. There is no energy transferred from the laser to the electron.

When the laser field is very strong ($a_0 \gtrsim 1$), the electron oscillation velocity will approach c, and then the $\mathbf{v} \times \mathbf{B}$ component in Lorentz force must be taken into account. The solution of Equation 2.7 in the relativistic regime can be found in Ref. [63]. Following their approach, we rewrite the laser field as $\mathbf{a}(z) = a_0 \sin(k_0 \xi)\mathbf{e}_x$, where $\xi = z - ct$ is the coordinate in the frame co-moving with the laser. The normalized momentum of the electron was found to be

$$\begin{aligned} u_x = \gamma\beta_x = \frac{dx}{d\xi} = a = a_0 \sin(k_0\xi), \\ u_z = \gamma\beta_z = \frac{dz}{d\xi} = \frac{a^2}{2} = \frac{a_0^2}{2}\sin^2(k_0\xi). \end{aligned} \tag{2.10}$$

We can see that the electron velocity is always positive in the longitudinal z direction, which means the $\mathbf{v} \times \mathbf{B}$ force pushes the electron to move forward. Integrating Equation 2.10 gives the electron trajectory

$$\begin{aligned} x = -\frac{a_0}{k_0}\cos(k_0\xi), \\ z = \frac{a_0^2}{8k_0}[2k_0\xi - \sin(2k_0\xi)]. \end{aligned} \tag{2.11}$$

Equation 2.11 indicates the electron not only moves forward but also oscillates with twice the laser frequency in the longitudinal direction. Figure 2.2 shows the electron

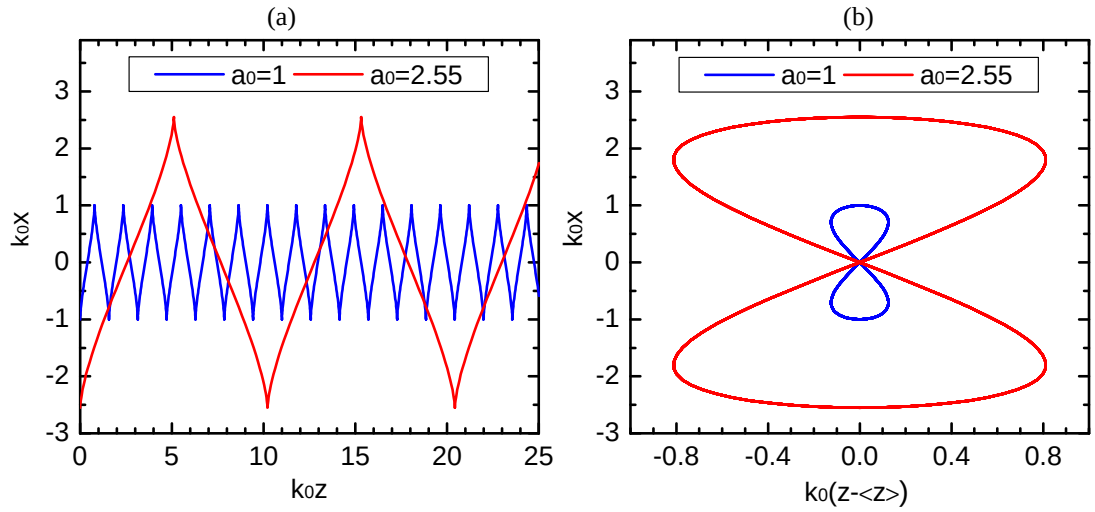

Figure 2.2: *Electron trajectories seen from (a) the laboratory frame, and from (b) the frame co-moving with the electron.*

trajectories corresponding to $a_0 = 1$ and $a_0 = 2.55$. When it is seen in the laboratory, the electron displays a zig-zag shaped trajectory, while the well-known eight-shaped motion is observed in the frame moving with the average velocity of the electron. Moreover, the longitudinal momentum scales with the square of the laser strength as $a_0^2/2$, while the transverse one linearly depends on the laser strength a_0. Hence, at higher electric field ($a_0 \gg 1$) the longitudinal motion of the electron becomes dominant over the transverse oscillation. It is also of interest to determine when the longitudinal motion becomes dominant. To do this, we consider the excursion distances that the electron moves in the x and z axes over one period. The distance along the x axis is four time the oscillation amplitude given by Equation 2.11, namely $L_x = 4a_0/k_0$, while that along the z axis can be calculated by

$$L_z = \int_0^{2\pi/k_0} \frac{dz}{d\xi} d\xi = \frac{a_0^2}{8k_0} \int_0^{2\pi/k_0} [2k_0 - 2k_0 \cos(2k_0\xi)] d\xi = \frac{\pi a_0^2}{2k_0}. \tag{2.12}$$

A critical value can be determined when the two distances become equal

$$L_x = 4\frac{a_0}{k_0} = L_z = \frac{\pi a_0^2}{2k_0}, \tag{2.13}$$

which yields $a_0 = 8/\pi \simeq 2.55$. To assess the corresponding laser intensity, we substitute Equation 2.6 into the definition $a_0 = eE_L/mc\omega_0$, and get a practical formula

$$a_0 = \sqrt{\frac{e^2}{2\pi^2 \epsilon_0 m_e^2 c^5} \lambda_0^2 I_0} \simeq 0.86\lambda[\mu\text{m}]\sqrt{I_0[10^{18}\text{W/cm}^2]}. \tag{2.14}$$

For laser wavelength of 0.8 μm, $a_0 = 2.55$ corresponds to $I_0 = 1.4 \times 10^{19}$ W/cm^2. Such a laser intensity can be reached by the state-of-the-art multi-terawatt laser facilities [35].

The analysis above shows the importance of operation in the relativistic regime in order to achieve electron motion along the laser propagation direction. Nevertheless, as shown in Figure 2.2(a), the electron is merely pushed forward in each light cycle but does not gain any energy from the laser. The overall net effect is only to transfer the electron to a new longitudinal position. Once the laser passes by, the electron will remain at rest.

However, it is noteworthy that the laser discussed in this section is an uniform and infinite plane wave. This is definitely not the real case in experiment, where the laser pulses are normally tightly focused. The laser intensity is not uniform but Gaussian-like in the transverse plane. As shown in the following part, the ponderomotive force associated with the laser intensity gradient will excite a plasma wave which plays as a medium to transfer laser energy to electrons.

2.1.3 Ponderomotive force

A plasma wave is driven by the laser pulse through the so-called ponderomotive force [25]. It is actually the force associated with the second-order electron motion. From Equation 2.7, it was found that the first-order electron quiver momentum in the nonrelativistic case is $\mathbf{p}_q = m_e c\mathbf{a}$ [See Equation 2.9]. Supposing there is a small perturbation of the electron motion, namely $\mathbf{p} = \mathbf{p}_q + \delta\mathbf{p}$ ($\delta\mathbf{p} \ll \mathbf{p}_q$), the net second-order motion over one laser cycle is given by

$$\begin{aligned}\left\langle \frac{d\delta\mathbf{p}}{dt} \right\rangle &= -m_e \left\langle [(\mathbf{v}_q \cdot \nabla)\mathbf{v}_q + c\mathbf{v}_q \times (\nabla \times \mathbf{a})] \right\rangle \\ &= -m_e c^2 \left\langle [(\mathbf{a} \cdot \nabla)\mathbf{a} + c\mathbf{a} \times (\nabla \times \mathbf{a})] \right\rangle \\ &= -m_e c^2 \nabla \left\langle \frac{a^2}{2} \right\rangle \equiv \mathbf{F}_p,\end{aligned} \tag{2.15}$$

where $\mathbf{F}_p = -m_e c^2 \nabla \langle \frac{a^2}{2} \rangle = -m_e c^2 \nabla \frac{a_0^2}{4}$ is the 3D ponderomotive force [25]. In the 3D nonlinear regime, the ponderomotive force is generalized to be $\mathbf{F}_{pN} = -m_e c^2 \nabla (1 + \frac{a_0^2}{2})^{1/2}$ [64]. Accordingly we can define the ponderomotive potential as $\Phi_{pN} = m_e c^2 (1 + \frac{a_0^2}{2})^{1/2}$.

Basically the ponderomotive force can be viewed as the radiation pressure of laser intensity. Such a force will eject charged particles out of the region of high laser intensity, and the ponderomotive force does not depend on the sign of charged particles. Furthermore, the ponderomotive force is inversely proportional to the charged particle mass $F_p \propto \frac{1}{m}$. Hence for a given laser field, the acceleration exerted on a proton is only 10^{-6} times that of an electron. That's why we will treat the ions as immobile in the process of plasma wave generation in Section 2.2.3.

As an example, when the peak laser intensity $I_0 \simeq 1.7 \times 10^{19}$ W/cm^2 (corresponding to $a_0 = 2\sqrt{2}$), the ponderomotive potential is $\Phi_{pN} = \sqrt{5} m_e c^2 \simeq 1.1$ MeV. Therefore it is not possible to accelerate electrons to high energy directly via the ponderomotive force, however the ponderomotive force makes a crucial contribution to the mechanism of LWFA: exciting plasma wave.

2.2 Laser-plasma interaction

The single-particle analysis shows that the laser electron interaction in vacuum is not suitable for electron acceleration. However, the physics will be significantly changed when the laser beam interacts with a plasma, in which the electrons exhibit a collective behavior.

2.2.1 Ionization

Plasma, after solid, liquid, and gas, is the fourth state of matter. Plasma is defined as an electrically neutral medium which exhibits collective behavior [65]. It is often stated that more than 99% materials all over the universe are in plasma state [66]. However,

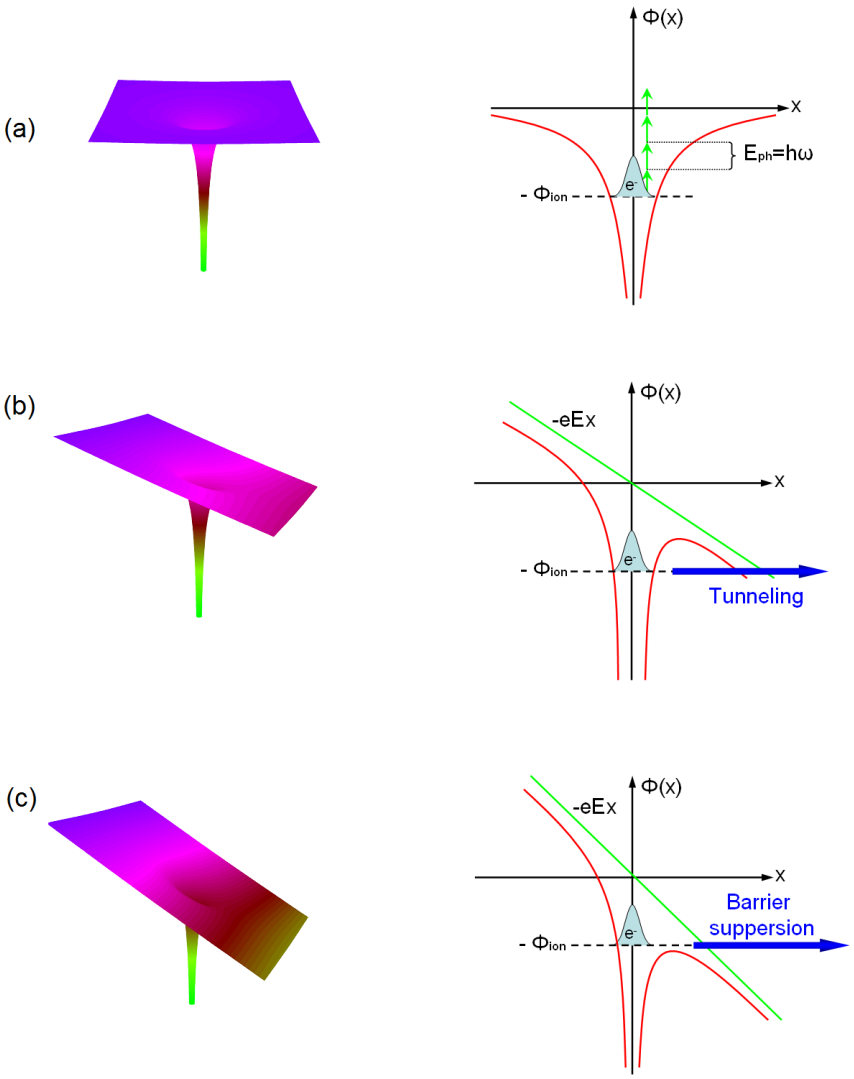

Figure 2.3: *Schematics of (a) the Coulomb potential and the multi-photon ionization, (b) the perturbed Coulomb potential by an external electric field and tunneling ionization, (c) the suppressed potential and barrier suppression ionization.*

plasma does not naturally exist in atmospherical environment where the shell electrons are bounded to the nuclei by Coulomb force. Plasma can be obtained by ionizing atoms in some special conditions, such as heating, discharge, strong electric field, and so forth.

In the domain of LWFA, plasma is sometimes produced by an external high voltage discharge [67] or more generally by the powerful laser pulse itself. In this thesis, we work with the latter, and the gas that we use is hydrogen. The photon energy of a Ti:sapphire laser ($\lambda_0 = 800$ nm) is about $\mathcal{E}_{ph} = \hbar\omega_0 \simeq 1.6$ eV, while the potential of the ground state of hydrogen is 13.6 eV. It is obvious that the laser photon is not able to ionize hydrogen by the photoelectric effect. However, if the laser intensity is very high, new processes of ionization will occur. The different regimes of ionization may be distinguished by the Keldysh parameter [68]

$$\Gamma = \omega_0 \sqrt{\frac{2\Phi_{ion}}{I_L}}, \tag{2.16}$$

which indicates the ratio between the atomic ionization potential Φ_{ion} and the laser intensity I_L. When $\Gamma \gg 1$, the binding potential inside the atom is not significantly disturbed by the external electric filed. In this sense, the atom can be ionized by the process of multi-photon absorption, as illustrated in Figure 2.3(a). For instance, the shell electron of hydrogen can overcome the potential barrier by properly absorbing 9 laser photons of 800 nm.

When the laser field is comparable to the Coulomb field inside the atom ($\Gamma \simeq 1$), the binding potential is drastically deformed, as shown in Figure 2.3(b). As seen, the barrier that the electron has to pass decreases, implying the electron can escape more easily. This mechanism is called tunneling ionization. The probability of tunneling ionization is predicted by the theoretical ADK model [69]. The more the potential is distorted, higher is the probability that the electron tunnels through the barrier.

When the laser field becomes so strong ($\Gamma \gg 1$) that the potential is completely depressed below the ground state of hydrogen, the electron is no longer bound, and the atom is ionized. This mechanism is called barrier suppression ionization (BSI), and shown in Figure 2.3(c). The threshold of laser intensity required by BSI can be estimated as follows. The effective potential seen by the electron is

$$V(r) = -\frac{e^2}{4\pi\varepsilon_0 r} - eE_L r. \tag{2.17}$$

There is a position r_{max} where the potential reaches its maximum. r_{max} can be easily found from $\frac{dV(r)}{dr} = 0$ to be $r_{max} = (e/4\pi\varepsilon_0 E_L)^{1/2}$. Equalling the maximum potential $V(r_{max})$ to the ionization potential Φ_{ion} gives the threshold of laser intensity for BSI (using Equation 2.6)

$$I_{BSI} = \frac{\pi^2 c\varepsilon_0^3 \Phi_{ion}^4}{2e^6}. \tag{2.18}$$

In order to ionize hydrogen via the BSI mechanism, the laser intensity needs to exceed 1.4×10^{14} W/cm^2. In our experiment, the laser intensity in the focal plane reaches the range of $10^{18} - 10^{19}$ W/cm^2 which is at least four orders of magnitude higher than that required for ionization of hydrogen. It means the leading edge of the focused laser will completely ionize the neutral hydrogen gas, while the laser bulk interacts with the preformed plasma.

The ionization process not only provides plasma, but also closely affects laser-plasma interaction. Especially for some petawatt laser facilities, even the amplified spontaneous emission (ASE) pedestal of the main pulse is intense enough to ionize the gas if the pulse contrast is not well controlled. This unexpected plasma formation may degrade the electron energy and pointing stabilities [70]. On the other hand, ionization offers a chance to tune the position of creation of an electron when it is trapped by plasma wave [71, 72]. This technique is known as ionization injection, by which the high electron energy up to 1.45 GeV was obtained from a 1.3 cm long gas-cell by Clayton *et al* in 2010 [73].

2.2.2 Electromagnetic waves in plasmas

As discussed before, the ponderomotive force of laser expels electrons from high laser intensity regions. In vacuum, electrons will go back to rest at their new positions, however in a plasma the electric field induced by space charge separation will pull the ejected electrons to their original positions. Because of the inertia of the electrons, they will overshoot and oscillate around their equilibrium positions. This oscillation forms a plasma wave. As the plasma wave is created by and closely follows the driving laser pulse, it is often called laser wakefield.

The periodic electron oscillation can be decomposed by Fourier analysis into a superposition of many sinusoidal oscillations. If we consider small amplitude oscillation, the waveform consists of only one harmonic component $e^{i(\mathbf{k}\cdot\mathbf{r}-\omega t)}$. From the Maxwell's equations (Appendix A.1), one can obtain the EM wave equation in plasma

$$\mathbf{k}\times\mathbf{k}\times\mathbf{E}_k = \mu_0\left(\frac{\rho_e e^2}{m_e} - \varepsilon_0\omega^2\right)\mathbf{E}_k, \tag{2.19}$$

where $\mu_0 = 4\pi\times10^{-7}$ H/m is the permeability of free space, and ρ_e represents plasma electron density.

For $\mathbf{k}||\mathbf{E}_k$, the left side of Equation 2.19 equals zero. The right side gives the frequency of plasma oscillation (or plasma frequency):

$$\omega \equiv \omega_p = \sqrt{\frac{\rho_e e^2}{m_e\varepsilon_0}}. \tag{2.20}$$

This plasma oscillation is also called a Langmuir wave. In the nonlinear regime, the plasma frequency is modified by the relativistic effect to $\omega_{pN} = \omega_p/\sqrt{\gamma}$. Such a wave is of vital importance for electron acceleration, because it is a longitudinal wave: direction of electric field is parallel to the light propagation direction.

For $\mathbf{k}\perp\mathbf{E}_k$, Equation 2.19 gives the dispersion relation of an electromagnetic field in plasma

$$\omega_0^2 = \omega_p^2 + c^2k^2. \tag{2.21}$$

Two cases can be drawn from Equation 2.21. For $\omega_0 > \omega_p$, k is real and the laser can propagate in the plasma, whereas k becomes imaginary for $\omega_0 < \omega_p$, and the wave is evanescent. The light is either transmitted or damped in the plasma depending on the plasma density. The critical density is defined when $\omega_0 = \omega_p$, which yields

$$\rho_c[10^{21}\mathrm{cm}^{-3}] = \frac{\omega_0^2 m_e\varepsilon_0}{e^2} = \frac{1.12}{\lambda_0^2[\mu\mathrm{m}]}. \tag{2.22}$$

Numerically for a laser wavelength of 0.8 μm, the corresponding critical density is 1.75×10^{21} cm^{-3}. For $\rho_e < \rho_c$ the plasma is called underdense, while on the contrary it is called overdense for $\rho_e > \rho_c$. LWFA is linked to the excitation of a plasma wave in the underdense regime.

Based on Equation 2.21, we can calculate the phase and group velocities of an EM wave in an underdense plasma

$$\begin{aligned} v_{ph} &= \frac{\omega_0}{k} = \sqrt{c^2 + \frac{\omega_p^2}{k^2}}, \\ v_g &= \frac{d\omega_0}{dk} = \frac{c^2}{v_{ph}} = \frac{c^2k}{\sqrt{c^2k^2+\omega_p^2}}. \end{aligned} \tag{2.23}$$

If the evolution of the driving laser pulse in the plasma is not significant, the phase velocity of the plasma wave is equal to the group velocity of the driving laser [18]. Therefore we can calculate the normalized phase velocity and relativistic factor of the plasma wave

$$\begin{aligned} \beta_p &= \frac{v_g}{c} = \sqrt{1-\frac{\rho_e}{\rho_c}}, \\ \gamma_p &= \frac{1}{\sqrt{1-\beta_p^2}} = \sqrt{\frac{\rho_c}{\rho_e}}. \end{aligned} \tag{2.24}$$

As will be presented, the phase velocity of the plasma wave is of great importance to determine the minimum energy required for electron trapping and the energy gain of accelerated electrons. Basically, the lower the density is, the higher the phase velocity becomes, and furthermore higher electron energy can be achieved. That is why for LWFA experiments the ultra-underdense regime ($\rho_e \ll \rho_c$) is desirable.

2.2.3 Plasma wave

In this section, we discuss the excitation of plasma wave by laser ponderomotive force, and the properties associated with the plasma waves in both linear and nonlinear regimes.

Linear regime

The general solution of the equation of linear plasma wave is given in Equation A.8. Particularly for a Gaussian laser pulse described Equation 2.1, the solutions are

$$\begin{aligned}
\frac{\delta\rho_e}{\rho_0} &= \sqrt{\frac{\pi}{2}}\frac{a_0^2}{4\sqrt{2\ln 2}}\frac{\tau_0}{k_p}\left[\omega_p k_p + \frac{8c}{w_0^2}\left(1-\frac{2r^2}{w_0^2}\right)\right]\exp\left(-\frac{\omega_p^2\tau_0^2}{16\ln 2}-\frac{2r^2}{w_0^2}\right)\sin(k_p\xi),\\
\frac{E_z}{E_0} &= \sqrt{\frac{\pi}{2}}\frac{a_0^2}{4\sqrt{2\ln 2}}\omega_p\tau_0\exp\left(-\frac{\omega_p^2\tau_0^2}{16\ln 2}-\frac{2r^2}{w_0^2}\right)\cos(k_p\xi),\\
\frac{E_r}{E_0} &= -\sqrt{\frac{\pi}{2}}\frac{a_0^2}{\sqrt{2\ln 2}}c\tau_0\frac{r}{w_0^2}\exp\left(-\frac{\omega_p^2\tau_0^2}{16\ln 2}-\frac{2r^2}{w_0^2}\right)\sin(k_p\xi),
\end{aligned} \tag{2.25}$$

where $\xi = z - v_g t$, $k_p = \omega_p/c$ is the wavenumber of the plasma wave, and $E_0 = m_e c\omega_p/e$ is the cold nonrelativistic wavebreaking field.

Figure 2.4 illustrates the electron density perturbation in a plasma for density $\rho_0 = 7\times10^{18}$ cm^{-3} excited by a laser pulse with $a_0 = 0.2$, $w_0 = 15$ μm, and $\tau_0 = 40$ fs. One may immediately observe that, according to Equation 2.25, the density part and the electric fields have the same transverse dimension which is determined by the size of the driving laser, and an identical oscillation period given by the plasma frequency. Furthermore we find the longitudinal and radial fields are out of phase of $\pi/2$. Especially interesting for LWFA is the phase region where the electron is longitudinally accelerated and transversely focused. As shown in Figure 2.4, such a region only occurs over a quarter of the period, for example, the interval $[\pi, 3\pi/2]$ in the first plasma cycle. This finding suggests that the electron bunch accelerated in a LWFA should be shorter than $\lambda_p/4$. For $\rho_e = 7\times10^{18}$ cm^{-3}, it corresponds to a bunch length of < 10 fs. Such short electron bunch is fairly attractive for studies like ultrafast phenomena [74, 75].

On the other hand, the strongest longitudinal field for acceleration arises on-axis ($r = 0$) where the radial field is zero, while the radial field, varying as $r\exp(-2r^2/w_0^2)$, reaches its maximum when $r = w_0/2$, as shown in Figure 2.5(a). Thus we can obtain the ratio between the maxima of the accelerating and focusing fields

$$\frac{E_r^{max}}{E_z^{max}} = \frac{2\exp(-\frac{1}{2})}{k_p w_0} \tag{2.26}$$

Quantitatively, for the parameters used in Figure 2.4, the value is $E_r^{max}/E_z^{max} \simeq 0.16$. Evidently it is the the longitudinal that dominates. Furthermore, we find the density perturbation and the plasma field components depend on the laser pulse duration τ_0 via $\tau_0\exp(-\omega_p^2\tau_0^2/16\ln 2)$. So there is an optimal pulse duration which matches the given

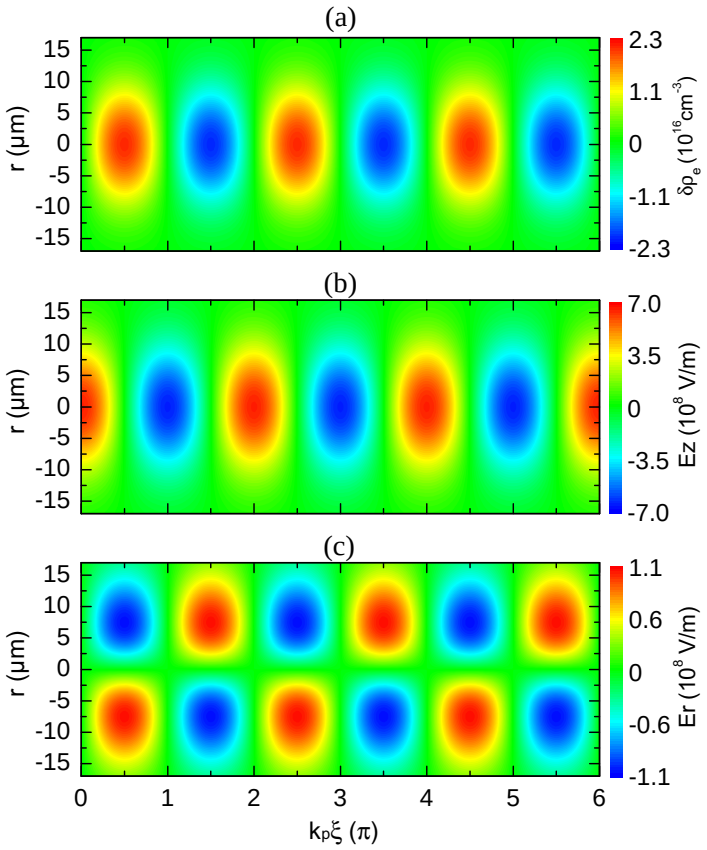

Figure 2.4: *(a) Density perturbation, (b) longitudinal, and (c) transverse electric fields of plasma wave excited by a laser pulse with* $a_0 = 0.2$*,* $w_0 = 15$ *μm,* $\tau_0 = 40$ *fs for a plasma density* $\rho_e = 7 \times 10^{18}$ cm^{-3}*.*

plasma density and most efficiently drives the plasma wave:

$$\tau_0 = \frac{\sqrt{8 \ln 2}}{\omega_p} \simeq \frac{2.36}{\omega_p} \tag{2.27}$$

The optimum pulse duration can be interpreted by the resonance between the laser ponderomotive force and plasma electron oscillation [76]. In the case of Figure 2.4, the optimum pulse duration is about 16 fs. Away from the optimum duration, the field amplitude drops quickly, as shown in Figure 2.5(b). The field magnitude shown in Figure 2.4 driven by a 40 fs laser pulse is merely 17% the optimal case. It highlights the laser pulse duration must be carefully chosen to match the optimal condition.

Nonlinear regime

When the laser intensity is high ($a_0 \gg 1$), the assumption of small density perturbation ($\delta\rho/\rho_0 \ll 1$) does not hold, so the nonlinear regime is reached. In this regime, electron oscillations consist of not only the fundamental but also higher harmonics of Fourier series. Therefore the shape of plasma wave will differ from the standard sinusoid that we presented before. Nonlinear plasma wave excitation in multi-dimension is not analytically solvable, so numerical simulations are widely employed to understand the features of laser-plasma interactions [77, 78]. In this section, we will numerically address this nonlinear problem in one dimension to get some insight of the underlying physics.

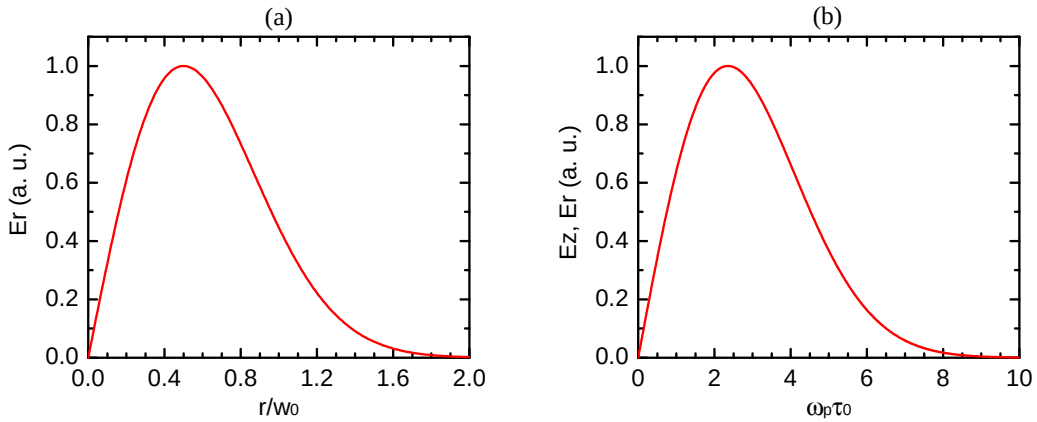

Figure 2.5: *(a) The radial electric field profile of a linear plasma wave. (b) The field strength as a function of driving pulse duration.*

Numerically solving Equations A.14 and A.16, we are able to obtain the density perturbation and plasma potential of a nonlinear plasma wave. Figure 2.6 displays plasma waves and their associated electric fields driven by laser pulses with different intensities. When the laser intensity is $a_0 = 0.2$, a linear standard sinusoidal plasma wave is created behind the laser, as obtained in previous section (Figure 2.4). With increasing laser intensity, the plasma electrons oscillate with a larger amplitude, and the wave shape gradually deviates from the sinusoidal case. In Figure 2.6(d) where $a_0 = 4$, the density distribution becomes highly peaked. Associated with this density steepening, the electric field exhibits the so-called "sawtooth" profile, namely a sharp ascent at the density peak and a linear drop between the density peaks.

The most significant feature is the incense of electric field amplitude with laser intensity. For $a_0 = 0.2$, the linear electric field strength is only $E_z \simeq 0.013E_0$, while it is increased to $E_z \simeq 1.8E_0$ for $a_0 = 4$. It is more than two orders of magnitude higher, which emphasizes the interest of LWFA in the highly nonlinear regime, as higher electric field means higher electron energy over a given accelerating distance. In this context, a question arises: is there an ultimate limit of the plasma electric field amplitude with increasing laser intensity?

To answer this equation, we need to examine the phenomenon called wavebreaking. A noticeable feature for $a_0 \gg 1$ is a large number of electrons in the narrow density peak regions, making local electron density 12 folds higher than background density as seen in Figure. 2.6(d). The plasma wave is said to "break", when the local plasma density becomes infinite, namely $\rho_e \to \infty$. In this condition, the velocity of the electrons approaches that of the plasma wave they build, $v_e \to v_p$. Mathematically, it occurs when $(1 + \phi) \to 1/\gamma_p$ (See the denominator in Equation A.14). Meanwhile, we know that behind the driving laser the minimum plasma potential is related to plasma wave magnitude E_z^{max} by [79]

$$\phi_{min} = \frac{1}{2}\left(\frac{E_z^{max}}{E_0}\right)^2 - \beta_p\left\{\left[1 + \frac{1}{2}\left(\frac{E_z^{max}}{E_0}\right)\right]^2 - 1\right\}^{1/2}. \tag{2.28}$$

At wavebreaking, $\phi_{min} = 1/\gamma_p - 1$. Substituting this value into above equation leads to the maximum amplitude of electric field sustained by the plasma wave

$$E_{wb} \equiv E_z^{max} = \sqrt{2(\gamma_p - 1)}E_0, \tag{2.29}$$

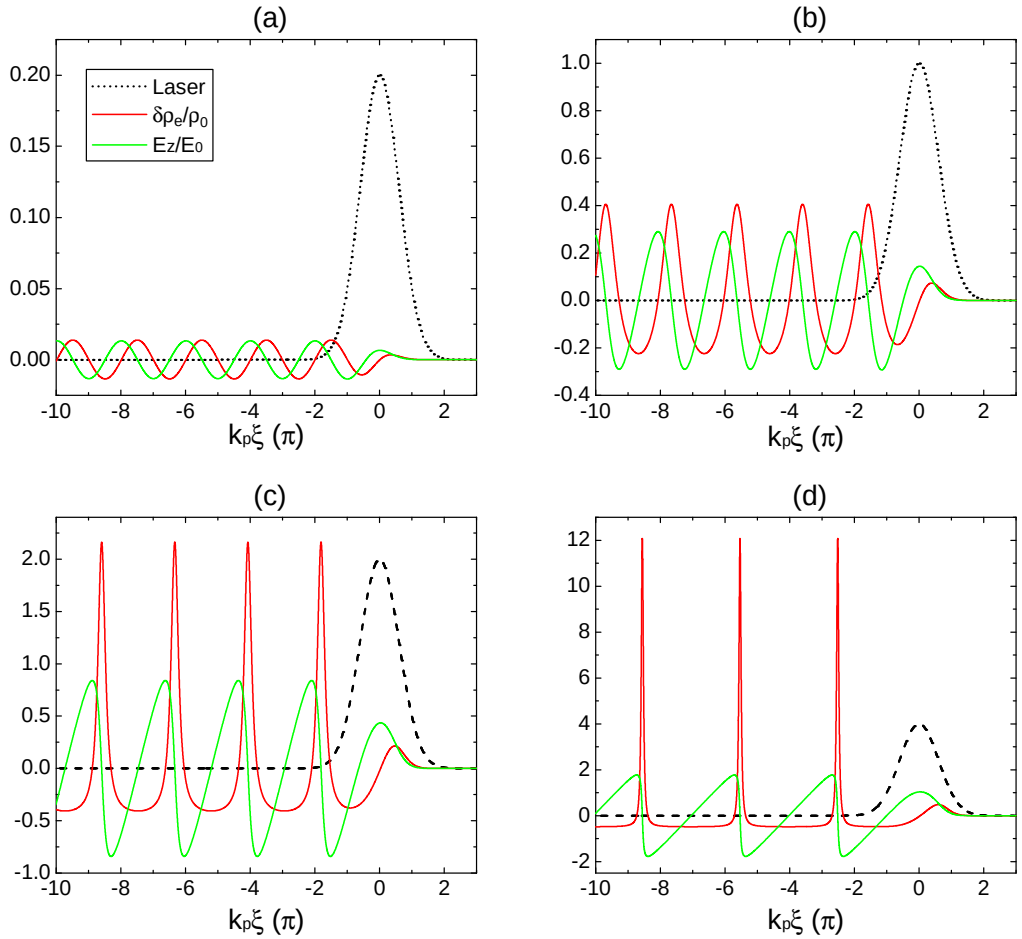

Figure 2.6: *Density perturbations and the associated electric fields of the plasma waves driven by temporal Gaussian laser pulses with duration of* $c\tau_0 = \lambda_p/2$ *at plasma density* $\rho_0 = 7 \times 10^{18}$ *cm*$^{-3}$. *The laser strengths in (a)-(d) are* $a_0 = 0.2$, 1, 2, 4, *respectively.*

where E_{wb} is often called the relativistic wavebreaking field. As an example, for a laser wavelength 0.8 μm and a plasma density 7×10^{18} cm^{-3}, the corresponding relativistic factor of phase velocity is $\gamma_p = \omega_0/\omega_p \simeq 16$, and the wavebreaking field $E_{wb} = 5.5E_0 \simeq 1.4$ TV/m. Even if thermal effects in plasma may reduce the maximum plasma wave amplitude [80, 81], relativistic wavebreaking was indeed reached in LWFA experiments [10].

It seems that wavebreaking limits the maximum electric field amplitude, so we should try the best to avoid it. As a matter of fact, wavebreaking is essential for trapping electrons from the background plasma. If there is no wavebreaking, all the electrons are bound to the collective plasma oscillation. None of them is able to move freely. On the contrary, when the plasma wave breaks, some of the electrons will get rid of the confinement of collective behavior, producing a chance for them to be trapped by the plasma wave.

2.3 Electron trapping

As in accelerator physics [3], an electron will gain energy from a wave, if it is located in an accelerating phase, and more importantly possesses an initial energy adequate to be trapped by the wave. If so, the electron is locked within a phase region of the wave where it gets accelerated. In this section, we will examine how an electron is trapped by the

plasma wave. In the early stage of LWFA development, external electron beams produced by RF accelerators were injected into plasma waves, however it is complicated [82] to manage electron sources and laser facilities together. As demonstrated in the following part, wavebreaking provides a simpler way to directly trap electrons from the background plasma.

The electron orbit in phase space (ξ, u_z) can be examined with the Hamiltonian $\mathcal{H}(\xi, u_z) = (\gamma_\perp^2 + u_z^2)^{1/2} - \beta_p u_z - \phi(\xi)$, where $\gamma_\perp = (1 + a^2)^{1/2}$ is the relativistic factor resulting from the transverse quiver motion of an electron in the laser field. Electron motion is governed by the following equations

$$\begin{aligned} \frac{d\xi}{dt} &= \frac{\partial \mathcal{H}}{\partial u_z} = \frac{u_z}{\sqrt{\gamma_\perp^2 + u_z^2}} - \beta_p, \\ \frac{du_z}{dt} &= -\frac{\partial \mathcal{H}}{\partial \xi} = \frac{\partial \phi}{\partial \xi} - \frac{1}{2\sqrt{\gamma_\perp^2 + u_z^2}} \frac{\partial \gamma_\perp^2}{\partial \xi}. \end{aligned} \tag{2.30}$$

As there is no explicit time dependence in the Hamiltonian, for a given electron orbit the Hamiltonian is a constant $\mathcal{H}(\xi, u_z) = \mathcal{H}_0 = const.$ Therefore the electron longitudinal momentum u_z can be written as a function of ξ

$$u_z(\xi) = \beta_p \gamma_p^2 (\mathcal{H}_0 + \phi) \pm \gamma_p \sqrt{\gamma_p^2 (\mathcal{H}_0 + \phi)^2 - \gamma_\perp^2}. \tag{2.31}$$

$u(\xi)$ is referred to as orbit in phase space.

Figure 2.7 demonstrates the electron orbits in phase space corresponding to different $\mathcal{H}_0$, where the driving laser pulse is Gaussian with $a_0 = 1.6$ and pulse duration $c\tau_0 = \lambda_p/2$. The plasma density therein is $\rho_e = 8 \times 10^{18}$ cm^{-3}. The fluid orbit, indicated by the black solid line in Figure 2.7, describes the electron initially at rest ($u_z = 0$) before the arrival of the laser pulse. In this case, there is no plasma wave, namely $\phi = 0$. So, the initial Hamiltonian is $\mathcal{H}_0 = 1$. Substituting this into Equation 2.31 gives the fluid orbit

$$u_z^{fluid}(\xi) = \beta_p \gamma_p^2 (1 + \phi) - \gamma_p \sqrt{\gamma_p^2 (1 + \phi)^2 - \gamma_\perp^2}. \tag{2.32}$$

Clearly, there are two different kinds of orbits: the closed orbits (in violet) correspond to trapped electrons, while the open orbits (in green) indicate the trajectories of untrapped ones. The curve (in red) separating them is called the "separatrix". The Hamiltonian of the separatrix is given by $\mathcal{H}_s = \gamma_\perp/\gamma_p - \phi_{min}$, where ϕ_{min} is the minimum plasma potential obtained in Equation 2.28. For $\mathcal{H}_0 > \mathcal{H}_s$, the electron orbits are open, which means the initial electron energy is either too low (the lower green lines in Figure 2.7) or too high (the upper green lines in Figure 2.7) to be trapped by the plasma wave. On the contrary, the orbits become closed for $\mathcal{H}_0 < \mathcal{H}_s$, corresponding to the trapped cases.

Let us assume there is an electron trapped in the first plasma bucket initially at position A in Figure 2.7. Because its velocity is lower than the phase velocity of the plasma wave $\beta_e < \beta_p$, the electron slips backwards with respect to the plasma wave. During this time the plasma wave accelerates the electron, so the electron's velocity increases and becomes equal to the phase velocity of the wave $\beta_e = \beta_p$ at position B. And then the electron keeps acquiring energy from the plasma wave until position C where it reaches the maximum energy gain. Typically, the accelerating process should stop here. If not, the electron will enter the decelerating phase, and give energy back to the plasma wave, corresponding to rotation in phase space. This phenomenon is known as "dephasing". Apparently, it's the separatrix orbit that requires minimal initial electron energy for tapping and offers the

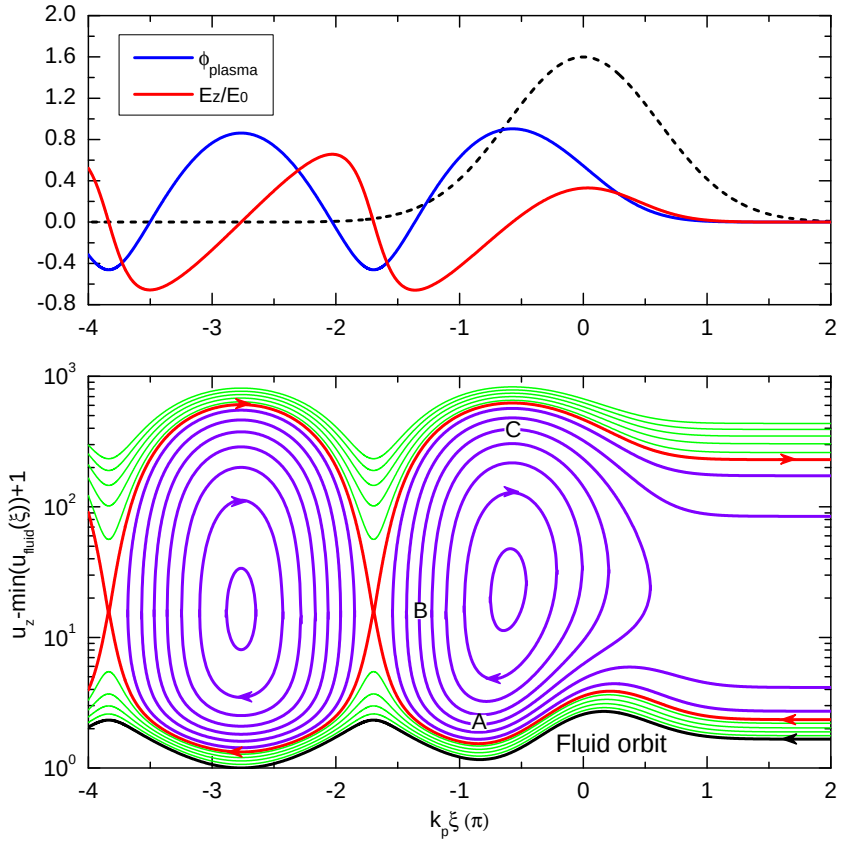

Figure 2.7: *Top: the plasma potential and associated electric field driven by a Gaussian laser pulse (dashed line) with $a_0 = 1.6$ and a duration of $c\tau_0 = \lambda_p/2$ for a plasma density $\rho_e = 8 \times 10^{18}$ cm^{-3}. Bottom: Electron trajectories in phase space (ξ, u_z). The red curve is the separatrix.*

highest final energy. The maximum net energy gain of a trapped electron is therefore given by

$$\begin{aligned}(\Delta u_z)^{max} =& \beta_p\gamma_p^2(\mathcal{H}_s + \phi_{max}) + \gamma_p\sqrt{\gamma_p^2(\mathcal{H}_s + \phi_{max})^2 - \gamma_\perp^2} \\ &- \beta_p\gamma_p^2(\mathcal{H}_s + \phi_{min}) - \gamma_p\sqrt{\gamma_p^2(\mathcal{H}_s + \phi_{min})^2 - \gamma_\perp^2}, \\ \simeq& 2\gamma_p^2\Delta\phi,\end{aligned} \tag{2.33}$$

where $\Delta\phi = \phi_{max} - \phi_{min}$.

Now let's examine the injection threshold, or the minimum energy that is required for electron trapping. For an electron with initial velocity u_z in a plasma, its orbit in phase space is characterized by the Hamiltonian $\mathcal{H}_0 = (1 + u_z^2)^{1/2} - \beta_p u_z$. On the other hand, we know that the minimum initial electron momentum for trapping is determined by the separatrix orbit. Matching them, that is $\mathcal{H}_0 = \mathcal{H}_s$, yields the trapping threshold [83]

$$u_z^{trap} = \gamma_p\beta_p(\gamma_\perp - \gamma_p\phi_{min}) - \gamma_p[(\gamma_\perp - \gamma_p\phi_{min})^2 - 1]^{1/2}. \tag{2.34}$$

ϕ_{min} is related to electric field of plasma wave via Equation 2.28. Figure 2.8 shows the trapping threshold calculated with parameters used for Figure 2.7. As seen, stronger plasma electric field requires lower initial electron energy to fulfill trapping. Particularly, this trapping threshold decreases to zero when the plasma electric field approaches the cold

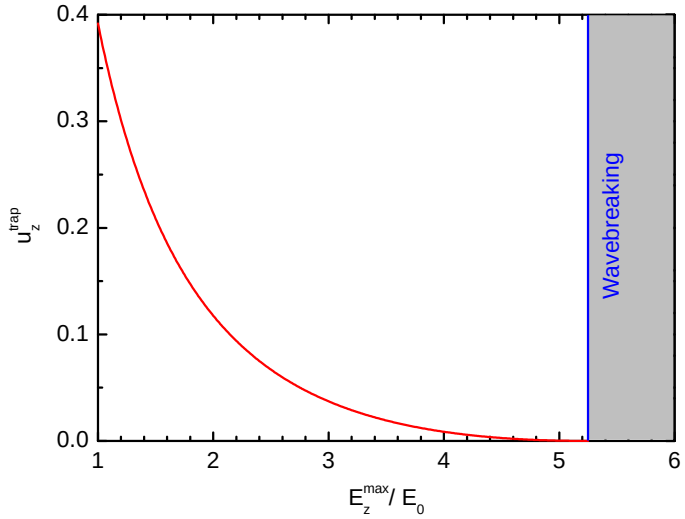

Figure 2.8: *The normalized electron momentum required for trapping as a function of electric field magnitude. The blue line indicates the electric field of cold wavebreaking* $E_{wb} \simeq 5.25E_0$.

wavebreaking field, namely $E_z^{max} \rightarrow E_{wb}$. E_{wb} is given by Equation 2.29, corresponding to $5.25E_0$ in this case. It implies an electron initially at rest would be trapped by the plasma wave when wavebreaking occurs. It is thus the plasma itself that provides the accelerated electrons.

We should stress that the above analysis is based on 1D cold plasma theory and does not take into account the plasma wave evolution. In fact, multi-dimensional effects such as transverse wavebreaking [84] and plasma wave evolution [85, 86] play important roles in electron self-trapping as well. The trapping threshold will be revisited in the section on the bubble regime.

2.4 Laser modulation in plasma

Up to this point, our analyses have been carried out in the frame of quasi-static state, where the evolution of the driving laser pulse is neglected. Actually, when the driving laser pulse generates density perturbations in the plasma, the optical properties of the plasma are changed accordingly. Therefore the plasma in turn modulates the driving pulse. Especially for LWFA, there are two important laser modulations: self-focusing and self-compression, corresponding to the variations of the transverse size and pulse duration of the driving laser pulse.

2.4.1 Self-focusing

In the LWFA experiments, the lasers are often tightly focused to achieve high intensity in the focal spot. Nevertheless, the intensity can only be maintained over the Rayleigh length z_R owing to diffraction. Therefore several guiding techniques have been developed to guide an intense laser beam (See Chapter 4). Among them, self-focusing is a convenient and widely used mechanism to maintain a high laser intensity over more than z_R, relying on relativistic modulation of the plasma index of fraction.

The propagation of a laser pulse in a plasma can be investigated in terms of the spatial index of refraction $n(r) = c/v_{ph}$. Recalling the expression of v_{ph} in Equation 2.23, the index of refraction for an underdense plasma ($\omega_p^2/\omega_0^2 \ll 1$) reads

$$n(r) = \frac{c}{v_{ph}} = \left(1 - \frac{\omega_p^2}{\gamma_\perp \omega_0^2}\right)^{1/2} \simeq 1 - \frac{1}{2}\frac{\rho_e(r)}{\gamma_\perp(r)\rho_c}, \tag{2.35}$$

It shows that the transverse variation of the index of refraction $n(r)$ can be altered by the relativistic factor $\gamma(r)$ or the density distribution $\rho_e(r)$. In the weakly relativistic case, Equation 2.35 may be expanded as [87]

$$n = 1 - \frac{\omega_p^2}{2\omega_0^2}\left(1 - \frac{a^2}{4} + \frac{\delta\rho_e}{\rho_0} - 2\frac{\delta\omega_0}{\omega_0}\right). \tag{2.36}$$

where $\delta\omega_0$ indicates the modulation of laser frequency. In the above expression, the $a^2/4$ term corresponds to the contribution of relativistic laser guiding.

Supposing the laser is Gaussian with intensity peaked on axis $a(r) = a_0 \exp(-r^2/w_0^2)$, we can obtain $\partial a^2(r)/\partial r < 0$. Accordingly, the transverse gradient of the index of refraction is negative, that is $\partial n(r)/\partial r < 0$ or $\partial v_{ph}(r)/\partial r > 0$. It implies that the on-axis phase velocity is lower than off-axis, making the laser wavefront curved. The plasma thus behaves like a convex lens to focus the laser beam towards the propagation axis. This mechanism is known as self-focusing, which is able to balance the laser natural diffraction. As shown in Equation 2.36, the modulation of the index of refraction leading to beam focusing scales with a^2. Therefore for a given beam divergence, there is a minimum threshold for laser intensity to balance the divergence. Through a rigorous derivation, the minimum laser power required for self-focusing, normally called critical power, is obtained by [88, 89, 90]

$$P_c = \frac{8\pi\varepsilon_0 m_e^2 c^5 \omega_0^2}{e^2\omega_p^2} \simeq 17\frac{\omega_0^2}{\omega_p^2}\ [\mathrm{GW}]. \tag{2.37}$$

For example, the critical power for $\lambda_0 = 0.8$ μm laser at plasma density $\rho_e = 7 \times 10^{18}$ cm^{-3} is $P_c = 4.25$ TW. In our experiment, the laser power is about 16 TW, which is around four times the required P_c. Consequently, the laser is capable of self-focusing until the laser power drops below the critical power owing to transfer its energy to the plasma wave.

The radial ponderomotive force expels electrons from the axis, creating a radial density gradient $\partial(\delta\rho_e(r))/\partial r > 0$. It thus produces a negative transverse gradient of the index of refraction $\partial n(r)/\partial r < 0$, and focuses the laser beam. The density profile excited by laser ponderomotive force is determined by Equation A.7. Notwithstanding, it was found that the ponderomotive force alone is not sufficient to channel the laser for laser power $P \ll P_c$ [18]. When laser power approaches the critical power $P \to P_c$, it is still relativistic self-focusing that dominates laser propagation, while ponderomotive channeling just enhances self-guiding. The contribution of ponderomotive channeling slightly relaxes the critical power for self-focusing to $P_c = 16.8(\omega_0^2/\omega_p^2)$ GW.

It was believed for some time that relativistic self-focusing was not able to guide a sufficiently short laser pulse, namely $c\tau_0 < \lambda_p$. Since the evolution of index of refraction is typically on the time scale of the plasma oscillation $1/\omega_p$, for such a short laser pulse there is not enough time for the plasma to effectively respond. This point was verified by several groups in experiments, where the authors demonstrated a laser pulse can only be properly self-guided when $c\tau_0 > \lambda_p$ [91, 92]. However, recent findings in the bubble regime suggest

that an ultrashort intense laser pulse can still be guided by self-focusing. Because the leading edge of the driving laser locally pump depletes before it diffracts, while the bulk laser is appropriately guided within the plasma bubble owing to the density depression [93, 94]. Self-guiding of a 50 fs (FWHM) long laser pulse over tens of Rayleigh lengths has been observed in the bubble regime for $c\tau_0 \simeq \lambda_w$ by Ralph *et al* in 2009 [95], where $\lambda_w = \frac{4}{k_p}\sqrt{a_0}$ denotes the nonlinear wavelength of the first plasma period [96].

2.4.2 Self-compression

Besides laser beam size evolution in the transverse direction, plasma density variation along the propagation axis modulates the laser pulse longitudinally as well. The density variation along the axis $\delta\rho_e(\xi)$ makes the laser pulse experiencing different local indexes of refraction, and consequently compresses or stretches the laser pulse in time.

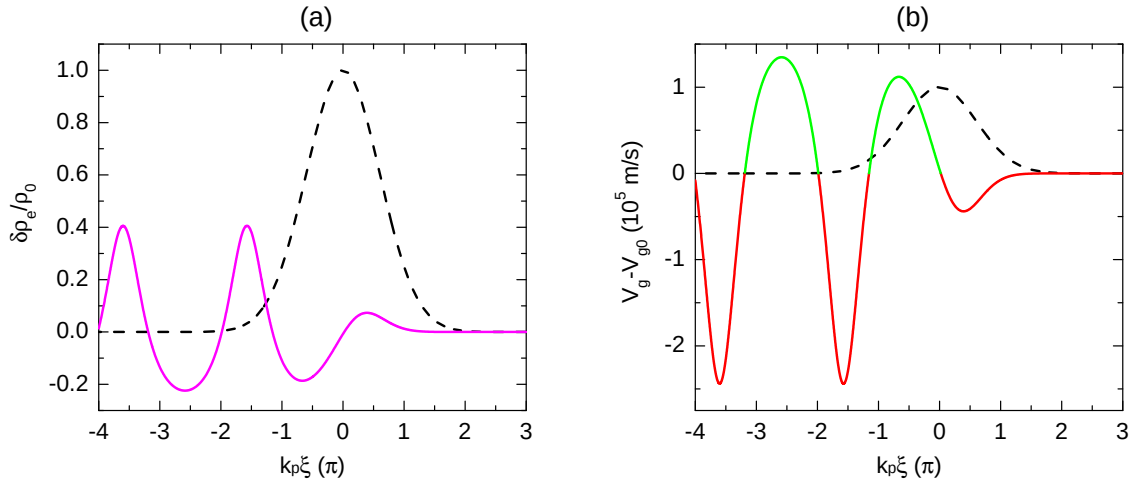

Figure 2.9: *(a) Plasma electron density perturbation (solid line) excited by a laser pulse (dashed line) with $a_0 = 1$, $c\tau_0 = \lambda_p/2$ for a plasma density $\rho_e = 7 \times 10^{18}$ cm^{-3}. (b) The associated relative group velocity of the laser pulse in the plasma. The green (red) lines correspond the local group velocities higher (lower) than that in the uniform background plasma.*

Figure 2.9(a) shows the 1D plasma density perturbation induced by a $a_0 = 1$ laser pulse with duration of $c\tau_0 = \lambda_p/2$. The background plasma density is $\rho_e = 7 \times 10^{18}$ cm^{-3}. It shows that the laser goes through different plasma density $\rho_e(\xi)$. A significant number of electrons accumulate at the leading edge of the driving pulse when it ploughs across the plasma, while a density depression is seen by the trailing edge of the driving laser. Through Equation 2.36, the local group velocity of the drive laser (or phase velocity of the plasma wave) can be evaluated by

$$v_g \simeq cn = c\left[1 - \frac{\omega_p^2}{2\omega_0^2}\left(1 - \frac{a^2}{4} + \frac{\delta\rho_e}{\rho_0} - 2\frac{\delta\omega_0}{\omega_0}\right)\right]. \tag{2.38}$$

$\delta\rho_e = 0$ gives to the laser group velocity in the background plasma: v_{g0}. For positive density variation $\delta\rho_e > 0$, the laser group velocity becomes smaller: $v_g - v_{g0} < 0$, whereas a negative one $\delta\rho_e < 0$ corresponds to higher laser group velocity: $v_g - v_{g0} > 0$, as illustrated in Figure 2.9. In this case, the laser back edge moves faster than its front edge. The laser pulse gets temporally compressed, which is also called pulse shortening.

This is indeed an important phenomenon in LWFA. Because it somewhat relaxes the requirement of laser duration for optimum plasma wave excitation [See Equation 2.27], as the feedback of plasma gradually modulates the driving laser to match the resonant condition. Relying on this approach, it was experimentally demonstrated that an initial 38 fs laser was compressed by a plasma of $\rho_e = 7.5 \times 10^{18}$ cm^{-3} to about $10-14$ fs [97, 98].

It is worth noting that as indicated by Fourier transformation a temporal compression of the laser will cause an increase of its spectral bandwidth. Particularly the laser leading edge becomes redshifted, and the back edge is mainly blueshifted [98]. As spectral modulation of the driving laser is the feedback from the plasma, it hence provides a good means to diagnose the excited plasma wave [62, 99].

2.5 Multi-dimensional plasma wave

In the preceding sections, we have examined nonlinear issues regarding LWFA in one dimension. Although several physical aspects were identified, a full picture of the LWFA process can be retrieved only in three dimension (3D). In this section, we will present the nonlinear phenomena in 3D. As mentioned before, the 3D nonlinear problem is not analytically solvable, so the discussions here are schematic and phenomenological, from particle-in-cell (PIC) simulations.

2.5.1 The bubble regime

The 3D highly nonlinear regime was first considered by Pukhov and Meyer-ter Vehn as a novel scheme to produce spectrally peaked electrons in LWFA [36]. When an ultrashort ($c\tau_0 \simeq \lambda_p$) and intense ($a_0 \gg 1$) laser pulse propagates in an underdense plasma, the ponderomotive force of the driving laser becomes so strong that all the plasma electrons are expelled outwards from the laser spot region. The ions keep stationary due to their inertia. Therefore the Coulomb force resulting from space charge separation tends to pull the expelled electrons back to their original positions. The ponderomotive and Coulomb forces together create an ion cavity free of plasma electron following the driving laser, as illustrated schematically in Figure 2.10. It is greatly different from what we saw in the linear regime, where a periodic plasma oscillation is generated behind the driver. As the ion cavity is almost perfectly spherical, it was named plasma "bubble". Historically speaking, the report of the bubble regime stimulated physicists to experimentally look for spectrally peaked electrons [37, 38, 39].

Subsequently Lu and coworkers developed phenomenological laws about the bubble regime based on currently attainable laser parameters ($a_0 \simeq 4$) [94]. Interestingly in Lu's description, the bubble regime is referred to as "blowout" regime. But, essentially they are the same. In this thesis, we follow the primary notation of Pukhov to term it as the bubble regime. The equation that describes the bubble shape in the ultrarelativistic limit is given by Lu *et al* [96, 100]

$$r_b \frac{d^2 r_b}{d\xi^2} + 2\left(\frac{dr_b}{d\xi}\right)^2 + 1 = 0, \tag{2.39}$$

where $r_b(\xi)$ is the radial coordinate of the bubble, and $\xi = 0$ is located at the bubble center. The associated longitudinal electric field inside the bubble is given by $E_z(\xi)/E_0 \simeq \frac{1}{4} k_p dr_b^2/d\xi$. The bubble radius R_b is determined when the ponderomotive force of the laser is balanced by the Coulomb force. Under the matching condition ($k_p w_0 = 2\sqrt{a_0}$,

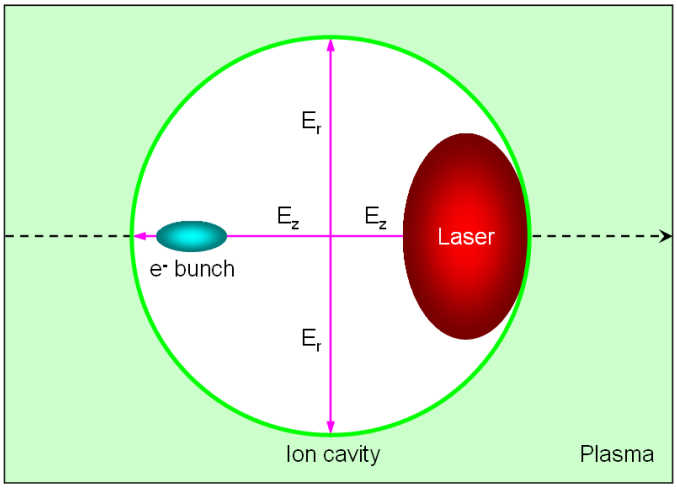

Figure 2.10: *Scheme of laser-plasma electron acceleration in the bubble regime. The laser creates an ion cavity free of plasma electrons. The trapped electrons surf on the longitudinal electric field inside the bubble and get accelerated.*

$c\tau_0 \leq w_0$), R_b is determined by [94]

$$k_p R_b = k_p w_0 = 2\sqrt{a_0}. \tag{2.40}$$

The relationship in Equation 2.40 holds for $a_0 > 2$. Actually it was shown by Lu *et al* in [94] that for $a_0 > 4$ the produced ion cavity is perfectly spherical, while for $4 > a_0 > 2$ the laser is still able to blowout the electrons but the bubble shape may slightly deviate from a sphere. The expression in Equation 2.40 can be written in terms of laser power as $P \simeq (a_0/2)^3 P_c$. It suggests that to reach $a_0 = 4$ the laser power must be greater than $8P_c$, namely 34 TW for a 0.8 μm laser at a plasma density 7×10^{18} cm^{-3}. For most current terawatt laser facilities, it remains challenging to attain such a power in the useful volume of the laser focal spot. However, it is worth noting that for an initial unmatched laser pulse ($w_0 > R_b$ or/and $a_0 < 4$), the self-focusing and self-compressing discussed before will favor the laser gradual evolution to the matched condition, as observed in experiments [97, 101].

The electric field distribution inside the bubble structure makes it ideal for electron acceleration. Firstly, the longitudinal accelerating field does not depend on radial position, which can greatly diminish the energy spread for off-axis injected electrons. Furthermore, the focusing ability of the radial electric field linearly increases with off-axis position ($E_r \propto r$), which is good for preserving the electron transverse emittance. Thirdly, the accelerated electrons and the driving laser pulse are spatially separated from each other (as illustrated in Figure 2.10), which is not only good for stable laser propagation but also favorable to conserve the electron quality.

2.5.2 Production of spectrally peaked electrons

Even though the bubble regime possesses excellent features for electron acceleration, it is still not sufficient to ensure the production of spectrally peaked electrons. As introduced before, it is the wavebreaking that triggers electron injection into the plasma bubble. Without special control over the injection process, the final electron energy spread is large. In this section, we examine how spectrally peaked electrons can be produced in the plasma bubble due to the effects of beam loading and electron rotation in phase space.

We would like to mention that in the conventional accelerator community, monoenergetic means the relative energy spread $\Delta\mathcal{E}/\mathcal{E}$ is on the order of one percent, while in the LWFA domain the electron distribution can be called quasi-monoenergetic when $\Delta\mathcal{E}/\mathcal{E}$ is less than 20%.

Effect of beam loading

In order to generate spectrally peaked electrons, the foremost task is to ensure that all the electrons experience a similar accelerating field. The process of electron injection must be controlled to trap electrons in a very localized region, so that the accelerating field experienced by the trapped electrons is the same. The influence of beam loading can favor us to accomplish this task.

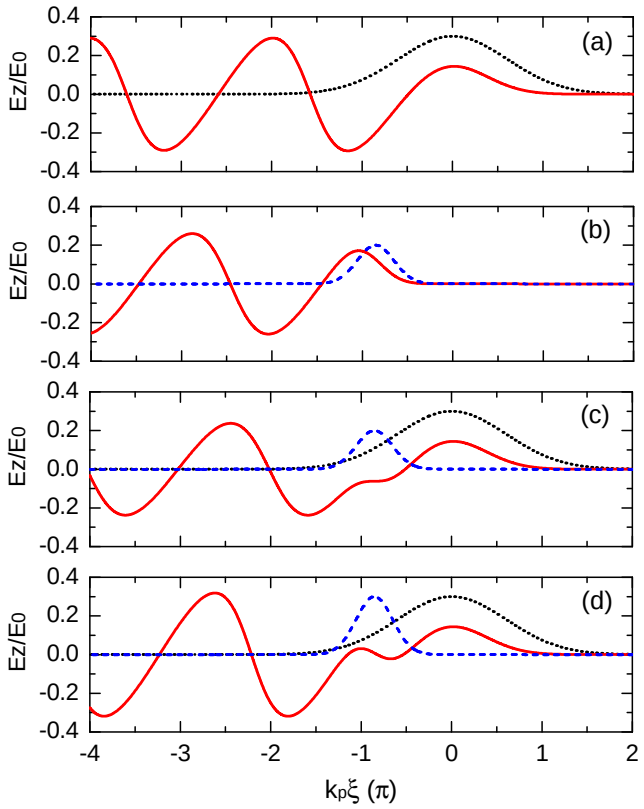

Figure 2.11: *Electric field of plasma wave excited (a) by only a laser pulse, (b) by only an electron bunch, (c)-(d) by both the laser and the electron bunch. The laser is with* $a_0 = 1$ *and* $c\tau_0 = \lambda_p/2$. *The electron bunch is 10 fs long with charge of* $\rho_{b0} = 0.2\rho_e$ *in (b)-(c) and* $\rho_{b0} = 0.3\rho_e$ *in (d).*

The trapped electrons produce a plasma wave as well, like in the mechanism of PWFA. Such a wakefield modifies the electric field distribution initially created by the driving laser. This phenomenon is termed as "beam loading" [102]. Taking into account the electron bunch, the 1D nonlinear plasma potential in Equation A.16 is modified to be

$$\frac{\partial^2\phi}{\partial\xi^2} = k_p^2\gamma_p^2\left\{\beta_p\left[1-\frac{1+a^2}{\gamma_p^2(1+\phi)^2}\right]^{-1/2}-1\right\}+k_p^2\frac{\rho_b(\xi)}{\rho_e}, \tag{2.41}$$

where $\rho_b(\xi) = \rho_{b0} \exp[-4 \ln 2(\xi - \xi_{b0})^2/c^2\tau_b^2]$ represents the electron bunch with Gaussian distribution in time. ρ_{b0}, ξ_{b0}, τ_b denote the peak charge density, center position, and FWHM duration, respectively. The longitudinal electric field of plasma wave is obtained by $E_z = -E_0 \partial\phi/\partial\xi$.

Figure 2.11 demonstrates the electric fields of plasma wave calculated using Equation 2.41 for a laser pulse ($a_0 = 1$, $c\tau_0 = \lambda_p/2$) with or without beam loading at a plasma density $\rho_e = 7 \times 10^{18}$ cm^{-3}. The electron bunch is 10 fs in duration with peak density $\rho_{b0} = 0.2\rho_e$ for (b)-(c) and $\rho_{b0} = 0.3\rho_e$ for (d). As seen, the magnitude of the electric field generated by the electron bunch is comparable to that excited by the driving laser. There are several interesting features shown in Figure 2.11. First of all, the electron bunch situates in the first half period of the plasma wave generated by the bunch itself, where the electric field is positive. It implies the electrons will be decelerated by this field, or in other words, the total accelerating gradient will become lower. Typically at the bunch center ξ_{b0}, the unloaded electric field $E_z(\xi_{b0}) = -0.2E_0$ [Figure 2.11(a)] is reduced to $E_z^{bl}(\xi_{b0}) = -0.06E_0$ in the case of Figure 2.11(c). Therefore the final achieved electron energy is decreased by beam loading. Moreover, for the case of optimum beam loading in Figure 2.11(c), the electric field is flat within the electron bunch. That is of great importance, since it means all the electrons experience nearly the same accelerating field and can get the same energy gain. Thirdly, the trapped electrons will turn off further electron injection. For the beam loaded case in Figure 2.11(d), the effective electric field at the end of the first plasma bucket is changed to be positive. This means not only further electron injection is not possible, but also some trapped electrons will give back their energies to the plasma wave.

The three natures of beam loading presented above, especially controlling electrons being trapped in a localized space and time, provide the possibility to generate spectrally peaked electrons. Recently, the influences of beam loading on electron energy, energy spread, and beam charge in the bubble regime have been characterized in theory and experiment [103, 104]. Nevertheless, beam loading alone does not seem sufficient to produce spectrally peaked electrons, as the flat accelerating field occurs only for the optimal loading case. A slight deviation from it may aggravate the electron energy spread.

Contribution of dephasing

Dephasing can compress the electron energy spread by rotating electrons in phase space. As shown in Section 2.3.1, the orbits of trapped electrons in phase space are closed. Once an electron reaches the maximum energy, it starts decelerating. The mechanism where the electron surpasses the maximum energy and enters the decelerating phase is often referred to as "dephasing" [18]. Here we examine how dephasing favors a decrease in electron energy spread.

Figure 2.12 illustrates an electron bunch rotation in phase space (ξ, u_z). The orbit is taken from the first plasma bucket given in Figure 2.7. Supposing the electron bunch is initially trapped at position A. It slips backwards with respect to the plasma wave, while it picks up energy and gradually catches the wave, as indicated by point B. After some time, the electrons at the front of the bunch reach the maximum energy (the top of the orbit) at $t_{dp} - \delta t$, as shown by position C_1 in Figure 2.12(a), where a significant amount of electrons are still far from the orbit top, leading to a relatively large energy spread. With time going by, the front electrons tend to be decelerated, while the back electrons still get accelerated. The time t_{dp}, as shown in Figure 2.12(b), when the bunch center arrives at the orbit top C_2 corresponds to a minimum energy spread $\Delta\mathcal{E}_2$. Afterwards the bulk of the electron bunch enters the decelerating phase, and the energy spread increases again,

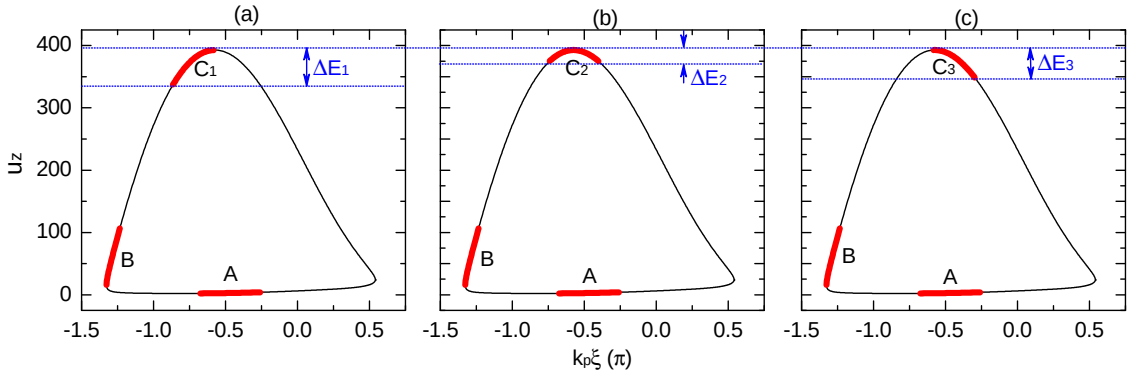

Figure 2.12: *Electron bunch rotation in phase space at (a) $t_{dp} - \delta t$, (b) t_{dp}, and (c) $t_{dp} + \delta t$. A, B, C indicates the positions of an electron bunch (red rod) rotating in phase space, and the blue dashed lines show the energy spreads.*

as shown by $\Delta\mathcal{E}_3$ at position C_3 in Figure 2.12(c).

So we do see that dephasing can produce an electron bunch with the same maximum energy but quite different energy spread. Ideally, the electrons should be extracted at the time t_{dp} as given in Figure 2.12(b). In experiment, this could be implemented by varying the plasma density to making the plasma length slightly longer than the dephasing length [105]. The appropriate effects of beam loading and dephasing played important roles in the demonstration of spectrally peaked electrons in 2004 [37, 38, 39].

2.5.3 Threshold of electron self-trapping

In Section 2.3.1, we examined electron self-trapping in the 1D nonlinear regime. Here we will consider the threshold of self-trapping in the 3D bubble regime. What we obtained for 1D plasma wave is wavebreaking occurs when the minimum plasma potential approaches $\phi_{min} \to (1/\gamma_p - 1)$. In the bubble regime, by examining the bubble evolution Kalmykov *et al* [85, 86] found a sufficient condition for electron trapping: the change of the electron's Hamiltonian in the co-moving frame must exceed its rest mass energy, namely $\Delta\mathcal{H} < -m_e c^2$. Nevertheless, it is difficult to use this finding to guide experimental work as it is purely theoretical. Another theoretical prediction of the electron self-trapping threshold was obtained by Thomas via studying the electron trajectory inside the plasma bubble [106]. It suggests self-trapping happens when

$$k_p R_b > 2\sqrt{\ln(2\gamma_p^2) - 1}, \tag{2.42}$$

where $\gamma_p = (\rho_c/3\rho_e)^{1/2}$ is the relativistic factor associated with the bubble phase velocity [93]. It suggests that the bubble size must be larger than a density dependant critical value to trap background electrons.

On the other hand, according to Lu's bubble phenomenological scaling laws [94], the bubble radius is related to the laser intensity by $k_p R_b = 2\sqrt{a_0}$. Hence Equation 2.42 yields

$$a_0 > \ln\left(\frac{2\rho_c}{3\rho_e}\right) - 1. \tag{2.43}$$

Furthermore when the laser waist matches the bubble size, the laser intensity is determined by laser power through $a_0 = 2(P/P_c)^{1/3}$ [94]. We can therefore rewrite Equation 2.43 as

a function of laser power

$$P > \frac{P_c}{8}\left[\ln\left(\frac{2\rho_c}{3\rho_e}\right)-1\right]^3 = \frac{\pi\varepsilon_0 m_e^2 c^5}{e^2}\frac{\rho_c}{\rho_e}\left[\ln\left(\frac{2\rho_c}{3\rho_e}\right)-1\right]^3. \tag{2.44}$$

The right-hand side of Equation 2.44 depends the inverse of plasma density ρ_e. The minimum laser power, fulfilling this inequality corresponds to a minimum value of ρ_e, which we term as density threshold. For a laser energy $\mathcal{E}_L$ and pulse duration τ_0, the laser power can be written as $P = \alpha\mathcal{E}_L/\tau_0$, where α indicates the fraction of laser energy contained within the FWHM laser focal spot. This factor α is important, as without external collecting scheme, the halos of the focal spot are not self-focused, so this part laser energy does not contribute to plasma wave excitation [98]. And then for a given P one can find the corresponding density threshold for self-trapping from Equation 2.44. But one needs to pay attention that the laser power will change by nonlinear laser propagation in the plasma, as presented in Section 2.4.2. An experimental study by Mangles *et al* has demonstrated that the laser temporal evolution indeed affects the determination of the self-trapping threshold [107].

The rate of laser pulse compression in the plasma was found to be [98]

$$\tau(l) = \tau_0 - \frac{\rho_e l}{2c\rho_c}, \tag{2.45}$$

where $\tau(l)$ is the pulse duration after a propagation length l in the plasma. In experiments, l is limited by either the plasma length or the laser pump depletion length $L_{pd} = c\tau_0\rho_c/\rho_e$. Interestingly for the later, the pulse duration will evolve to $\tau(l = L_{pd}) = \tau_0/2$, and laser power is accordingly doubled. Taking this into account, the threshold in Equation 2.44 is relaxed to

$$P > \frac{P_c}{16}\left[\ln\left(\frac{2\rho_c}{3\rho_e}\right)-1\right]^3 = \frac{\pi\varepsilon_0 m_e^2 c^5}{2e^2}\frac{\rho_c}{\rho_e}\left[\ln\left(\frac{2\rho_c}{3\rho_e}\right)-1\right]^3. \tag{2.46}$$

Numerically solving the above equation provides the self-trapping threshold.

Other studies on the threshold of electron self-trapping are reported as well. Froula *et al* performed experiments in the density range of 10^{18} cm^{-3}, and found electrons started to be self-trapped when [108]

$$P > 3P_c = \frac{24\pi\varepsilon_0 m_e^2 c^5}{e^2}\frac{\rho_c}{\rho_e}. \tag{2.47}$$

Another empirical scaling suggested by Mangles *et al* was found by examining a lot of experimental results in LWFA to be $a_0 > 3.8$ [109]. Recalling $a_0 = 2(P/P_c)^{1/3}$ and considering pulse compression, we can rewrite this expression as

$$P > 3.4P_c = \frac{27.2\pi\varepsilon_0 m_e^2 c^5}{e^2}\frac{\rho_c}{\rho_e}. \tag{2.48}$$

The predictions of Equations 2.46-2.48 are plotted in Figure 2.13. Generally, lower plasma density requires higher laser power for electron self-trapping. In more details, all these predictions lead to similar results for laser power around 12 TW. Apart from that, Equations 2.47 and 2.48 produces similar results which are different from the case of Equation 2.46. The former two equations overestimate the density threshold for high densities, while significantly underestimate it in the low density range. The validity of Equation 2.47 was only tested with a given laser facility of 200 TW and limited density range $\rho_e = 3 - 9 \times 10^{18}$ cm $^{-3}$ [108], whereas Equation 2.46 was tested and found to produce reasonable predictions over a broad laser and density range [107].

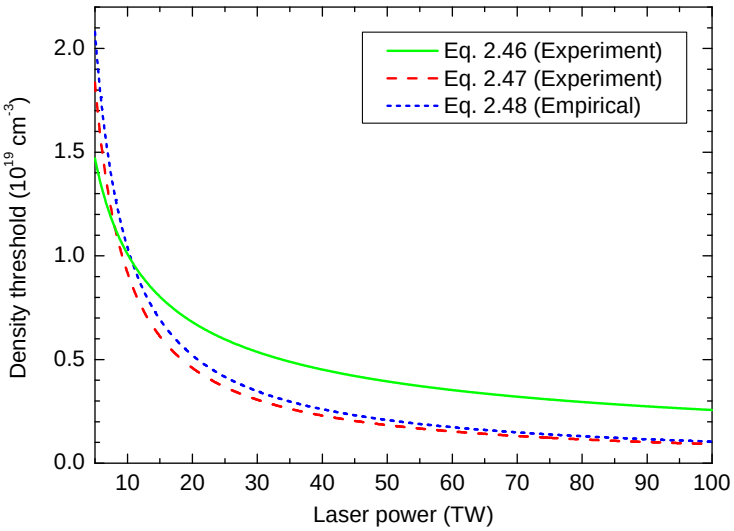

Figure 2.13: *Density threshold for electron self-trapping as a function of laser power.*

2.6 Limits on acceleration

In this section, we consider the limits of electron energy gain in LWFA. Besides the limitation of electric field amplitude in plasma by wavebreaking, there are other mechanisms that restrict the accelerating distance, namely: laser diffraction, dephasing, and laser pump depletion. In many cases, diffraction is the severest limitation. To prevent or compensate it, an intense laser can be guided by self-focusing (See Section 2.4.1), or an external waveguide. External guiding techniques will be discussed more detailedly in Chapter 4. Here we concentrate on the other two limits exerted on LWFA.

2.6.1 Dephasing

The concept of dephasing has been introduced in Section 2.5.2, which describes how an electron reaches its maximum energy and enters the decelerating phase. The length that the electron moves before dephasing is often called the dephasing length L_d. In 1D linear regime, L_d is determined as follows. In the co-moving frame, the maximum length of accelerating field in one period is $\lambda_p/2$. Supposing the accelerated electron propagates at the speed of light c, keeping in mind that the plasma wave moves forward with velocity of v_g, the 1D dephasing length, L_d^{1D}, is calculated by

$$L_d^{1D} = \frac{\lambda_p}{2(c-v_g)}c = \frac{\lambda_p}{2(1-\beta_p)} \simeq \frac{\rho_c}{\rho_e}\lambda_p = \frac{\omega_0^2}{\omega_p^2}\lambda_p. \tag{2.49}$$

The above expression can be easily generalized to 2D. Considering that for a 2D plasma wave there is only a quarter period ($\lambda_p/4$) where the longitudinal electric field is accelerating and the radial field is focusing, the dephasing length becomes half the 1D value: $L_d^{2D} = L_d^{1D}/2 = \lambda_p\omega_0^2/(2\omega_p^2)$.

Furthermore in the 3D bubble regime, the distance in the co-moving frame for dephasing becomes the bubble radius R_b. The phase velocity of the plasma wave is modified to $\beta_p = 1 - 3\omega_p^2/(2\omega_0^2)$. Accordingly the dephasing length L_d^{3D} is given by

$$L_d^{3D} = \frac{R_b}{1-\beta_p} \simeq \frac{2}{3}\frac{\omega_0^2}{\omega_p^2}R_b = \frac{4}{3}\frac{\omega_0^2}{\omega_p^2}\frac{\sqrt{a_0}}{k_p}. \tag{2.50}$$

The above equation shows that the 3D nonlinear dephasing length depends on both the plasma electron density and laser intensity. A longer L_d^{3D} can be achieved by either decreasing the plasma density or improving the laser intensity.

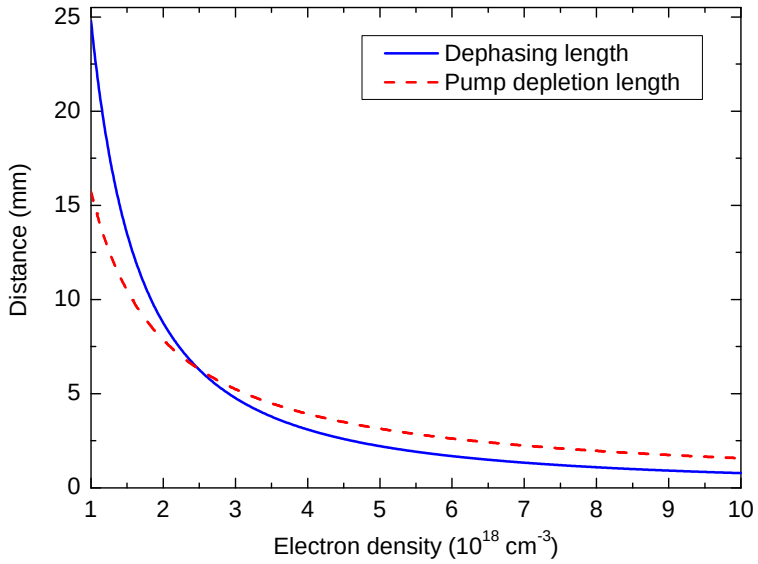

Figure 2.14: *The 3D dephasing length and pump depletion length as a function of plasma electron density. The laser pulse is 40 fs in duration with* $a_0 = 4$.

2.6.2 Pump depletion

Another underlying limit is pump laser depletion. It concerns the length L_{pd}, after which the driving laser energy is depleted. When the pump laser travels in a plasma, it transfers its energy to drive the plasma wave. Consequently, the laser energy becomes lower and lower. The pump depletion length L_{pd} is defined when the energy contained by the plasma wave equals that of the driving laser, namely $E_z^2 L_{pd} = \int E_\perp^2 d\xi$, where E_z is the electric field of the plasma wave, and $E_\perp$ denotes the electric field of the driving laser. For a Gaussian driving laser pulse with resonant duration, the linear pump depletion length is given by [110]

$$L_{pd}^L = \frac{4.35}{a_0^2}\frac{\omega_0^2}{\omega_p^2}. \tag{2.51}$$

In the nonlinear regime, pump depletion length is estimated via the etching velocity $v_{etch} \simeq c\omega_p^2/\omega_0^2$ [93]. v_{etch} describes the erosion velocity of the laser front that excites the plasma wave. The laser will be depleted after a length given by

$$L_{pd}^{NL} = \frac{c}{v_{etch}} c\tau_0 = \frac{\omega_0^2}{\omega_p^2} c\tau_0. \tag{2.52}$$

It was verified in PIC simulation [94] that this expression of nonlinear pump depletion length L_{pd}^{NL} is valid for the 2D and 3D nonlinear cases.

Figure 2.14 exhibits the 3D dephasing length L_d^{3D} and pump depletion length L_{pd}^{NL} as a function of plasma density for the case of an $a_0 = 4$ laser pulse with 40 fs FWHM duration. Typically, the two distances are of the order of several millimeters for densities above 3×10^{18} cm^{-3}. Below $\rho_e = 2.5 \times 10^{18}$ cm^{-3} it is the pump depletion that limits the acceleration process, while the dephasing length becomes the limitation for high densities.

In terms of utilization efficiency of the driving laser, one should work around the density where $L_d^{3D} \simeq L_{pd}^{NL}$. In this sense, a significant amount of laser energy has been transferred to the plasma wave when the electrons reach their maximum energy.

2.6.3 Phenomenological laws

Lu *et al* systematically examined the scalings of LWFA in different regimes and developed a framework for the 3D bubble regime [94]. These scaling laws play an important role in LWFA designs, and were verified by many recent experiments. Table 6.1 lists some of the main scalings that will be often used in this thesis.

Particularly interesting for us is the electron energy gain, which is calculated by integration over the accelerating distance L: $\mathcal{E}_e = e\int_L E_z(l)dl$. The maximum of the longitudinal electric field inside the bubble was obtained by 3D PIC simulation to be $E_z^{max} = \sqrt{a_0}E_0$ [94]. It was also found that E_z has a linear dependence on the bubble radius, so the average accelerating field is half the peak, namely $\langle E_z\rangle = E_z^{max}/2 = \sqrt{a_0}E_0/2$. When the acceleration process is restricted by dephasing (namely $L_d^{3D} < L$), the energy gain is given by

$$\mathcal{E}_e = \langle E_z\rangle L_d^{3D} \simeq \frac{2a_0}{3}\frac{\omega_0^2}{\omega_p^2}m_ec^2 \simeq m_ec^2\left(\frac{e^2P}{m_e^2c^5}\right)^{1/3}\left(\frac{\rho_c}{\rho_e}\right)^{2/3}. \tag{2.53}$$

In practical units, the above expression becomes

$$\mathcal{E}_e[\mathrm{GeV}] \simeq 1.7\left(\frac{P[\mathrm{TW}]}{100}\right)^{1/3}\left(\frac{0.8}{\lambda_0[\mu\mathrm{m}]}\right)^{4/3}\left(\frac{1}{\rho_e[10^{18}\ \mathrm{cm}^{-3}]}\right)^{2/3}. \tag{2.54}$$

Figure 2.15 demonstrates electron energy gain as a function of plasma density and laser power calculated through Equation 2.54. Typically, a 0.8 μm laser with power of 100 TW can accelerate electrons to 1.7 GeV at a plasma density of $\rho_e = 1\times10^{18}$ cm^{-3}. Meanwhile, it is worth noting that the energy gain displays a stronger dependence on plasma density than on laser power. Hence in order to achieve higher electron energy, performing towards lower ρ_e is desirable. Nevertheless, one must always keep the laser size matching condition in mind, which requires $w_0 = \lambda_p\sqrt{a_0}/\pi \propto (\rho_e)^{-1/2}$. When ρ_e is decreased, the laser power must be increased accordingly to meet the requirement for producing a larger bubble, as $P = I_0\pi w_0^2/2 \propto \rho_e^{-1}$. Actually, the threshold of self-trapping in Equation 2.46 also requires higher laser power in order to trap electrons from plasma with lower density. Therefore in experiment all the laser and plasma parameters must be carefully chosen.

Furthermore, an empirical law of the electron beam charge was drawn from the 3D simulation work. The electron number of the accelerated bunch, N_e, is approximated to

Table 2.1: *Summary of the scaling laws for different regimes in [94]. $\mathcal{E}_e$ represents the energy gain of an electron accelerated over the dephasing length.*

	a_0	w_0	L_d	L_{pd}	γ_p	$\mathcal{E}_e/m_ec^2$
Linear	<1	λ_p	$\frac{\omega_0^2}{\omega_p^2}\lambda_p$	$\frac{\omega_0^2}{\omega_p^2}\frac{c\tau_0}{a_0^2}$	$\frac{\omega_0}{\omega_p}$	$a_0^2\frac{\omega_0^2}{\omega_p^2}$
1D Nonlinear	>1	λ_p	$4a_0^2\frac{\omega_0^2}{\omega_p^2}\lambda_p$	$\frac{1}{3}\frac{\omega_0^2}{\omega_p^2}c\tau_0$	$\sqrt{a_0}\frac{\omega_0}{\omega_p}$	$4a_0^2\frac{\omega_0^2}{\omega_p^2}$
3D Nonlinear	>2	$\frac{\sqrt{a_0}}{\pi}\lambda_p$	$\frac{4}{3}\frac{\omega_0^2}{\omega_p^2}\frac{\sqrt{a_0}}{k_p}$	$\frac{\omega_0^2}{\omega_p^2}c\tau_0$	$\frac{1}{\sqrt{3}}\frac{\omega_0}{\omega_p}$	$\frac{2}{3}a_0\frac{\omega_0^2}{\omega_p^2}$

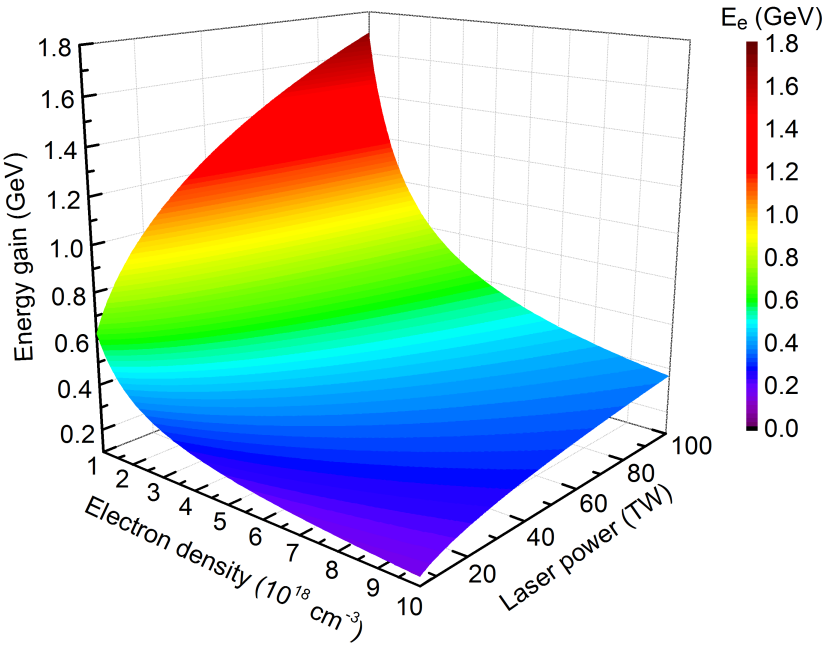

Figure 2.15: *Electron energy gain from Equation 2.54 for plasma density ranging from* 10^{18} cm^{-3} *to* 10^{19} cm^{-3} *and laser power varying between* $5 - 100$ TW.

be [94]

$$N_e = \frac{8}{15k_0 r_e}\sqrt{\frac{e^2 P}{m_e^2 c^5}} \simeq 2.5 \times 10^9 \frac{\lambda_0[\mu\text{m}]}{0.8}\sqrt{\frac{P[\text{TW}]}{100}}, \tag{2.55}$$

where $r_e = e^2/m_e c^2$ is the classical electron radius. As an example, a 100 TW laser with wavelength of $\lambda_0 = 0.8$ μm can produce 2.5×10^9 electrons from the first bucket, corresponding to a beam charge of 0.3 nC. Multiplying the electron number N_e and electron energy $\mathcal{E}_e$ yields the total energy can be extracted by the electron bunch, by which one can furthermore assess the efficiency of LWFA by $\eta_{lwfa} = N_e \mathcal{E}_e / \mathcal{E}_L$. In the matching condition pulse duration obeys $c\tau_0 \simeq R_b$, which leads to $\eta_{lwfa} \propto 1/a_0$. It suggests a_0 should not be too large to obtain a high efficiency.

2.7 Particle-in-cell simulation

As stated before, 3D nonlinear laser-plasma interaction is not analytically solvable, so numerical modeling is employed. Among the various methods, particle-in-cell (PIC) simulation is often used. The primary concept of PIC approach is to track the motions of the charged particles in their self-consistent and external electromagnetic fields [111]. In principle, to implement PIC simulation one needs to solve the Lorentz equation (Equation 2.7) for all the charged particles and update the electromagnetic fields by the Maxwell's equations (See table A.1). However, for plasma physics the total number of particles is extremely huge, so the so-called macro-particle is normally adopted. A macro-particle represents several real particles, which allows to rescale the total particle number and makes the simulation possible. Even so, standard PIC simulations, especially for 3D cases, are still fairly time-consuming.

In this thesis, the simulation was done by collaborating with Hugo Ferrari at the CONICET in Argentina for using the PIC code CALDER-CIRC [112]. It solves Maxwell's equations via Fourier decomposition, which allows the code capturing the 3D nature of laser-plasma interaction, while the computational load is comparable to 2D calculation. The performance of this code has been benchmarked with 3D full PIC simulation [112]. It was found by Davoine *et al* that 3D simulations can give a more accurate description of nonlinear laser-plasma interaction, which is not possible for 1D or 2D simulations [113]. Lately, the code was developed by adding dielectric boundary conditions to describe laser-plasma interaction inside capillary tubes [114]. The modified code can well predict the results of laser-plasma interaction inside capillary tubes as observed in experiments [46, 115]. Figure 2.16 displays an example of the laser wakefields in a capillary tube for a plasma density 7×10^{18} cm^{-3}.

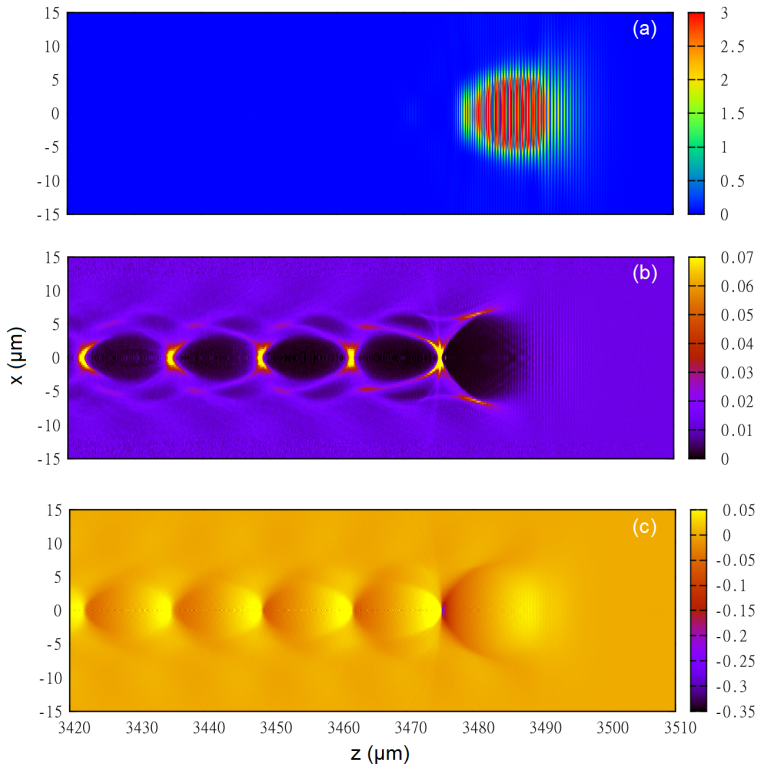

Figure 2.16: *(a) Normalized laser intensity, (b) plasma electron density normalized to the critical density, and (c) the associated longitudinal electric field normalized by the cold wavebreaking electric field E_0 from 3D PIC simulation with the code CALDER-CIRC. The initial laser parameters at z=0 are $a_0 = 1.6$ and $\tau_0 = 40$ fs. The plasma electron density is 7×10^{18} cm^{-3}.*

2.8 Summary

This chapter discusses the mechanism of electron acceleration using laser wakefield. The plasma wave driven by the ponderomotive force of an intense laser pulse, propagating at a speed slightly less than c, can sustain an electric field of the order of $\sim$ 100 GV/m, which provides the possibility to accelerate electrons to high energy over a short distance. In the nonlinear regime, when the laser power is in excess of the critical power, the

driving laser pulse can keep self-focused and compress its temporal duration owing to the interactions with the excited plasma wave. Consequently, the intensity of the driving laser increases, producing a plasma bubble free of electron which can trap some electrons from the background plasma and accelerates them to high energy. The electron acceleration process terminates owing to either slippage of the electrons to the decelerating phase (the dephasing length) or depletion of the pump laser (the pump depletion length). The scaling law developed in the 3D bubble regime indicates the maximum electron energy gain is $\mathcal{E}_e[\mathrm{MeV}] = \frac{1}{3} a_0 \rho_c / \rho_e$, which suggests that 1.7 GeV electron beam can be achieved by employing a 100 TW laser at a low plasma density 1×10^{18} cm^{-3}.

Chapter 3

Betatron X-ray radiation

As presented in Chapter 2, besides the longitudinal electric field for acceleration, there is also a radial component of electric field associated with the plasma bubble. Therefore the trapped electrons are not only accelerated, but also transversely wiggled. This transverse oscillation consequently generates an electromagnetic radiation, called betatron radiation. In this chapter, we address the mechanism of betatron radiation and its properties.

3.1 Introduction

X-rays are indispensable tools to investigate microscopic structures and dynamics in matter. With the growing demands of ever shorter wavelength and higher brightness of X-ray, many large synchrotron facilities have been established worldwide, as shown in the Introduction. Since LWFA is able to shrink the accelerator dimension, it is thus of great interest to consider how LWFA could be applied to generate X-rays.

Studies were carried out in two different directions. The first one imitates traditional synchrotron, which sends the electrons obtained from a LWFA to an externally inserted undulator to produce synchrotron radiation. The feasibility of this concept was demonstrated by two different groups using gas jet and gas-cell in 2008 and 2009, respectively [55, 56], where visible to soft X-ray radiations were observed. The main disadvantage of this approach is the difficulty to extend the photon energy to the hard X-ray domain. Because the emitted radiation wavelength λ_X depends on the period of the magnetic field of the undulator λ_B as $\lambda_X = \lambda_B/(2\gamma^2)$, where $\gamma m_e c^2$ represents the electron energy. Typically, λ_B is in the millimeter range [56]. To achieve X-ray with wavelength $\lambda_X = 1$ nm, the electron energy must scale to as high as $\gamma \sim 10^3$. It is still very challenging to produce stable electron beams with such high electron energy by present LWFAs.

The above-mentioned requirement on electron energy is greatly relaxed by the second scheme using a "plasma wiggler" [116]. The radial electric field in a plasma channel forces the electrons to oscillate in the transverse plane, similar to the periodic magnetic fields of an undulator. Likewise, oscillating electrons emit a synchrotron-like radiation, referred to as "betatron radiation". Figure 3.1 schematically illustrates the mechanism of betatron radiation inside a plasma bubble. The electrons injected from off-axis locations at the rear of the bubble oscillate and produce radiations in the forward direction. The oscillation amplitude gradually decreases owing to the increase of the effective mass of the electron (γm_e) by the relativistic effect (See more details in Section 3.4). As the plasma itself plays the roles of accelerator and wiggler together, this mechanism therefore makes the radiation source fairly compact, usually at university laboratory scale. Furthermore, the radiation wavelength is determined by the plasma wavelength through $\lambda_X \simeq \lambda_p/(2\gamma^2)$.

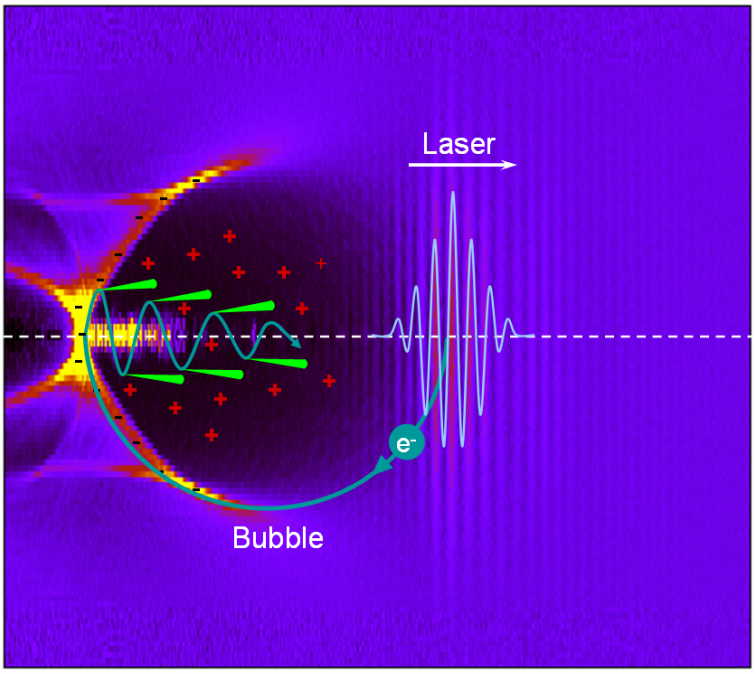

Figure 3.1: *Schematic of betatron radiation in the bubble regime. The accelerated electron transversely oscillates inside the plasma bubble, producing an X-ray pulse. The laser propagates to the right-hand side of this image. See more details in Section 3.4.*

For a typical value of the plasma density employed in LWFA, $\rho_e = 1 \times 10^{19}$ cm^{-3}, the corresponding plasma wavelength is $\lambda_p \simeq 10$ μm. In this case, to reach the X-ray domain of $\lambda_X = 1$ nm, the electron energy could be as low as $\gamma \simeq 100$. Such an electron energy is readily available from contemporary LWFAs.

Proof-of-principle experiments observed betatron radiation in the X-ray domain with photon energy of ~ 1 keV [1] in 2004 [57], and later in 2010 the X-ray peak brightness was impressively boosted to the order of 10^{22} photons/s/mm^2/mrad^2/0.1%BW by working in the highly nonlinear bubble regime [58]. Such a high brightness is comparable to third generation conventional synchrotron light sources [4]. Since the first demonstration various diagnostics have been implemented to characterize the properties of betatron radiation, like X-ray source size[117, 118, 119, 120], pulse duration [121], spectrum [122], and so forth. Among them, the most interesting feature is the pulse duration. It is not trivial to accurately measure it in experiment. A reasonable approximation is the length of electron bunch [57, 58], by which the X-rays are emitted. A very recent study by Lundh *et al* shows that the electron bunch could be as short as few femtoseconds [52], and simulation shows the X-ray pulse duration is very similar, around 10 femtoseconds as well [59]. This ultrashort nature, along with the high peak brightness, makes betatron X-ray very suitable as a research tool on time-resolved ultrafast dynamics. Lately, single-shot phase contrast imaging with these betatron light sources has been demonstrated in experiment [123, 124]. In this context, we could argue that betatron X-ray is a good complement for conventional synchrotron lights. As even for the fourth generation synchrotrons it is still rather difficult to decrease the radiation pulse duration to a few femtoseconds [125], nevertheless synchrotrons can perform at high repetition rate (~ 100 Hz), yielding higher

[1] Using $\mathcal{E} = \hbar 2\pi c/\lambda$, a photon energy of 1 keV corresponds to a wavelength of ~ 1.24 nm.

average X-ray flux [7].

Betatron X-ray radiation, along with electron acceleration, is the other main subject of this thesis study. We have investigated the influences of capillary guiding on X-ray characteristics, as described in Ref. [48]. In this chapter, the basic theory about betatron radiation will be presented.

3.2 Radiation by a moving electron

According to the theory of electrodynamics [126], an accelerated charged particle emits electromagnetic radiation. Here we only consider the case of high energy electrons. Before discussing the radiation of a specific case of electron motion, the general theories of radiation are presented in this section.

We start with the retarded potentials of a moving electron with normalized velocity of $\boldsymbol{\beta}$. The Lineard-Wiechert potentials are given as [126]

$$\begin{aligned} \Phi &= -\frac{e}{4\pi\varepsilon_0}\left[\frac{1}{r(1-\mathbf{n}\cdot\boldsymbol{\beta})}\right]_{ret}, \\ \mathbf{A} &= -\frac{e\mu_0}{4\pi}\left[\frac{\mathbf{v}}{r(1-\mathbf{n}\cdot\boldsymbol{\beta})}\right]_{ret}, \end{aligned} \tag{3.1}$$

where r is the distance between the electron and the observer, and unit vector $\mathbf{n}$ denotes the observation direction. Recalling the relationships in Equation 2.3, one can obtain the associated electric and magnetic fields

$$\begin{aligned} \mathbf{E} &= -\frac{e}{4\pi\varepsilon_0}\left\{\frac{(1-\boldsymbol{\beta}^2)(\mathbf{n}-\boldsymbol{\beta})}{r^2(1-\mathbf{n}\cdot\boldsymbol{\beta})^{\mathbf{3}}} + \frac{\mathbf{n}\times[(\mathbf{n}-\boldsymbol{\beta})\times\dot{\boldsymbol{\beta}}]}{cr(1-\mathbf{n}\cdot\boldsymbol{\beta})^{\mathbf{3}}}\right\}_{ret}, \\ \mathbf{B} &= \frac{e\mu_0 c}{4\pi}\left\{\frac{(1-\boldsymbol{\beta}^2)(\mathbf{n}-\boldsymbol{\beta})}{r^2(1-\mathbf{n}\cdot\boldsymbol{\beta})^{\mathbf{3}}} + \frac{\mathbf{n}\times\dot{\boldsymbol{\beta}}+\mathbf{n}\times[\mathbf{n}\times(\boldsymbol{\beta}\times\dot{\boldsymbol{\beta}})]}{cr(1-\mathbf{n}\cdot\boldsymbol{\beta})^{\mathbf{3}}}\right\}_{ret}. \end{aligned} \tag{3.2}$$

In the above expressions, one may find that the first terms decrease as the inverse square of the distance, which is the normal Coulomb field, and the second terms are relative to acceleration of the particle, which is known as acceleration field [126]. Neglecting the high-order small amounts $\mathcal{O}(\frac{1}{r^2})$ in Equation 3.2, the Poynting's vector is calculated to be

$$\mathbf{S}\cdot\mathbf{n} = \frac{e^2}{16\pi^2\varepsilon_0 c}\left|\frac{\mathbf{n}\times[(\mathbf{n}-\boldsymbol{\beta})\times\dot{\boldsymbol{\beta}}]}{r(1-\mathbf{n}\cdot\boldsymbol{\beta})^3}\right|^2. \tag{3.3}$$

Two radiation features can be immediately drawn from above expression. The angular distribution of radiation is determined by the relationship between observation direction $\mathbf{n}$, electron velocity $\boldsymbol{\beta}$, and acceleration $\dot{\boldsymbol{\beta}}$. Furthermore, the opening angle of radiation is determined by the term $1-\mathbf{n}\cdot\boldsymbol{\beta}$ in the denominator. In the ultrarelativistic case, a forward directional beam will be produced.

The power radiated per solid angle Ω can be easily derived from Poynting's vector to be

$$\frac{dP}{d\Omega} = \frac{e^2}{16\pi^2\varepsilon_0 c}\frac{\left|\mathbf{n}\times[(\mathbf{n}-\boldsymbol{\beta})\times\dot{\boldsymbol{\beta}}]\right|^2}{(1-\mathbf{n}\cdot\boldsymbol{\beta})^5}, \tag{3.4}$$

Therefore the energy radiated per solid angle is

$$\frac{d\mathcal{E}}{d\Omega} = \int_{-\infty}^{\infty}\frac{dP}{d\Omega}\,dt = c\varepsilon_0\int_{-\infty}^{\infty}|r\mathbf{E}|^2\,dt. \tag{3.5}$$

The above expression can be also written in frequency space via Fourier transformation as

$$\frac{d\mathcal{E}}{d\Omega} = 2c\varepsilon_0 \int_0^\infty |r\mathbf{E}|^2 \ dt = 2c\varepsilon_0 \int_0^\infty |r\mathbf{E}|^2 \ d\omega \equiv \int_0^\infty \frac{d^2I}{d\omega d\Omega} \ d\omega. \tag{3.6}$$

Using Equations 3.4∼3.6, one can eventually obtain the frequency and angular distribution of radiation of a moving electron as

$$\frac{d^2I}{d\omega d\Omega} = \frac{e^2}{16\pi^3\varepsilon_0 c} \left| \int_{-\infty}^{\infty} \frac{\mathbf{n} \times [(\mathbf{n} - \boldsymbol{\beta}) \times \dot{\boldsymbol{\beta}}]}{(1 - \mathbf{n} \cdot \boldsymbol{\beta})^2} e^{i\omega(t - \mathbf{n}\cdot\mathbf{r}/c)} \ dt \right|^2. \tag{3.7}$$

A more rigorous derivation of Equation 3.7 is given in Ref. [126]. If $\boldsymbol{\beta}$ and $\dot{\boldsymbol{\beta}}$ are known, one can calculate the associated radiation with Equation 3.7. However, it is not easy to solve this equation analytically. Hence some studies are dedicated to numerically computing it [127].

3.3 Radiation in a plasma column

In this section, we will consider the betatron radiation of an ultrarelativistic electron ($\gamma \gg 1$) that propagates in a plasma column. The plasma column is cylindrical and free of electron, namely an ion channel, which is a good approximation of the bubble regime. The schematic physics is illustrated in Figure 3.2. An important aspect of this study, as presented below, is that the electron motion is analogous to that in a traditional wiggler. Thereby many important features about betatron radiation can be captured.

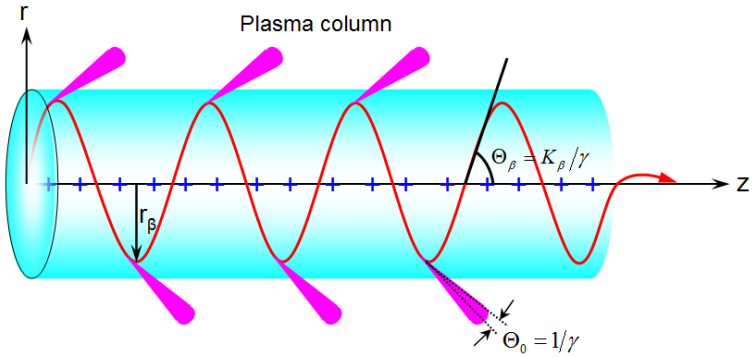

Figure 3.2: *Electron trajectory and betatron radiation in a plasma column.*

3.3.1 Electron trajectory

The electrostatic field associated with the plasma column is described by Gauss's law (See Appendix A.1)

$$\nabla \cdot \mathbf{E} = \frac{e\rho_e}{\varepsilon_0}. \tag{3.8}$$

As the plasma column is 2D cylindrically symmetrical, the $\mathbf{E}$ field is along the radial direction. Thus Equation 3.8 can be simplified to

$$\frac{1}{r}\frac{\partial}{\partial r}(rE_r) = \frac{e\rho_e}{\varepsilon_0}, \tag{3.9}$$

which gives the transverse field

$$E_r = \frac{e\rho_e}{2\varepsilon_0} r. \tag{3.10}$$

The electron motion in this electrostatic field is governed by the Lorentz equation (Equation 2.7)

$$\frac{dp}{dt} = -eE_r = -\frac{e\rho_e^2}{2\varepsilon_0} r, \tag{3.11}$$

where $p = \gamma m_e v$ is the momentum. The relativistic factor γ consists of the transverse component $\gamma_\perp$ and the longitudinal one γ_z, which obeys $\gamma = \gamma_\perp \gamma_z$. If the transverse oscillation is small and the initial longitudinal velocity is high, $\gamma_\perp \ll \gamma_{z0}$ will hold. In this case, the electron energy is dominated by its longitudinal movement, leading to $\gamma \simeq \gamma_z = \gamma_{z0}$. Thus Equation 3.11 can be written as

$$\frac{dv_r}{dt} = \frac{d^2 r}{dt^2} = -\frac{e\rho_e^2}{2m_e\varepsilon_0\gamma} r = -\frac{\omega_p^2}{2\gamma} r \equiv \omega_\beta^2 r, \tag{3.12}$$

where $\omega_\beta = \omega_p/\sqrt{2\gamma}$ is the betatron frequency. One can then obtain the electron oscillation and its velocity as

$$\begin{aligned} \beta_r = \frac{v_r}{c} &= r_\beta k_\beta \cos(k_\beta ct), \\ r &= r_\beta \sin(k_\beta ct), \end{aligned} \tag{3.13}$$

where $k_\beta = \omega_\beta/c$ is the betatron wavenumber and r_β indicates the amplitude of the oscillation. The maximum of normalized electron transverse momentum is often referred to as the betatron strength parameter: $K_\beta = \gamma\beta_r^{max} = \gamma r_\beta k_\beta$. As will be presented later, K_β is a very important parameter to distinguish different radiation regimes.

Now let us consider how the transverse oscillation influences the longitudinal motion. Owing to $\gamma_\perp \ll \gamma_z$, the normalized velocity becomes $\beta \simeq \beta_{z0}$, where $\beta = (\beta_r^2 + \beta_z^2)^{1/2}$. So the longitudinal velocity is affected to be

$$\beta_z = \sqrt{\beta_{z0}^2 - \beta_r^2}. \tag{3.14}$$

Along with Equation 3.13, this yields

$$\begin{aligned} \beta_z &\simeq \beta_{z0}\left(1 - \frac{r_\beta^2 k_\beta^2}{4\beta_{z0}^2}\right) - \frac{r_\beta^2 k_\beta^2}{4\beta_{z0}} \cos(2k_\beta ct), \\ z &\simeq z_0 + \beta_{z0}\left(1 - \frac{r_\beta^2 k_\beta^2}{4\beta_{z0}^2}\right) ct - \frac{r_\beta^2 k_\beta}{8\beta_{z0}} \sin(2k_\beta ct). \end{aligned} \tag{3.15}$$

Equation 3.15 suggests the electron oscillates in the longitudinal direction with twice betatron frequency. Together with the transverse oscillation, it exhibits the eight-shaped motion when seen from the electron co-moving frame, as shown before in Figure 2.2. This is the typical trajectory of an electron in a synchrotron wiggler. Likewise, the electron motion in a plasma column shall produce a synchrotron-like radiation.

3.3.2 Spectral features

As demonstrated above, once the electron motion is known, the corresponding radiation can be calculated using Equation 3.7. Specially for the case of plasma column, Equation

3.7 is analytically solvable. Of particular interest is the radiation emitted along the longitudinal axis, namely $\theta = 0$. In this case, the radiated intensity is given by Esarey *et al* [116] to be

$$\left.\frac{d^2I}{d\omega d\Omega}\right|_{\theta=0} = \sum_{n=1}^{\infty} \frac{e^2}{\pi\varepsilon_0 c}\frac{\omega}{\omega_n}\frac{\gamma^2 N_\beta^2 F_n R_n}{1+K_\beta^2/2}, \tag{3.16}$$

where n is odd, because the even harmonics vanish. ω_n is the nth harmonic frequency of radiation, given by

$$\omega_n = 2n\omega_\beta \frac{\gamma^2}{1+K_\beta^2/2} \simeq 2n\gamma^2\omega_\beta, \tag{3.17}$$

and N_β is the number of oscillation periods that the electron undergoes. F_n indicates the nth harmonic amplitude

$$F_n = n\alpha_n[\mathcal{J}_{(n-1)/2}(\alpha_n) - \mathcal{J}_{(n+1)/2}(\alpha_n)]^2, \tag{3.18}$$

where $\mathcal{J}_n$ is the first kind Bessel function of the nth order, and

$$\alpha_n = \frac{n(\omega/\omega_n)K_\beta^2}{4(1+K_\beta^2/2)}. \tag{3.19}$$

R_n is the spectrum function

$$R_n = \frac{\sin^2[n\pi N_\beta(\omega/\omega_n - 1)]}{[n\pi N_\beta(\omega/\omega_n - 1)]^2}. \tag{3.20}$$

Figure 3.3 displays several spectra calculated with the above equations for a 15 MeV electron. The ambient plasma density is taken as $\rho_e = 7\times10^{18}$ cm^{-3}, and the electron performs ten oscillations $N_\beta = 10$. As given in Equation 3.18, the harmonic amplitude strongly depends on α_n which is further dominated by K_β. So we will examine how the radiation spectrum evolves with K_β. In practical units, $K_\beta = \gamma r_\beta k_\beta = 1.33\times10^{-10}\sqrt{\gamma\rho_e[cm^{-3}]}r_\beta[\mu m]$.

In the case of Figure 3.3(a), a small oscillation amplitude $r_\beta = 0.1$ μm is used, corresponding to $K_\beta = 0.2$. As seen, the spectrum is very pure with only the fundamental harmonic ($n = 1$). The radiated photon energy is given by $\mathcal{E}_{ph} = \hbar\omega_{n=1} \simeq \hbar 2\gamma^2\omega_\beta \simeq 22.4$ eV. The frequency width $\Delta\omega$ for $\omega_{n=1}$ is determined through Equation 3.20 to be $\Delta\omega/\omega_{n=1} = 1/N_\beta = 1/10$. It suggests purer radiation is attainable by using larger N_β. This regime with $K_\beta \ll 1$ is well known as undulator regime. It is particularly interesting for implementing free electron laser (FEL), because all the emitted photons could be highly coherent.

When K_β becomes of the order of unity for a large oscillation amplitude $r_\beta = 0.5$ μm, higher order harmonics clearly appear, as shown in Figure 3.3(b), where 5 harmonics are appreciable. Owing to the larger amplitude of the oscillation, the photon energy of the fundamental harmonic degrades to $\mathcal{E}_{ph} = 16$ eV, evaluated by Equation 3.17. With an even larger r_β of 1.6 μm in Figure 3.3(c), a typical value observed in our experiment, high order harmonics become stronger and numerous, and the harmonic amplitudes follow a synchrotron-like distribution. Figure 3.3(d) illustrates an example of spectrum when the electron energy is higher $\gamma = 200$, leading to $K_\beta = 8$. In this case, many harmonics are excited, closely spaced, and unresolved. Their envelope can be well described by synchrotron radiation. The most striking feature is that photon energies extend to as high as ~ 10 keV. This regime of $K_\beta \gg 1$ is known as the wiggler regime. Most present

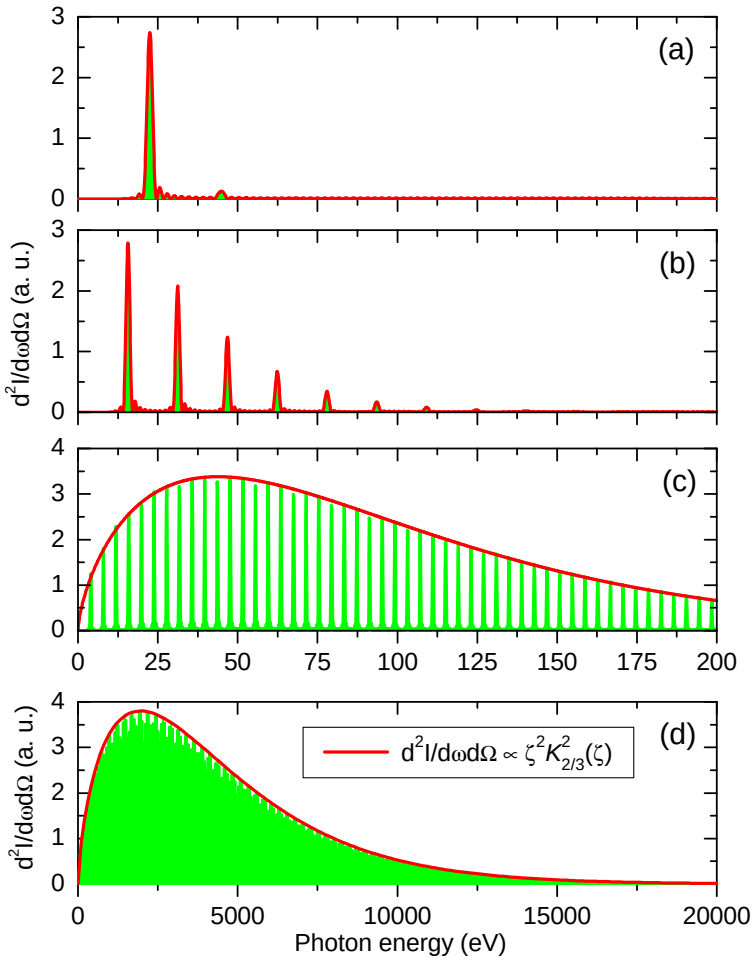

Figure 3.3: *Calculated betatron radiation spectra in a plasma column with density of* 7×10^{18} cm^{-3}. *The electron energy is 15 MeV, and oscillation amplitudes are (a) 0.1 μm, (b) 0.5 μm, and (c) 1.6 μm. (d) shows the case of a 100 MeV electron with an oscillation amplitude of 1.6 μm.*

experiments about laser-plasma betatron radiation operate in this regime, where ~ 1 keV energy photons with high brightness are produced.

Figure 3.3(d) suggests that the envelop of the spectrum in the wiggler regime can be described as the synchrotron radiation. Recently, it was demonstrated that the spectrum of betatron radiation is indeed synchrotron-like [122]. Ref. [116] furthermore examines the asymptotic spectrum when $K_\beta \gg 1$, which reads

$$\left.\frac{d^2I}{d\omega d\Omega}\right|_{\theta=0} \simeq N_\beta \frac{3e^2}{2\pi^3\varepsilon_0 c}\gamma^2\zeta^2\mathcal{K}^2_{2/3}(\zeta), \tag{3.21}$$

where $\zeta = \omega/\omega_c$, and $\mathcal{K}_{2/3}$ is the second kind modified Bessel function of 2/3 order. ω_c is the widely used critical frequency in the synchrotron radiation community[2]

$$\omega_c = 3\gamma^2 K_\beta \omega_\beta. \tag{3.22}$$

[2]A different definition of ω_c may be found in other literature with a difference of a factor of 2. In this thesis, we follow the definition from Refs. [116, 126].

Accordingly, the critical energy is defined as $\mathcal{E}_c[\mathrm{keV}] = \hbar\omega_c = 1.1\times10^{-23}\gamma^2\rho_e[\mathrm{cm}^{-3}]r_\beta[\mu\mathrm{m}]$. For example, the spectra in Figure 3.3(c)-(d) have critical energies of 0.1 keV and 4.7 keV, respectively. Obviously, the value of $\mathcal{E}_c$ is mainly determined by electron energy. It is useful to calculate the spectrum of angularly integrated radiation, which is given by

$$\frac{dI}{d\omega} = 2\pi\int_{-\pi/2}^{\pi/2}\frac{d^2I}{d\omega d\Omega}\sin\theta\ d\theta = \sqrt{3}N_\beta\frac{\gamma e^2}{\pi\varepsilon_0 c}\frac{\omega}{\omega_c}\int_{2\omega/\omega_c}^{\infty}\mathcal{K}_{5/3}(\zeta)\ d\zeta. \tag{3.23}$$

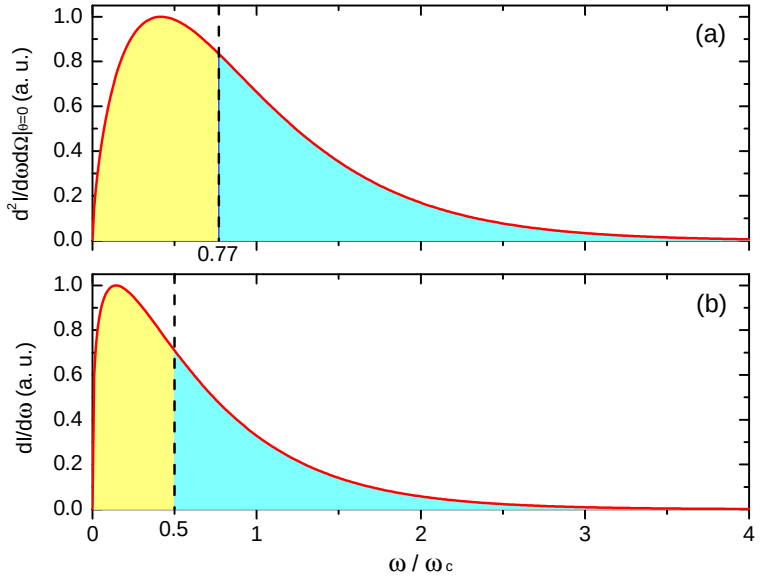

Figure 3.4: *(a) The on-axis and (b) angularly integrated spectra. The dashed lines indicate the frequencies below (green) and above (blue) which half of the energy is radiated.*

Figure 3.4 demonstrates the on-axis and angularly integrated spectra obtained with Equations 3.21 and 3.23. The on-axis radiation is fully described by the term $\zeta^2\mathcal{K}_{2/3}^2(\zeta)$. It peaks at the frequency $\omega \simeq 0.42\omega_c$. Half radiation energy is produced for $\omega < 0.77\omega_c$ and the other half is for $\omega > 0.77\omega_c$, as seen in Figure 3.4(a). Moreover, for $\omega \ll \omega_c$, the increase of radiation intensity can be approximated by $(\omega/\omega_c)^{2/3}$, while for the frequency $\omega \gg \omega_c$ the radiation intensity exponentially drops as $\exp(-2\omega/\omega_c)$. These quantities change when off-axis radiation is taken into account, as presented in Figure 3.4(b). The radiation intensity exhibits its maximum at a lower frequency $\omega \simeq 0.14\omega_c$, and diminishes rapidly when $\omega > \omega_c$. Particularly, half radiation energy is produced at frequencies $\omega < \omega_c/2$ and the other half is for $\omega > \omega_c/2$, namely $\int_0^{\omega_c/2}\frac{dI}{d\omega}d\omega = \int_{\omega_c/2}^{\infty}\frac{dI}{d\omega}d\omega$. In this sense, one can understand the critical energy ω_c as twice the frequency below and above which half radiation energy is created.

Moreover, the power produced by a single electron can be calculated by the relativistic Larmor formula

$$P_s = \frac{e^2}{6\pi\varepsilon_0 c}\gamma^2\left[\left(\frac{du}{dt}\right)^2 - \left(\frac{d\gamma}{dt}\right)^2\right]. \tag{3.24}$$

For the trajectory of betatron oscillation given by Equations 3.13 and 3.15, the radiated power averaged over an oscillation period is

$$\bar{P}_s = \frac{e^2 c}{12\pi\varepsilon_0}\gamma^2 k_\beta^2 K_\beta^2 = \frac{e^2 c}{12\pi\varepsilon_0}\gamma^4 k_\beta^4 r_\beta^2 \propto \gamma^2 r_\beta^2. \tag{3.25}$$

Furthermore, the total emitted energy, the product of $\bar{P}_s$ and the interaction time $N_\beta \lambda_\beta / c$, is given by

$$\bar{W}_s = \frac{e^2}{6\varepsilon_0} N_\beta \gamma^2 k_\beta K_\beta^2 = \frac{e^2}{6\varepsilon_0} N_\beta \gamma^4 k_\beta^3 r_\beta^2 \propto \gamma^{5/2} r_\beta^2. \tag{3.26}$$

As seen, both the radiated power and energy strongly scale with γ and r_β. This suggests significantly higher P_s and W_s could be reached by working in the wiggler regime ($K_\beta \gg 1$) rather than the undulator regime ($K_\beta \ll 1$).

3.3.3 Spatial distributions

Besides spectral feature, the other important nature of radiation is the spatial distribution. It determines how the radiation looks when detected somewhere. In order to study the spatial distribution of radiation, one needs the corresponding 3D electron trajectory. In the previous section, the electron motion was assumed to take place in a 2D plane (r, z). The corresponding electron trajectory was described by Equations 3.13 and 3.15. Here we will introduce the electron movement in the transverse (x, y) plane to get 3D trajectory in the coordinate (x, y, z).

Equation 3.13 can be split along the two transverse directions (x, y) as

$$\begin{aligned} \frac{d^2x}{dt^2} &= \frac{dv_x}{dt} = -\frac{e\rho_e^2}{2\gamma\varepsilon_0} x, \\ \frac{d^2y}{dt^2} &= \frac{dv_y}{dt} = -\frac{e\rho_e^2}{2\gamma\varepsilon_0} y. \end{aligned} \tag{3.27}$$

The motion of electron is then determined by its initial condition (x_0, y_0, p_{x0}, p_{y0}). Without loss of generality, we assume the electron is initially located at somewhere in the x axis. Equation 3.27 is numerically solved with different initial parameters with the fourth-order Runge-Kutta method. The associated radiation is calculated using Equation 3.7 at each time step.

Figure 3.5 illustrates the electron trajectory and radiation pattern for three typical cases obtained with a 100 MeV electron propagating in a plasma column at density $\rho_e = 7 \times 10^{18}$ cm^{-3}. For all these cases, the electron is initially at $x_0 = 1.6$ μm, $y_0 = z_0 = 0$. In Figure 3.5(a) $p_{y0} = 0$, which implies initially the electron is at rest. Thus the orbit degrades to the 2D movement. As seen in Figure 3.5(b), an elliptical trajectory is exhibited in the transverse plane for $p_{y0} = 3m_e c$. From the viewpoint of 3D, the motion is helical. Figure 3.5(c) illustrates a circular motion in the transverse plane for $p_{y0} = 8m_e c$, where the local electrostatic force matches the centrifugal force of the electron.

Figure 3.5(d)-(f) display the radiation profiles corresponding to the motions in Figure 3.5(a)-(c), respectively. The color scale represents the amplitude of radiated energy. One can see that the radiation profiles reflect the electron transverse motions. Such radiation patterns observed in experiments have been used by Phuoc *et al* to infer the parameters of electron motions in plasma cavity [128, 129]. Two angles are widely employed to describe the radiation profile. The first is the opening angle Θ_0 (as illustrated in Figure 3.2) which determines the radiation divergence at a given moment. The angular distribution of the radiation in the wiggler regime is given by [126]

$$\frac{dI}{d\Omega} = \int_0^\infty \frac{d^2I}{d\omega d\Omega}\, d\omega = \frac{7e^2}{96\pi\varepsilon_0 c} \frac{N_\beta \gamma^2 \omega_c}{(1+\gamma^2\theta^2)^{5/2}} \left[1 + \frac{5\gamma^2\theta^2}{7(1+\gamma^2\theta^2)}\right]. \tag{3.28}$$

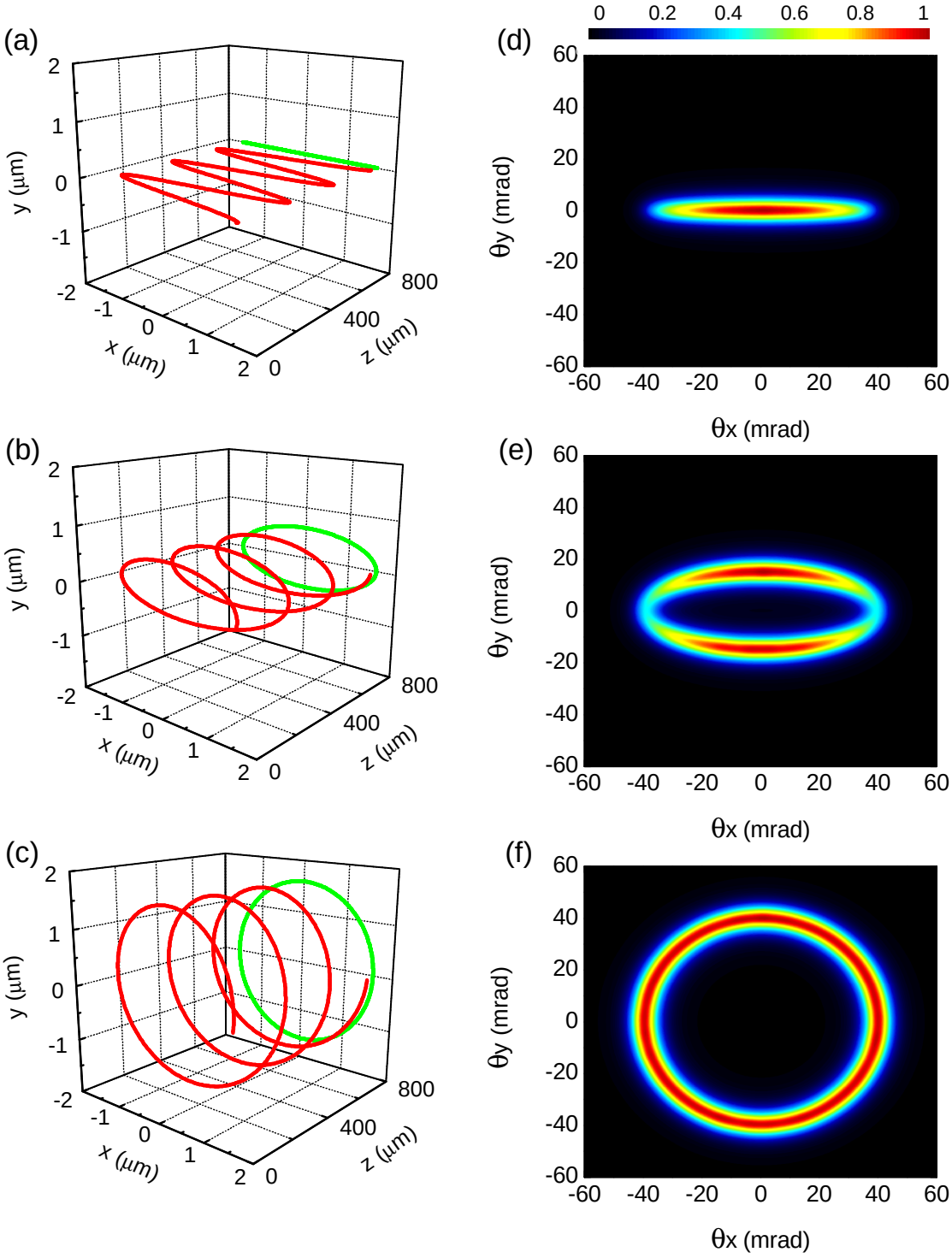

Figure 3.5: *3D trajectories and transverse projections of an electron with energy of 100 MeV in a plasma column with density of* $\rho_e = 7 \times 10^{18}$ cm^{-3}. *Initially the electron is at* $x_0 = 1.6$ μm, $y_0 = 0$ *with momentum (a)* $p_{y0} = 0$, *(b)* $p_{y0} = 3m_e c$, *(c)* $p_{y0} = 8m_e c$. *(d)-(f) are the corresponding radiation profiles.*

The denominator in Equation 3.28 suggests the radiation is collimated within a cone, the half opening angle of which can be estimated by

$$\Theta_0 \simeq \frac{1}{\gamma}. \tag{3.29}$$

Typically in Figure 3.5(d), the width of the radiation profile along the y axis is given by $\Theta_0 = 1/200 = 5$ mrad. This is also the width of the lobes in Figure 3.5(e)-(f).

The other angle Θ_β is often referred to as radiation opening angle, which represents the maximal angle that the radiation can reach in the electron oscillation plane. Thus one can evaluate Θ_β when the electron cross the z axis via

$$\begin{aligned} \Theta_{\beta x} &= \left.\frac{dx}{dz}\right|_{x=0} = r_{\beta x} k_\beta = \frac{K_{\beta x}}{\gamma}, \\ \Theta_{\beta y} &= \left.\frac{dy}{dz}\right|_{y=0} = r_{\beta y} k_\beta = \frac{K_{\beta y}}{\gamma}, \end{aligned} \tag{3.30}$$

where $r_{\beta x}$, $r_{\beta y}$ represent respectively the electron oscillation amplitudes along the x and y axes. For example in Figure 3.5(b), $r_{\beta x} = 1.6$ μm, $r_{\beta y} = 0.6$ μm, which correspond to the strength parameters $K_{\beta x} \simeq 8$ and $K_{\beta y} \simeq 3$. Thus the opening angles of the radiation are estimated to be $\Theta_{\beta x} = 8/200 = 40$ mrad, and $\Theta_{\beta y} = 3/200 = 15$ mrad.

It is interesting to discuss the magnitude relationship between Θ_0 and Θ_β. $\Theta_\beta \ll \Theta_0$ corresponds to $K_\beta \ll 1$. It is actually the known undulator regime. In this case, the source oscillation amplitude is small compared to its angular width. The radiation divergence is thus dominated by the beam divergence itself. The main interest of this regime is that the radiation exhibits an interference pattern which yields a narrow spectrum. That's why normally free electron lasers operate in the undulator regime. Whereas for $\Theta_\beta \gg \Theta_0$, the radiation enters the wiggler regime ($K_\beta \gg 1$). As presented before, the spectrum becomes broad owing to independent contributions by the excited harmonics. Furthermore, the radiation divergence is then characterized by the oscillation amplitude of electron.

3.4 Radiation in a plasma column with acceleration

In Section 3.3, the physics of betatron radiation was obtained for a given longitudinal electron energy. This is certainly not the case for electron motion in LWFA, where the longitudinal acceleration of electron can not be neglected. In this sense, the radiation properties should differ somewhat from what we presented before. In this part, we are going to examine the radiation features when electron acceleration is taken into account. It is sometimes referred to as "bubbletron" radiation [106] to distinguish from betatron radiation without electron acceleration.

3.4.1 Electron motion

Firstly let's see how the electron motion is modified when a longitudinal accelerating field $\mathbf{E}_z$ is present. Electron acceleration along the z axis is given by

$$\frac{d(\gamma\beta_z)}{dt} = \frac{e}{m_e c} E_z, \tag{3.31}$$

which leads to

$$\gamma\beta \simeq \gamma\beta_z = \gamma_0\beta_0 + \frac{eE_z}{m_e c} t, \tag{3.32}$$

where $\gamma_0\beta_0$ denotes the initial normalized momentum, and $\beta \simeq \beta_z$ is used again. The transverse motion is given by Equation 3.11

$$\frac{d(\gamma v_r)}{dt} = v_r\frac{d\gamma}{dt} + \gamma\frac{dv_r}{dt} = -\frac{\omega_p^2}{2}r. \tag{3.33}$$

Substituting Equation 3.32 into the above expression, keeping in mind $\beta \to 1$, and recalling $v_r = dr/dt$, one can get

$$\left(\frac{eE_z}{m_e c}t + \gamma_0\beta_0\right)\frac{d^2r}{dt^2} + \frac{eE_z}{m_e c}\frac{dr}{dt} + \frac{\omega_p^2}{2}r = 0. \tag{3.34}$$

Solving this equation with initial conditions $r(0) = r_0$ and $v_r(0) = 0$ yields [130]

$$\begin{aligned} r(t) = \frac{\pi E_0}{\sqrt{2}E_z}\sqrt{\gamma_0\beta_0}r_0 \Big[&\mathcal{J}_1\left(\sqrt{2\gamma_0\beta_0}E_0/E_z\right)\mathcal{Y}_0\left(\sqrt{2\gamma\beta}E_0/E_z\right) \\ &-\mathcal{Y}_1\left(\sqrt{2\gamma_0\beta_0}E_0/E_z\right)\mathcal{J}_0\left(\sqrt{2\gamma\beta}E_0/E_z\right)\Big], \end{aligned} \tag{3.35}$$

where $\mathcal{Y}$ is the Bessel function of the second kind. When $2\sqrt{\gamma_0\beta_0}E_0 \gg E_z$, the above expression can be further simplified to

$$\begin{aligned} r(t) &= r_0\left(\frac{\gamma_0\beta_0}{\gamma\beta}\right)^{1/4}\cos\left[\frac{E_0}{E_z}\left(\sqrt{2\gamma\beta} - \sqrt{2\gamma_0\beta_0}\right)\right], \\ &\simeq r_0\left(\frac{\gamma_0}{\gamma}\right)^{1/4}\cos\left[\frac{E_0}{E_z}\left(\sqrt{2\gamma} - \sqrt{2\gamma_0}\right)\right]. \end{aligned} \tag{3.36}$$

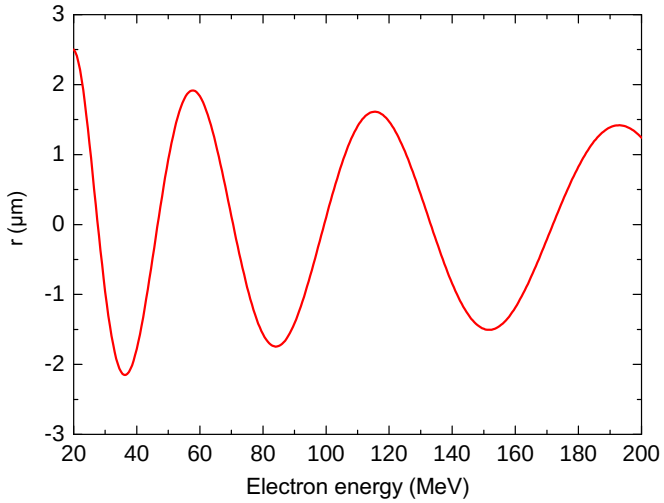

Figure 3.6: *Trajectory of an electron accelerated from 20 to 200 MeV with $r_0 = 2.5$ μm. The damping of the oscillation amplitude and the lengthening of the oscillation period are clearly visible.*

Figure 3.6 illustrates the betatron trajectory of an electron initially at $r_0 = 2.5$ μm accelerated from 20 to 200 MeV. The accelerating field is assumed equal to E_0. Two features of the motion can be drawn. Firstly, the oscillation amplitude is gradually damped due to the increase of the relativistic factor. As shown in Figure 3.36, $r \propto \gamma^{-1/4}$. Furthermore, the oscillation period slowly lengthens. That's because the relativistic electron mass increases as γm_e, which leads to the decrease of the betatron oscillation frequency according to $\omega_\beta = \omega_p/\sqrt{2\gamma}$ (or $\lambda_\beta = \sqrt{2\gamma}\lambda_p$).

3.4.2 Spatial and spectral features

It is also of great interest to examine the spatial distribution of the radiation and furthermore how the radiation spectrum is modified by the acceleration process. To do this, we need the electron movement parameters: $\mathbf{r}(t)$, $\beta(t)$, and $\dot{\beta}(t)$. Therefore Equations 3.31 and 3.33 are numerically solved for different initial cases with the fourth-order Runge-Kutta method.

Figure 3.7(a)-(b) are two typical 3D trajectories of an electron accelerated along the z axis from 20 to 200 MeV in a plasma with density $\rho_e = 7 \times 10^{18}$ cm^{-3}. The longitudinal accelerating field is supposed to be equal to the cold wavebreaking electric field, namely $E_z = E_0 \simeq 255$ GV/m. Initially the electron is at $x_0 = 2.5$ μm and with $p_{x0} = 0$. For the case of $p_{y0} = 0$ in Figure 3.7(a), the trajectory degrades to 2D, as shown in Figure 3.6. The electron experiences more than 3 periods, and its oscillation amplitude decreases from 2.5 μm to about 1.4 μm. When the initial transverse momentum is $p_{y0} = 3m_e c$, the electron exhibits a spiral motion, as seen in Figure 3.7(b). The corresponding radiation is calculated at each time step through Equation 3.7, and integrated over the propagation time. One can see that the radiation emission patterns are clearly related to the electron trajectories. Owing to the increase of electron energy, both the emission divergence $\Theta_\beta = K_\beta/\gamma$ and width of the lobes $\Theta_0 = 1/\gamma$ decrease accordingly. This is particularly appreciable in Figure 3.7(d). The most significant feature is that the radiation tends to be more intense when oscillation amplitude diminishes, because the intensity of the instantaneous radiation increases quickly with increasing electron energy by $\frac{dP}{d\Omega} \propto \gamma^6$ [126].

The modification of the radiation spectrum by electron acceleration has also been studied. As we are mainly interested in on-axis radiation, only this case is considered here. The on-axis spectrum given by Equation 3.21 was derived for constant electron energy. The modified spectrum can be computed by integrating Equation 3.21 over the electron energy range $[\mathcal{E}_{int}, \mathcal{E}_{fin}]$

$$\left.\frac{d^2 I_{acc}}{d\omega d\Omega}\right|_{\theta=0} = \frac{3e^2}{2\pi^3 \varepsilon_0 c} \int_{\mathcal{E}_{int}}^{\mathcal{E}_{fin}} d\gamma^2 \zeta^2 \mathcal{K}_{2/3}^2(\zeta), \tag{3.37}$$

where I_{acc} denotes the radiated intensity when electron acceleration is taken into account. Figure 3.7(e)-(f) demonstrate the calculated spectra for the two orbits in Figure 3.7(a)-(b). Their shapes look similar to synchrotron spectrum. Therefore we tried two kinds of fit. The first is a least squares fit. Treating ω_c as a free variable, the best fit comes when the difference χ^2 between the spectra of Equations 3.37 and 3.21 becomes minimum. χ^2 is calculated through

$$\chi^2 = \int_0^\infty \left(\left.\frac{d^2 I_{acc}}{d\omega d\Omega}\right|_{\theta=0} - \left.\frac{d^2 I}{d\omega d\Omega}\right|_{\theta=0} \right)^2 d\omega. \tag{3.38}$$

The corresponding critical frequency is noted as ω_c^{fit}. The dashed lines in Figure 3.7(d)-(e) are the results given by this least squares fit. Interestingly, it is found that $\omega_c^{fit} \simeq 0.56\omega_c^{max}$ for the 2D linear oscillation, and $\omega_c^{fit} \simeq 0.58\omega_c^{max}$ for the 3D spiral motion, where ω_c^{max} is the critical frequency corresponding to the maximum electron energy. In this calculation, the maximum electron energy is $\mathcal{E}_{fin} = 200$ MeV. Analytical study of the radiation spectrum of an electron accelerated in a plasma bubble gives $\omega_c^{fit} \simeq 0.57\omega_c^{max}$ [106], which is quite close to this numerical analysis.

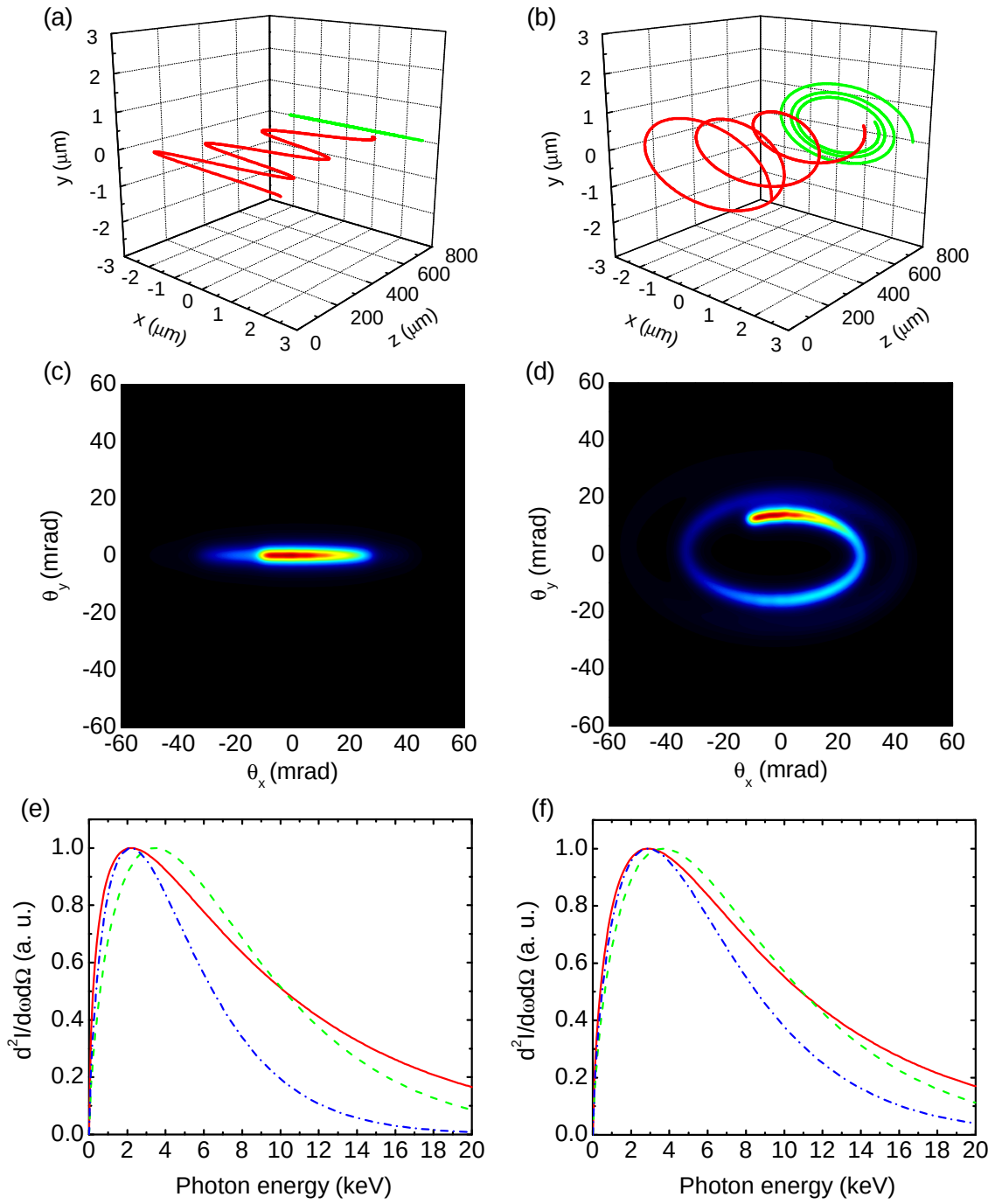

Figure 3.7: *Trajectories of an electron accelerated from 20 to 200 MeV in a plasma with density of $\rho_e = 7 \times 10^{18}$ cm^{-3}. The electron is launched at $x = 2.5$ μm with momentum of (a) $p_{y0} = 0$ and (b) $p_{y0} = 3m_e c$. (c)-(d) are the corresponding radiation patterns. (e)-(f) present the calculated on-axis spectra (red solid), the least squares fit (green dash), and the peak fit (blue dash dot).*

The other interesting fit is a "peak fit". The spectrum is fitted using Equation 3.21 to have the same peak position as the numerical spectrum, indicated by the dash dotted lines in Figure 3.37(e)-(f). It is obvious that below the peak frequency the peak fits excellently agree with the numerical spectra, while above it the numerical spectra deviate from the

fit and display more enhanced high energy tails. Another feature of interest is the peak photon energy is 2.9 keV for the spiral case, slightly larger than that of the linear oscillation case of 2.2 keV. This is because the peak photon energy (or critical energy) linearly scales with oscillation amplitude. In the case of linear oscillation in Figure 3.7(a), the oscillation magnitude can become very small, $r_\beta \to 0$, when the electron goes across the z axis, whereas this does not happen for the spiral motion where the electron rotates around the z axis but never crosses it.

It is worth mentioning that the calculated radiation spectra, red solid lines in Figure 3.7(e)-(f), are indeed observed in PIC simulations of betatron radiation in the bubble regime (See more details in Chapter 6). We have also experimentally observed the X-rays showing similar spatial patterns as displayed in Figure 3.7(d) [46].

3.5 Emission from an electron bunch

Up to now, we considered the typical results of betatron radiation emitted by a single electron. In experiment, it is an electron bunch, or many electrons together, which contribute to the radiation. We now discuss the radiation produced by an electron bunch. If all the electrons have the same energy and oscillation amplitude, the radiations shall be the same as what we calculated above. However in most experiments, the electron energy spread is relatively large or Maxwellian-like [48]. Thus the radiation properties may become different from the case of single electron.

Firstly we consider the spatial profiles of radiation. As shown in Figures 3.5 and 3.7, the spatial profile is determined by the electron trajectory, and more precisely by the initial position and momentum. Normally the trapping processes of different electrons should be independent except when some collective electron oscillation are deliberately introduced, for example, by tailoring the laser wavefront [131, 132]. The combination of the radiations from electrons with various initial conditions will generate numerous spatial distribution patterns. Here we examine two typical cases.

Figure 3.8(a) depicts the initial conditions of the first case, where 18 electrons are uniformly distributed on a circle with radius of 2.5 μm in the transverse (x, y) plane. Every electron has an initial momentum $p_0 = 3m_e c$ along the counterclockwise direction of the local tangent, as indicated by the arrows. The electrons are accelerated from 20 to 200 MeV along the z axis by a longitudinal electric field $E_z = E_0$. The radiation profile, as shown in Figure 3.8(c), looks like a ring with opening angle of $\Theta_\beta \simeq 15$ mrad. Besides, the profile is symmetrical, completely different from that of single electron [See Figure 3.7(d)]. The other example is 5 electrons initially located along the x axis from 0.5 to 2.5 μm with equal separation of 0.5 μm. All those electrons have initially the same momentum along the y axis of $p_{y0} = 3m_e c$. Like in the first case, the electrons are accelerated from 20 to 200 MeV, but the radiation profile is dominated by electrons with larger oscillation amplitudes, as both the opening angle Θ_β and radiated power P_s are proportional to r_β.

Now let's examine how the radiation spectrum varies with respect to the electron energy spread. We suppose that the electrons are trapped with an initial energy of 20 MeV and accelerated by the plasma wave at a density of $\rho_e = 7 \times 10^{18}$ cm^{-3}. The initial conditions of these electrons are the same: $r_\beta = 2.5$ μm and $p_\perp = 0$. The final energy range of electrons is $40 - 200$ MeV, and the energy distribution of the electrons is assumed to be Maxwellian with a temperature of 30 MeV, namely $\mathcal{N}_e(\mathcal{E}) = \exp[-(\mathcal{E} - 40)/30]$, as shown in Figure 3.9(a). It is a function close to the typical electron spectra observed in our experiments (See Chapter 6). The radiation is proportional to the electron number [116], and for a given electron energy, the radiated energy can be calculated, using Equation

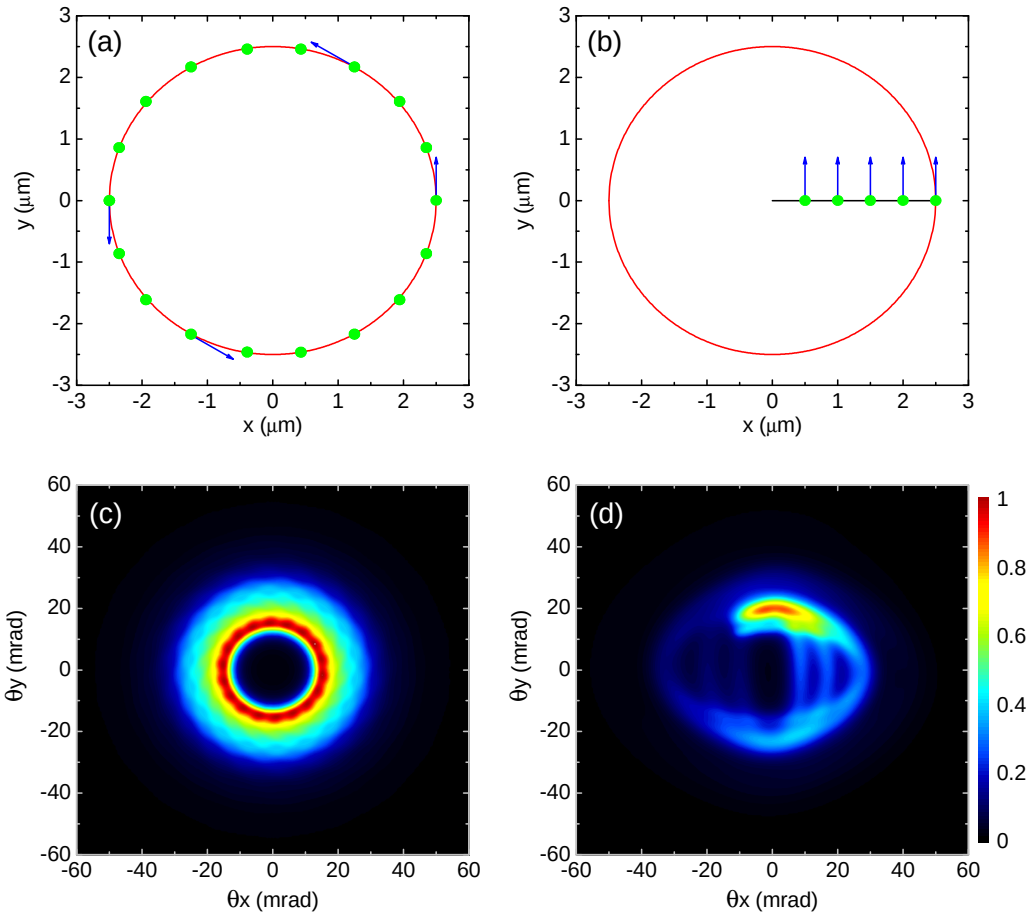

Figure 3.8: *Examples of radiation pattern calculated for two electron distributions. Initial conditions: (a) 18 electrons uniformly distribute on a circle of radius of 2.5 μm, (b) 5 electrons equably locate along the x axis. The arrows indicate the directions of initial momentum of $3m_ec$. (c)-(d) are the respective radiation profiles.*

3.23, via

$$I_X(\mathcal{E}) = \mathcal{N}_e(\mathcal{E}) \int_{\gamma_0}^{\gamma} \int_{\omega_1}^{\omega_2} \frac{d^2I}{d\omega d\gamma'} \, d\omega d\gamma' \tag{3.39}$$

where $\gamma_0 = 40$ corresponds to the electron initial energy. $\hbar\omega_1 = 0.1$ keV and $\hbar\omega_2 = 20$ keV represent the range of photon energies taken into account. The distribution of I_X computed numerically is plotted with a red solid line in Figure 3.9(a). It is found that the electrons with a final energy of 112 MeV contributes most to the radiation. The peak of the emitted radiation as a function of electron energy can be understood by the optimum values of electron energy and number, as more energetic electrons create more emission while their number tends to decrease. In this case it is not the most energetic electrons that dominate the radiation. This finding suggests it is more relevant to use electron mean energy (about 70 MeV) rather than maximum energy (200 MeV) to correlate the properties between electron beam and radiation, as presented in Refs. [48, 131].

Another interesting feature is the on-axis radiation spectrum, since it is usually what we measure in experiments [46, 48]. In most cases, the radiations from different electrons

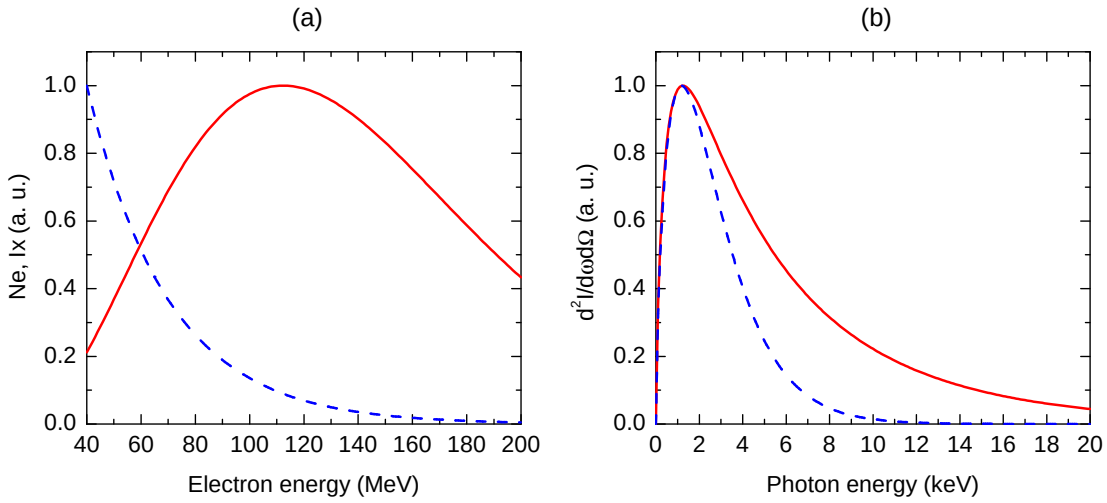

Figure 3.9: *(a) Energy distribution (blue dashed line) of an electron bunch with a temperature of 30 MeV and the radiate intensity (red solid line) calculated by Equation 3.39. (b) Numerically calculated spectrum (red solid line) of on-axis radiation, and the peak fit (blue dashed line) .*

incoherently overlap on axis, thus using Equation 3.37 the spectrum is obtained via

$$\left.\frac{d^2 I_b}{d\omega d\Omega}\right|_{\theta=0} = \frac{3e^2}{2\pi^3 \varepsilon_0 c} \mathcal{N}_e(\mathcal{E}) \int_{\gamma_0}^{\gamma} d\gamma'^2 \zeta^2 \mathcal{K}_{2/3}^2(\zeta). \tag{3.40}$$

For the electron spectrum in Figure 3.9(a), the on-axis spectrum is calculated numerically and shown in Figure 3.9(b) as a red solid line, as well as the corresponding peak fit (blue dashed line). As one can see, the numerical spectrum of the electron bunch is still synchrotron-like, with a peak photon energy of 1.2 keV. Compared to the peak fit spectrum, the spectrum calculated for the electron bunch displays a larger amount of high energetic photons, as already seen in the case of a single accelerated electron in Figure 3.7(f). This phenomenon is attributed to the fact that the electron energies are not constant but increase during the propagation.

It should be noted that what we presented here are simplified examples. The physics of electron acceleration and betatron radiation should be more complex in experiments. Therefore 3D PIC simulations play an important role in interpreting experimental observations.

3.6 Mapping electron acceleration via betatron radiation

In this section, we introduce an important application of betatron radiation, as a diagnostic to map the process of electron acceleration in plasma. Optical methods are often employed as diagnostics [49, 50, 51], however it can be complicated to implement them, and local plasma information can not always be retrieved. As presented below, betatron radiation can provide a relatively simple way to visualize the process of LWFA.

When an off-axis electron is trapped by the plasma wave and gets accelerated, it starts to oscillate transversely and emit photons. These two processes happen simultaneously, and provide a way to study the dynamics of electron acceleration via the emitted radiation. Typically in experiments, the amplitude of the transverse oscillation of electrons is of the order of a few microns, which is small compared to the longitudinal acceleration distance

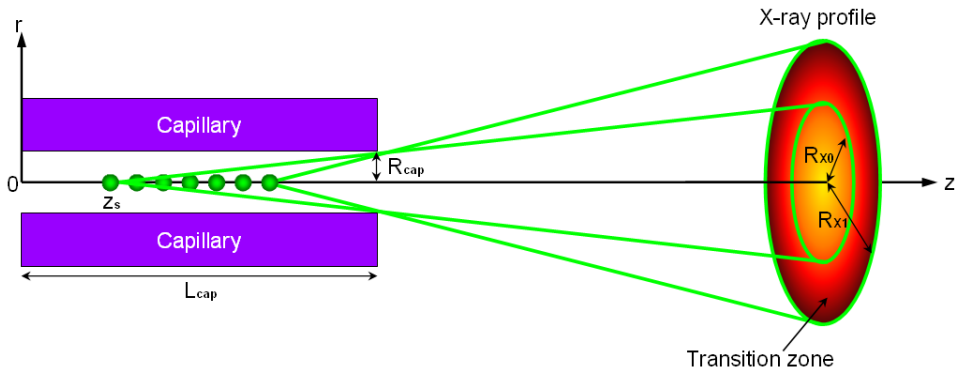

Figure 3.10: *Schematic illustration of the X-ray profile produced by betatron radiation from an extended source inside a capillary tube.*

of several millimeters. Thus in the following analysis, the emission source is viewed as 1D along the z axis. Figure 3.10 illustrates schematically the geometry of the X-ray emission produced by a line source inside a capillary tube. At a given position z, the opening angle of the X-ray emission determined by the capillary size is $\Theta_{cap} = \arctan[R_{cap}/(L_{cap} - z)]$. R_{cap}, L_{cap} are the radius and length of the capillary tube, respectively. In most cases, the emission occurs in the wiggler regime, for which $\Theta_\beta > \Theta_{cap}$ normally holds. It means the emitted radiation cone is cropped by the rim of capillary exit. The photons hitting the capillary wall are absorbed there. In other words, the radiation emitted at different longitudinal positions project the border of capillary exit, working as an aperture, onto the detector with different sizes. Closer is the emission to the capillary exit, larger the shadow is. The superposition of emission cones with different aperture sizes establish a transition zone at the edge of the far-field X-ray profile. The starting point of trapping and the longitudinal extension of acceleration can be easily characterized by the size of the transition zone with a geometrical method. The starting position can be inferred by $z_s \simeq L_{cap} - R_{cap}L_X/R_{X0}$. L_X represents the distance from capillary entrance to the detector, and R_{X0} is the inner radius of the X-ray transition zone. For a typical experimental setup, $L_X \gg L_{cap}$. The length of the emitting zone is thus given by $\Delta z = R_{cap}L_X(1/R_{X0} - 1/R_{X1})$, where R_{X1} is the outer radius of the transition zone.

Furthermore the intensity gradient in the transition region yields the longitudinal profile of the emission process. The signal on the detector is

$$S_X(r) = \int_0^{2\pi} S_X(r,\theta)\, d\theta = \int_{z(r)}^{L_{cap}} \frac{dI_X(z')}{dz'}\, dz', \tag{3.41}$$

where r is the radial coordinate on the detector, $z(r) = L_{cap} - R_{cap}L_X/r$ is the corresponding longitudinal position of emission inside the capillary tube, and $dI_X(z')/dz'$ indicates the X-rays produced per unit length around z'. Note it is an integration with variable lower limit in Equation 3.41, so taking the derivative leads to

$$\frac{dI_X(z)}{dz} = -\frac{\partial S_X(r(z))}{\partial r}\frac{r^2(z)}{R_{cap}L_X}, \tag{3.42}$$

where $r(z) = R_{cap}L_X/(L_{cap} - z)$. For a known X-ray intensity distribution, the longitudinal profile of emission can be obtained through Equation 3.42.

It is important to know the precision of the above analysis method. There are two possible uncertainties introducing errors in this calculation using Equation 3.42. The first

one is the determination of the longitudinal coordinate z. As shown before, z is calculated through

$$z(r) = L_{cap} - L_X \frac{R_{cap}}{r}. \tag{3.43}$$

In measurement, the resolution of r is limited by the pixel size of the X-ray CCD camera δs_{pixel}. So the error of z is

$$\delta z = L_X \frac{R_{cap}}{r^2} \delta r = L_X \frac{R_{cap}}{r^2} \delta s_{pixel}. \tag{3.44}$$

The second possible error is the transverse source size, because the above analysis was derived for a 1D line source. The influence of the transverse source size is illustrated in Figure 3.11. If one deduces an emission region from z_s to z_e using the 1D formula, the

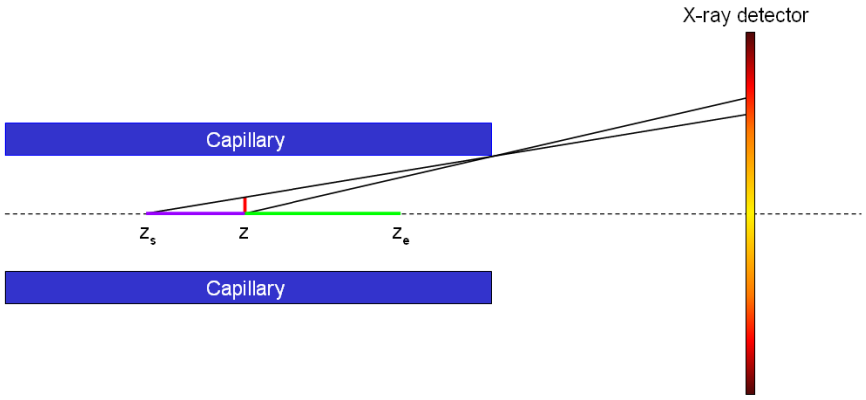

Figure 3.11: *Influence of the transverse source size on the X-ray profile.*

region might be different when taking into account the source size. For example, if the source has a transverse size at z (indicated by the transverse red line), it would project the capillary border equivalent to the emissions produced from 1D source between z_s and z. The distance between z_s and z, D^z_{zs}, is therefore the error of the 1D determination method at z. D^z_{zs} can be geometrically calculated by

$$D^z_{zs} = \frac{L_{cap} - z}{R_{cap}/r_s - 1}, \tag{3.45}$$

where r_s is the source size.

For a typical setup in our experiment (See more details in Chapter 5), a capillary length $L_{cap} = 30.5$ mm, a distance from capillary exit to X-ray camera $L_X = 110$ cm, a capillary radius $R_{cap} = 89$ μm, and a radius coordinate on the X-ray detector $r(z) \simeq 3.7$ mm, Equation 3.44 corresponds to a resolution of about 180 μm. Furthermore if we assume the transverse source size is $r_s = 2$ μm, Equation 3.45 would introduce an error of ~ 600 μm at $z = 4$ mm. $z = 0$ is at the capillary entrance. One can clearly see that it is the transverse source size that dominantly limits the resolution of this 1D analysis.

This diagnostic method provides deep insights into the associated mechanisms on laser evolution, electron trapping, dephasing, and so on [46, 60]. Putting an external aperture in the radiation path, this method can be applied to a gas jet target as well. It is worth noting that in our case the capillary tube is versatile: besides guiding the laser, its exit naturally performs as an aperture, making the setup quite compact.

3.7 Summary

The accelerated electrons are transversely wiggled by the radial electric field in the plasma bubble, generating a synchrotron-like X-ray radiation, often termed as betatron radiation. The radiation spectrum is determined by the betatron strength parameter $K_\beta = \gamma r_\beta k_\beta$. $K_\beta \ll 1$ corresponds to the undulator regime, in which only the fundamental harmonic ($\omega_n = 2\gamma^2\omega_\beta$) is excited. On the contrary, it is the wiggler regime for $K_\beta \gg 1$, where the on-axis radiation spectrum becomes broad and described by the shape of $\frac{d^2I}{d\omega d\Omega} \propto \zeta^2\mathcal{K}^2_{2/3}(\zeta)$. The average power radiated by an electron oscillating in a plasma column strongly depends on the electron energy and the oscillation amplitude as $\bar{P}_s \propto \gamma^2 r_\beta^2$. The radiation is confined in a cone with half opening angle of $\Theta_\beta = K_\beta/\gamma$.

When the electron acceleration process is taken into account, the betatron oscillation amplitude gradually decreases and the oscillation period lengthens due to the increase of the electron relativistic mass. Accordingly, the radiation spectrum deviating from the standard synchrotron type has to be calculated numerically. The spatial radiation pattern, essentially related to the electron trajectory, can be used to deduce the electron motion parameters in the plasma bubble. Furthermore, X-rays emitted by electrons at different longitudinal positions project the rim of capillary tube exit to the far-field with different shadow sizes, which results in a transition zone of intensity in the X-ray image. This relationship in turn provides a diagnostic to the electron acceleration process in plasma by using betatron radiation.

Chapter 4

Properties of capillary tubes

Dielectric capillary tubes[1] *play a key role in our laser wakefield accelerator. In this chapter we will first introduce the theory concerning laser coupling and guiding properties in capillary tubes, and then discuss laser propagation when plasma is present inside capillary tube. Moreover, an important issue of target design, measuring and controlling the gas density evolution inside capillary tubes, is addressed numerically and experimentally.*

4.1 Introduction

As presented in Chapter 2, high laser intensity ($\gtrsim 10^{19}$ W/cm^2) is required in order to explore the strongly nonlinear bubble regime. To approach this regime with the state-of-the-art laser facility based on the CPA technology [30], the amplified laser beam has to be tightly focused onto plasma target. However in this case, the achieved high laser intensity can only be maintained over a short distance, the Rayleigh length, determined by the limit of diffraction, as depicted in Figure 4.1(a). As an example, for a Gaussian Ti:sapphire laser beam with $\lambda_0 = 800$ nm and a waist of $w_0 = 12$ μm, the corresponding Rayleigh length is $z_R = \pi w_0^2/\lambda_0 \simeq 565$ μm. As the electron energy increases with the acceleration length (See more details in Section 2.6), various techniques have been developed to guide the focused laser over a longer distance. Among them, self-guiding (See more details in Section 2.4.1) is one of the most widely employed methods due to its simplicity. Relying on this scheme, a powerful laser ($P_L > P_c$) can be guided over the pump depletion length, typically several millimeter long (See Figure 2.14). The main drawback of self-guiding is that the laser power must be in excess of the critical power given by $P_c\,[\mathrm{GW}] = 17\omega_0^2/\omega_p^2$, which increases rapidly with dropping plasma density. For a plasma density $\rho_e = 1 \times 10^{18}$ cm^{-3}, P_c becomes as high as 30 TW.

Another often employed guiding approach is plasma channelling [133, 134, 135, 136]. In this scheme, a plasma is created either by an external electrical discharge [133, 134] or by a heating laser pulse [135, 136], and then the hot on-axis plasma electrons move outward owing to radial hydrodynamic expansion, resulting in a density depletion on axis and a nearly parabolic transverse density profile, which is called plasma waveguide. Under the matching condition, lasers with intensity as high as 10^{18} W/cm^2 were successfully guided by plasma waveguide over many Rayleigh lengths [135, 137]. Sub-GeV to 1 GeV electron beams were generated by LWFAs with the plasma channels [38, 40, 105]. However there are some limits of plasma guiding as well. Firstly, the incident laser parameters (spot size, duration, energy) have to be tightly tuned in accordance with channel parameters

[1] In the following part of this thesis, the word "dielectric" will be omitted for simplicity.

[138]. Secondly, the guiding mechanism relies on plasma density and its spatial profile, whereas many applications need plasma parameters very different from those required for laser guiding. Last but not the least, due to the ultimate dynamics of channel formation, thermal heating, becomes inefficient at low plasma densities, so that suitable plasma waveguide could only be produced at plasma density in excess of 10^{19} cm^{-3} by laser heating [40] or of the order of 10^{18} cm^{-3} when an external magnetic field is applied to control the shape of the plasma channel [139].

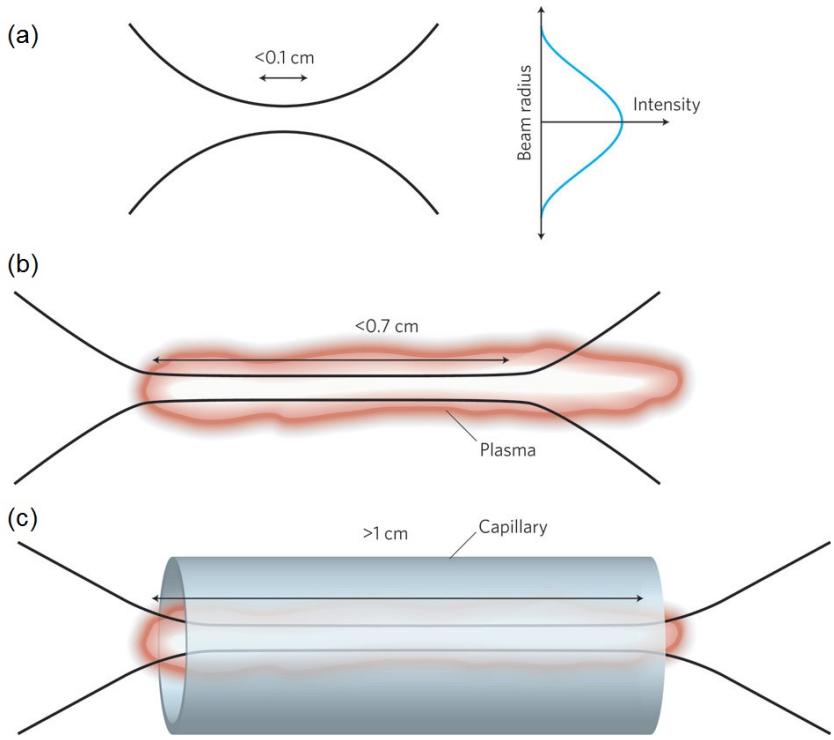

Figure 4.1: *Typical lengths of laser guiding for different mechanisms illustrated in Ref. [47]. (a) Without guiding, as in vacuum, a focused laser beam will naturally diffract over a Rayleigh length, typically a distance of hundreds of microns. (b) When a plasma is present, self-guiding can extend laser propagation to a few millimeters. (c) Beside self-focusing, a capillary tube is able to collect laser energy lies outside the central laser spot, permitting a longer distance of guiding in the scale of centimeter.*

In this context, a question arises: Is there a method to guide an intense laser without requiring the properties of laser and shapes of plasma medium?

The use of capillary tube, where the laser is guided by Fresnel reflection at inner capillary wall [140], looks very promising for laser-guiding [46, 47]. This guiding scheme does not rely on laser power, neither plasma density, providing the opportunities to explore a large domain of laser/plasma parameters. In the nonlinear regime where self-focusing takes place, capillary tubes are able to collect the laser energy contained in the focal halos to assist self-focusing of the laser spot over a longer distance than in gas jet or gas-cell, as shown in Figure 4.1(c). Consequently, higher electron energy and more intense X-rays than in a gas jet or gas-cell can be expected when using capillary tubes. It was also shown by Genoud *et al* that increasing the plasma length in a capillary tube reduces the initial laser intensity required for reaching the threshold of electron self-injection [46]. Studying of capillary guiding has been carried out in our group (ITFIP, LPGP) for more than ten years [61, 62]. As a first step, monomode guiding of 10^{16} W/cm^2 intense laser

pulses was demonstrated in experiments [141, 142, 143], and then extending the generated plasma wave into ~ 10 centimeter long. Meanwhile, the associated diagnostics were successfully performed during the thesis of Franck Wojda [62, 99, 144]. In this thesis, we are particularly concentrated on exploring the properties of the electrons produced by capillary-guided LWFA operating in the nonlinear regime and the associated betatron X-rays.

In this chapter we first present how the laser couples and propagates in capillary tubes with or without plasma. Then, the issue of temporally and spatially determining and controlling gas density inside capillary tube is addressed.

4.2 Description of capillary tubes

The capillary tubes employed in our experiments have thick cylindrically shaped outer wall. The capillary wall is made of glass (Composition: $80\%SiO_2+15\%B_2O_3+5\%K_2O$), and the relative permittivity of the glass is $\varepsilon_r \simeq 2.25$. Those capillary tubes are commercially available from the manufacturer Friedrich & Dimmock. In order to avoid perturbation of laser propagation induced by surface roughness, we choose the high wall precision (HWP) capillary tubes.

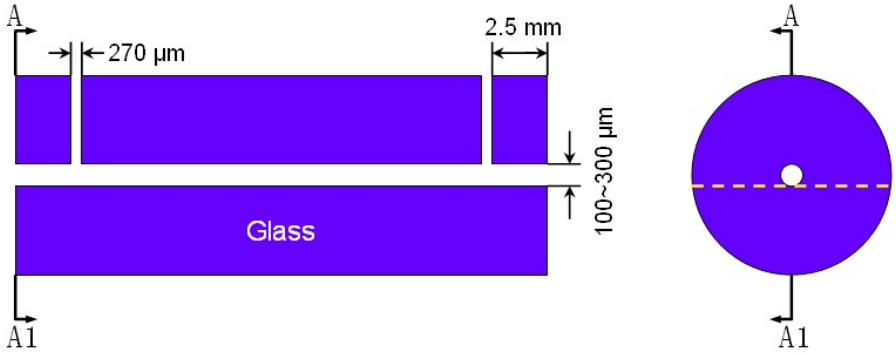

Figure 4.2: *Schematic drawing of capillary tube with characteristic dimensions.*

Figure 4.2 illustrates the structure of capillary tube with characteristic dimensions. The outer radius of the capillary wall is always 5.5 mm, while the inner radius is chosen for a given laser spot size to achieve either monomode or multimode guiding. Typically in our case, the inner radius is in the range of $100 - 300$ μm. In principle, the capillary tubes could be arbitrarily long, however the target holder used in the present work was designed for a length within 50 mm.

To study laser-plasma interaction, we inject neutral hydrogen gas into the capillary tubes, and then the laser leading edge ionizes the gas into a plasma (See Section 2.2.1). Two small slits are cut in the capillary tubes, through which the gas is fed into the capillary core. As seen later, a stable homogeneous gas medium is obtained between the two capillary slits. The slits are cut with the help of a precision diamond wire saw. The diameter of the cutting wire is about 220 μm, which makes slightly larger slits with width of 270 μm, as indicated in Figure 4.2. Determining the slit width is a compromise between gas filling and laser guiding. Using a larger slit, gas filling becomes faster and less turbulent, however more laser energy will be lost in the slit section. The 270 μm slit is a good balance for these two considerations.

The distance from the slit to capillary end is 2.5 mm. Ideally we want this distance to be as short as possible to avoid unwanted density ramp between the slit and capillary end (See Section 4.5). Nevertheless, owing to the design of the capillary holder, this distance could not be shorter than 2.5 mm. On the other hand, cutting a slit very close to the capillary end would make the tube very fragile. All the slits are cut down to the bottom of the inner capillary core, as seen in the side view in Figure 4.2. We find in experiment that such a completely cut slit allows stable gas filling into the capillary tubes.

4.3 Optical properties of capillary tube

An important issue is how a laser couples to the eigenmodes of the capillary tube and how it propagates afterwards. In the following part, we will examine those optical properties of capillary tube. Especially, the matching condition of monomode guiding and the influence of laser fluctuations will be presented. Note that in this section capillary tubes are assumed to be evacuated.

4.3.1 Eigenmodes of capillary tube

The electromagnetic field inside capillary tubes is described by Maxwell's equations under a certain set of boundary conditions. Solving these equations, one will obtain the eigenmodes of capillary tube [140]. An incident linearly polarized Gaussian laser beam can be efficiently coupled to the linearly polarized family of hybrid modes, namely the EH_{1m} modes. The transverse electric components of the EH_{1n} modes at zero order are given by [140]

$$E_{1m}(r,z,t) = \mathcal{J}_0(k_{\perp m} r)\exp(-k_m^l z)\cos[\omega_0 t - k_{zm} z], \tag{4.1}$$

where $k_{\perp m} = u_m/R_{cap}$, and u_m is the mth root of $\mathcal{J}_0(x) = 0$. Table 4.1 gives the first nine values of u_m. k_{zm} is the longitudinal wavenumber given by $k_{zm} = (k_0^2 - k_{\perp m}^2)^{1/2}$. The exponential decay term in Equation 4.1 indicates laser damping due to the loss by reflection at the dielectric capillary wall. The characteristic damping coefficient k_m^l is given by [140]

$$k_m^l = \frac{u_m^2}{2k_{zm}^2 R_{cap}^3}\frac{1+\varepsilon_r}{\sqrt{\varepsilon_r - 1}}. \tag{4.2}$$

As we can see, k_m^l strongly depends on the capillary radius, the wavelength of the incident laser beam, and the mode order through u_m. Laser damping is usually described by the attenuation length L_m^l defined as

$$L_m^l = \frac{1}{k_m^l} = \frac{2k_{zm}^2 R_{cap}^3}{u_m^2}\frac{\sqrt{\varepsilon_r - 1}}{1+\varepsilon_r}. \tag{4.3}$$

After a propagation distance of L_m^l the field amplitude decreases to $1/e$. For example, the damping lengths L_m^l of a Ti:sapphire laser ($\lambda_0 = 800$ nm) within a 50 μm radius capillary tube are tabulated in Table 4.1. L_m^l drops rapidly with increasing m, which means higher order modes are damped more quickly. Therefore it is more interesting to use the fundamental mode to achieve long laser propagation distance.

The dispersion relation of an EM wave in capillary tube is $k_0^2 = (k_{zm}^2 + k_{\perp m}^2)$, through which one can determine the group velocity when $k_{\perp m}^2 \ll k_0^2$ as

$$v_{gm} \simeq c\left(1 - \frac{k_{\perp m}^2}{k_0^2}\right)^{1/2}. \tag{4.4}$$

Table 4.1: *u_m, L_m^l, v_{gm}, and $\mathcal{F}_m^{max}$ for the first nine modes of a capillary with radius of 50 μm and a laser wavelength of $\lambda_0 = 800$ nm.*

m	u_m	L_m^l (cm)	v_{gm}/c	$\mathcal{F}_m^{max}$ (10^{-5})
1	2.404826	91.7	0.99998	2.034
2	5.520078	17.4	0.9999	4.604
3	8.653728	7.1	0.9998	7.2011
4	11.79153	3.8	0.9995	9.8049
5	14.93092	2.4	0.9993	12.4113
6	18.07106	1.6	0.9989	15.0189
7	21.21164	1.2	0.9985	17.6272
8	24.35247	0.9	0.9981	20.2359
9	27.49348	0.7	0.9975	22.8449

The third column in Table 4.1 gives v_{gm}. It is noticeable that the group velocity decreases as the mode order increases.

Another important issue associated with capillary tube is the threshold of material damage, which determines the intensity which can be guided by a capillary tube. To examine this, we introduce the normalized flux at the capillary wall, $\mathcal{F}_m$, defined as the ratio of the radial component of the Poynting vector ar $r = R_{cap}$ to the longitudinal component of the on-axis Poynting vector. $\mathcal{F}_m$ is given by [140]

$$\mathcal{F}_m = \frac{k_{\perp m}^2}{k_0^2} \mathcal{J}_1^2(k_{\perp m} R_{cap}) \frac{\cos^2\theta + \varepsilon_r \sin^2\theta}{\sqrt{\varepsilon_r - 1}}. \tag{4.5}$$

It is clear that $\mathcal{F}_m$ depends on the azimuthal angle θ and mode order m. $\mathcal{F}_m$ is minimum for $\theta = 0,\ \pi$ and maximum for $\theta = \pi/2,\ 3\pi/2$. So it will be the maximum value that determines the threshold of capillary breakdown. As shown in the last column in Table 4.1, $\mathcal{F}_m^{max}$ increases by one order of magnitude from the fundamental mode to the ninth mode. It again highlights the interest of the use of the fundamental mode. For a glass capillary, the ionization threshold is of the order of 10^{14} W/cm^2 for a 800 nm laser pulse with duration of the order of 100 fs [145]. The maximum intensity guided by a capillary of 50 μm radius on the fundamental EH_{11} mode without wall ionization is thus of the order of 10^{19} W/cm^2. The ability to guide such laser intensities makes capillary tubes suitable candidates for intense laser-plasma interactions.

Figure 4.3 presents the distributions of the transverse field of the first three EH_{1m} modes for a capillary with 50 μm radius. As seen, the fields of the higher modes are not smooth. Their field directions change in the transverse plane. Only the EH_{11} mode has a smooth transverse profile pretty similar to a Gaussian distribution. The fundamental mode is therefore preferable to optimize the coupling of the incident laser beam energy.

4.3.2 Laser coupling

When a laser beam is focused at the entrance of a capillary tube, it couples its energy to the capillary eigenmodes and gets transmitted. In this section, we will show the coupling of two laser spots: Gaussian beam and Airy beam, both of which are widely used in our experiments. As demonstrated before, monomode guiding with the fundamental EH_{11} mode has many interesting features, so the condition for monomode coupling will be particularly discussed.

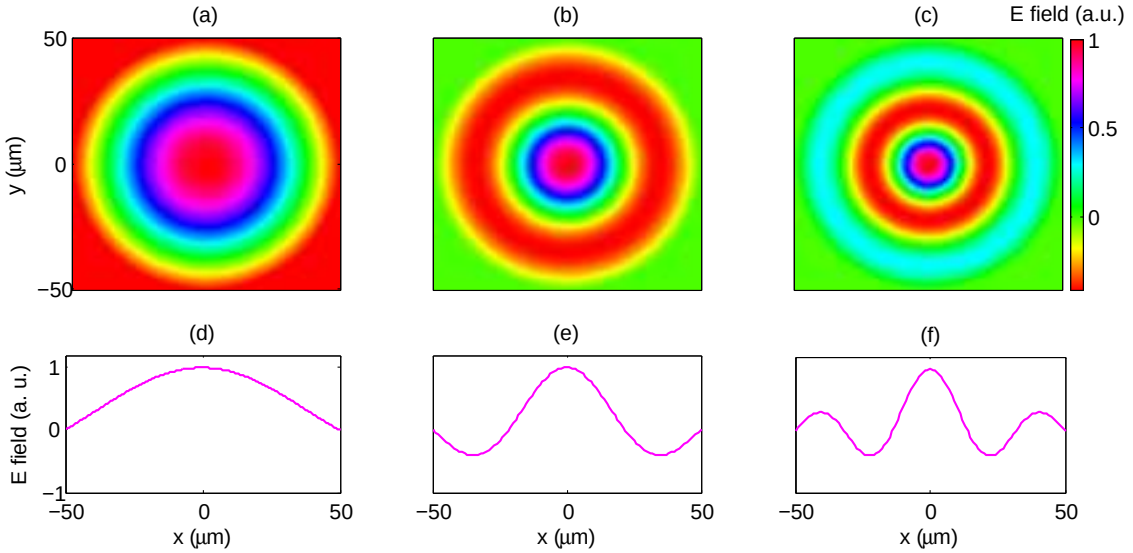

Figure 4.3: *Electric field distributions in the transverse plane for the eigenmodes: (a) EH_{11}, (b) EH_{12}, (c) EH_{13} of a 100 µm diameter capillary tube. (d)-(f) are the field profiles along the horizontal direction going across the beam centers.*

Coupling of a Gaussian beam

In many experimental cases, laser beams, like CW HeNe laser, are generated with the TEM_{00} mode and a Gaussian transverse field distribution. Supposing a linearly polarized Gaussian beam is focused at the capillary entrance ($z = 0$), the radial variation of the electric field is written as $E_G(r) = E_L \exp(-r^2/w_0^2)$, while the electric field inside capillary tube is described as a superposition of the EH_{1m} eigenmodes defined by Equation 4.1. At the entrance (z=0), the continuity of the field can be written as

$$E_L \exp(-r^2/w_0^2) = \sum_{m=1}^{\infty} A_m E_{1m} = \sum_{m=1}^{\infty} A_m \mathcal{J}_0\left(u_m \frac{r}{R_{cap}}\right). \tag{4.6}$$

The coefficient A_m indicates the amplitude of the EH_{1m} mode, which can be determined using the orthogonality of bessel functions

$$A_m = 2E_L \frac{\int_0^1 x \exp(-x^2 r^2/R_{cap}^2)\mathcal{J}_0(u_m x)dx}{\mathcal{J}_1^2(u_m)}. \tag{4.7}$$

Then one can compute the coupling efficiency C_m, defined as laser energy coupled to the EH_{1m} mode, through

$$C_m = 2\left(\frac{R_{cap}}{w_0}\right)^2 \frac{[\int_0^1 x \exp(-x^2 r^2/R_{cap}^2)\mathcal{J}_0(u_m x)dx]^2}{\mathcal{J}_1^2(u_m)}. \tag{4.8}$$

As seen, C_m depends on the mode order, m, the capillary radius, R_{cap}, and the laser waist, w_0.

Figure 4.4 presents the repartition of the incident laser energy on the first five eigenmodes as a function of the ratio of the capillary radius to the laser waist, R_{cap}/w_0. It shows that quasi-monomode coupling can be achieved when $R_{cap}/w_0 \simeq 1.55$ (or $w_0/R_{cap} \simeq 0.65$). In this case, almost 98% of the incident laser energy is coupled to the fundamental EH_{11} mode, and higher modes are coupled to merely 1% of the laser energy. The other 1% laser

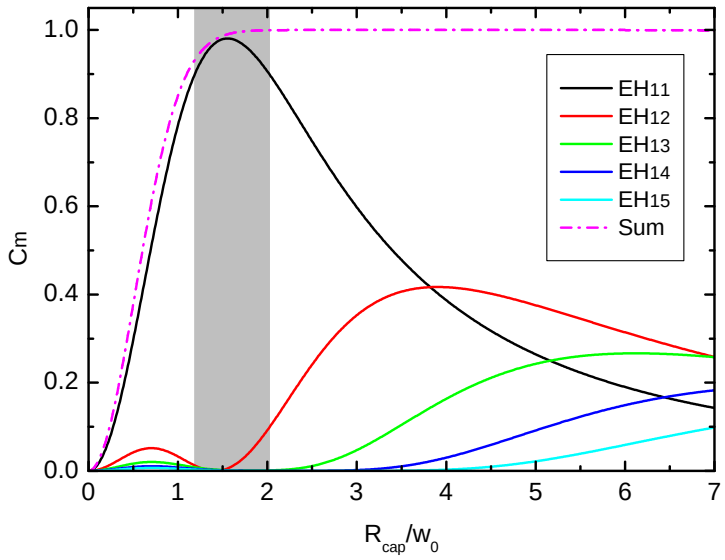

Figure 4.4: *Coupling efficiency of a Gaussian beam to the first five eigenmodes as a function of R_{cap}/w_0. The gray area indicates the range of values of R_{cap}/w_0 where more than 90% of the laser energy is coupled to the EH_{11} mode.*

energy is lost into the front surface of capillary tube. It may not be easy to match the laser size exactly to be $R_{cap}/w_0 = 1.55$ in experiment, however we find that more than 90% laser energy can be coupled to the fundamental mode if only $R_{cap}/w_0 \in [1.2, 2]$, as represented by the gray area in Figure 4.4, which provides a large range of freedom for efficient coupling.

When $R_{cap}/w_0 \to 0$, if, for example, the laser waist increases, it is still the fundamental mode that predominates the coupling, however the coupling efficiency decreases quickly. That's because more laser energy is radiated onto the front surface around the capillary hole and lost. As R_{cap}/w_0 increases, the laser waist becomes smaller compared to the optimal waist for quasi-monomode coupling. In this case, the laser energy is nearly 100% coupled into the capillary tube, as indicated by the sum curve in Figure 4.4. However, less and less energy is coupled to the fundamental mode, while more and more higher order modes are excited, resulting in undesired mode beating and severe laser attenuation during the propagation in the capillary tube.

Coupling of an Airy beam

Another important case is the coupling of an Airy laser beam, because the focal spot profile of a powerful laser is close to an Airy distribution rather than a Gaussian function (See Chapter 6). In multi-terawatt laser facilities, to avoid optical damage in amplification stages, a flat-top laser beam is usually amplified. When such a beam is focused, the focal spot is Airy-like [146]. The amplitude of electric field of an Airy beam focused at capillary entrance ($z = 0$) is written as

$$E_A(r) = E_L \frac{\mathcal{J}_1(\nu_1 r/r_0)}{r}, \tag{4.9}$$

where $\nu_1 = 3.8317$ is the first root of the equation $\mathcal{J}_1(x) = 0$, and r_0 is the radius of the first zero. Like for a Gaussian beam, the continuity of the electric field at the capillary

entrance leads to

$$E_L \frac{\mathcal{J}_1(\nu_1 r/r_0)}{r} = \sum_{m=1}^{\infty} A_m E_{1m} = \sum_{m=1}^{\infty} A_m \mathcal{J}_0\left(u_m \frac{r}{R_{cap}}\right). \tag{4.10}$$

As before, the coupling efficiency C_m can be calculated by

$$C_m = \frac{4}{\mathcal{J}_1^2(u_m)} \left[\int_0^1 \mathcal{J}_1\left(\frac{\nu_1 R_{cap}}{r_0} x\right) \mathcal{J}_0(u_m x) dx\right]^2. \tag{4.11}$$

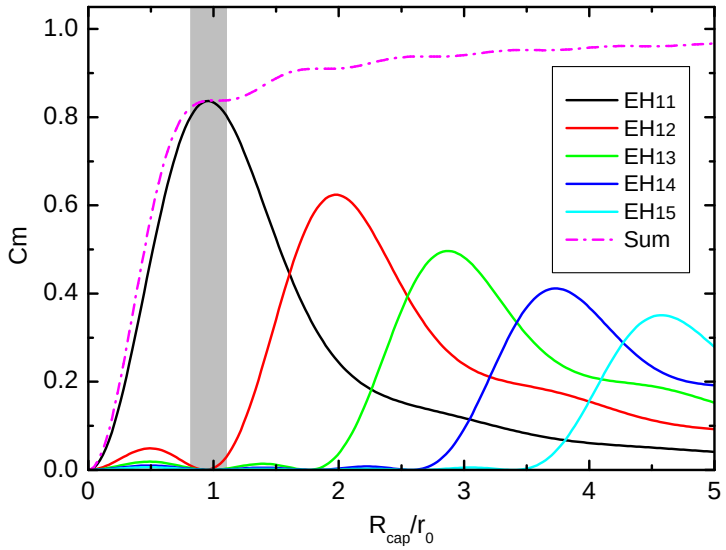

Figure 4.5: *Coupling efficiency of an Airy beam to the first five eigenmodes as a function of R_{cap}/r_0. The gray area indicates the condition when more than 80% laser energy is coupled to EH_{11} mode.*

Figure 4.5 shows the coupling efficiencies of the first five eigenmodes as a function of R_{cap}/r_0. We find that monomode guiding of an Airy beam can be achieved when $R_{cap}/r_0 \simeq 1$. However in this case only 83% laser energy is coupled to the fundamental mode, while the other 17% energy contained by the laser halos within $r > R_{cap}$ is damped into the capillary wall. When R_{cap}/r_0 increases, more laser energy can be coupled but essentially to the high order modes. It is apparently less efficient to use an Airy beam than a Gaussian beam in terms of laser coupling and monomode guiding. Another issue is capillary breakdown. The front surface of the capillary tube is exposed to a greater energy for an Airy beam than for one with a Gaussian profile, and hence the peak laser intensity has to be lowered to avoid capillary damage.

Influence of laser fluctuations

So far the properties of laser coupling has been discussed assuming a perfect laser/capillary alignment, namely the incident laser is exactly aligned with respect to capillary axis. However this ideal alignment is not usually achievable in experiments, as powerful laser beams exhibit shot-to-shot pointing fluctuation. It is thus important to examine the influence of laser fluctuations on the coupling to capillary tubes. A theoretical model regarding the influence was given by Veysman *et al* in Ref. [147]. Here we present an experimental study in the parameter range interesting for our LWFA experiments.

The fluctuations of the laser beam can be described by the spatial displacement δR and the incident angle θ_{in} with respect to the capillary axis. The experimental procedure is first searching for a as good as possible laser/capillary alignment, and then vary δR or/and θ_{in} to see how the transmitted laser changes consequently. To do so, we use a stable CW HeNe laser ($\lambda_0 = 632$ nm) and a 5-degree motorized capillary holder (See Section 5.2), which allows us to control δR or θ_{in} by shifting or rotating the capillary tube.

The capillary tube tested was 30 mm long with a diameter of 127 μm. The 5 mW output laser was expanded by a telescope to have a beam waist of $\sim$ 2 mm, and then focused by a $f = 25$ cm lens. Figure 4.6 schematically represents laser guiding by the

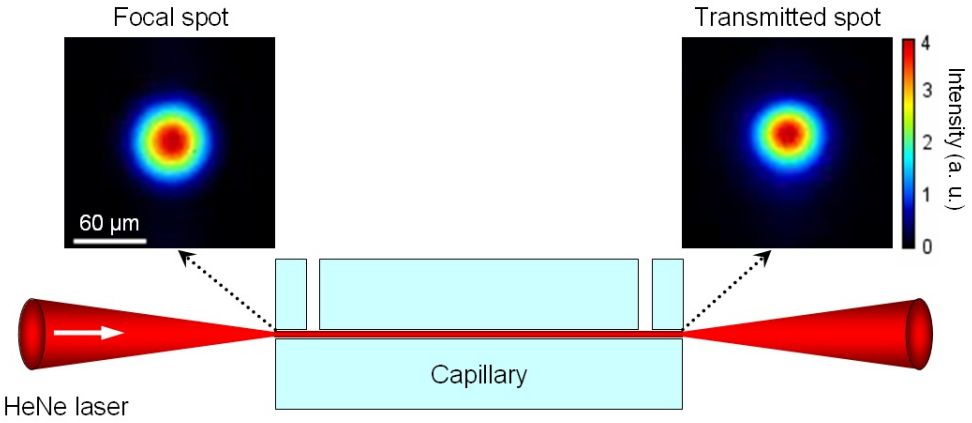

Figure 4.6: *Schematic of laser guiding by capillary tube together with the focal spot and the transmitted laser spot in experiment.*

capillary tube. All the measurement were performed in air. The focal spot was measured by a 12 bit charge coupled device (CCD) camera together with a 20× objective. The focal spot was found to be Gaussian with a waist of about 43 μm, which corresponds to $w_0/R_{cap} \simeq 0.68$, almost matching the criterion of monomode guiding. Also shown in Figure 4.6 is the transmitted laser, which is symmetrical and in quasi-monomode. To approach the best alignment, the transmitted laser was optimized to reach the maximal amplitude and symmetry. In this case, a transmission of $90 \pm 2\%$ was obtained. The transmission is defined as the ratio of incident and transmitted laser energies at the capillary entrance and the exit, respectively. As a first step, the experimental transmission should be compared with the theoretical value to check if we really get the ideal alignment.

Using the values in Figure 4.4, the coupling of EH_{11} mode is 97% for $w_0/R_{cap} = 0.68$ ($R_{cap}/w_0 \simeq 1.47$). Furthermore, the attenuation length is calculated through Equation 4.3 to be $L_1^l \simeq 230$ cm for $\lambda_0 = 632$ nm and $R_{cap} = 63$ μm. So the theoretical transmission is given by $Tr_1 = C_1 \exp(-2L_{cap}/L_1^l) \simeq 94\%$, which is very close to the experimental value, suggesting a nearly perfect alignment was achieved in experiment.

Figure. 4.7 presents the energy distribution of the transmitted laser in the plane of the capillary exit for different displacements at the capillary entrance while keeping $\theta_{in} = 0$. As seen, when there is no displacement, $\delta R = 0$, the transmitted laser is symmetrical and monomode. With δR increasing, asymmetry of the energy distribution is more appreciable, and the maximum intensity drops as well. When $\delta R \geq 40$ μm, or $\delta R/R_{cap} \geq 63\%$, the displacement leads to dramatic changes of energy repartition, where several lobes appear. In order to achieve a roughly monomode guiding in this case, the laser displacement should be less than 20 μm or $\delta R/R_{cap} \leq 30\%$.

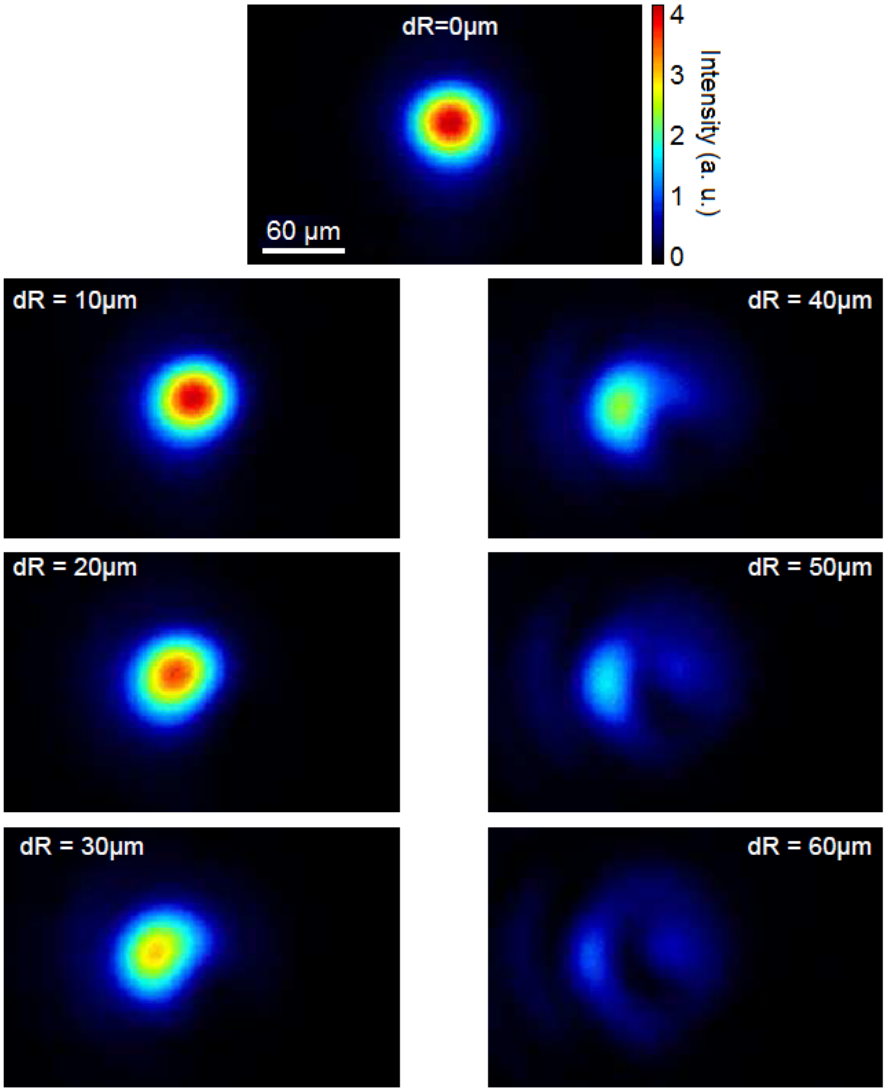

Figure 4.7: *Energy distributions of the laser beam at the capillary exit for different displacements at the entrance of the capillary tube from 0 to 60 µm with step of 10 µm.*

Shown in Figure 4.8 are the energy distributions in the plane of the capillary exit when the incident θ_{in} is varied and δR is fixed to be zero. We find that the transmitted spot gradually degraded in intensity and symmetry as θ_{in} becomes larger. A symmetrical and intense output profile could be achieved in this case only if $\theta_{in} \leq 1.7$ mrad. This finding agrees well with the theoretical predictions [147]. The corresponding transmissions concerning those variations are quantified in Figure 4.9. One can see that the transmission is optimal for the best alignment, namely $\delta R = 0$ and $\theta_{in} = 0$, where monomode guiding is achieved. The transmissions exponentially drops (fitted by Gaussian function) as either displacement δR or incident angle θ_{in} increases. This measurement illustrates the importance of optimizing the alignments in experiments.

The normalized transmission is higher than 90% if $\delta R/R_{cap} \leq 2.2$ or $\theta_{in} \leq 3$ mrad. Beyond this fluctuations range the transmissions are still high, however the transmitted laser distributions display several lobes as seen in Figures 4.7 and 4.8. It is therefore not possible to use such a guided laser to drive a symmetrical plasma wave for LWFA.

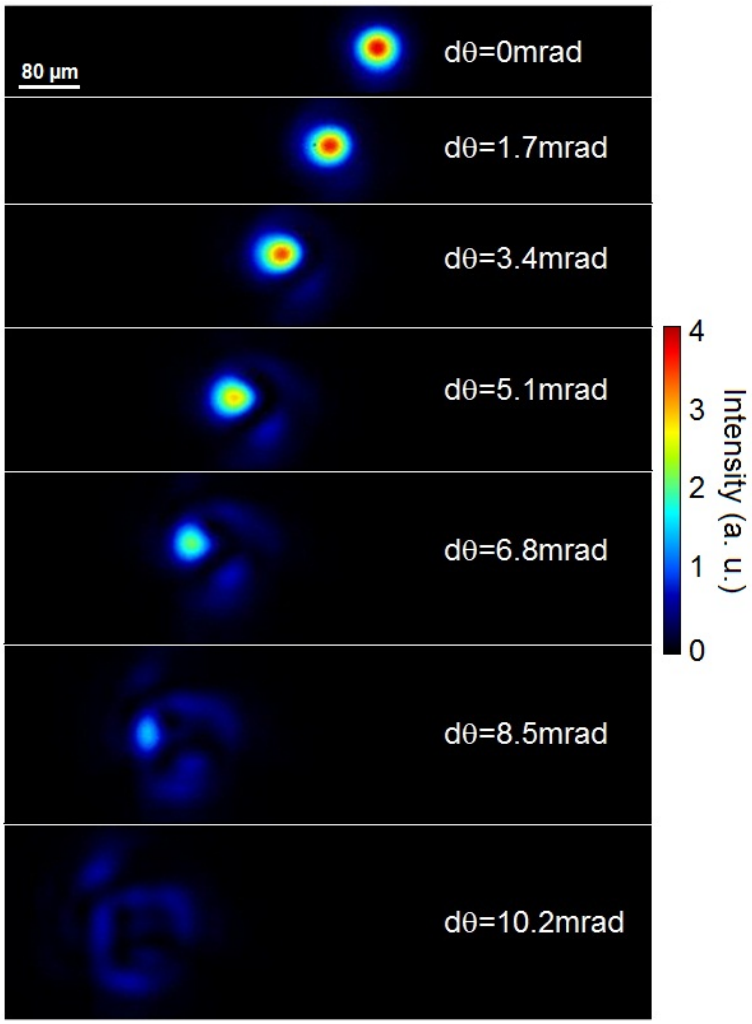

Figure 4.8: *Energy distributions of the laser at the capillary exit for different incident angles from 0 to 10.2 mrad with a step of 1.7 mrad.*

But non-symmetrical coupling might be interesting to trigger some special effects, such as in Ref. [131] where the laser wavefront was deliberately tilted to control photon energy. Another issue one has to take into account is the capillary damage, as the energy deposited on the capillary wall quickly increases with δR and θ_{in}. To diminish the risk of capillary breakdown, the fluctuation of laser pointing must be well controlled.

4.4 Guiding of intense laser by capillary tube with plasma

Up to this point, we have presented the pure optical properties of capillary tubes, whereas in most cases the tubes are filled with gas to study laser-plasma interaction. In this section we examine how an intense laser propagates in a capillary tube when plasma is present. Both numerical [114] and experimental [46, 47, 48] work demonstrated that capillary tube not only guides the laser but also in the nonlinear regime collects the energy associated with laser halos in the focal spot to favor laser keeping self-focused over a longer distance than in a gas-cell or gas jet. In those studies the laser power was well above the critical power, that is $P_L \gg P_c$, so self-focusing played a significant role for laser guiding. In

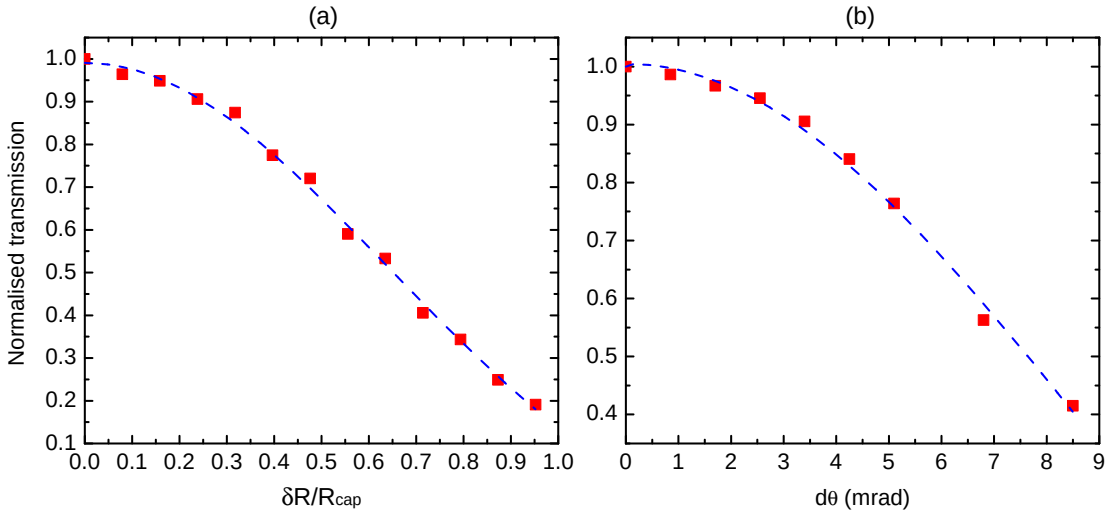

Figure 4.9: *Transmissions, normalized to the results of the best alignment, corresponding to the measurements shown in Figures 4.7 and 4.8, respectively. The dashed lines are Gaussian fits.*

this part, we examine the laser propagation when its power is comparable to the critical power, namely $P_L \leq P_c$. In this case, the plasma density is very low and self-trapping does not occur. This study is of particular interest to use capillary tube for future staging acceleration with an externally injected electron bunch.

The simulation was performed using the code WAKE [148] which was modified by B. Paradkar at LPGP to add the capillary boundary. The incident laser is Gaussian in space and time with a FWHM pulse duration of 40 fs, a transverse waist of $w_0 = 15$ μm, and a normalized laser intensity of $a_0 = 1.5$. The laser power is therefore $P_L \simeq 16.8$ TW. Those parameters are close to those of the LLC multi-TW laser we used for our electron acceleration experiments. The plasma electron density is set as $\rho_e = 1 \times 10^{18}$ cm^{-3}, which corresponds to the critical power of $P_c \simeq 29.5$ TW. It yields $P_L/P_c \simeq 0.57$, suggesting self-focusing should not be an important issue.

Figure 4.10 presents the simulation results for two different targets: capillary tube and gas jet. The capillary radius is chosen to meet the requirement of quasi-monomode guiding, e.g. $R_{cap} = 1.55 w_0$. The evolutions of the normalized laser intensity are shown in Figure 4.10(a). In the case of capillary tube, the laser is well guided without appreciable energy loss until $z = 7$ mm. The laser intensity evolution exhibits oscillations with a period of about 2 mm, which are due to the beating of the modes excited by the Gaussian distribution of the incident laser beam. For the capillary radius used in this simulation, $\sim$ 98% of the incident laser energy is coupled to the fundamental EH_{11} mode, where about 0.44% and 0.15% are coupled to the second (EH_{12}) and the third (EH_{13}) modes. The beating of the mth higher order mode with the fundamental mode is represented by the term $\Delta k_{zm} = k_{z1} - k_{zm}$, and the characteristic beating length is given $L_{bm} = 2\pi/\Delta k_{zm}$. For this simulation case, the beating length are respectively 2.1 mm and 0.8 mm for the second and third modes. In Figure 4.10(a), the beating of the third and the fundamental modes indicated by the markers A and A' shows a beating length of about 0.9 mm, while the beating of the second and the fundamental modes noted by the markers B and B' corresponds to a beating length of approximately 2.2 mm. The beating lengths observed in the simulation well agree with the theoretical estimations given above. Owing to a shorter damping length of 7 mm given by Equation 4.3, the beating of the third and fundamental

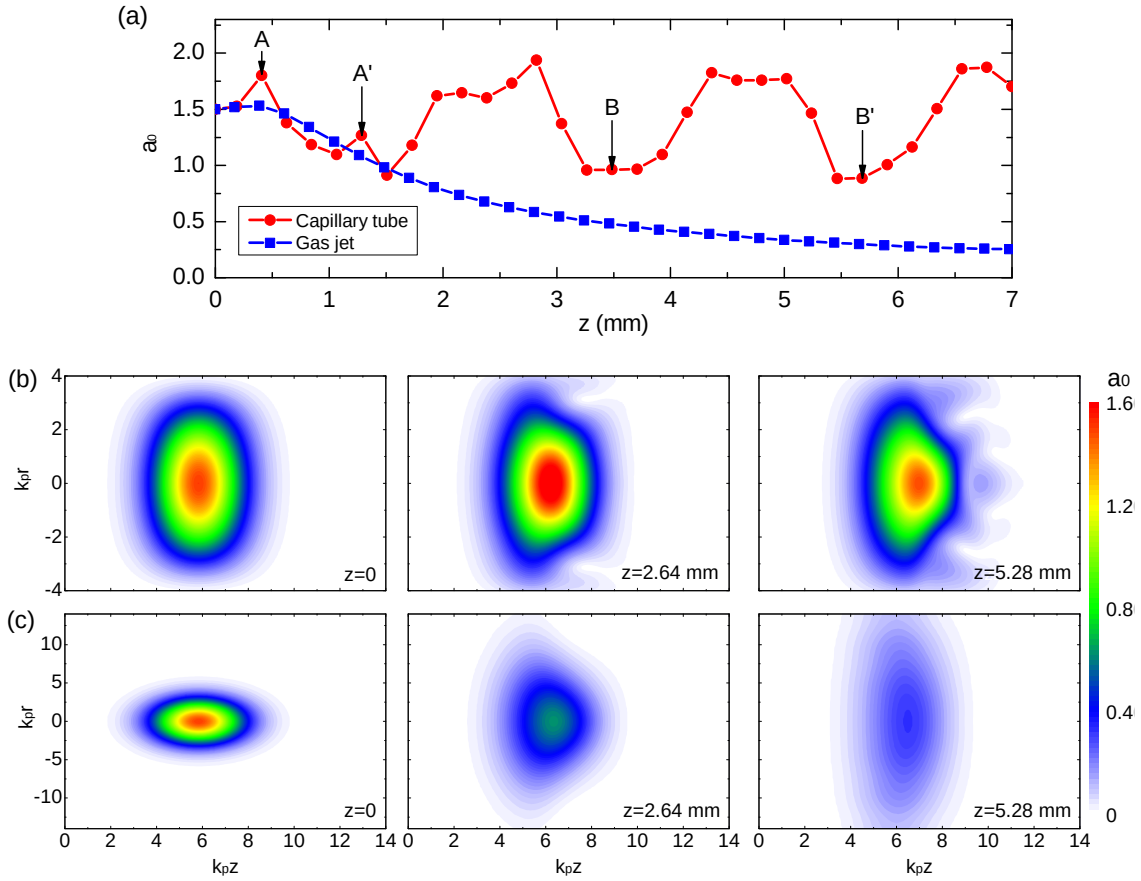

Figure 4.10: *(a) Evolution of normalized laser intensity a_0 for two different targets: capillary tube and gas jet. The plasma electron density is $\rho_e = 1 \times 10^{18}$ cm^{-3}. Snapshots of laser longitudinal profiles at three different positions for capillary tube [panel (b)] and gas jet [panel (c)]. The laser beam propagates from right to left in those images.*

modes is suppressed faster than that between the second and the fundamental modes. In the case of gas jet, the laser is merely self-guided over less than one Rayleigh length ($z_R = \pi w_0^2/\lambda_0 \simeq 0.88$ mm). Afterwards diffraction dominates, and the laser intensity decreases rapidly.

Figure 4.10(b) shows the laser profiles inside capillary tube at different longitudinal positions. The laser shape is preserved throughout the propagation even though the laser tail is modulated by the excitation of a plasma wave in its wake (the density perturbation is not shown in these images). By contrast in Figure 4.10(c), in the case of gas jet the laser size gradually increases and the laser intensity significantly decreases as predicted by diffraction. Note that the vertical scales are different in Figure 4.10(b) and (c).

4.5 Determination of gas density in capillary tube: fluid simulation

4.5.1 Introduction

The LWFA experiments are usually carried out at gas pressures lower than the atmospheric pressure, and the intense, short pulse laser needs to propagate in vacuum in order to avoid

undesirable pulse modulation or material damage before interacting with the target. Thus the target is usually placed inside an evacuated chamber and gas is fed inside capillary tubes through slits (See Section 4.6). For most experimental cases, the knowledge and control of gas density[2] inside the capillary tube are crucial to define the regime of laser-plasma interaction. Therefore the characterization of the target gas or plasma distribution is an important issue for experimental design.

When hydrogen gas is used, the laser intensity used in LWFA is more than three orders of magnitude above the ionization threshold (See Section 2.2.1) and allows to realize plasma density profiles along the radius and the propagation length directly deduced from gas profiles. The duration of gas filling needs to be determined and optimized for each capillary parameters set in order to be able to minimize the amount of gas leaking into the main vacuum chamber before the arrival of the laser pulse. In this sense, a full spatial and temporal characterization of gas flow inside capillary tube is required.

Interferometry has been used to diagnose targets such as gas jets [149, 150] and plasma waveguide [151]. The gas evolution in gas-cell and capillary tubes has not been well investigated. In the frame of a LWFA experiment using gas-cell, the spatial distribution of gas flow in the stationary state was obtained by simulation [45], whereas the temporal gas evolution inside capillary tube was not known. Therefore the valve for gas filling was opened for a long duration (200 ms for the gas-cell in Ref. [45]) to reach the stable state of gas. In this case, significant amount of gas leaks into the vacuum chamber before the arrival of the laser pulse. Consequently the pump system is subjected to a heavy load, making repetitive operation of LWFA more difficult.

So far, no investigation has been carried out to study the correlations between gas density/profile and capillary diameters (length, diameter, slit size, etc). The first attempt of gas density measurement was carried out during the thesis of Franck Wojda [62], however approximate results were obtained because of strong mechanical vibrations and of shaking of the target induced by gas shock. During my PhD study, many efforts were put to address this issue of gas filling in both simulation and experiment. We particularly developed a new capillary housing (See Section 5.2) which is robust enough for gas shock. Furthermore, a new gas filling system was built up to precisely control the process of gas filling.

Experimental measurements of gas density evolution inside capillary tubes will be presented in Section 4.6. In this section, we first show the results of numerical simulations. Particularly, the spatial distribution of gas flow in the stationary state was obtained by this numerical modelling. Together with the temporal evolution of gas density measured in experiment, the features of gas filling are fully determined.

4.5.2 Governing equations

The process of gas filling is a fluid dynamics problem. In order to use the correct governing equations to describe it, one needs first of all to determine in which regime (continuous flow or molecular flow) it operates. Usually these two flow regimes are distinguished by the Knudsen number defined as

$$Kn = \frac{\ell_f}{D_{cap}}, \tag{4.12}$$

where ℓ_f is the molecular mean free path length, and D_{cap} is the diameter of the capillary tube. In kinetic theory, the mean free path describes the average distance a particle travels

[2] Unless otherwise specified in this thesis, gas density refers to number density rather than mass density.

between collisions with other moving particles, and it is given by

$$\ell_f[\text{cm}] = \frac{1}{\sqrt{2}\pi\rho d^2} \simeq \frac{3.1\times10^{-20}T[\text{K}]}{\text{P[mbar]}d^2[\text{cm}^2]}, \tag{4.13}$$

where the formula of ideal gas $\text{P} = \rho\kappa_B T$ is used; P, ρ, and T are the gas pressure, density, and temperature, respectively; $\kappa_B = 1.38\times10^{-23}$ J/K is the Boltzmann constant, and d denotes the particle hard shell diameter. For hydrogen molecule, $d = 2.62\times10^{-8}$ cm at standard temperature and pressure (namely 20 °C and 1 atm).

Since ℓ_f increases as the pressure is lowered, the domain of large values of Kn represents molecular flow while the low values of Kn correspond to the continuum regime. Typically when $Kn > 1$ or $\ell > D_{cap}$, the gas is in the typical molecular regime, where the particles are free and collisionless. The motion of particle is changed when interacting with boundary wall. This regime often appears in microfluid, and is modeled using the so-called Direct simulation Monte Carlo method [152]. As an example, for a capillary with 178 μm diameter, $Kn > 1$ means gas density $\rho < 1.8\times10^{16}$ cm^{-3}.

For $Kn < 0.01$ or $\ell_f < 0.01D_{cap}$, the gas flow can be treated as a continuous flow described by the classical fluid dynamics. For the 178 μm capillary diameter, $Kn < 0.01$ requires gas density $\rho > 1.8\times10^{18}$ cm^{-3}. Note that this density requirement decreases for larger capillary diameter. Typically in our experiments, the plasma density is $\rho_e > 5\times10^{18}$ cm^{-3} (or neutral hydrogen gas density of $\rho_{H_2} > 2.5\times10^{18}$ cm^{-3}). It suggests we work in the fluid regime. It is worth pointing out that under a looser criterion of $Kn < 0.1$ the gas flow can be still reasonably described by the fluid equations with the help of the slip boundary condition [153].

The range $0.01 < Kn < 1$ is the transition regime between continuous flow and molecular flow. For the 178 μm diameter capillary, it corresponds to the density range of 1.8×10^{16} cm$^{-3} < \rho < 1.8\times10^{18}$ cm^{-3}. Recently the Direct simulation Monte Carlo method has been extended to study the features of gas flow in this transition regime [154].

The gas filling process refers to both the molecular and the continuum regimes, while the gas at the stationary state is determined by fluid dynamics in the continuum regime. This is a classical field of fluid, and has been extensively investigated [155]. The continuous flow can be described by an analytical model which consists of three conservation equations:

• Continuity equation (conservation of mass)

$$\frac{\partial\rho}{\partial t} + \nabla\cdot(\rho\mathbf{v}) = 0, \tag{4.14}$$

• Navier-Stokes equation (conservation of momentum)

$$\rho\left(\frac{\partial\mathbf{v}}{\partial t} + \mathbf{v}\cdot\nabla\mathbf{v}\right) = -\nabla\text{P} + \nabla\cdot\mathsf{T} + \mathbf{f}_b, \tag{4.15}$$

where T is the stress tensor and $\mathbf{f}_b$ indicates body force (such as gravity) per unit volume acting on the fluid. Equation 4.15 is actually Newton's second law applied to fluid motion. T describes viscous stresses that originate from the friction between the fluid and a surface. In Cartesian coordinates, T is a 3×3 matrix whose element is given by [155]

$$\mathsf{T}_{ij} = \kappa\left[\left(\frac{\partial v_i}{\partial x_j} + \frac{\partial v_j}{\partial x_i}\right) - \frac{2}{3}\delta_{ij}\frac{\partial v_m}{\partial x_m}\right], \tag{4.16}$$

where κ is the dynamic viscosity. $i, j, m = 1, 2, 3$, and δ_{ij} denotes the Kronecker delta function ($\delta_{ij} = 1$ if $i = j$ and $\delta_{ij} = 0$ if $i \neq j$).

• Equation of energy (conservation of energy)

$$\rho \frac{d\mathcal{E}_{in}}{dt} + \mathrm{P}(\nabla \cdot \mathbf{v}) = \frac{\partial}{\partial t} q_h - \nabla \cdot \left(\frac{\partial \mathbf{q}_c}{\partial t} \right) + \mathsf{T}_{ij} \frac{\partial v_i}{\partial x_j}, \tag{4.17}$$

where $\mathcal{E}_{in}$ represents internal energy per unit mass, and the total energy per unit mass can be calculated through $\mathcal{E} = \mathcal{E}_{in} + |\mathbf{v}|^2/2$. The first term on the right-hand side denotes the external heat source, and the second term corresponds to heat loss due to conduction.

As $\mathcal{E}_{in}$ is a function of temperature T, the three conservation equations are based on a set of variables (P, ρ, $\mathbf{v}$, T). Usually the ideal gas law (equation of state), $\mathrm{P} = \rho k_B T$, is added to enclose the equations.

Another important issue which has to be taken into account is turbulence [156]. To estimate if there is turbulence in a flow, the Reynolds number is widely used

$$Re = \frac{\varrho v D_H}{\kappa}, \tag{4.18}$$

where ϱ is the mass density, D_H is the hydraulic diameter. As seen, Re is a dimensionless number that indicates the ratio of inertial forces to viscous forces and consequently quantifies the relative importance of these two types of forces for given flow conditions. Experimental observations demonstrate that the duct flow is laminar when $Re < 2300$, where viscous forces are dominant and the flow is characterized by smooth motion. The duct flow becomes turbulent when $Re > 4000$, which is dominated by inertial forces and likely to produce chaotic eddies, vortices and other instabilities. In the interval of $2300 < Re < 4000$, it is called transition flow. Even though the transition flow is not completely turbulent, the effects of turbulence are significant and must be taken into account. It was also found in experiment that the onset of turbulence in microtube with dimension of micrometer occurs at a relatively low value of $Re \simeq 1800$ [157].

Quantitatively, for hydrogen gas, the dynamics viscosity is $\kappa_{H_2} = 9 \times 10^{-6}$ Pa·s at 27 °C. The gas velocity can be as high as sonic (1.3 km/s) inside capillary tube (See Section 4.5.4). For a hydrogen gas from reservoir of stagnant pressure of 500 mbar (corresponding to density of $\varrho = 0.045$ kg/m^3), its density drops to 0.028 kg/m^3 when the speed of flow is sonic (See more details in Section 4.5.4). For the gas filling pipe of 1/16 inch diameter, the Reynolds number is estimated to be $Re \simeq 6400$. Obviously, the flow is turbulent.

Turbulence is an interesting and challenging domain in fluid dynamics, extensively discussed in literature, for example Ref. [158]. Details of turbulence are absolutely beyond the scope of this thesis. Here we just give a brief introduction of turbulence modeling. The description idea is that a turbulent flow is composed by eddies of different sizes. The sizes define a characteristic length scale for the eddies, which are also characterized by velocity scales and time scales dependent on the length scale. Large eddies are unstable and eventually break up, producing smaller eddies, and the kinetic energy of the initial large eddy is divided into the smaller eddies that stemmed from it. These smaller eddies undergo the same process, giving rise to even smaller eddies which inherit the energy of their predecessor eddy, and so on. In this way, the energy is passed down from the large scales of the motion to smaller scales until reaching a sufficiently small length scale such that the viscosity of the fluid can effectively dissipate the kinetic energy into internal energy. Based on this mechanism, several different numerical models have been developed [159]. Unfortunately, there is not yet a single, practical turbulence model that can reliably predict all turbulent flows with sufficient accuracy. In this work, we have chosen the

standard two equation $\varkappa - \epsilon$ model developed by Jones and Launder [160], which is the most widely-used engineering turbulence model for industrial applications. By definition, this model includes two transport equations to represent the turbulent properties of flow. The first one, $\varkappa$, represents the energy in turbulence, while the second one, ϵ, describes turbulent dissipation.

4.5.3 Model setup in FLUENT

The governing equations shown in Section 4.5.2 can be analytically solved only with very simple boundary conditions, whereas for most real cases we need to resort to numerical computation. In this context, a specific domain called computational fluid dynamics (CFD) has grown up very quickly in recent years, which uses numerical methods and algorithms to solve the fluid problems.

With the development of supercomputers, ongoing research in CFD yields softwares that improve the accuracy and speed of complex simulation scenarios. In the work of this thesis, we employed the commercial software ANSYS FLUENT, which basically solves the governing equations numerically using the finite volume method [161]. It is a powerful and flexible general-purpose CFD software package oriented to model flow, turbulence, heat transfer, and reactions for various applications.

To successfully implement a simulation with the FLUENT software, we proceed along the following steps:
(I) Building the model and meshing

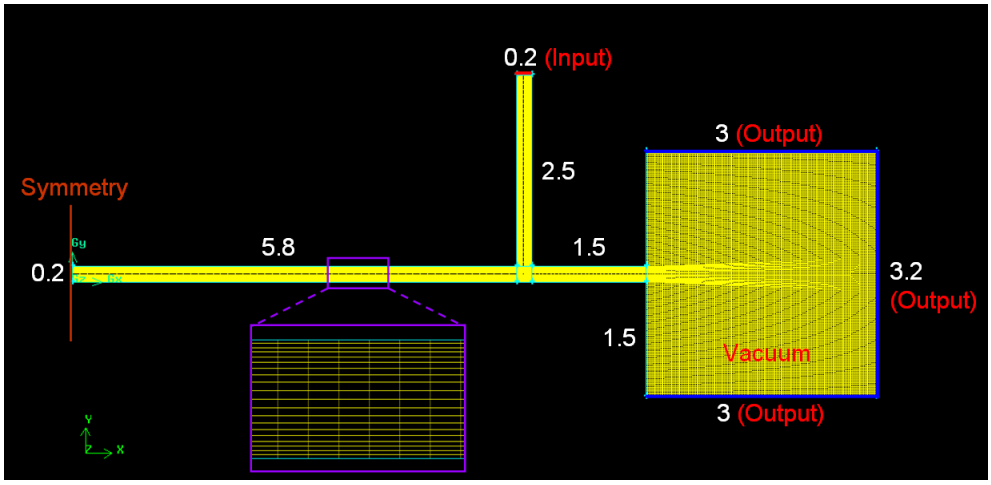

Figure 4.11: *A typical model and mesh used in FLUENT simulation. The numbers indicate the lengths of the lines beside them in unit of millimeter. A small region is zoomed to show the fine structure of the mesh inside the capillary tube.*

The simulation models are created and meshed with the software FLUENT Gambit. Figure 4.11 illustrates a typical model discussed in the following sections. The dimensions are set to be close to the experimental ones. The slit is 200 μm wide and 1.5 mm away from the capillary end. The diameter of capillary is 200 μm, and the tube length is 15 mm. With the help of symmetry boundary, only half the capillary is actually simulated. Around the capillary end, a rectangle box is employed to imitate the vacuum background. The size of the vacuum box is determined from two considerations: on one hand, it should be large enough to obtain the gas density full variation over its characteristic scale, and on the other hand, it should be limited to a size insuring that the flow can be treated within

the continuum approximation as the gas density drops in the vacuum background [149]. It may become so low that the continuity requirement of fluid dynamics does not hold any more. A set of simulations with different vacuum box sizes was carried out. It was found that when using a box of 3.2×3 mm^2, the gas flow in the vacuum box remains in the fluid regime and the normalized on-axis gas density at the box output boundary decreases to about $< 1\%$ of the maximum density in the capillary tube. Thus the gas outside this vacuum box could be neglected.

Next, the model has to be meshed for numerical calculation. There are many rules developed in order to achieve a good mesh; a key criterion is the detailed dynamics of fluid can be resolved, specially for a turbulent flow. Thus in our simulations, the meshes near boundaries are refined as shown in the zoomed inset in Figure 4.11.

(II) Assigning the boundary conditions

The boundaries are assigned as the same as in experiment (See more details in Section 4.6.1). The input boundary has a stagnant pressure varying in the range of $100 - 500$ mbar. The pressures at the output boundaries are set to be 0.5 mbar. It is worth pointing out that the exact value of the initial pressure assigned at the output boundaries is not so important provided it meets the requirement of continuous flow. Because the gas flow becomes supersonic in the vacuum box region, the real pressure at the output boundaries is consequently calculated from the upstream flow. All the walls are assumed to be isothermal at room temperature of 293 K.

(III) Setting-up the physical models

As mentioned above, the standard $\varkappa - \epsilon$ turbulent model with default parameters is employed to simulate the flow. Other two-equations turbulent models, for instance the $\varkappa-\omega$ model, were tested as well. No appreciable difference between them was found for our cases. The $\varkappa-\epsilon$ model is solved by the implicit density-based solver, which is particularly designed for problems of compressible flow. The gas is hydrogen, treated as ideal gas. As the local temperature varies significantly according to gas velocity, the viscosity κ will change accordingly. Therefore Sutherland's formula is employed to describe the dynamic viscosity of an ideal gas as a function of temperature [162]

$$\kappa = \kappa_0 \frac{T_0 + C_s}{T + C_s} \left(\frac{T}{T_0}\right)^{3/2}, \tag{4.19}$$

where κ_0 is the reference viscosity at a given temperature T_0. C_s is Sutherland's constant. Typically for hydrogen gas, $\kappa_0 = 8.76 \times 10^{-6}$ at $T_0 = 293$ K, and $C_s = 72$.

(IV) Control of iteration

The solution is viewed as converging when the residual of iteration becomes less than 10^{-6}; meanwhile the relative difference between the inward flows at the inlets and the outward flows at the outlets is below 10^{-6}.

4.5.4 Results of 2D stationary state

Simulation results

Before going to 3D study, we will first present the results of 2D simulations in this section. 2D simulations are less time-consuming, while able to reflect many fundamental gas dynamics. Here we present the results of the stationary state study, namely for a given set of boundary conditions the gas features do not vary with time any more. This stationary state is of great interest for many experiments of laser-plasma interaction.

Figure 4.12 displays the simulation results at stationary state for the model shown in Figure 4.11. The distance in Figure 4.12 is measured from the center of the tube z_0. The

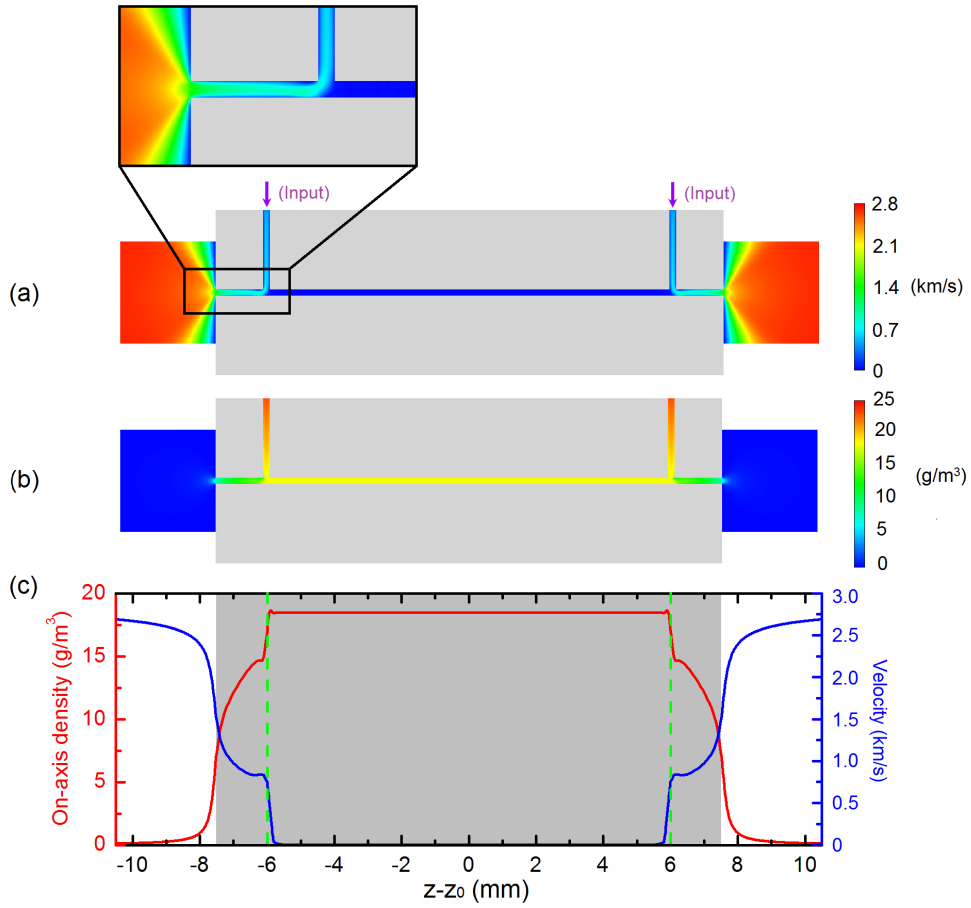

Figure 4.12: *(a) velocity and (b) density distributions of neutral hydrogen gas at stationary state inside a capillary tube for an input pressure of 300 mbar. A small area of the capillary end part is zoomed to show the fine local distribution. The grey areas are the capillary material. (c) the on-axis gas density and velocity as a function of the distance along the capillary tube, where z_0 is the center of the tube, and the two dashed lines indicate the positions of the two slits. The parameters are the same as for Figure 4.11.*

input pressure is chosen to be 300 mbar, a typical value used in our LWFA experiments. When the gas flow moves forward inside the slit, it hits the capillary wall and is split into two branches. One fills the main part of the capillary tube between the two slits, while the other leaks out from the capillary ends.

Several features associated with gas flow at stationary state can be drawn immediately. First of all, the density drops when the gas moves inside the slit. That's because the total pressure[3] is determined by the input condition. When gas velocity increases, the dynamics pressure of gas for compressible flow, quadratically depending on the Mach number, $\mathrm{P}_d \propto M_a^2$, rises significantly. M_a represents the ratio of gas velocity and the local speed of sound. As a consequence, the static pressure, or gas density, diminishes. The gas density filled into the main part of capillary tube is about $\varrho = 18.5$ g/m^3 in Figure 4.12. Therefore the filling efficiency, defined as the ratio of the density in the capillary main part and the density at input, is about $\eta_f = 75\%$ in this case. Secondly, an immobile and

[3]In fluid dynamics, total pressure is the sum of static pressure and dynamic pressure. Specifically, static pressure is the value measured by barometer at a point in a fluid flow, while dynamics pressure represents the kinetic energy per unit volume of a moving flow.

perfectly uniform gas is achieved between the two slits. Such a shock-free gas medium plays a crucial role in our LWFA experiments. Lastly, the gas turns 90° from the slit to capillary end for going out (See the zoom in Figure 4.12). This 2D motion induces the on-axis density profile between slit and capillary end as displayed in Figure 4.12(c).

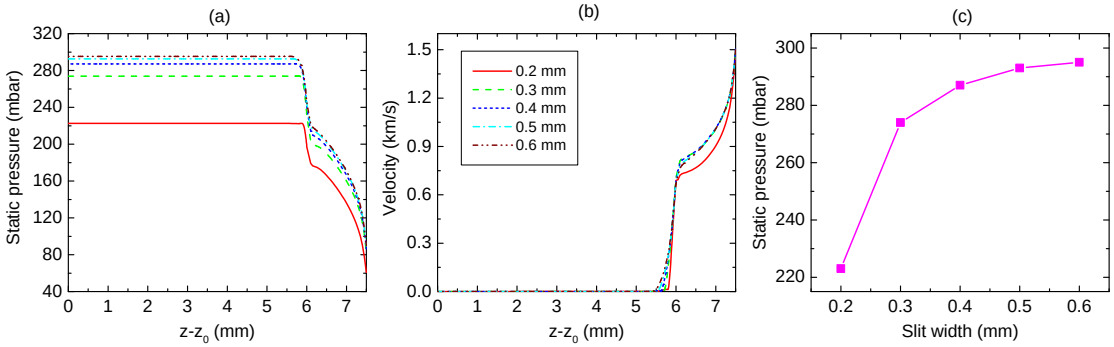

Figure 4.13: *On-axis gas static pressure (a) and velocity (b) as a function of the distance from the center of the capillary tube for different values of the slit width indicated in the legend. (c) shows the static pressure in the central part of the tubes as a function of the slit width. The parameters are the same as for Figure 4.12.*

An important issue is the relationship between the gas features and capillary structure parameters (length, diameter, and slit width). As mentioned above, the slit width is a key parameter to determine the filling efficiency. Figure 4.13 shows the main features of gas flow at the stationary state when the slit width varies from 0.2 to 0.6 mm. All the other parameters are the same as for Figure 4.12. Figure 4.13(a) shows the on-axis static pressures as a function of the distance along the capillary tube. From now on, we will give the static pressure instead of gas density, as it is more convenient to compare with the input condition in unit of mbar. One can easily convert it to density through the state equation of ideal gas for room temperature of 20 °C. As shown in Figure 4.13(a) and (c), the profile of pressure does not appreciably change with respect to the slit size, nevertheless the pressure fed into the capillary central part increases significantly. Especially for the case of 0.3 mm wide slit, the static pressure P_s increases from 223 mbar to 274 mbar. That's mainly because the slit size becomes larger than the capillary diameter of 0.2 mm, and much more gas can be filled into the tube. In this sense, the larger is the slit, the higher pressure can be achieved in the tube. Particularly for a slit width of 0.6 mm, the pressure achieved is $P_s = 295$ mbar, which is close to the input pressure of 300 mbar. However, it is not that desirable to use such a wide slit, since more laser energy will be lost at the slit position. Figure 4.13(b) shows that there is no significant difference between the gas velocity profiles for the different slit widths. That is because gas velocity is determined by the gradient of gas pressure. The similar pressure profiles along the capillary tube for slit widths larger than 0.2 mm, exhibited in Figure 4.13(a), result in the similar velocity profiles shown in Figure 4.13(b).

In experiments, the capillary tube is mounted into a housing which is connected to the gas reservoir by a filling pipe (See more details in Section 4.6.1). In order to take into account the influence of housing and filling pipe on gas characteristics in the capillary tube, a more realistic model was simulated. As shown in Figure 4.14, the capillary holder is cylindrical with a radius 0.8 mm larger than the capillary radius, and the diameter of the filling tube is 1 mm. The real length of the filling tube is around 1 m in our setup, however calculating such a long tube is extremely time-consuming and absolutely beyond

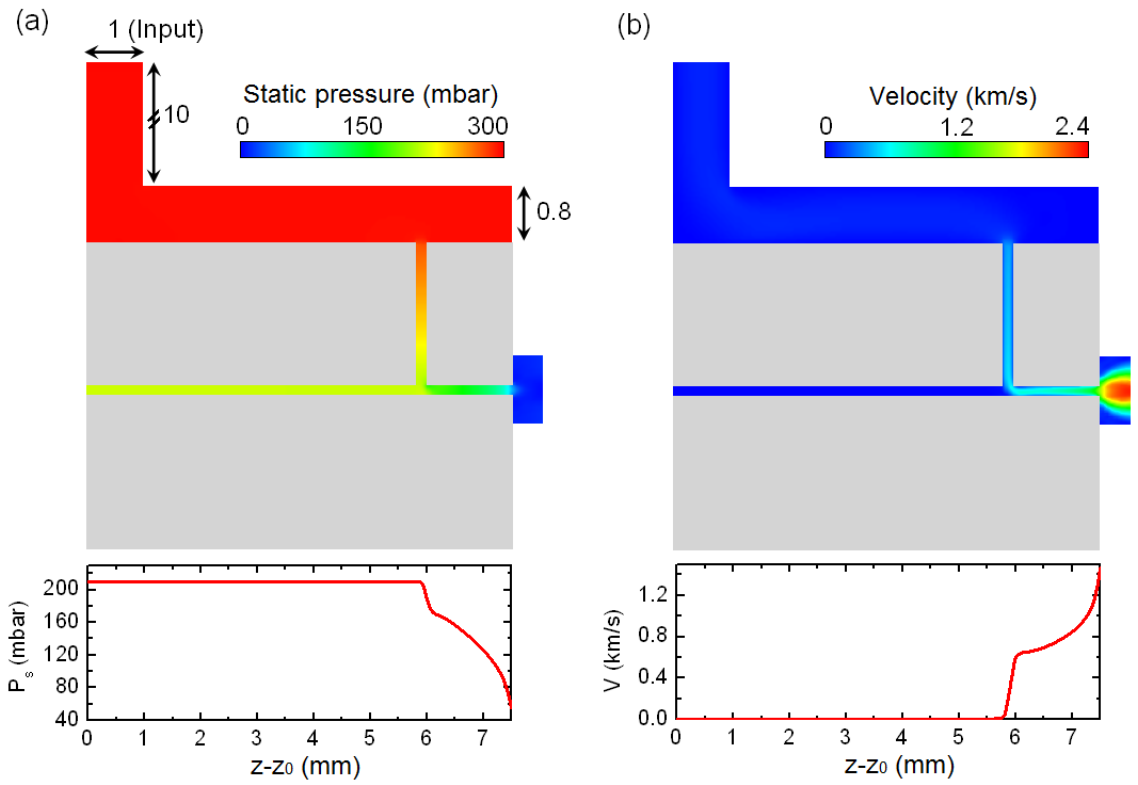

Figure 4.14: *Distributions of (a) static pressure and (b) gas velocity in the capillary tube obtained when the housing and filling pipe are included in the calculation. The line-outs represent the corresponding profiles on the capillary tube axis. The other parameters are the same as for Figure 4.12.*

our machine capacity, so a 10 mm long tube was modelled. As seen below, the length of the filling pipe actually does not affect the gas properties at the stationary state, but affects the characteristic time of gas filling and leaking. Furthermore, as we have already obtained the distributions of gas expansion into vacuum in Figure 4.12 and a theoretical estimation of gas expansion (See the following subsection), a smaller vacuum box was used for the simulation presented in Figure 4.14 to save computation time.

Figure 4.14 shows that at the stationary state gas distribution inside the capillary tube is nearly the same as the one shown in Figure 4.12 for the case without housing and filling pipe. It is easy to understand this result. As the dimensions of the housing and filling pipe are much larger than the slit, the gas flow is chocked by the slit. The upstream gas is uniform and equal to reservoir pressure. The static pressure of gas towards the inner side of the capillary tube ($z - z_0 < 6$ mm) reaches 210 mbar, which is slightly lower than the value of 223 mbar achieved for the case without housing and filling pipe. That is because the gas is not exactly immobile at the slit top, which corresponds to a local static pressure lower than 300 mbar, whereas the pressure was set to be 300 mbar at the slit top (input) for the case of Figure 4.12.

Theoretical analysis of gas expansion from capillary end

One disadvantage of capillary tubes, compared to supersonic gas jet, may be that the gas distribution does not have sharp edges. As seen in Figure 4.12, there is an appreciable

amount of gas around the capillary ends. To estimate this amount, one needs the on-axis gas profile, which can be obtained from numerical simulation. In this section, we present a theoretical estimation of the on-axis density profile when gas expands from capillary end into vacuum.

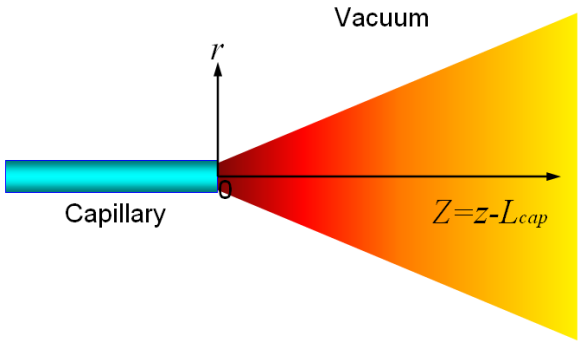

Figure 4.15: *Schematic illustration of gas expansion from capillary tube into vacuum background. The origin of the coordinates (r, Z) is set at the capillary exit.*

We consider a very simple model with only a gas flow coming out from a capillary tube, as illustrated in Figure 4.15. The goal here is to find the on-axis density profile $\rho(Z)$ for $Z > 0$, where $Z = z - L_{cap}$ and z is the coordinate defined in Figure 4.15. Since outside the capillary exit is the vacuum background, the gas moving in the capillary tube experiences a pressure drop to reach a sonic chocked flow at the capillary exit [155], namely $Ma = 1$ at $Z = 0$. After leaving the capillary, gas freely expands into the vacuum background, which typically exhibits a Gaussian radial density profile [149] as

$$\rho(r, Z) = \rho(0, Z)e^{-r^2/\Delta r^2(Z)}, \tag{4.20}$$

where $\Delta r(Z)$ indicates the transverse size of gas plume at the position Z. As observed in experiments by Geddes *et al* with a sonic gas jet, the gas expands in the transverse direction at the speed of sound [163], so $\Delta r(Z)$ can be estimated through $\Delta r(Z) = r_0 + Z$, where r_0 is the waist of transverse distribution at the capillary exit ($Z = 0$), so $r_0 \simeq R_{cap}$.

Integrating equation 4.20 along the radial direction gives the total gas particle number at Z:

$$N(Z) = \int_0^\infty \rho(r, Z)2\pi r dr = \rho(0, Z)\pi(\Delta r)^2. \tag{4.21}$$

At the capillary exit it gives $N(Z = 0) = \rho(0, 0)\pi R_{cap}^2$. Using the conservation of the number of particles, one can obtain the on-axis density profile of the expanding flow ($Z > 0$) by

$$\rho(0, Z) = \rho(0, 0)\left[\frac{R_{cap}}{R_{cap} + Z}\right]^2. \tag{4.22}$$

This expression shows that the on-axis density profile depends on the capillary radius and the distance from the capillary end.

Figure 4.16 presents the on-axis density profile predicted by Equation 4.22 for a capillary tube with diameter of 178 μm, and the profile obtained from FLUENT simulation. The two profiles exhibit similar decreasing tendencies, however the theoretical prediction drops more rapidly. The difference may be understood as follows. In simulation, the friction effect of capillary wall makes the flow becoming sonic not exactly at the capillary exit but slightly earlier inside the capillary tube, so the flow becomes supersonic when

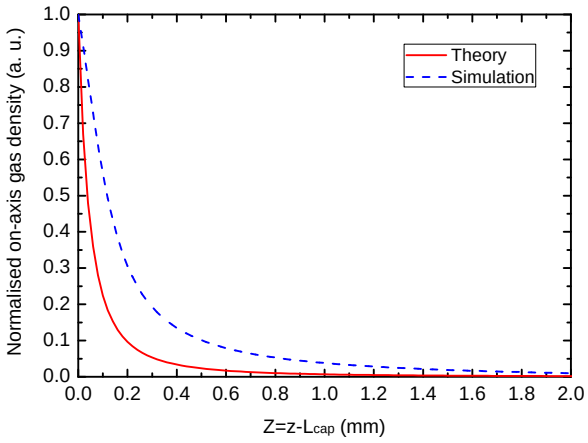

Figure 4.16: *Theoretical on-axis density profile given by Equation 4.22 for a capillary tube of 178 µm diameter (red solid curve), and the profile obtained with FLUENT simulation (blue dashed line). $Z = 0$ is located at the capillary exit.*

the gas leaves the capillary tube. In this case, the longitudinal gas velocity is higher than the velocity of gas transverse expansion; namely the transverse size of gas flow, $\Delta r(Z)$, increases more slowly with Z than the prediction of $\Delta r(Z) = r_0 + Z$. Thus $\rho(0, Z)$ is relatively higher in simulation than the theoretical approximation. Nevertheless, the theoretical prediction, once we know its error with respect to the simulation result, is still very useful for a rough estimation in experiment.

4.5.5 Results of 2D transient simulation

Up to this point, we have presented the gas features in the stationary state, however an important question is to determine when the stationary state can be reached for a given setup of gas filling. To answer this question, one needs to investigate the temporal evolution of gas density inside capillary tubes. In this section, we will show the results of transient (or unsteady) evolution of gas density, which demonstrate how the gas evolves in the filling system and when the stationary state is reached in a capillary tube.

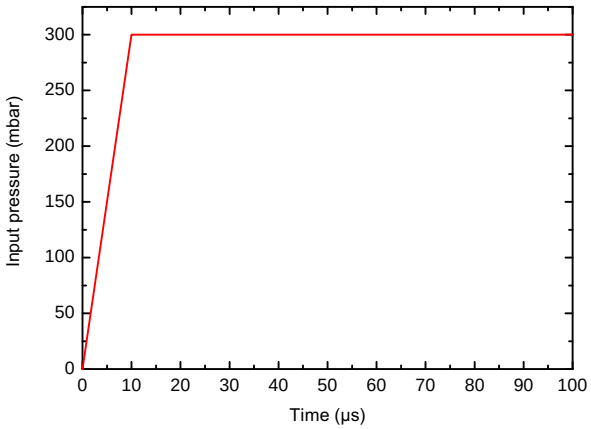

Figure 4.17: *The input pressure for transient simulation given by Equation 4.23.*

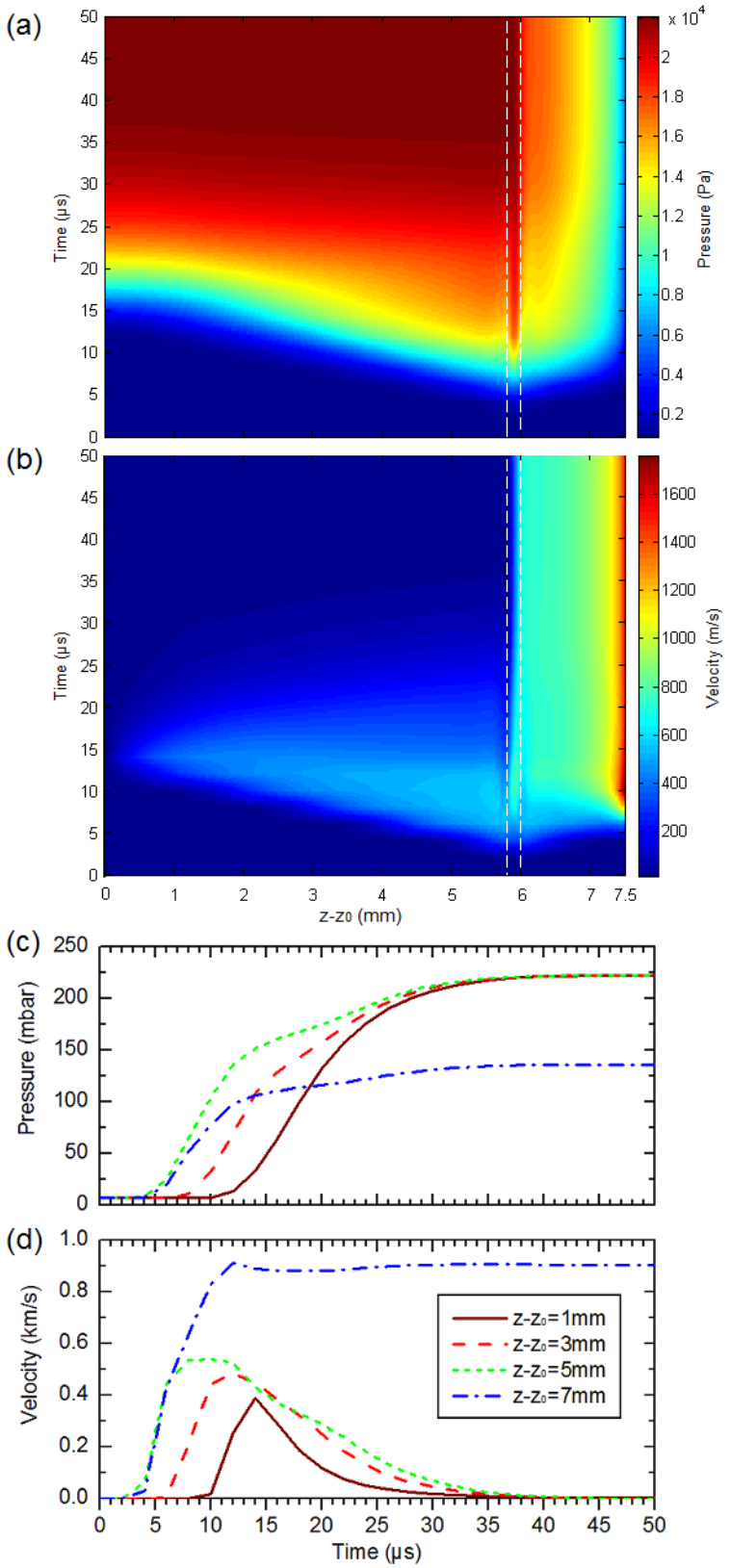

Figure 4.18: *Time evolution of the on-axis (a) gas static pressure and (b) velocity in a 15 mm long, 200 µm diameter capillary tube with a 200 µm wide slit, where the two dashed lines indicate the slit position. (c) Evolutions of static pressure at four different locations along the capillary axis.*

As a first step of transient simulation, we use the capillary model given in Figure 4.11, while the boundary and initial conditions are adjusted to approach the experimental ones. In experiment, all the filling components downstream the gas reservoir are pumped down to $< 10^{-5}$ mbar, so the initial condition of gas inside the capillary tube should be $\mathrm{P}_{H_2}(t = 0) = 0$ and $v_{H_2}(t = 0) = 0$. Nevertheless in order to meet the requirement of continuous flow ($Kn < 0.1$), we assume that the capillary tube is initially filled with a gas pressure of 7 mbar, i.e. $\mathrm{P}_{H_2}(t = 0) = 7$ mbar. This assumption may shorten somewhat the filling time, compared to the experimental case of initial condition of vacuum.

The input pressure can be viewed as constant in experiment owing to the use of a real-time pressure regulator (See more details in Section 4.6.1). Simulation are performed for an input pressure $\mathrm{P}_{in} = 300$ mbar, which is a medium value in the pressure range (100−500 mbar) explored in experiment. To avoid numerical problems, the input pressure is required to gradually increase from the initial pressure $\mathrm{P}_{H_2}(t = 0)$ to the constant value of P_{in}. In our case, the input pressure is given by

$$\mathrm{P}_{in}[\mathrm{mbar}](t) = \begin{cases} 7 + \frac{293}{\Delta t \times N} t, & \text{if } \mathrm{P}_{in} < 300, \\ 300, & \text{if } \mathrm{P}_{in} \geq 300, \end{cases} \tag{4.23}$$

where $\Delta t = 0.1$ μs is the time step of calculation. N is used to control the ramp of pressure increase. A typical value of $N = 100$ was found to be suitable for our simulation cases to avoid problems of numerical convergence. It means the input pressure linearly increases from 7 to 300 mbar over 10 μs and then remains stable for $t > 10$ μs, as shown in Figure 4.17. The output boundary condition is the same as for the stationary state. The transient calculations are stopped when the gas distributions become nearly the same as the results of stationary state.

Figures 4.18 demonstrates the transient evolutions of static pressure and gas velocity inside the capillary tube for the model shown in Figure 4.11. The time evolution of the gas static pressure and velocity along the capillary central axis are illustrated in Figures 4.18(a)-(b), where the two white dashed lines indicate the slit of 200 μm wide. As seen, the hydrogen gas coming from the inlet arrives at the junction of the slit and the capillary axis at $t = 5$ μs. Then the gas is split into two parts. One part leaks out from the capillary end, while the other part moves towards the capillary center with a speed of around 400 m/s, filling the capillary tube. Consequently, the local static pressures inside the capillary tube increase. The gas arrives at the symmetry of the capillary center ($z = z_0$) at $t \simeq 14$ μs. This gas then collides with the filling gas coming from the other direction (not shown in Figures 4.18 owing to symmetry) and becomes immobile at this position. With more and more gas being filled into the capillary, the local static pressure rises rapidly, and meanwhile the gas on-axis velocity drops owing to a lower pressure gradient between the inlet and the capillary central region. This filling process is clearly reflected in Figure 4.18(c)-(d) by the evolutions of the gas static pressure and velocity at four different on-axis points, namely $z - z_0 = 1$, 3, 5, 7 mm. Three of them are located in the main capillary part, while one, $z - z_0 = 7$ mm, is between the slit and the capillary end. They show that the gas becomes stable for $t > 40$ μs. As shown before, the gas is stationary and uniform in the central capillary part, while at $z - z_0 = 7$ mm the local static pressure is lower and the gas leaks out with a speed of 900 m/s. The transient calculation was terminated at $t = 50$ μs when the stationary state has been reached.

We examined how the filling process is affected by the capillary parameters since different capillary diameters and lengths were used in our experiments. Appendix B shows a set of simulation results performed for capillary tubes with different lengths.

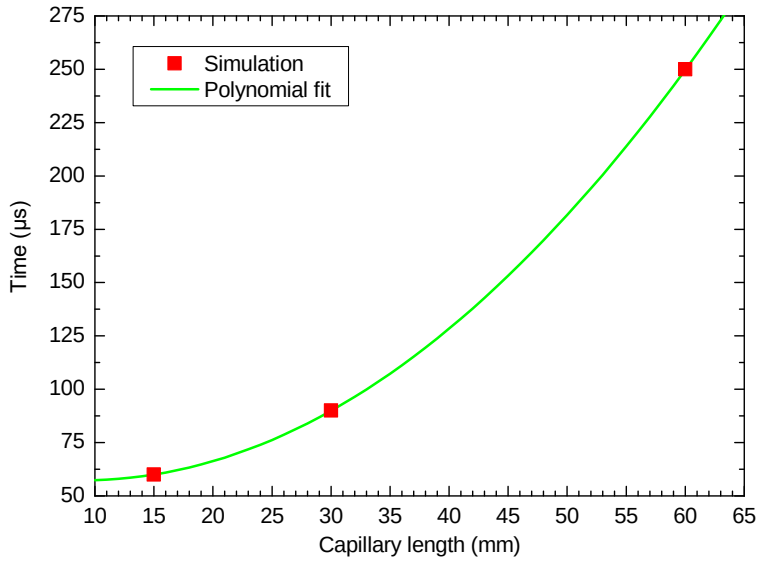

Figure 4.19: *Time necessary to reach the stationary state as a function of the capillary tube length and a polynomial fit.*

The capillary models are similar to the model in Figure 4.11 except for the length of the tube. The input pressure is the same as given in Figure 4.17.

We first examine the influence of slit width. In Figures B.1-B.3, the slit is 300 μm wide, while the right side of the slit is kept at 1.5 mm from the capillary end. The slit/diameter ratio thus becomes 1.5 instead of 1 used for Figure 4.18. Noticeable differences are observed between Figures B.1 and Figure 4.18. With a wider slit, the gas filling process is faster. The gas propagates in the capillary central part with a higher speed of 800 m/s. As a consequence, the local pressure increases more rapidly, and overshoots (a local pressure larger than the input pressure, $P_s > P_{in}$) at $t \simeq 25$ μs. However this overshot state is not stable, as the gas is expelled to lower pressure regions, and the local overshot pressure drops. This phenomenon induces overshot-to-undershot oscillations which are clearly visible in Figure B.1(c)-(d). The oscillation magnitude decreases with time, and eventually the stationary state is reached at $t \simeq 60$ μs.

The influences of the capillary length on the gas filling process was studied as well. Figures B.2-B.3 display the simulation results of gas filling for 30 mm and 60 mm long capillary tubes with 300 μm wide slit, respectively. Compared to the case of 15 mm long shown in Figure B.1, the filling process is smoother. A gas oscillation occurs between $t = 50-80$ μs in the 30 mm long capillary, but without overshot. For the 60 mm long capillary tube, the static pressure inside the tube gradually increases without oscillation. This occurs mainly because it takes more time for the gas to reach the capillary symmetrical plane in a longer capillary tube. At the same time, the input flux tends to become stable owing to pressure adjustment in the slit region, so pressure overshot is less excited in a long capillary. Eventually stationary states are achieved in the 30 mm and 60 mm long capillary tubes at $t \simeq 90$ μs and $t \simeq 250$ μs respectively, when the gas distribution becomes unvaried with time. An empirical formula for the arrival time of the stationary state as a function of capillary length is obtained as $t_{sta} = 0.074L_{cap}^2 - 1.33L_{cap} + 63.3$. As expected, the capillary length does not affect the filling efficiency. For all the three cases in Figures B.1-B.3, an efficiency of 90% ($P_{H_2} \simeq 270$ mbar) is achieved.

Finally, we present the results of transient simulations for capillary tubes together with

the holder and filling pipe (the model illustrated in Figure 4.14). This simulation should give us a whole picture of gas evolution in the filling system. The boundary setups are the same as above. Shown in Figure 4.20(a)-(d) are the contour plots of gas velocity at four different times: $t = 5$, 10, 15, 47.5 μs. They respectively represent four important times in the procedure: (a) the gas coming from the input port propagates in the filling pipe; (b) the gas has filled the capillary housing and starts to fill the capillary slit; (c) the gas feeds the capillary main part and meanwhile leaks into the vacuum box; and (d) the first stationary state is reached.

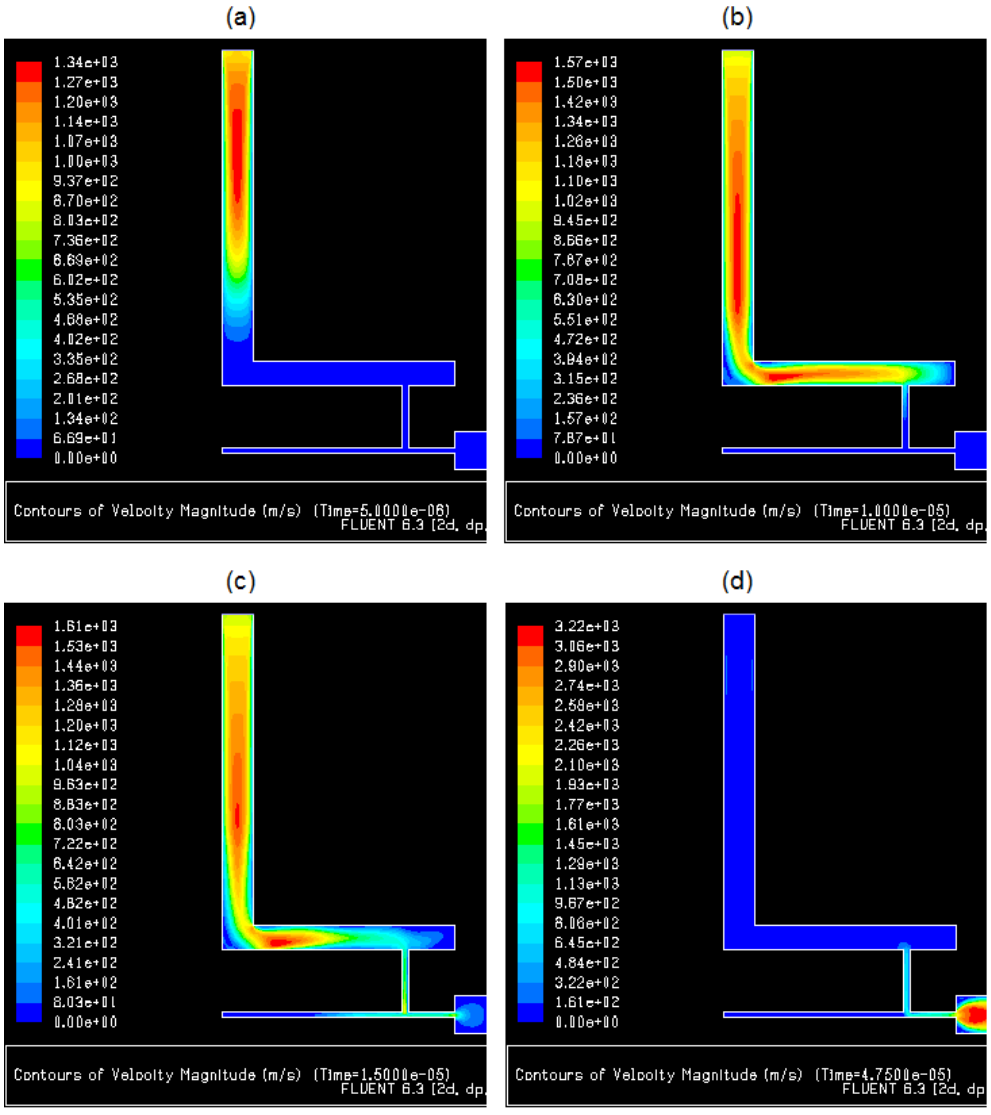

Figure 4.20: *Contour maps of gas velocity inside the capillary tube with the holder and filling pipe at different times of* $t =$ *(a) 5, (b) 10, (c) 15, (d) 47.5* μ*s.*

Even though the gas velocity is zero inside the central part of the capillary tube in Figure 4.20(d), it is still not the final stationary state seen in Figure 4.14. To give a clearer picture of the filling process, the evolution of on-axis gas static pressure and velocity are shown in Figures 4.21. One can immediately find that the process is quite different from Figures 4.18 which presents the capillary model without housing and filling pipe.

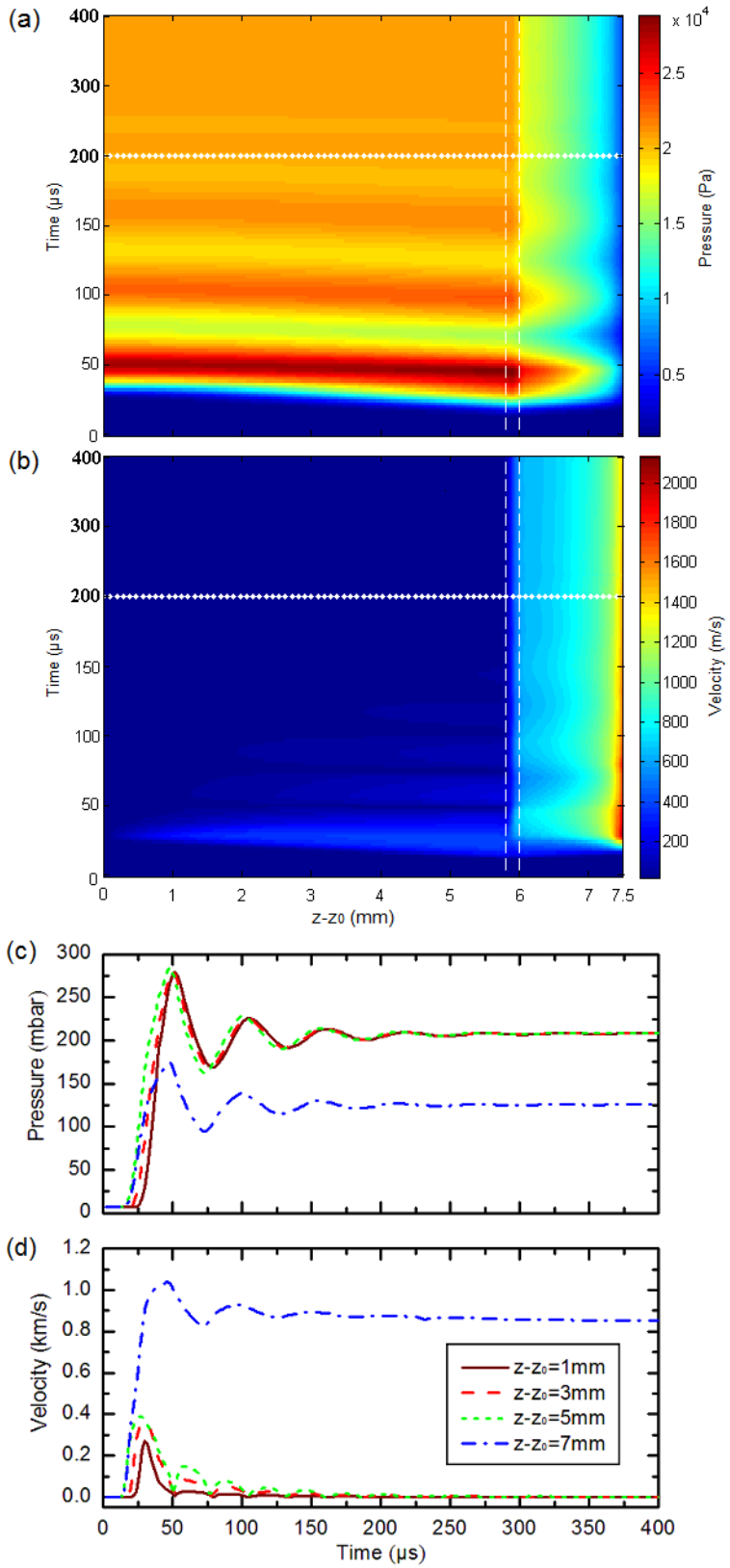

Figure 4.21: *Time evolution of the on-axis (a) gas static pressure and (b) velocity in the capillary connected to filling pipe, where the two vertical dashed lines indicate the slit position. Different time scales are used below and above the horizontal dotted line. Time evolutions of (c) static pressure and (d) velocity at four different locations along the capillary axis.*

The key difference is that here the gas experiences several oscillations before reaching the stationary state. This specific phenomenon can be easily understood as follows. When the gas comes from the input port, it moves quickly through the filling tube and stops at the end of the capillary holder. With continuous gas pouring into this region, even though a slight amount of gas leaks into the capillary tube through the slit [as seen in Figure 4.20(b)], the local pressure in the holder region above the slit becomes higher than the input pressure. Subsequently, the gas pressure reaches a maximum inside capillary tube at $t \simeq 50$ μs. The overshot gas is expelled along pressure gradient to other areas, which results in undershot local pressure in the end region of the holder. It further results in the pressure minima inside the capillary tube. With time increasing, this oscillation is gradually damped and the stationary state eventually arrives inside the capillary tube at $t \simeq 350$ μs. It is obvious that the filling process becomes significantly longer and more complicated when the filling pipe and capillary holder are taken into account.

4.5.6 Results of 3D simulation

As illustrated in Figure 4.2, the capillary tube we use is not symmetrical around the axis, so the real gas filling process might be different from that observed in the 2D models. In order to obtain a better knowledge of gas distribution inside capillary tubes, 3D simulations are definitely required.

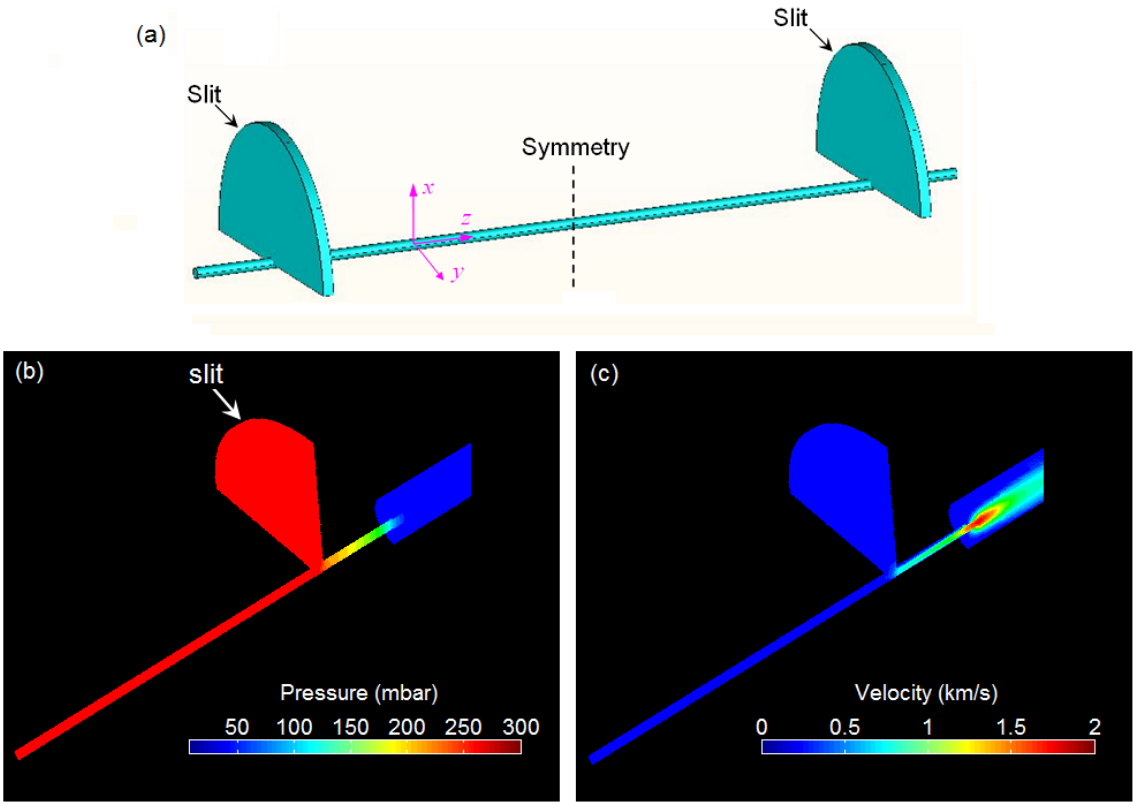

Figure 4.22: *Model of the capillary tube with the same dimensions as for the 2D model given in Figure 4.11. Contour cut-view in the $x-z$ plane of (a) the gas static pressure and (b) velocity. Owing to the symmetry boundary, only half of the capillary tube was simulated.*

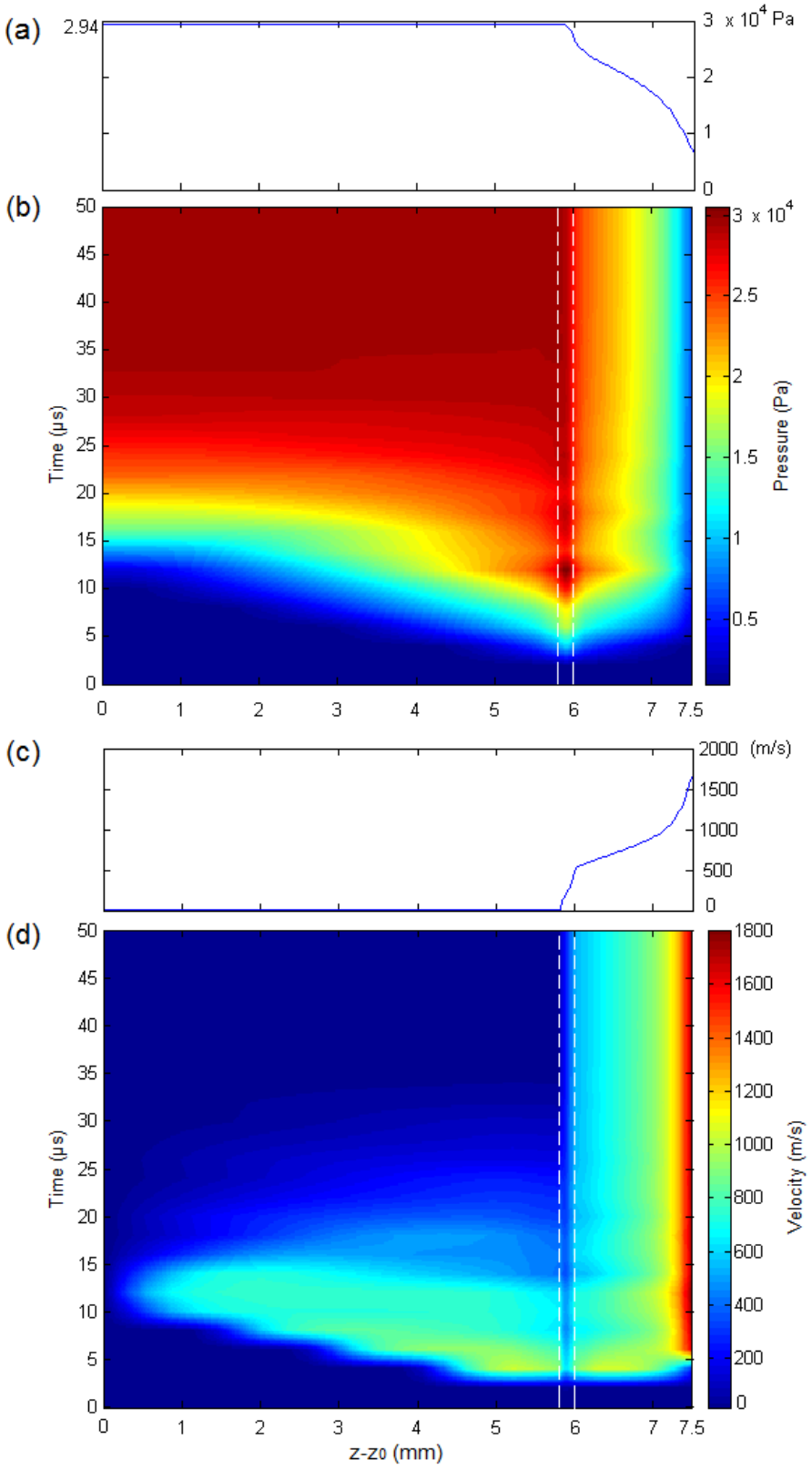

Figure 4.23: *On-axis profiles of (a) gas static pressure and (c) velocity obtained with transient 3D simulation at $t = 50$ µs. Time evolutions of (b) gas static pressure and (d) velocity profiles along the capillary axis, where the two vertical dashed lines indicate the slit position.*

In this section, we present the results of 3D fluid simulations for both the stationary and transient states. The 3D model shown in Figure 4.22(a) is generalized from the 2D model given in Figure 4.11. The dimensions and boundary conditions are kept the same. Owing to the symmetry boundary, only half of the capillary tube was simulated.

Figure 4.22(b)-(c) exhibits the contour cut-views in the $x-z$ plane of the gas static pressure and velocity obtained from the stationary state simulation. The input pressure is set as usual as 300 mbar. As seen, the pressure is uniform and nearly equal to the input pressure inside the slit and main part of the capillary tube. This result is slightly different from what is shown in Figure 4.12 from the 2D simulation. In the 3D case, the gas is almost immobile in the slit and the static pressure inside capillary tube of 294 mbar is relatively higher than 220 mbar obtained in the 2D model. This difference may be interpreted as follows. In the 3D model, the input port is a piece of half cylinder, whereas the 2D inlet is a line. The inlet/outlet size ratio in increased from 1 : 1 for the 2D model to 13 : 1 for the 3D model, which means the amount of outflow takes a smaller fraction from the inflow in the 3D case. A higher pressure of 294 mbar is therefore fed into the capillary tube. The filling efficiency is nearly 100%.

Shown in Figure 4.23 are the results of the transient simulation. The input pressure is the same as for the 2D cases shown in Figure 4.17. It is found that in the 3D case that gas reaches the capillary symmetrical plane ($z = z_0$) at $t \simeq 13$ μs, and finally reaches the stationary state when $t > 40$ μs. Apart from a higher filling efficiency, the process of gas filling is similar to the 2D case as shown in Figures 4.18. The line-outs of on-axis gas static pressure and velocity in Figures 4.23(a) and (c) are roughly the same as those from 2D simulation as well. A small difference is the gas dynamics in the slit region. A noticeable pressure overshoot is seen at $t = 12$ μs in the slit in Figure 4.23(b). Two weaker overshoots appear later at $t = 18$ μs and 23 μs, respectively. This phenomenon of overshoot however was not observed in the 2D results. That's essentially because in the 2D case the gas flow comes from a slit comparable to the capillary diameter, whereas in the 3D model the gas flow comes from half circumference, in which case the gas converges to the center of the circle making local "over-injection". The oscillation of overshot tends to attenuate and finally disappears owing to pressure self-adjusting in the slit region.

4.5.7 Limits of fluid simulations

We have shown the results of gas dynamics inside the capillary system from fluid simulations carried out with FLUENT. These simulations are very helpful to understand how the gas evolves in the filling system and especially to know the gas distribution along capillary axis at the stationary state. The latter point is of great importance for PIC simulations or to estimate the laser evolution before it enters the capillary tube.

Nevertheless, there is still one vital question remaining: at what time is the stationary state realized for a given filling system? Because we are really interested in working with a stable gas distribution, we could in principle obtain the filling time from 3D FLUENT simulations, however there are some difficulties to accomplish this. First of all, it is extremely time-consuming. In our setup of gas filling (See Section 4.6), there is an one meter long flexible pipe to connect the gas reservoir and capillary housing. The mesh number would become unacceptable concerning our cluster capacity to model all the components. Furthermore, it is not easy to describe the flexible pipe very precisely as it is often twisted in experiments. Secondly, the fluid simulation can only work properly for the regime of continuous flow, however in experiment the filling process begins and terminates with vacuum background. The temporal evolution of gas flow in the molecular regime is therefore impossible to model correctly with fluid simulations. Last but not least, in real case the

reservoir pressure is not exactly constant even though there is a self-adaptive pressure regulator, and the effective valve opening duration also changes with respect to the reservoir pressure. Those effects are not easy to include in fluid simulation, but they indeed affect the filling process.

Owing to these reasons, it was crucial to experimentally characterize the temporal evolution of gas density inside capillary tubes to determine the required time to reach a stationary state in the experimental configuration.

4.6 Determination of gas density in capillary tube: experiment

As discussed above, it is important to determine the time when the stationary state is achieved in a capillary tube. It tells us when we should send the laser pulse for laser-plasma interaction. In this section, we report on a method developed to address this issue [164]. The determination of the average density along the capillary axis is obtained by interferometry through the measurement of the real-time phase variation when gas is fed into the tube. The time evolution of gas is determined from the measurement of the continuous fringe displacement as a function of time by following the temporal intensity variation inside a given interval located at a fixed position on the beam axis. As demonstrated below, this method is very efficient for optimizing a gas filling system, and can be applied to other similar plasma targets such as gas-cell or gas jet as well.

4.6.1 Gas filling system

In this section, we introduce the design of our gas filling system. The setup shown in Figure 4.24 is improved from the previous work [62], where the gas injection process was controlled manually. It is important to precisely control the gas filling process on one hand to achieve the desired plasma density in the capillary tube, and on the other hand, to minimize gas leakage into vacuum chamber. If the valve for gas filling is opened for a duration longer than the one necessary to reach the stationary state of gas inside the capillary tube, a significant amount of gas will leak into the target chamber. Gas leakage is an important consideration, because (*i*) there is a high risk to damage to the turbo pump, and because (*ii*) it may result in undesirable nonlinear modifications of the laser beam interacting with a large volume of gas before focusing.

Figure 4.24(a) shows schematically the system of gas injection, and Figure 4.24(b) is a photograph of the setup for the interferometric measurements at LPGP in 2012 [164]. The filling procedure is mainly controlled through a pressure regulator and a solenoid valve. The inlet port of the regulator (Bronkhorst pressure controller) is connected to the gas bottle of either hydrogen or argon with output pressure up to 30 bar, while the outlet port is connected to the reservoir. The regulator that we used is able to provide a desired pressure in the reservoir ranging from 50 to 500 mbar with an error of merely 1%. The inset in Figure 4.24(a) shows the principle of the regulator's function. A high-accuracy pressure sensor measures the real-time pressure P_2 at the outlet port (namely the reservoir pressure), and feeds back to the controller $P-600$. The controller calculates the difference between P_2 and the desired pressure in the reservoir, and regulates the flow rate through a valve. Finally the desired pressure can be precisely produced in the reservoir. When the reservoir pressure is ready, we open the solenoid Valve1 to inject gas into capillary tube.

The solenoid valve (Pfeiffer Vacuum DVI 005 M) is driven by a 24V, 10 W electrical signal which is further triggered by a digital TTL signal. The valve is capable of functioning

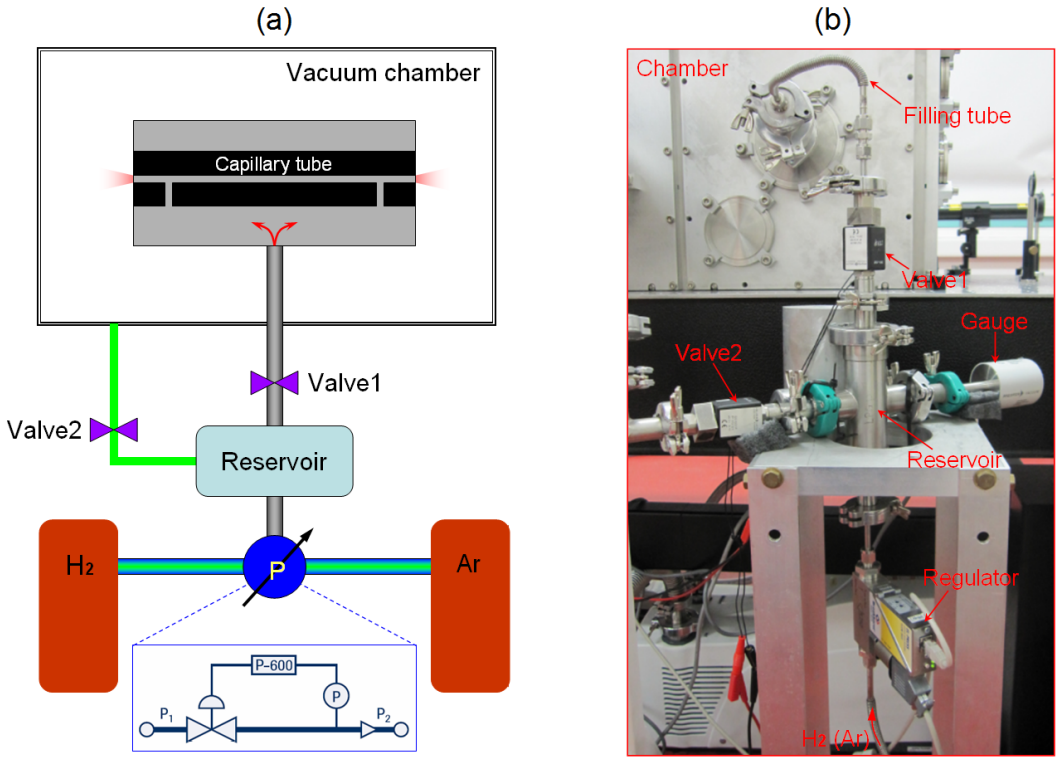

Figure 4.24: *(a) Schematic illustration of the system for gas injection into capillary tube. (b) Photograph of the experimental setup at LPGP for interferometric measurements.*

under a pressure difference up to 1.5 bar. The TTL signal is used to control the opening duration of the valve. The duration of the electrical signal can be decreased to as short as 27 ms, below which the valve is not able to open normally for a high reservoir pressure ($\sim$ 500 mbar). The effective duration of valve opening is shorter than the electrical pulse duration because of the internal delay of the valve, of the order of 20 ms. In the following part, the duration of valve opening should be understood as the duration of the electrical pulse. As the valve has to be placed outside the vacuum chamber owing to self-heating during operation, a flexible pipe with inner diameter of 1/4 inch and with a total length of 110 cm connects the valve to the capillary housing.

The filling procedure is briefly described as follows: (*i*) pumping the chamber and filling pipes down to $< 5 \times 10^{-5}$ mbar; (*ii*) setting the reservoir pressure; (*iii*) opening the valve with a desired duration. After valve opening, the regulator automatically works to feed the reservoir to the desired pressure.

4.6.2 Principle of the interferometric measurement

Interferometry is widely employed in gas/plasma diagnostics. In this thesis, we used a Mach-Zehnder (shortened as "MZ" in the following) interferometer [146] to measure gas density in capillary tubes. The MZ interferometer, as illustrated in Figure 4.25, consists of two separate optical paths. The incident HeNe laser is split 50/50 by a cube into two beams, reflected by two mirrors, and then recombined by a second cube to produce interference. In one optical path, one can put the sample to be tested which will introduce a relative phase shift between the two laser beams. The phase shift can be measured by the spatial shift of the interference fringes. To avoid disturbances of air flow, the

interferometer is usually built up in a vacuum chamber. The lengths of the two optical paths should not differ too much since the coherence length of the HeNe laser is around 20 cm. If a pulsed laser is employed, the two optical paths must be nearly equal to get interference.

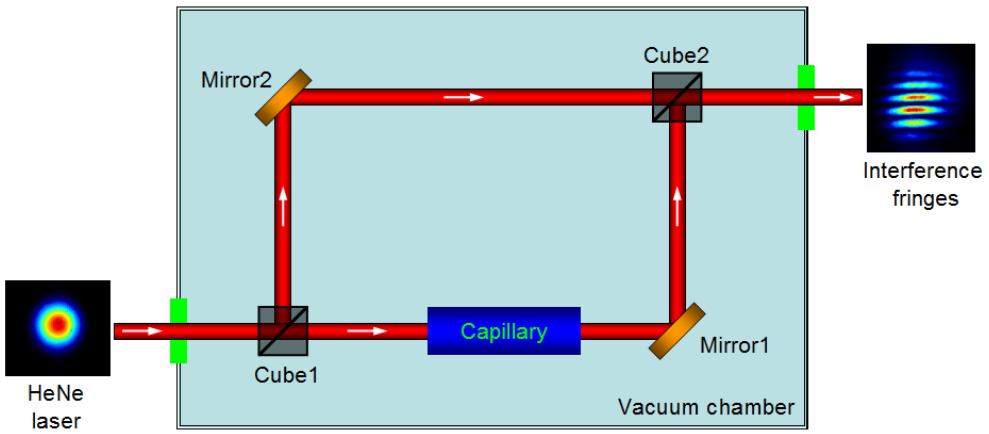

Figure 4.25: *Schematic illustration of the Mach-Zehnder interferometer used in our experiments. The optical path with capillary tube is called "sample beam", while the other is called "reference beam".*

The phase shift between the two laser beams depends on the difference between the indexes of refraction along the optical paths as

$$\begin{aligned}\Delta\psi(t) &= \frac{2\pi}{\lambda_0}\int_L [n_s(l,t) - n_r(l)]dl, \\ &= \frac{2\pi}{\lambda_0}\int_L [n_s(l,t) - 1]dl,\end{aligned} \tag{4.24}$$

where $\Delta\psi$ is the phase shift, L is the optical path length between the two cubes, and $n_s(l)$ and $n_r(l)$ represent the indexes of refraction for the sample and reference beams, respectively. As it is in vacuum, $n_r(l) = 1$ holds. Following Born and Wolf [165], the index of refraction of gas n can be written as a function of the gas density ρ to be

$$n = 1 + \frac{3}{2}A_r m_g \rho, \tag{4.25}$$

where A_r is the molar refractivity, and m_g is the mass of gas atom. A_r is calculated via $A_r = \frac{4}{3}\pi N_A \alpha_p$. N_A represents the Avogadro constant, and α_p is the mean polarizability of a molecule. Using tabulated physical constants [166], the term $3A_r m_g/2$ is calculated to be 5.22×10^{-24} cm^3 for hydrogen and 10.5×10^{-24} cm^3 for argon at standard temperature and pressure. The phase shift is linked to gas density through

$$\Delta\psi(t) = \frac{3\pi A_r m_g}{\lambda_0}\int_L \rho_s(l,t)dl. \tag{4.26}$$

Equation 4.26 implies that the measurement of the time variation of the interference fringe is thus a direct measurement of the evolution in time of the gas density integrated over the direction of propagation of the laser beam inside capillary tubes. In order to quantify the gas density, one needs the spatial distribution of gas along capillary axis.

For a stationary gas distribution in capillary tubes, we can get the spatial distribution from the FLUENT simulations presented in the Section 4.5. As shown in Figure 4.12,

the density profile can be written as $\rho(l,t) = \vartheta(l)\rho^*(t)$, in which $\vartheta(l) = \rho(l)/\rho^*$ is the normalized density profile and ρ^* denotes the plateau density between the two capillary slits. Substituting this expression into Equation 4.26, the plateau density in the stationary state is determined by

$$\rho^*(t) = \frac{\lambda_0 \Delta\psi(t)}{3\pi A_r m_g \int_L \vartheta(l) dl}. \tag{4.27}$$

The term $\int_L \vartheta(l)dl$ can be numerically calculated. Once the phase shift $\Delta\psi(t)$ is measured, one can first obtain the plateau density $\rho^*(t)$ through Equation 4.27, and then get the density profile by $\rho(l,t) = \rho^*(t)\vartheta(l)$.

It should be mentioned that interferometry in the direction transverse to the capillary axis would bring a more precise spatial determination of the gas density. However in our case, as shown in Figure 4.25, longitudinal interference was chosen owing to the following considerations. (*i*) Within the parameter range of capillary tube, the transverse phase shift induced by hydrogen or argon gas requires a high stability and resolution. For example, for a capillary tube of 200 μm diameter, when gas density is $\rho_{H_2} = 1 \times 10^{19}$ cm^{-3}, the maximum phase shift is merely $\Delta\psi/(2\pi) \simeq 0.016$. Such a small phase variation is far below the typical noise level of a few percent in our experiment. The transverse phase shift would be measurable if we ionize the gas into plasma like in Ref. [151]. (*ii*) In our present capillary housing, the capillary tube is mounted into an enclosed metallic holder for gas filling. It was not possible to build transverse interference with such an arrangement.

4.6.3 Experimental measurements and results

As presented above, characterization of temporal gas density evolution becomes the issue of measuring the temporal phase shift of interference fringes. One approach is to use an ultrashort pulsed laser and change the arrival time of the laser pulse with respect to the opening of valve for gas filling [149], so many shots have to be repeated to get a well-resolved evolution profile. In this section, we introduce a scheme using continuous HeNe laser together with a photodiode [164]. Temporal phase shift is inferred by following the intensity variation in time of a fraction of the most intense fringe for a given reservoir pressure and valve opening duration. This diagnostic scheme provides an efficient way to determine the influence of capillary parameters or/and valve opening on the gas filling process.

Experimental setup

The experimental arrangement used for the characterization of gas density inside capillary tubes is illustrated in Figure 4.26. The gas filling system was introduced in Section 4.6.1. A collimated HeNe laser (5mW, 632 nm) with beam waist of 2 mm was used. The laser entered the vacuum chamber through an optical window with transmission of more than 99% for wavelength of 632 nm. The MZ interferometer was constructed in vacuum using two 50/50 beamsplitter cubes and two Al mirrors of flatness $\lambda_0/10$. Two identical lenses of focal length $f = 25$ cm were used to focus the beam at the entrance of the capillary tubes, and to collect the beam emerging after propagation through the capillary tubes. In the conditions of this experiment, the focal spot waist was 44 ± 4 μm, and typical transmission of $> 90\%$ of laser energy was measured. The produced interference fringes were measured by the 12 bit CCD camera and a photodiode at the same time. The slit in front of the photodiode was about 0.5 mm wide, selecting one third the most intense fringe. To fully characterize the gas filling process, two oscilloscopes were used to record the photodiode signal simultaneously with different time scales. The gas filling process,

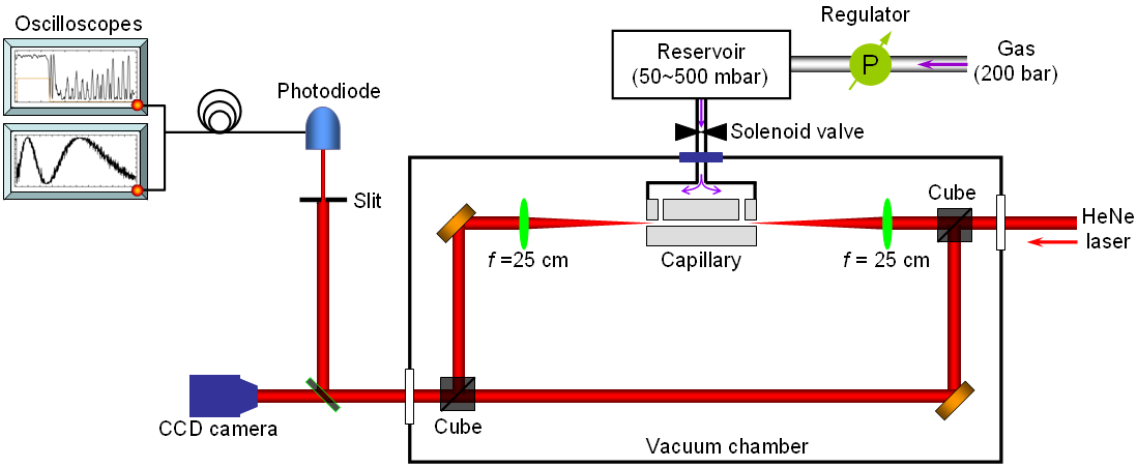

Figure 4.26: *Schematic illustration of the interferometric measurement.*

oscilloscope and camera acquisitions were synchronized by a numerical Stanford pulse generator and automatically controlled by a LabVIEW program.

In order to achieve good quality (straight, high contrast) interference fringes, the capillary tubes must be very carefully aligned with the laser. Quasi-monomode guiding should be achieved in the capillary tubes, and furthermore the transmitted light has to be precisely collimated by the second lens to plane wave. If not, the fringes would not be straight. To give an idea of the influence of laser wavefront on the interference pattern, Figure 4.27 shows three fringe patterns produced by different configurations of laser wavefronts, which are typical cases observed in experiments. They are calculated using two Gaussian beams

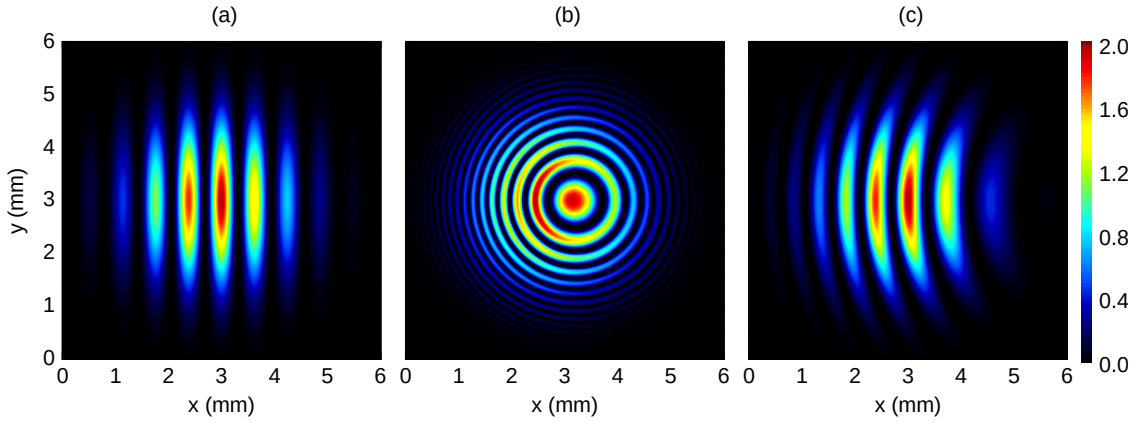

Figure 4.27: *Three fringe patterns numerically calculated using two laser beams with (a) plane wavefronts; (b) one plane wavefront and one curved wavefront with radius $R = 0.5$ m; (c) one plane wavefront and one curved wavefront with radius $R = 5$ m.*

with waist of $w = 2$ mm and a tilt angle of 1 mrad (See more details in Appendix A.4). The two beams are assumed to have the same peak intensity. Figure 4.27(a) is the desired pattern produced by two collimated beams with plane wavefronts. The fringes are straight. In Figures 4.27(b)-(c), one of the wavefront is set to be spherical. The radius of curvature of the wavefronts are $R = 0.5$ and 5 m, respectively. The curved wavefront could be introduced by the second $f = 25$ cm lens downstream capillary tube if it is not exactly focused at the capillary exit. The case of $R = 0.5$ m corresponds to a strongly

bent wavefront. As shown in Figure 4.27(b), the interference pattern becomes circular, like Newton's rings, instead of straight fringes. If the lens is slightly misplaced, it may introduce a weakly bent wavefront with a larger radius, which gives banana-shaped fringes, as exhibited in Figure 4.27(c).

Since the method using a CCD camera to characterize gas density for gas jet has been well investigated [149, 150], we first measured the gas density evolution inside the capillary tubes with the CCD camera, and then benchmarked the result with that obtained using the photodiode scheme. After verification, the dependences of gas filling process on the capillary parameters and valve opening duration were systematically studied.

Measurement with CCD camera

This section presents the results measured with the 12 bit CCD camera for a 20 mm long, 102 μm diameter capillary tube. Argon was used to produce a more easily detectable fringe shift than hydrogen for a given gas density. Figure 4.28 shows an image sequence taken by the CCD camera at different time delays. The achieved fringes were fairly straight as those in Figure 4.27(a). A red line is plotted on purpose in Figure 4.28 to give a position of reference, so it is easy to appreciate the fringe shift. $t = 0$ corresponds to the start of the electrical pulse for valve opening. It is the reference position of fringe when there is no gas filled into the capillary tube. The duration of valve opening was 20 ms (namely $t = 0-20$ ms), and the reservoir pressure was 125 mbar. At $t = 30$ ms, the fringe positions are still nearly the same as $t = 0$, implying no gas reaches the capillary tube yet. However with time passing by, the fringes perceptibly shift upwards at $t = 40$ ms. This fringe shift becomes even more pronounced in Figure 4.28(d), and clearly visible at $t = 60$ ms. The most intense fringe indicated by the arrow is just above the red line in Figure 4.28(a), while it was clearly moved upwards at $t = 60$ ms in Figure 4.28(e). As explained before, the fringe shift is relative to the phase shift of the sample laser beam, which is introduced by gas filling into the capillary tube.

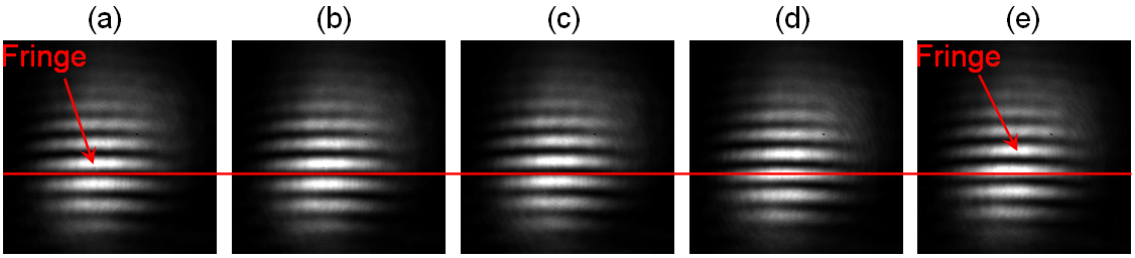

Figure 4.28: *Image sequence of the interference fringes taken at (a) 0, (b) 30 ms, (c) 40 ms, (d) 50 ms, (e) 60 ms. $t = 0$ is the start of the electrical pulse for valve opening. The red line is plotted as a reference position; the fringe shift is clearly visible at $t = 50$ and 60 ms.*

The phase shift $\Delta\psi(t)$ corresponding to the fringe shift is quantified by the method developed by Takeda *et al* [167]. The algorithm is briefly introduced as follows. We especially concentrate on 1D calculation, as the fringes are straight in our case and the fringe shift is perpendicular to the fringe direction. For the image in Figure 4.29(a), the fringe intensity I_f at a given horizontal position x_0 is

$$I_f(x_0, y) = \mathcal{A}(x_0, y) + \mathcal{B}(x_0, y)\cos[\psi(x_0, y)], \tag{4.28}$$

where $\mathcal{A}(x_0, y)$ indicates the background variation, $\mathcal{B}(x_0, y)$ is relative to the local fringe

contrast, and $\psi(x_0, y)$ is the interference phase to be determined. The above equation can be written as

$$I_f(x_0, y) = \mathcal{A}(x_0, y) + \mathcal{C}(x_0, y) + \mathcal{C}^*(x_0, y), \tag{4.29}$$

where $\mathcal{C}(x_0, y) = \frac{1}{2}\mathcal{B}(x_0, y)\exp[i\psi(x_0, y)]$, and $*$ denotes the complex conjugate. Next, Equation 4.29 is Fourier transformed with respect to y, yielding

$$I_f(x_0, \omega) = \mathcal{A}(x_0, \omega) + \mathcal{C}(x_0, \omega - \omega_f) + \mathcal{C}^*(x_0, \omega + \omega_f), \tag{4.30}$$

where ω_f indicates the characteristic spatial frequency of the fringes. Equation 4.30 implies that the three terms $\mathcal{A}$, $\mathcal{C}$, and $\mathcal{C}^*$ are separated in frequency domain. One is able to filter out any of the two terms convolved with ω_f, saying $\mathcal{C}$. Applying inverse Fourier transformation to $\mathcal{C}(x_0, \omega - \omega_f)$, $\mathcal{C}(x_0, y)$ is obtained. Finally, the phase term can be calculated through

$$\psi_d(x_0, y) = \Im\{\ln[\mathcal{C}(x_0, y)]\}, \tag{4.31}$$

where $\Im$ denotes the imaginary part.

As the interference pattern dominated by the cosine function is periodic, the phase $\psi_d(x_0, y)$ given by Equation 4.31 varies within the interval of $[-\pi, \pi]$. However in reality, the phase varies continuously. The discontinuities of numerically calculated phase can be corrected by adding an offset phase $\psi_{off}(x_0, y)$, namely

$$\psi(x_0, y) = \psi_d(x_0, y) + \psi_{off}(x_0, y). \tag{4.32}$$

ψ_{off} is determined by the following consideration. In many experiments, the width of interference fringe is much larger than the pixel size of CCD, so the phase difference between two adjacent points should be much smaller than 2π, that is $|\psi_d(x_0, y_{j+1}) - \psi_d(x_0, y_j)| \ll 2\pi$. When the phase difference is comparable to 2π, say for example $|\psi_d(x_0, y_{j+1}) - \psi_d(x_0, y_j)| > \pi$, the $(j+1)$th phase $\psi_d(x_0, y_{j+1})$ must be compensated by adding $\psi_{off}(x_0, y_{j+1}) = 2m_{j+1}\pi$. m_j is characterized by the sign of phase jump (positive or negative) to be

$$m_j = \begin{cases} 0, & \text{if } j = 1 \\ m_{j-1}, & \text{if } |\psi(x_0, y_j) - \psi(x_0, y_{j-1})| < \pi \\ m_{j-1} + 1, & \text{if } \psi(x_0, y_j) - \psi(x_0, y_{j-1}) < -\pi \\ m_{j-1} - 1, & \text{if } \psi(x_0, y_j) - \psi(x_0, y_{j-1}) > \pi \end{cases} \tag{4.33}$$

Equations 4.32 and 4.33 together allow us to obtain the desired continuous phase term.

Figure 4.29 shows an example of phase retrieving following the above procedure. The first fringe image in Figure 4.28 is reused here. First, we chose a region where the fringe signal is strong and the contrast is high and make a line ($x = 145$ and $y \in [125, 275]$) along the direction of fringe shift, as indicated in Figure 4.29(a). The fringe intensity profile along this line is given in Figure 4.29(b). The intensity profile can be described by Equation 4.28. Applying the procedure of phase computation to this intensity profile, we finally retrieve the corresponding phase distribution plotted in Figure 4.29(c). The obtained phase profile at $t = 0$ is therefore the reference to determine the phase shift at a later time. Also plotted in Figure 4.29(c) is the phase profile determined at $t = 60$ ms. One can immediately see the phase shift (the gray area) between them. The phase shift determined by averaging over the range $y \in [125, 275]$ is $\Delta\psi|_{t=60ms} = (0.65 \pm 0.0087) * 2\pi$, which corresponds to the number of fringe shift $\Delta\psi/(2\pi) = 0.65$. The RMS error of this determination is around 1%.

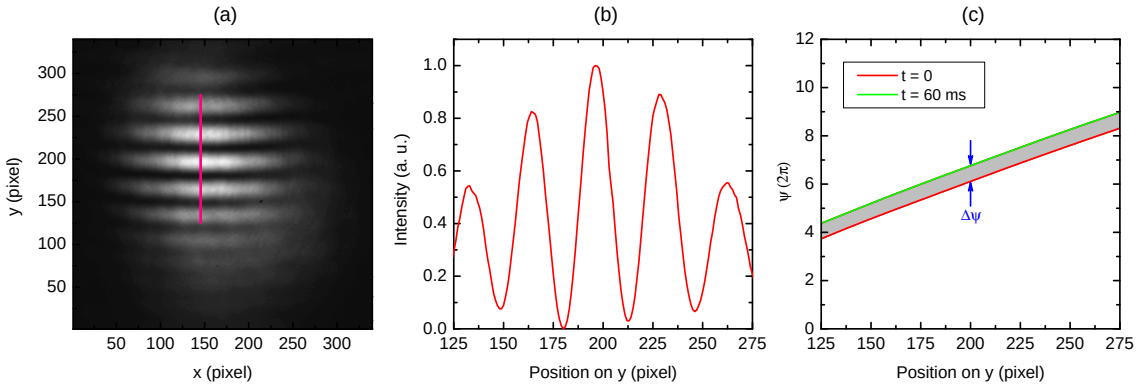

Figure 4.29: *(a) Fringe pattern at $t = 0$ in Figure 4.28. (b) Intensity line-out along the line in (a). (c) The corresponding phase profile of the intensity line-out. Also plotted in (c) is the phase profile of the fringes at $t = 60$ ms shown in Figure 4.28(e).*

The temporal phase shift, displayed in Figure 4.30 is obtained by repeating the above calculation for the hundreds of fringe images taken at different time delays. The gas dynamics during the filling process will be presented together with the measurement using photodiode in the following subsection. For the stationary state ($t = 70 - 170$ ms in Figure 4.30), using Equation 4.27 and the equation of state of ideal gas one can compute the static pressure inside the capillary tube to be 80 ± 3 mbar, corresponding to a gas filling efficiency of $\eta_f \simeq 64\%$.

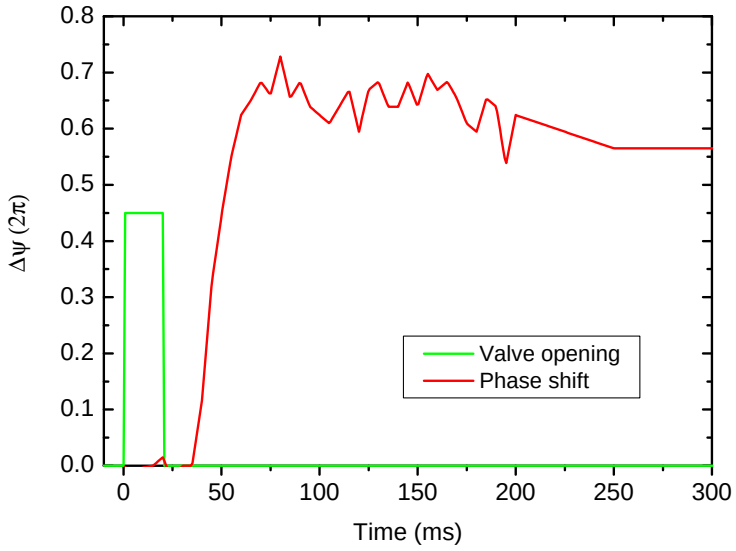

Figure 4.30: *Phase shift induced by argon gas filled into the 102 μm, 20 mm long capillary tube when the reservoir pressure is 125 mbar.*

There are two issues regarding the diagnostic method with CCD camera, which must be carefully treated:

• Direction of fringe shift

In order to obtain the temporal phase shift $\Delta\psi(t)$, one needs to record fringe images with a high sampling frequency in time to know which direction the fringes shift. For example, we can clearly see the fringes shift upwards in Figure 4.28. It is not possible to

determine the phase shift without knowing the shift direction, as both the two directions are possible, whereas they lead to different values of phase shift: $\Delta\psi$ or $2\pi - \Delta\psi$.

• Step of density scan

One important calibration is the relationship between the reservoir pressure and gas density inside the capillary tubes at a given time delay. Nevertheless one should not use a too large step for reservoir pressure scan. As the fringe pattern described by the cosine function (See Equation 4.28) is periodic, the phase shifts $\Delta\psi$ and $2m\pi + \Delta\psi$ will produce exactly the same shifted fringe pattern, and therefore indistinguishable. In this sense, a small step corresponds to phase shift less than 2π shall be used to rule out the other possibilities.

These two arguments require to perform a lot of repeated acquisitions to calibrate one capillary tube, so it becomes considerably time-consuming if we want to explore a large range of capillary parameters and investigate the influence of gas species. In this context, we sought a more efficient method.

Measurement with photodiode

In this section, we present the scheme developed to determine temporal gas density evolution inside capillary tubes using a photodiode. The configuration of this measurement is illustrated in Figure 4.26. A narrow slit is placed in the optical path to select a fraction of the most intense interference fringe. The selected light shines onto a sensitive photodiode whose signal is recorded by oscilloscopes. The temporal variation of the photodiode signal is related to the fringe shift (phase shift), and can be used to infer gas density evolution. The mechanism is described as follows.

The photodiode signal, $S_p(t)$, is proportional to the fraction of light from the interference pattern going through the rectangular aperture. As the aperture is large, diffraction is neglected. The signal is given by

$$S_p(t) = \alpha_{ph} \iint_{\Omega_p} I_f(x, y, t) H(x, y)\, dx\, dy, \tag{4.34}$$

where α_{ph} is a constant associated to the photodiode responsivity to the 633 nm laser beam, and Ω_p is the surface of the photodiode; $I_f(x, y, t)$ is the intensity of the interference pattern, x and y are the coordinates in the plane transverse to the beam propagation, and $H(x, y)$ is the 2D Heaviside function describing the rectangular aperture. The interference pattern can be written as

$$I_f(x, y, t) = I_1(x, y) + I_2(x, y) + 2\sqrt{I_1(x, y) I_2(x, y)} \times \cos[\Delta\psi_0(x, y) + \Delta\psi(t)], \tag{4.35}$$

where $I_1(x, y)$, $I_2(x, y)$ are the transverse distributions of energy of the two beams exiting the interferometer; $\Delta\psi_0(x, y)$ is the initial phase difference, and $\Delta\psi(t)$ is the phase shift to be measured. Substituting Equation 4.35 into Equation 4.34 (See the derivation in Appendix A.4), the photodiode signal as a function of time can be reformed as

$$S_p(t) = \mathcal{A} + \mathcal{B} \cos[\theta_0 + \Delta\psi(t)], \tag{4.36}$$

where $\mathcal{A}$, $\mathcal{B}$, and θ_0 are coefficients determined by the aperture size and the energy distribution of each beam in the transverse plane. The phase term of above equation may be extracted by defining the normalized signal $S_N(t)$ as

$$S_N(t) = \frac{S_p(t) - \min(S_p)}{\max(S_p) - \min(S_p)} = \frac{1 + \cos[\theta_0 + \Delta\psi(t)]}{2}, \tag{4.37}$$

and inversing the cosine function

$$\Delta\psi_d(t) = \arccos[2S_N(t) - 1] - \arccos[2S_N(0) - 1], \tag{4.38}$$

where $S_N(0)$ is the initial photodiode signal in vacuum before valve opening. The phase shift obtained from Equation 4.38 oscillates inside the interval $[0, \pi]$, which is not physically true but just owing to the definition of the inverse cosine function. Likewise, the discontinuities of the phase $\Delta\psi_d$ are corrected by adding an offset phase $\Delta\psi_{off}$. The determination of $\Delta\psi_{off}$ is explained as follows.

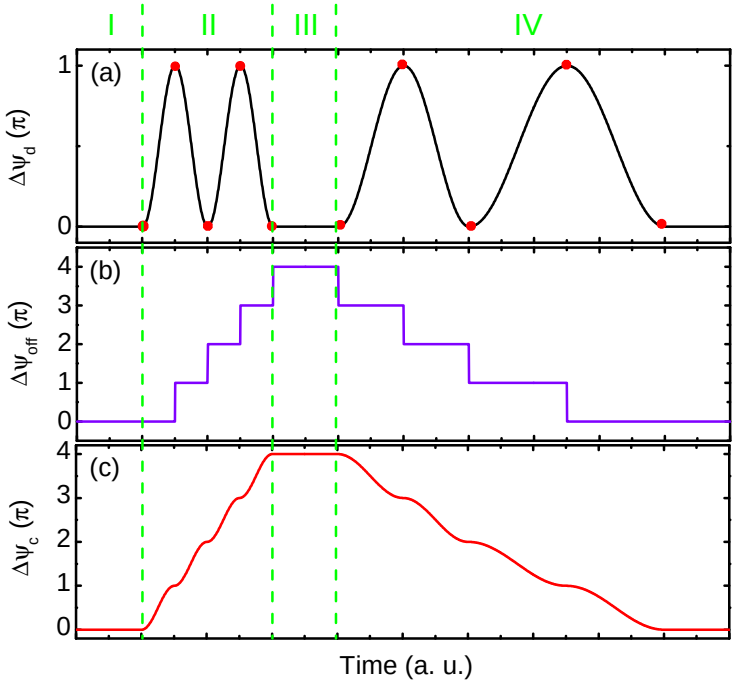

Figure 4.31: *(a) Example of the discontinuous phase evolution in time calculated from Equation 4.38, where the red dots mark stationary points. (b) Offset phase distribution corresponding to (a). (c) The corrected continuous phase evolution. The four parts of gas filling are separated by the dashed lines and indicated on the top.*

Figure 4.31(a) shows the typical behavior of the phase distribution $\Delta\psi_d(t)$ calculated using Equation 4.38 from a measured photodiode signal. The phase evolution can be fully determined by taking into account the time sequence for filling gas into the capillary tube, which can be schematically separated into four parts: part I is the initial state in vacuum, where the phase shift is equal to zero; part II is the time interval when gas is continuously filling the tube, and the phase shift is assumed to be continuously increasing; part III is the time interval when a stationary state is reached inside the tube, and the phase shift is constant; part IV is the time interval when gas leaks into the vacuum chamber through the capillary tube ends, producing a decrease of the average pressure inside the tube, and the phase shift is assumed to decrease continuously. The slope of the phase shift in time is thus determined using these physical assumptions. $\Delta\psi_{off}(t)$ [see Figure 4.31(b)] between two stationary points of the discontinuous distribution is determined by adding (subtracting) π if the two stationary points are located before (respectively, after) the stationary state. Finally, the continuous phase evolution is retrieved by adding the local phase variation to

the phase offset as

$$\Delta\psi(t) = \Delta\psi_{off}(t) + \begin{cases} |\Delta\psi_d(t) - \Delta\psi_d(\tau_i)|, & \text{if } \tau_i < t \leq \tau_{i+1} \\ |\Delta\psi_d(t) - \Delta\psi_d(\tau_{j+1})|, & \text{if } \tau_j < t \leq \tau_{j+1} \end{cases} \tag{4.39}$$

where τ_i (τ_j) is the time of the ith (jth) stationary point before (after) the stable state. Once the phase is properly corrected by this procedure, one can obtain the variation of the integrated gas density through Equation 4.27.

One important issue for using the photodiode is the slit width. On one hand, the slit should be as large as possible to select more laser energy in order to reach a high signal/noise ratio, whereas on the contrary the contrast of signal will decrease with slit width increasing. So there is an optimal width of a given setup. Figure 4.32(a) shows a

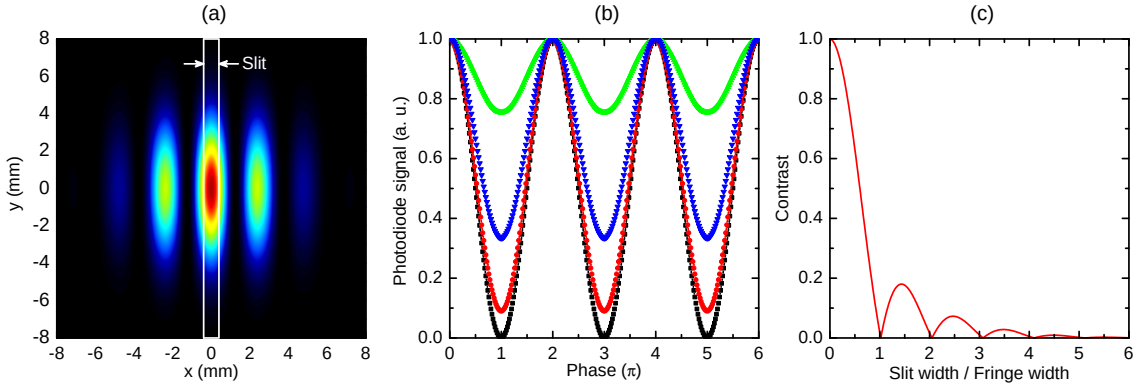

Figure 4.32: *(a)Interference fringe calculated using two Gaussian beams with waist of 2 mm and a cross angle of 0.7 mrad. The two vertical lines indicate the size of the rectangular aperture chosen to select spatially the part of the signal sent to the photodiode. (b) Photodiode signal as a function of phase shift in time for an aperture width of 0.1 mm (blue star), 0.3 mm (green triangle), 0.6 mm (red spot), and 0.8 mm (black square). The curves are normalized to their respective maxima. (c) Signal contrast as a function of slit width for the fringe pattern in (a).*

fringe pattern calculated with two Gaussian beams with waists of 2 mm and a cross angle of 0.7 mrad. The two vertical lines indicate the slit. Displayed in Figure 4.32(b) are the photodiode signal as a function of the phase shift for different aperture widths. It shows that increasing the width of the aperture lowers the contrast of the photodiode signal, defined as

$$C_{ph} = \frac{\max(S_p) - \min(S_p)}{\max(S_p) + \min(S_p)}. \tag{4.40}$$

Because fringe pattern is periodic, the contrast oscillates with slit width as well. However it is obvious that the general trend of contrast is dropping. Especially when the slit width is an integral of fringe width, the contrast becomes zero. In that case, no matter how the fringe shifts, the photodiode signal does not change at all. Taking this into account, the optimal opening size should be a compromise between signal contrast and signal/noise ratio. Typically in our experiment, the width of the aperture was selected to be 0.3 mm, about one third the fringe period, corresponding to a contrast of 0.8. In this case, the noise to signal ratio was measured to be around 5%. Using a larger aperture did not significantly reduce the noise/signal ratio, whereas it degraded the contrast considerably.

Figure 4.33 exhibits the phase shift deduced by the diagnostics using the photodiode and the CCD camera. The experimental conditions are the same as for Figure 4.30. As

shown, the two measurements agree very well with each other, which suggests using the photodiode is a reliable scheme to measure gas density. The main advantage of using a photodiode is that the temporal evolution of gas density can be obtained with a single rather than hundreds of repeated gas filling sequence in the case of CCD camera measurement [149]. The other advantage is that the time resolution is better for the measurement of photodiode. In Figure 4.33, one can clearly see the density fluctuations for $t > 80$ ms. These fluctuations are due to gas oscillation between the reservoir and capillary housing as explained in Ref. [164], however these oscillations were not resolved when the CCD camera was employed owing to a relatively large time step.

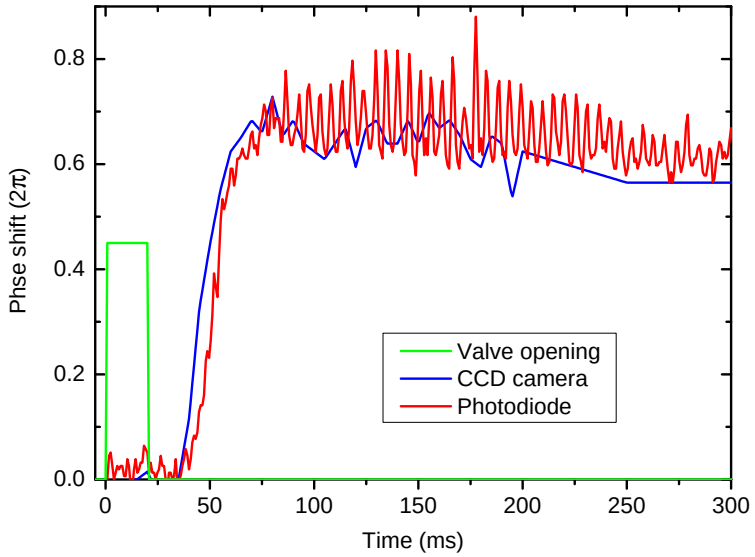

Figure 4.33: *Comparison of the measurements using the CCD camera and photodiode. The parameters are the same as for Figure 4.30.*

Characterization of hydrogen gas filling process

In this section, we present the results for characterizing the filling process of hydrogen gas, as hydrogen gas is usually used in our laser-plasma interaction experiments. Figure 4.34 shows a typical measurement of the phase shift induced by hydrogen gas. The capillary tube was 30 mm long with a diameter of 178 μm. The valve opening was 27 ms and the reservoir pressure was 500 mbar. Two oscilloscopes were used with sampling frequencies of 10 kHz and 100 Hz in order to analyse the detailed dynamics of gas filling [Figure 4.34(a)] and the overall evolution of gas density [Figure 4.34(b)]. The phase shift was calculated using the method described in the preceding subsection.

The photodiode signal in Figure 4.34 is constant from the gate opening time until 24 ms, then drops down and oscillates quickly between 0 and 10 V before reaching a spiky regime over a 100 ms scale. The corresponding dynamics of gas evolution can be interpreted as follows. Once the valve is opened, gas starts filling the 4.5 mm diameter, $\sim$ 110 cm long metallic pipe connecting the reservoir to the capillary tube. At around $t \simeq 26$ ms, a fast variation of the photodiode signal occurs owing to gas filling the capillary tube. The gas density in the capillary tube quickly increases and reaches a maximum at about $t \simeq 34$ ms. The fluctuations of gas density after $t > 40$ ms can be attributed to a small oscillation of the hydrogen gas flow between the valve and the capillary housing, inducing gas instability in the capillary tube. The time for a density fluctuation to make a

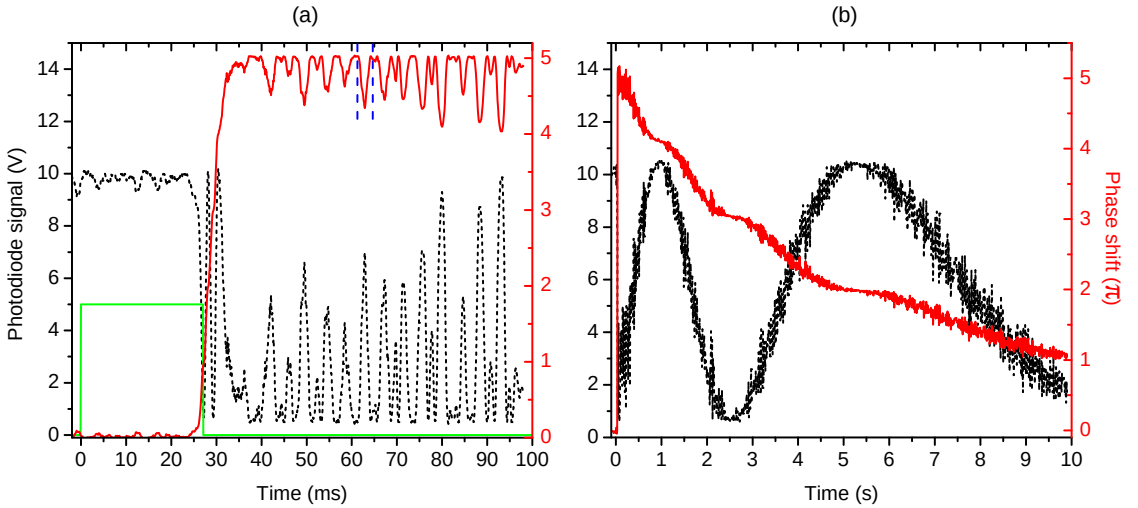

Figure 4.34: *Measured photodiode signal (black dotted curve, left hand axis) and the corresponding calculated phase shift (red solid curve, right hand axis) as a function of time for two different time scales in (a) and (b); the electrical gate for valve opening (green line) is set as $t = 0 - 27$ ms. The two blue dashed lines in (a) highlight one oscillation with period of 2.3 ms.*

round trip between these two points is estimated to be $2L_f/v_{H_2} \simeq 2.2$ ms, where $L_f \simeq 1.4$ m is the whole length of the filling pipe with connectors, and v_{H_2} the speed of sound of hydrogen (about 1.3 km/s). The typical period of the oscillation in Figure 4.34(a) for $t \geq 40$ ms is 2.3 ms, which is consistent with the period of 2.2 ms for gas oscillation. After this rapid filling process, the gas density slowly drops over the time scale of second as seen in Figure 4.34(b), corresponding to the leaking of the gas filling the metallic pipe into the vacuum chamber through the two small capillary exits (178 μm diameter holes). The largest time range that the oscilloscope can cover is up to $t = 10$ s, when there is still a phase shift of $\Delta\psi(t = 10s) \simeq \pi$. Real-time observation shows that the photodiode signal returns to its initial value at $t > 15$ s. This characteristic time scale of phase returning confirms that the spikes with ms time scale in Figure 4.34(a) during the stationary state are not associated to phase returning.

Furthermore, the leaking process can be estimated theoretically. As discussed before, the gas flow is sonic at the capillary exits. The choked sonic gas flow is given by [155]

$$\mathcal{F} = \kappa_g^2 \left(\frac{2}{\kappa_g + 1}\right)^{(1/2)(\kappa_g+1)/(\kappa_g-1)} \rho\Omega_s (R_g T)^{1/2}, \tag{4.41}$$

where κ_g is the heat capacity ratio, $\Omega_s = \pi R_{cap}^2$ denotes the exit area, $R_g = 8.31$ J/K/mol is the gas constant. For hydrogen gas, $\kappa_g = 1.4$ and $R_g = 287$, so Equation 4.41 can be simplified to be

$$\mathcal{F} = 0.6847\rho\Omega_s (R_g T)^{1/2}. \tag{4.42}$$

Supposing the total gas particle number is N, gas flow is correlative to the variation of the total gas particle number through $dN = -\int 2\mathcal{F}\ dt$. The factor of 2 is due to the fact that there are two capillary exits. The total gas particle number can be furthermore approximated by $N = \rho V$, where V stands for the whole volume of the filling pipe upstream

the capillary hosing. Then one can obtain the evolution of gas density in the pipe via

$$\frac{d\rho}{dt} = -2\frac{\mathcal{F}}{V} = -2\underbrace{\frac{0.6847\Omega_s(R_gT)^{1/2}}{V}}_{\mathcal{A}}\rho \equiv -2\mathcal{A}\rho. \tag{4.43}$$

Integrating the above equation yields the evolution of gas density

$$\rho(t) = \rho_0 e^{-2\mathcal{A}t}, \tag{4.44}$$

where ρ_0 is the initial gas density inside pipe before dropping. We can define the characteristic time $\Delta\tau$ when the gas density decreases to $1/e$ of the initial value, namely $\rho(t = \Delta\tau) = \rho_0/e$. Using Equation 4.44, $\Delta\tau$ is given by

$$\Delta\tau = \frac{1}{2\mathcal{A}}. \tag{4.45}$$

In our case, the capillary diameter is 178 μm, $T = 293$ K, and $V \simeq 2\times10^{-4}$ m^3, yielding $\mathcal{A} \simeq 0.025$, which yields $\Delta\tau = 20$ s. It is reasonably consistent with the experimental observation. The rather long characteristic time of gas leakage is an important issue in experiments, which greatly limits the repetition rate of operation. For example, during the campaign at the Lund Laser Centre time interval of 40 s between two consecutive shots was used for data acquisition. One can find that $\Delta\tau$ is proportional to V, which implies decreasing the volume of filling pipe can shorten the time of gas leaking. In our setup, the main problem is that the solenoid valve for gas injection has to be placed outside the vacuum chamber owing to heating-up during operation. Using a vacuum compatible valve could be a good improvement in future.

The temporal evolution of the phase shift in the 178 μm diameter, 30 mm long capillary tube for different reservoir pressures when the duration of valve opening is fixed to 27 ms is shown in Figure 4.35(a), and in Figure 4.35(b) for a fixed reservoir pressure of 500 mbar and different values of the valve opening duration. In the range of pressure explored, a stationary state is established at about $t \simeq 34$ ms, indicated by the dashed lines in Figures 4.35(a)-(b). For a fixed pressure, the increase of the duration of valve opening does not change the phase shift behavior, showing that 27 ms is longer than the characteristic time necessary to reach a stationary state. In order to quantify the plateau gas density inside the capillary tube at the stationary state, a 2D FLUENT simulation was carried out to obtain the gas density profile [164]. The plateau gas densities calculated for the curves of Figure 4.35(a) are shown in Figure 4.35(c), which increase linearly with the reservoir pressure.

The highest gas density achieved in the capillary tube is $10 \pm 0.4 \times 10^{18}$ cm^{-3} for 500 mbar in the reservoir. Noting that a pressure of 500 mbar corresponds theoretically to a gas density of $\rho_0 = 12.35 \times 10^{18}$ cm^{-3} at 20 °C, the gas density achieved experimentally in the capillary tube corresponds to $81 \pm 3\%$ of the one in the reservoir. This observation can be explained by gas expansion when the valve is opened: the reservoir has a volume of about 176 cm^3, and the total volume, including pipe, connectors, and capillary housing, increases at valve opening to approximately 198 cm^3. Consequently the gas density is expected to drop down to $(176/198)\rho_0 \simeq 89\%\rho_0$. The losses due to gas leaking from the capillary tube itself can account for the measured value of $(81 \pm 3\%)\rho_0$. For a fixed reservoir pressure [500 mbar for Figure 4.35(b) and (d)], when the valve opening duration is increased beyond 27 ms, the gas density in the capillary tube does not increase further. It means that for our setup the filling process is saturated even for the shortest valve opening duration (27 ms). This information is of interest to minimize the opening duration of the

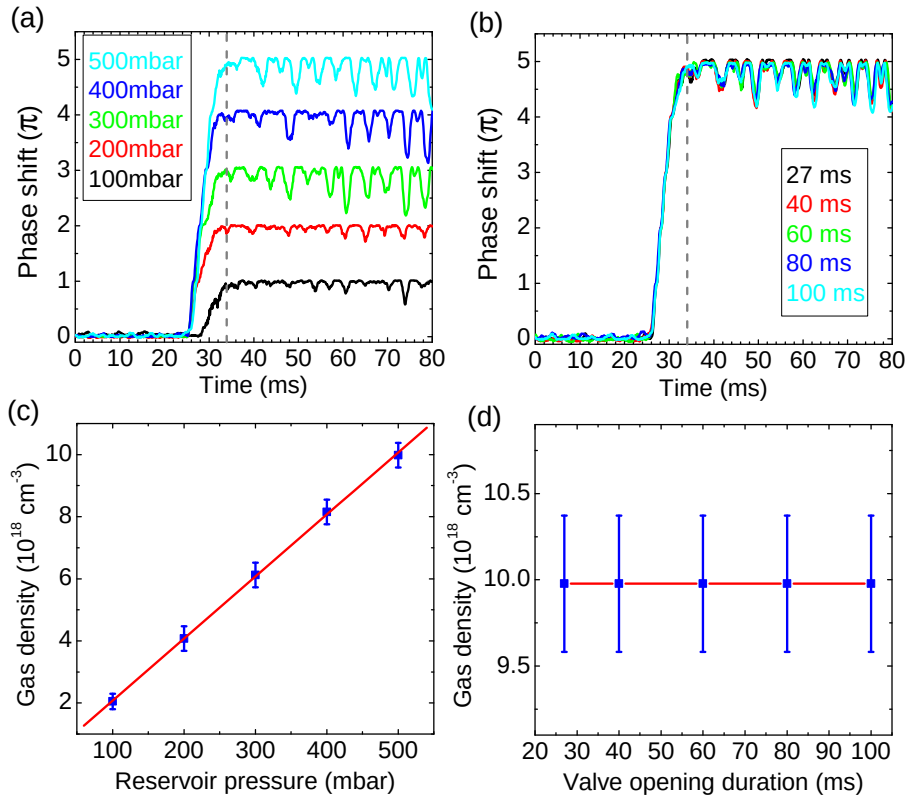

Figure 4.35: *Phase shift as a function of time for different values of (a) reservoir pressure and a valve opening duration of 27ms, and (b) duration of valve opening and a reservoir pressure of 500mbar. (c) and (d) show plateau densities of gas at $t = 34$ ms obtained from (a) and (b), respectively. Error bars indicate the standard deviations of fluctuations of gas density in the stationary state ($t = 34 - 80$ ms).*

valve and avoid unnecessary gas leakage into the vacuum chamber. It should be noted that the gas density in the capillary tube can be increased for a given reservoir pressure by using a larger slit as shown in simulations [45]. However in the case of capillary tubes, the slit size should be kept as small as possible to avoid discontinuities of laser reflection at the capillary wall.

A systematic study was conducted to investigate the influences of capillary diameter on the gas filling process. To accomplish this parameter scan in a reasonable time scale, we specially looked into the capillary diameter range of $127-203$ μm, which is typically used in the laser-plasma acceleration experiments. We compared the filling processes of two different gases, hydrogen and argon, to study the role of gas species. Figure 4.36 presents the results of four 20 mm long capillary tubes with different diameters. For a fixed duration of valve opening of 27 ms, as seen before, the hydrogen gas density (or static pressure) at the stationary state linearly increases with reservoir pressure in the range of $100 - 500$ mbar. There is no significant difference between the four diameter cases. This finding probably because all these capillary diameters explored are smaller than the slit size of about 270 μm. In this case, the evolution of gas inside the capillary tubes is dominated by the inflow from the slit even though a larger diameter results in higher outflow. For a given reservoir pressure of 500 mbar, the effects of valve opening, varying from 27 to 100 ms, was examined as well. As demonstrated above, filling of hydrogen gas already becomes saturated for the shortest duration of 27 ms. Nevertheless, valve opening has

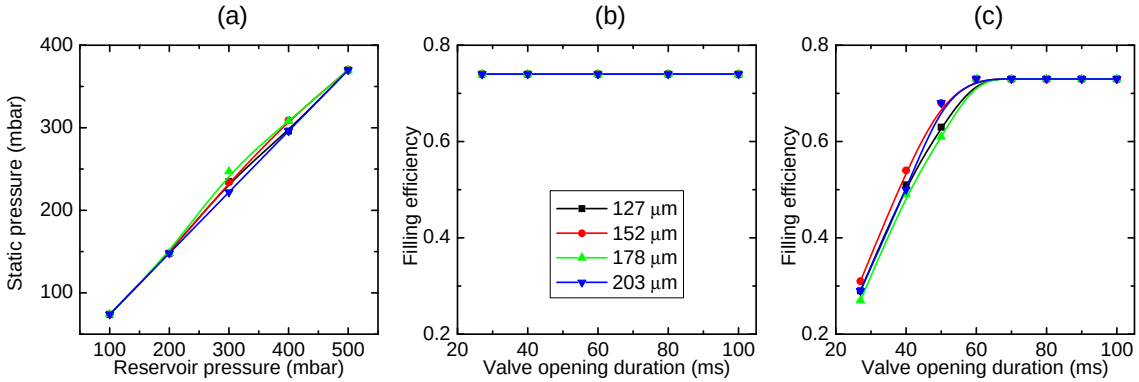

Figure 4.36: *(a) Static pressure of hydrogen gas filled into the capillary tubes with different diameters; filling efficiencies as a function of valve opening duration for (b) hydrogen gas and (c) argon gas at a reservoir pressure of 500 mbar.*

a strong influence on the filling efficiency of argon gas, as shown in Figure 4.36(c). The four filling efficiencies increase rapidly with the duration of valve opening, and become saturated when the duration of valve opening is in excess of 60 ms. Owing to a higher molecular mass, argon gas moves more slowly than hydrogen gas, so a longer duration of valve opening is required to fill argon gas into a capillary tube. It is noticeable that the filling efficiency tends to be the same for the two gases as long as the valve is opened longer than 60 ms.

4.7 Single-slit capillary tube

In this section, we introduce a special kind of capillary tube with only one slit, which is designed to produce a tapered plasma density profile inside the capillary tube. Both downramp and upramp density profiles are extensively investigated to control electron self-trapping or to extend the acceleration distance to achieve higher electron energy [168, 169, 170, 171, 172]. Downramp means plasma density decreases along the laser propagation direction, while upramp denotes the opposite. The concepts of using these density ramps are briefly introduced as follows.

Downramp was proposed to facilitate electron-trapping via slowing down the phase velocity of plasma wave [168]. As demonstrated in Chapter 2, self-trapping requires the velocity of electron in excess of the phase velocity of plasma wave, that is $v_e \geq v_p$, to ensure the electron is able to catch the plasma wave. A rigorous expression of the phase velocity of plasma wave is given by [21]

$$\beta_p = \frac{\beta_g}{1 + \frac{\xi}{\lambda_p}\frac{d\lambda_p}{dz}}, \tag{4.46}$$

where ξ is the coordinate in the laser frame, and z is the direction of laser propagation. The term $\lambda_p^{-1} d\lambda_p/dz$ can be expressed as a function of plasma density to be $\frac{1}{2} d \ln \rho_e/dz$. In the case of downramp, namely $d\rho_e/dz < 0$, the phase velocity is lowered in the region behind the laser owing to $\xi < 0$. Therefore the initial electron energy required for electron self-trapping is reduced accordingly.

On the other hand, density upramp was put forward to overcome the limit of electron dephasing [171]. In an uniform plasma, the accelerated electron slips forward with respect to the driving laser, and finally enters the decelerating phase region. When there is a

positive density gradient, the driving laser encounters higher density as it moves forward, during which the plasma wavelength is decreasing. As a consequence, the node of plasma wave phase change (from accelerating to decelerating) shifts towards the driving laser as well. In an ideal density tailoring, the speed of phase node shift is equal to that of electron slippage, so the electron could be "locked" in accelerating phase till the laser is depleted. Therefore higher electron energy can be obtained than in an uniform plasma.

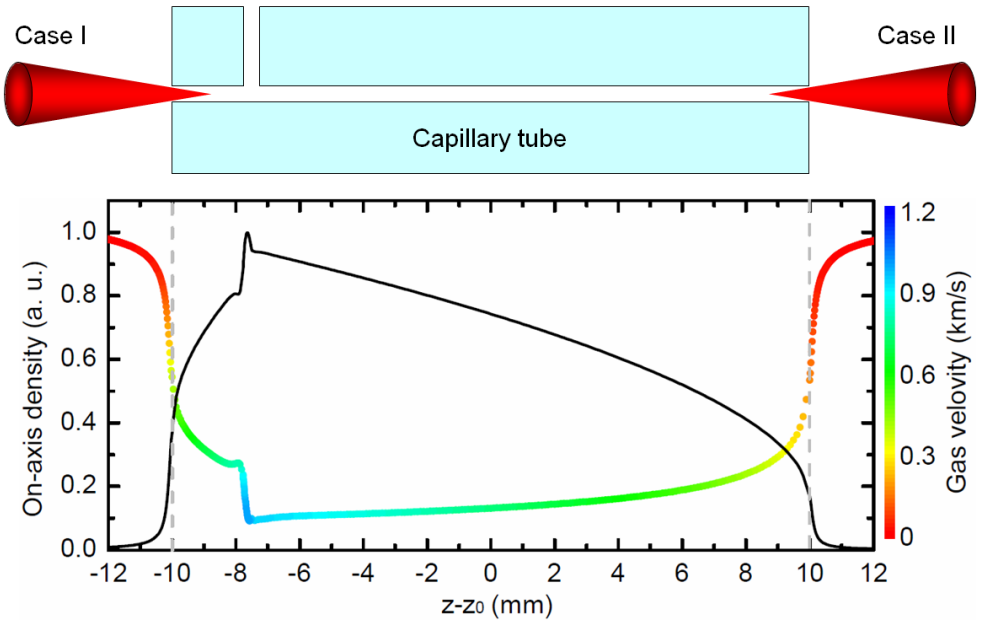

Figure 4.37: *On-axis gas density and velocity inside a single-slit capillary tube obtained with FLUENT simulation. The two dashed lines represent the capillary ends. Case I and II indicate two different directions of laser coupling, which correspond to downramp or upramp of plasma density along the laser propagation path.*

The previous studies concerning density tapering were carried out using gas jet or plasma waveguide [169, 170]. We are therefore motivated to generate those density ramps inside the capillary tubes to investigate if there is an enhancement of laser tapered-plasma interaction by capillary guiding. The gas distributions were obtained with FLUENT simulations. The capillary tube is 20 mm long, 178 μm in diameter, as illustrated in Figure 4.37. There is only one slit of 270 μm located at 2.5 mm from the left capillary end. $\varkappa-\epsilon$ turbulence model was employed to simulate at the stationary state. Line-outs of on-axis gas density and velocity are shown in Figure 4.37.

As seen in Figure 4.37, there are two density ramps beside the slit. In case I, the laser propagates from the left-hand side. The laser mainly experiences a density downramp. One may note that there is also an undesired upramp between the slit and the capillary left-hand end. This upramp can be minimized by shifting the slit as closely as possible to the capillary end. However, the distance of 2.5 mm could not be shortened in our present capillary holder design. If the laser propagates from the right-hand side as shown by case II in Figure 4.37, it sees a density upramp. An important issue for upramp is that the plasma density becomes low at the entrance part of capillary tube, so it requires a powerful laser to launch electron self-trapping [107], and then the trapped electrons can be phase-locked in the plasma wave. It is worth mentioning that the density gradient can be changed by varying the capillary length. This point is interesting for controlling electron self-trapping for the case of density downramp, since localized electron trapping happens

only if $k_p L_\downarrow < 1$ [168]. $L_\downarrow$ represents the characteristic length of the density transition. One may find in Figure 4.37 that the gas is not immobile inside the single-slit capillary tube, which is different from the case of two-slit capillary tube (See Figure 4.12). The moving gas might worsen the stability of laser-plasma interaction, as the stable shock-free gas flow was found significantly beneficial for improving electron stability [45].

Both the downramp and upramp density profiles inside single-slit capillary tubes were examined during our second campaign on laser electron acceleration at the Lund Laser Centre (LLC). More details will be reported in our future publications.

4.8 Summary

The fundamental EH_{11} mode of capillary tube is ideal for laser guiding owing to its smooth traverse field distribution and long attenuation length. The efficiency of laser coupling to the capillary tube depends on the laser spot size compared to the tube radius R_{cap}. For a Gaussian spot with waist w_0, about 98% of the laser energy can be coupled to the fundamental mode when $w_0 \simeq 0.65 R_{cap}$, while for an Airy spot with radius at the first minimum $r_0 \simeq R_{cap}$, the coupling efficiency reaches 83%.

Spatial distribution of gas inside the capillary tubes was characterized using fluid simulations at the stationary state. It shows a stable, uniform gas medium is achieved between the two capillary slits, beside which there are two density ramps extending out of the capillary ends. A theoretical estimation suggests the on-axis gas density drops as $\rho_{H_2} \propto (R_{cap} + Z)^{-2}$ when the gas expands in the vacuum chamber, where R_{cap} and Z denote the capillary tube radius and the distance from the capillary exit. The evolution of gas density inside the capillary tubes was determined using a scheme based on the Mach-Zehnder interferometer [164]. For a 30 mm long, 178 μm capillary tube, hydrogen gas reached the stationary states 34 ms later than the start of valve opening. Owing to gas leakage from the capillary holes during the filling process, the gas density achieved in the tube at the stationary state corresponds to $81 \pm 3\%$ of the one in the reservoir. It was found that the filling efficiency does not significantly depends on the capillary diameter, as long as the slit width (~ 270 μm) is larger than the capillary diameter. Another important result is that the filling efficiency of hydrogen gas does not increase with the duration of valve opening for the reservoir pressure range of 50-500 mbar, which implies the filling process has been saturated for the shortest opening duration (27 ms) that can be used for the solenoid valve. As the valve controlling gas injection has to be placed outside the vacuum chamber, a $\sim$ 1 m long filling pipe was employed in our setup, which results in a long characteristic decay time of the order of $\sim$ 10 s for gas leaking from the capillary tube to the vacuum chamber. This essentially limits the repetition rate of the operation, which can be significantly decreased by using a vacuum-compatible valve to shorten the gas filling pipe.

Chapter 5

Experimental methods

This chapter shows the main instruments and methods employed during our experiments on laser wakefield electron acceleration and X-ray production. The multi-terawatt laser facility at the Lund Laser Centre is first introduced, including two important techniques: focal spot correction and laser pointing stabilization. Then we present the designs of the motorized target housing system. The experimental setups of the electron spectrometer and X-ray detectors employed for the two campaigns at the LLC are described along with the corresponding diagnostic methods.

5.1 High power laser system

5.1.1 Chirped pulse amplification technology

To achieve relativistic laser-plasma interaction, high intensity lasers are required. In this section, we briefly introduce the chirped pulse amplification (CPA) technology, relying on which the current state-of-the-art multi-terawatt lasers are built. The concept of CPA was proposed in the 1980s [173], which is one of the most important evolutions for intense laser development. Before it, the peak power of pulsed laser was restricted to GW scale by damage to the gain medium owing to nonlinear optics such as self-focusing, laser filament, and so forth. The CPA technique however cleverly overcomes these issues.

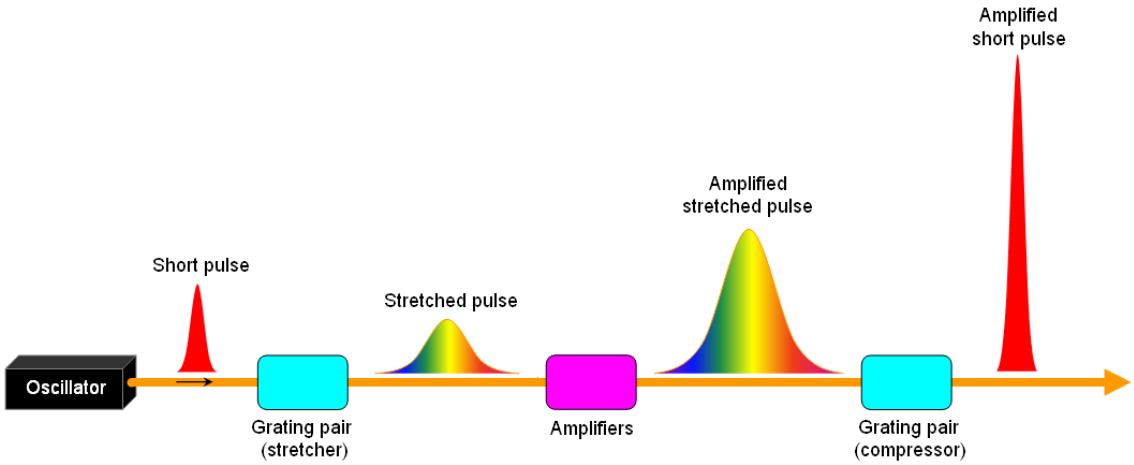

Figure 5.1: *Schematic diagram of a chirped-pulse amplified laser.*

Figure 5.1 schematically illustrates the scheme of the CPA technique. The ultra-

short laser pulse with duration on the femtosecond scale produced by an oscillator is first stretched out in time using a grating pair (termed as "stretcher"). After that, the laser pulse becomes positively or negatively chirped, and meanwhile the pulse duration is extended to time scale of picosecond. Accordingly, the peak power of the stretched pulse becomes much lower than the short pulse from the oscillator, so it is safe to amplify such a beam within the limit of gain medium as much as possible. After amplifying, the laser beam is sent to another grating pair with negative dispersion (referred to as "compressor") to remove the chirp, temporally compressing the pulse. In this case, the final amplified short pulse possesses extremely high peak power ranging from tens of terawatt to petawatt class. When such a power laser is focused, the peak intensity at focus can reach as high as 10^{21} W/cm^2.

5.1.2 Multi-terawatt laser facility at the Lund Laser Centre

The experiments throughout this thesis were carried out using the femtosecond multi-terawatt laser facility at the Lund Laser Centre (LLC) in Sweden, which is a high power laser system based on the CPA technology [173]. The laser installation is schematically illustrated in Figure 5.2 and briefly described as follows.

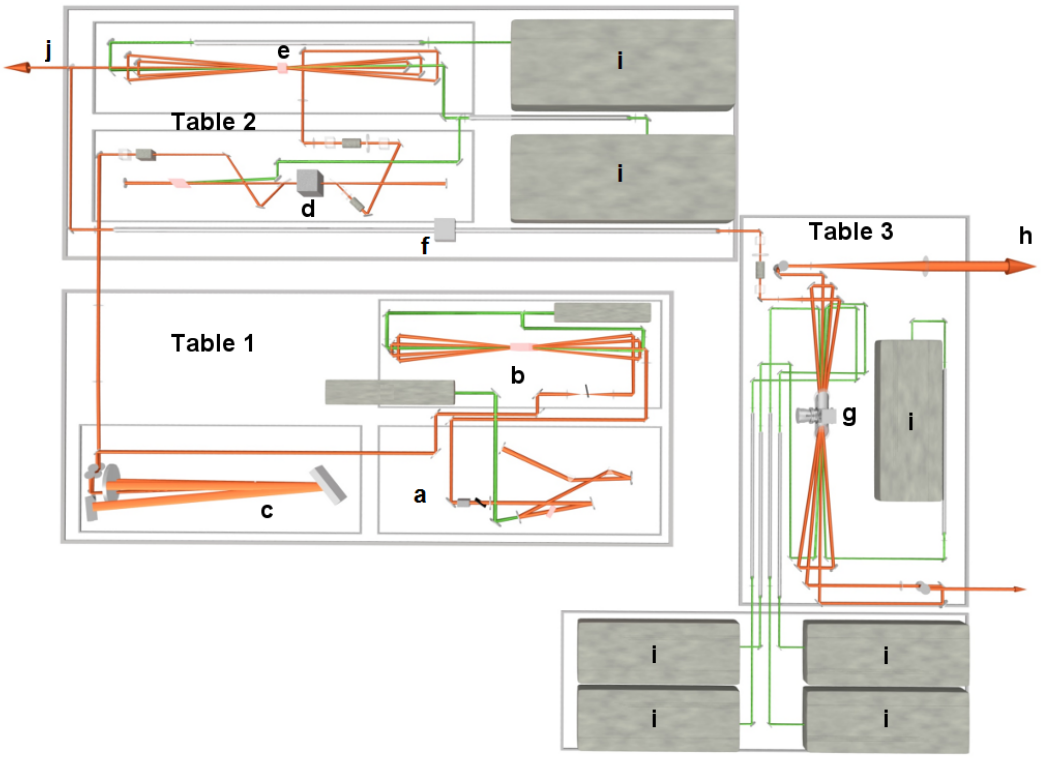

Figure 5.2: *Schematic arrangement of the LLC multi-terawatt laser. The elements are respectively: a) mode-locked oscillator, b) pre-amplifier, c) stretcher, d) regenerative amplifier, e) multi-pass amplifier, f) spatial filter, g) second multi-pass amplifier, h) the stretched amplified main beam to the compressor (not shown), i) Nd:YAG pump lasers, j) beam part for high order harmonic study.*

The front end is a titanium-doped sapphire (Ti:sapphire) Kerr lens mode-locked oscillator [174], and produces 80 MHz laser pulses with energy of ∼nJ. Ti:sapphire is especially

suitable for ultrashort laser pulse generation owing to its relatively large spectral bandwidth ($\sim$ 50 nm) [175]. It operates most efficiently at a central wavelength around 800 nm. Using a Pockels cell together with a polarizer, ten pulses per second are selected from the pulse train generated by the oscillator. Before amplifying, the 10 Hz laser pulses pass through a pre-amplifier ended with a saturable absorber to improve laser temporal contrast. Immediately after that, the laser is sent to a stretcher where its duration increases up to approximately 300 ps. The stretched pulse is consecutively amplified through three stages. The first is a regenerative amplifier [176], in which the laser makes 15 round trips within the closed cavity, and then it enters the first five-pass amplifier [177], reaching energy of 300 mJ. 200 mJ of that is taken by another experiment (indicated by j in Figure 5.2). The other 100 mJ is further amplified by a second four-pass stage using cryogenically cooled Ti:sapphire crystal. All the amplifiers are pumped by 10 Hz frequency-doubled Q-switched Nd:YAG lasers. After full amplification, the laser energy can reach 2 J before compression. The amplified laser pulse is compressed down to $\sim$ 40 fs (FWHM duration). Typically, 1 J laser energy can be delivered on target.

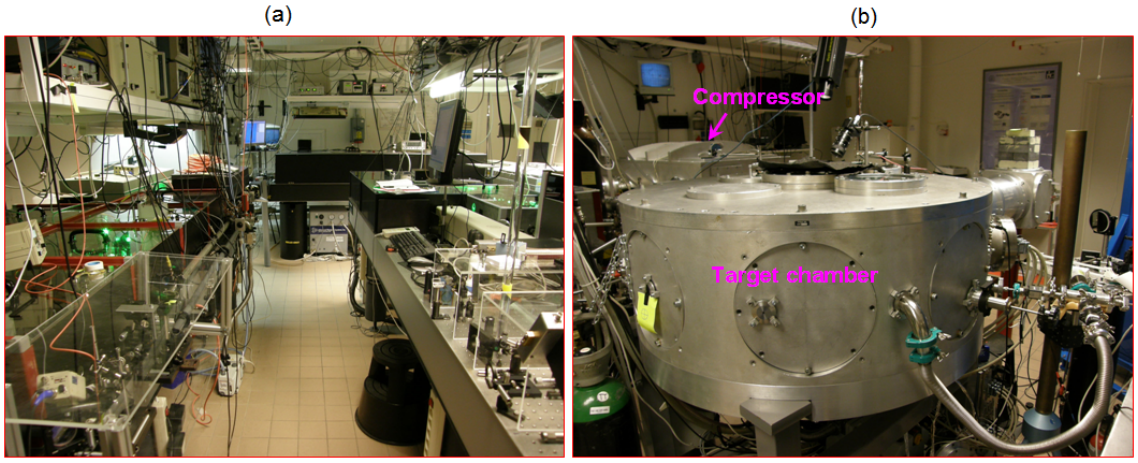

Figure 5.3: *Photographs of (a) the laser room and (b) the target area at the LLC. The gas filling system, extension tube for parabolic mirror, and diagnostics around the target chamber can be seen as well.*

Figure 5.3(a) is a photograph of the LLC laser room. All the optical components are arranged on three tables as illustrated in Figure 5.2. The amplified laser beam is then sent to the compressor located in the target room [Figure 5.3(b)], where most of the experiments were performed.

Focal spot correction

Among the properties characterizing laser performance, focal spot shape and pointing stability are essential in the case of capillary tubes, as demonstrated in Chapter 4. Many efforts have been put at the LLC to address these two issues via adaptive optics and pointing stabilization technique. Owing to their importance for our experiment, we will briefly introduce these two schemes here. More details can be found in [62, 76].

In a large high power laser system, wavefront aberrations are introduced into the laser beam by such as misalignments of components in the optical chain, misalignment of the focusing mirror, thermal effects, and so on. When such an aberrated beam is focused, the focal spot is far from the ideal case of an Airy distribution. Therefore, adaptive optics is

adopted to correct the focal spot by compensating the deformation. The goal is to control the wavefront shape and achieve a symmetrical and close to diffraction-limited focal spot in the far-field.

The system mainly consists of a deformable mirror and a wavefront sensor. The deformable mirror is composed of piezoelectric ceramics and actuators. When a voltage is applied to the actuators, they locally deform the ceramics and furthermore the output wavefront. The deformable mirror is placed directly after the compressor. The wavefront is measured after the focusing mirror using a specially-designed sensor based on a four-wave shearing interferometer. In this case, any aberration upstream the focal plane can be taken into account. The detected wavefront is decomposed using the series of Zernike polynomials (See the patterns in Appendix A.5) to find the applied voltage pattern for the actuators. There is a feedback loop between the wavefront sensor and the deformable mirror to shape the beam wavefront. Normally, a satisfying corrected wavefront could be obtained after only a few iterations.

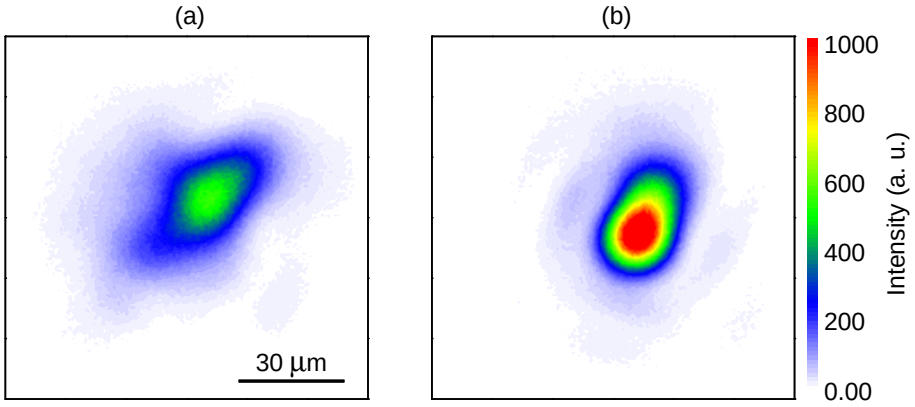

Figure 5.4: *Focal spot of fully amplified laser pulse measured (a) without and (b) with correction during the second campaign at the LLC. Increase of laser intensity is clearly visible when the beam is corrected.*

Shown in Figure 5.4 are the focal spots of the fully amplified laser pulse (700 mJ on target) with or without correction by the deformable mirror. The focusing optics was a 14° off-axis $f = 76$ cm parabolic mirror. The images were taken with a 12 bit CCD camera when the laser was properly attenuated. One can immediately see that the laser peak intensity increases significantly when the wavefront aberrations are compensated by the deformable mirror, and moreover the spot is less elliptical. Nevertheless, the corrected spot is still not circular, which is believed to be due to angular chirp of the compressor gratings but not to phase aberration.

Even though the spot is still not ideal, the capillary tubes are able to sustain hundreds of shots without dramatic damage. This achievement must be partially attributed to another success of stabilizing the laser pointing.

Laser pointing stabilization

Another key issue of laser performance is pointing stability. It is particularly crucial when capillary tubes are used as target. As shown in Chapter 4, if the incident laser deviates from the capillary axis, higher modes are excited inside the capillary tube and coupling efficiency drops. More importantly, the capillary front face could be damaged directly by only one laser pulse, resulting in an “ultrashort” lifetime of target. In this sense, the laser

pointing must be carefully stabilized.

Pointing instability can be caused by mechanical vibrations, air turbulence, and so on. Recently the laser pointing stability was significantly improved at the LLC. Perturbations, like mechanical and air influences, were reduced by isolating the pump systems from the laser room. Furthermore, an active stabilization system was implemented in order to lock the laser pulse to the desired position. This scheme was reported on in Ref. [178]. The stabilization system consists of two pairs of piezoelectric mirror together with a position sensing detector (PSD). One pair controls the near-field, while the other takes care of the far-field, so the laser axis can be regulated. The two PSDs record the real-time laser positions. Once the detected positions deviate from the expected ones, the piezoelectric mirrors will compensate the offsets, getting the beam back. A LabVIEW program was developed by the LLC team to manage the feedbacks between the PSDs and the piezoelectric mirrors.

Quantitatively, without control the RMS (root mean square) pointing fluctuation was 6.7 μrad in the focal plane. The pointing instability was decreased to 3.7 μrad by removing the perturbations from the laser room. When the active stabilization system was launched, the fluctuation went down by 30% to merely 2.6 μrad [178]. Typically in our experiments, the focal length of the parabolic mirror is 76 cm, which corresponds to a RMS fluctuation of approximately 2 μm in the focal plane. The focal spot size (first minimum of Airy pattern) is 19.8 μm. The pointing fluctuation is therefore about 10% of the focal spot size. When a large capillary tube of 178 μm diameter is adopted, such a pointing instability should not considerably deteriorate laser coupling and capillary guiding.

5.2 Motorized capillary housing

As presented before, the capillary tubes must be correctly aligned with respect to the laser axis to achieve good coupling and guiding. To do so, one needs to move the tube in five dimensions, namely three translations x, y, z and two rotations θ_h, θ_v. A new motorized capillary housing was designed in our group during my PhD study. One critical problem of our old housing [62] was vibration, as the capillary holder was loosely mounted into the motor system. When the valve was opened, the strong gas force shook the capillary holder, making laser coupling less efficient. This issue is solved in the new design. First of all, several damping bellows are employed to weaken the gas shock. Secondly, the capillary holder is strongly fixed to the housing base by mechanical force. Using this new housing, no appreciable vibration of capillary tube was found when gas was filled.

Figure 5.5 shows a schematic illustration of the motorized housing. One 50 mm range translation stage and one 15 mm stage are used to displace the capillary in the plane perpendicular to laser propagation. The third translation stage is put along the laser path, permitting us to shift the capillary entrance with respect to laser focal spot position. The capillary tube is rotated horizontally and vertically by two motors to change the angle between laser path and capillary axis. The capillary entrance center is set as the origin of the rotations. A precision of ~ 0.1 μm per step can be achieved with those motors (Newport products).

In order to characterize capillary alignment, a CCD camera is used to measure laser transmission through the tube, and also check focal spot quality before alignment. The steps of capillary alignment are as follows:
(I). Shifting the camera along laser axis to find the focal plane.
(II). Moving the camera along laser propagation direction by a distance the same as capillary length. In this case, the laser will focus at capillary entrance. If one wants to

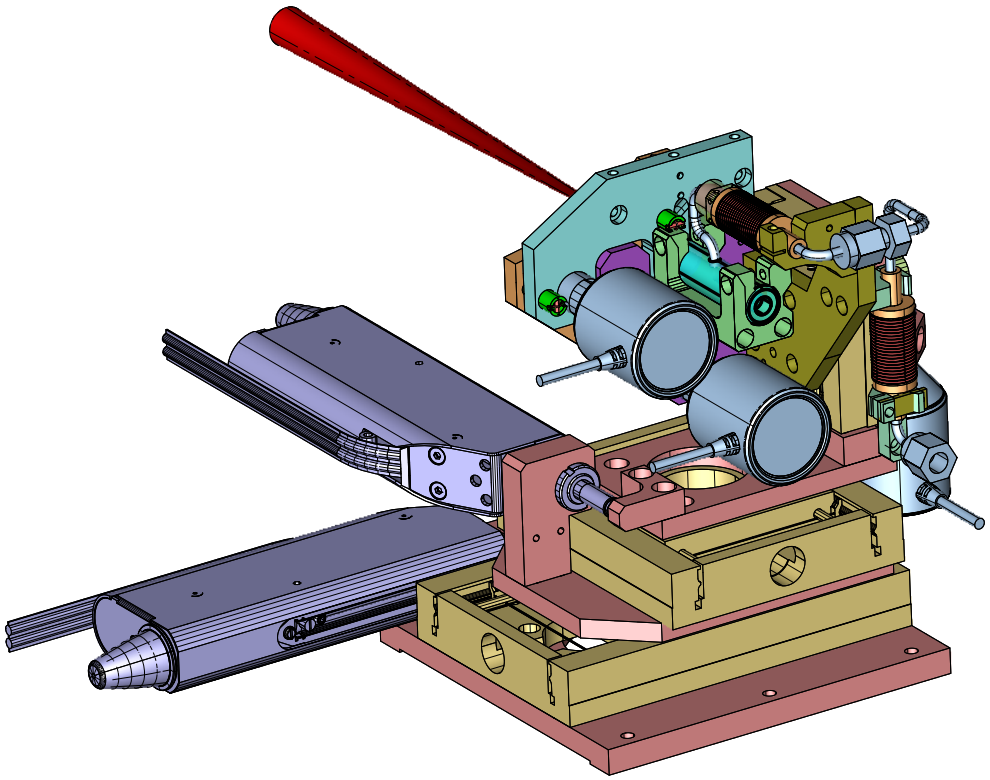

Figure 5.5: *Schematic drawing of the motorized capillary housing viewed from the back. A laser beam (the top red cone) focuses at the capillary entrance. Designed by J.-C. Lagron at LPGP.*

focus inside the tube, the distance of camera retreat has to be adjusted accordingly.
(III). Move in the capillary tube and shift it along laser axis till a sharp capillary hole is observed by the camera.
(IV). Translating and rotating the tube until the best transmission is found.

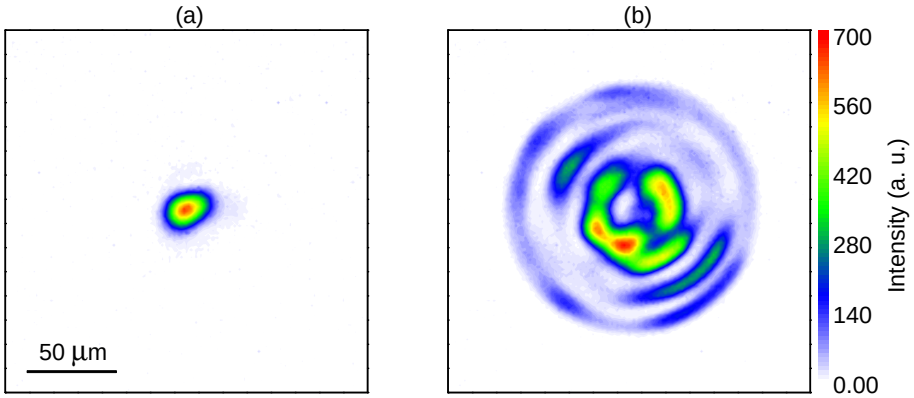

Figure 5.6: *(a) Focal spot of the LLC laser, and (b) transmission from a 20 mm long, 152 µm diameter capillary tube. Different laser attenuations were used in (a) and (b). Multimodes are excited in the tube, however the transmission is pretty symmetrical.*

For a matched capillary tube, the optimal alignment is monomode guiding. However,

in our experiment at the LLC the laser focal spot with radius of ~ 20 μm was much smaller compared to the capillary radii ranging from $50-125$ μm. In this case, high order modes are excited in the tube as well. We therefore optimize the alignment until a symmetrical transmission is achieved. In this case, the light should propagate in the tube without large angle with respect to the capillary axis, minimizing the risk of capillary damage. Figure 5.6 displays the focal spot of the LLC laser and a typical output laser energy distribution obtained from a 20 mm long, 152 μm diameter capillary tube when it was well aligned. Both images were recorded using an 8 bit CCD camera, so the laser beam was strongly attenuated without seeing the rings of Airy pattern in the focal spot. The transmission is estimated to be around 80%, and more importantly it is reasonably symmetrical. After more than 100 high intensity laser shots, no vital damage of the tube was observed at the entrance.

5.3 Experimental setup at the LLC

Two campaigns were conducted at the LLC during my thesis to investigate laser wakefield electron acceleration and betatron radiation inside capillary tubes. This section presents the experimental setup which was similar for the two campaigns.

The Ti:sapphire laser operates in the chirped pulse amplification (CPA) mode and was able to deliver a laser pulse with an energy of 650 mJ at 800 nm central wavelength on target. The FWHM pulse duration measured day-to-day was $\tau_{fwhm} = 40 \pm 5$ fs. Figure 5.7 illustrates the experimental setup. The laser beam was focused by a $f = 76$ cm parabola

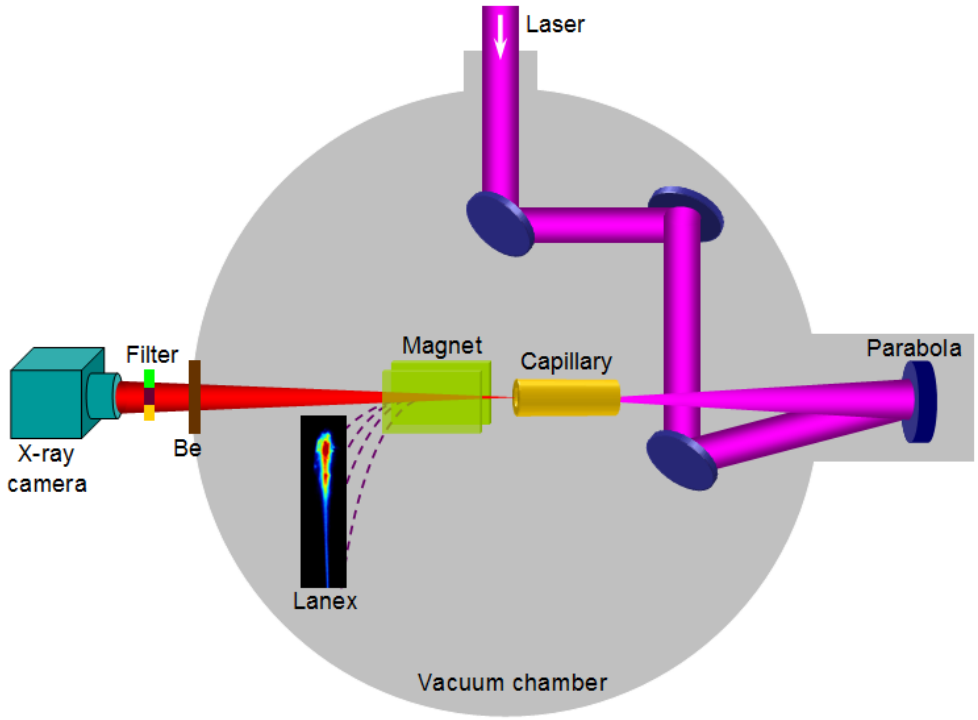

Figure 5.7: *Schematic diagram of the experimental arrangement. Elements inside the chamber were under vacuum. The Lanex screen shows a typical electron spectrum of the accelerated electrons obtained in the experiment.*

at 1 mm inside the capillary tubes. Using the motorized holder, capillary tubes were aligned with respect to the laser axis. Gases were filled into the capillary tubes through

two ∼270 μm wide slits situated at 2.5 mm from each capillary end. The plasma density inside the capillary tubes was adjusted by controlling the upstream reservoir pressure (See Chapter 4). A 12 cm long permanent magnet with a central field of 0.7 T over a 15 mm gap deflected electrons downwards onto a Lanex (Kodak Regular) phosphor screen which was imaged by a CCD camera. Electron energy and beam charge were characterized as detailed in Section 5.4. On the same laser shots, the far-field betatron radiation was recorded using a 16 bit X-ray CCD camera placed outside the target chamber (See Section 5.5). A filter consisting of several metal pieces was inserted in front of the X-ray camera to give a rough estimation of the photon energy. Razor blade was placed just downstream the magnet to evaluate the X-ray source size, as discussed in Section 5.5.

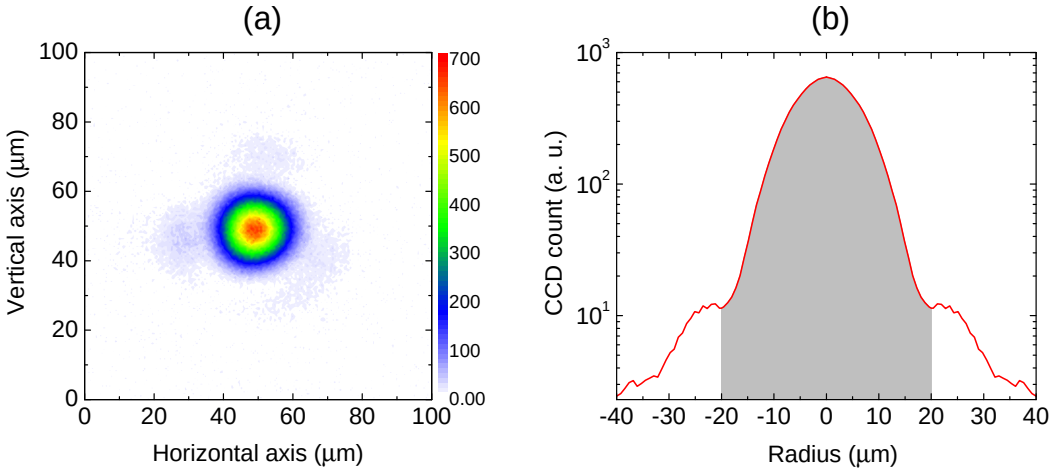

Figure 5.8: *(a) Energy distribution in the focal plane; (b) Averaged radial profile of laser energy in logarithmic scale. The grey shaded area, with a boundary at the first minimum of the focal spot, contains about* 84% *laser energy in the focal plane.*

The energy distribution in the transverse plane delivered by the laser system exhibits a nearly flat-top cylindrically symmetrical distribution before focusing. In the focal plane, the corresponding energy distribution is close to an Airy pattern, as exhibited in Figure 5.8. The focal spot shown in Figure 5.8(a) was optimized to achieve a symmetrical distribution by tuning the deformable mirror placed after the compressor to compensate for aberrations in the laser wavefront. The average radius of the focal spot at the first minimum can be determined from the radial profile of energy distribution averaged over the angles; it was measured to be 19.7 ± 0.8 μm, which yields an on-axis peak intensity of $(5.4 \pm 0.1) \times 10^{18}$ W/cm^2 and a normalized laser vector potential of $a_0 \simeq 1.6$. The energy fraction contained within the grey shaded area in Figure 5.8(b) is estimated to be equal to 84% of the energy in the focal plane.

The capillary tubes employed in this experiment range from 152 μm to 254 μm in diameter and from 8 mm to 30 mm in length. For the focal spot shown in Figure 5.8, the focal spot diameter at first minimum over capillary diameter ratio is in the range 0.26 to 0.16, and gives rise to multimode excitation at the entrances of the capillary tubes [140]. Using small capillary tubes ($R_{cap} \simeq 20$ μm) to match the focal spot was not possible as the laser intensity outside the central focal spot was still so high that the capillary front surface could be broken immediately by laser radiation. The laser stabilization system [178] did not function during the first campaign owing to some technical problems, however it worked correctly during the second campaign.

5.4 Electron beam characterization

This section describes the diagnostic methods characterizing the electron beams produced in our electron acceleration experiments for the main parameters: electron energy, beam charge, and beam divergence.

5.4.1 Electron spectrometer

Traditionally, various electron spectrometers have been developed in the community of RF accelerators, however they are designed to provide a high energy resolution at a given electron energy, which is specially oriented for monoenergetic electron beams. On the contrary, electrons generated by LWFAs usually own large energy spread, which could cover an energy range from tens of MeVs to GeV class in a single bunch [179]. Furthermore, the electron bunches generated by LWFAs are merely a few femtoseconds long with peak currents of a few kiloamperes [52], which are very different from those in RF accelerators. Specific spectrometers are therefore needed for LWFA produced electrons.

The most commonly used spectrometer design in LWFAs is composed of a magnet together with a scintillating screen imaged by a 16 bit CCD camera with a high dynamic range. Other candidates for electron detection could be image plates [180]. Nevertheless image plates have to be read out after the experiment, which is not suitable for high repetition rate data acquisition. What we adopted in experiments is the Kodak Lanex

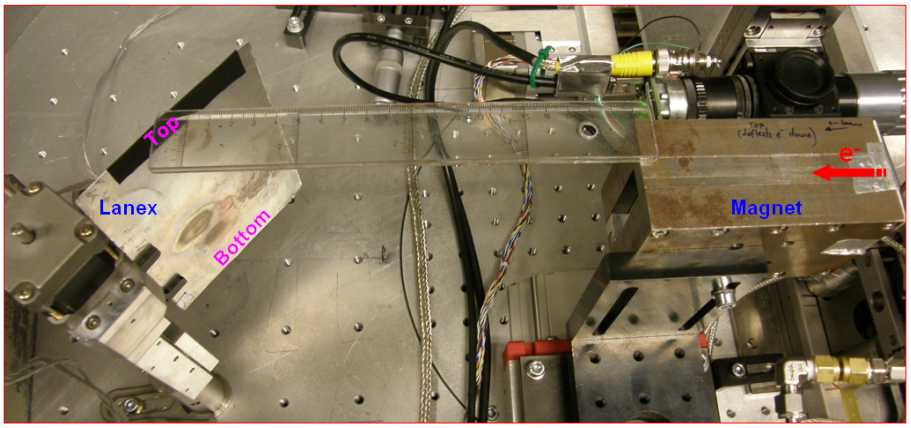

Figure 5.9: *The permanent magnet and the Lanex screen placed in the vacuum chamber at the LLC. The electrons enters the magnet from the right, and get bent downwards onto the Lanex screen.*

Regular scintillating screen. Shown in Figure 5.9 is the typical setup of the spectrometer used during our experiments at the LLC. A 12 cm long (along laser propagation direction) permanent magnet with central field of 0.7 T was used. The magnet is normally placed just behind the target. When the electrons pass through the magnet, they are deflected downwards by the Lorentz force and hit the Lanex screen located downstream. Both the magnet and the Lanex screen were mounted onto manual or motorized translations stages. Once the magnet is shifted off-axis, we can move the Lanex screen up towards the laser axis to measure electron beam profile, pointing, and so on.

The Lanex screen consists of a $\sim$ 100 μm thick phosphor layer of gadolinium oxysulphide (Gd_2O_2S:Tb). When it is illuminated by an ionizing radiation, the layer will produce fluorescent light over a time scale of $\sim$ 660 μs [181]. The emission has a sharp spectrum peak at 546 nm. Usually the Lanex screen was protected by an aluminium shield from

direct exposure to the intense laser light. The Lanex screen is imaged by a CCD camera placed outside the chamber. A narrow-band filter matched to the peak fluorescence of the Lanex was often placed in front of the CCD camera to reduce background light.

As presented below, this compact spectrometer allows us to measure simultaneously electron energy spectrum, beam charge, beam divergence for a single shot.

5.4.2 Electron beam energy spectrum

To obtain the energy spectrum of electron beams, one needs to know the dispersion of the spectrometer $\mathcal{E}_e(y)$, namely the electron energy $\mathcal{E}_e$ as a function of the vertical coordinate on Lanex screen y. The spatial parameter associated with a spectrometer is schematically illustrated in Figure 5.10(a). Before and after the magnet, the electrons do uniform linear

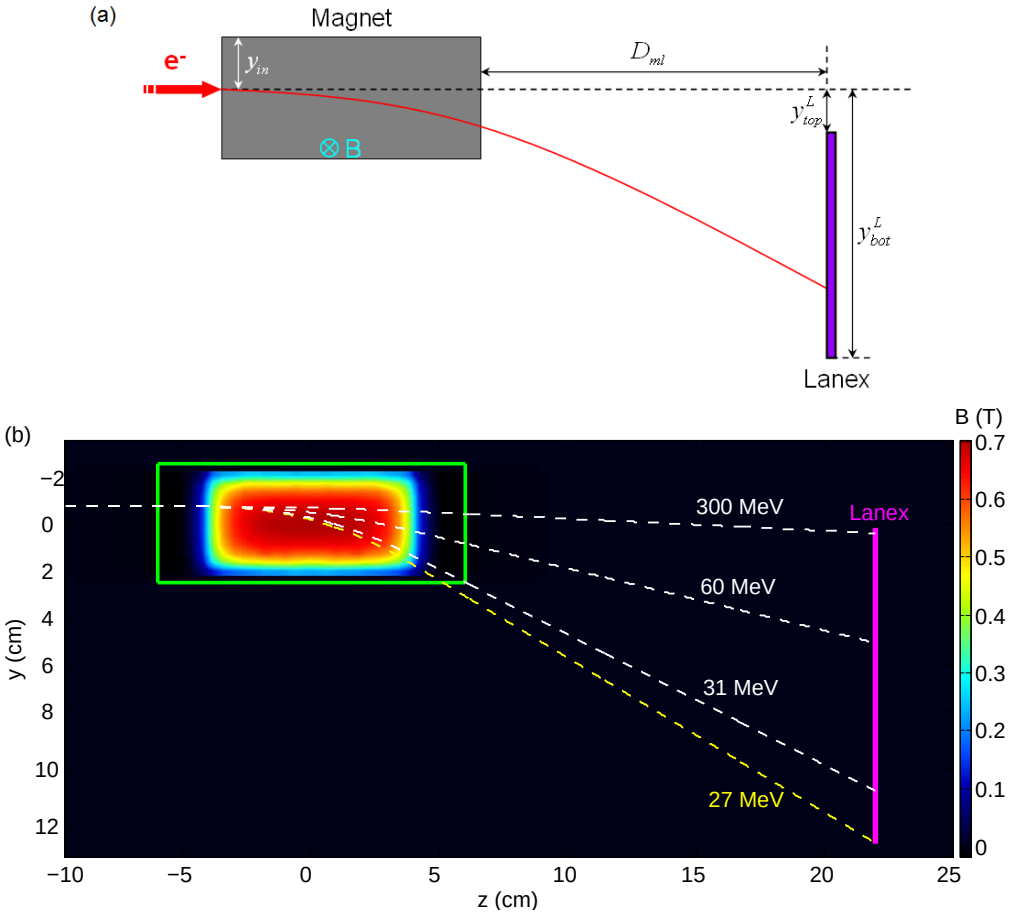

Figure 5.10: *(a) Illustration of the spatial parameters associated with a spectrometer, where the magnetic field points into the paper. (b) Numerically calculated trajectories of electrons with different energies for the setup of campaign II. The green square represents the magnet borders.*

motion, while in the magnetic filed, they are rotated. The magnetic force exerted on an electron is $\mathbf{F}_B = -e\mathbf{v} \times \mathbf{B}$. Since $\mathbf{F}_B \cdot \mathbf{v} = 0$ always holds, the magnetic force does not do work. It will change the direction of motion but never change electron energy, suggesting γ of electron is constant. In this sense, the electron motion is described by

$$\gamma \frac{d\mathbf{v}}{dt} = -\frac{e}{m_e}\mathbf{v} \times \mathbf{B}. \tag{5.1}$$

γ is linked to electron energy via $\gamma \simeq 1+2\mathcal{E}_e$[MeV]. The electron trace can be then obtained though $\mathbf{r} = \int \mathbf{v}dt$.

If the magnetic field is uniform, Equation 5.1 can be solved analytically. However the field that we used varies in space, as seen in Figure 5.10. The field measured by the manufacturer has a central peak of 0.7 T and gradually decreases to zero towards the magnet borders. A program was written to calculate numerically the electron trajectories in the magnetic field using the fourth-order Runge-Kutta method. The magnetic field was measured with spatial steps of 0.48 mm and 0.44 mm along and perpendicular to the laser axis, respectively. A very short time step $\Delta t_s = 80$ fs (corresponding to a spatial step of 24 μm) therefore was adopted to resolve the spatial detail of the field. The precision of the code was verified by comparing with theoretical result when assigning the magnetic field as uniform. The error between them is less than 0.2%.

Table 5.1: *Spatial configurations of the electron spectrometer for the two campaigns at the LLC.*

Campaign	y_{in} (cm)	D_{ml} (cm)	y^L_{top} (cm)	y^L_{bot} (cm)	Energy range (MeV)
I	−1.6	20	−1.2	6.8	[42, 690]
II	−0.7	16	1.8	13.6	[31, 380]

A specific electron trajectory depends on the position where the electron enters the magnet y_{in}, the distance between the magnet end and the Lanex screen D_{ml}. The energy range that the Lanex can measure depends on its top and bottom positions: y^L_{top} and y^L_{bot}. Table 5.1 gives the setup parameters of the spectrometers used in the two campaigns carried out at the LLC. The magnetic field center is set as the coordinate origin (0, 0). Here we use the case of campaign II as an example. Figure 5.10(b) exhibits four typical traces for electron energies of 27, 31, 60, and 300 MeV. As seen, the lower the electron energy is, the more they are deflected downwards. The Lanex bottom corresponds to electron energy as low as 27 MeV, indicated by the yellow dashed curve in Figure 5.10(b). However, such a low energy electron is so strongly bent that it hits the magnet inner bottom before escaping from the magnet. The energy threshold of electron escape is 31 MeV. This kind of spectrometer is thus called as "magnet-limited", as it is the magnet but not the Lanex that sets the low limit of detection. The dispersion curve of the spectrometer is plotted in Figure 5.11(a). The electron energy range covered by the spectrometer is [31, 380] MeV when the electrons enter perpendicularly to the manget.

The spectrometer resolution is mainly restricted by electron beam divergence, as the dispersion curve is rather sensitive to the incident angle of electrons θ_{in}. Figure 5.11(a) illustrates schematically the trajectories of electron entering either perpendicularly into the magnet (red solid curve) or with an incident angle (blue dashed curve). It shows that for a given electron energy, different incident angles lead to different positions on the Lanex screen. Figure 5.11(b) shows the dispersion curves of the spectrometer for three incident angles $\theta_{in} = -5$, 0, and 5 mrad, respectively. The positive direction is defined towards the top-right direction in Figure 5.11(a). We can see that a given Lanex position corresponds to a relatively lower electron energy for the case of positive incident angle, and the opposite happens to the negative incident angle. They together result in the error of electron energy determination. Figure 5.11(c) presents the energy error of the spectrometer for an electron bunch with a full opening angle of 10 mrad. One can immediately find the error rapidly increases with increasing electron energy. For an energy of 50 MeV, the error is about 3 MeV (corresponding to an energy resolution of 6%), whereas it degrades to 80 MeV for

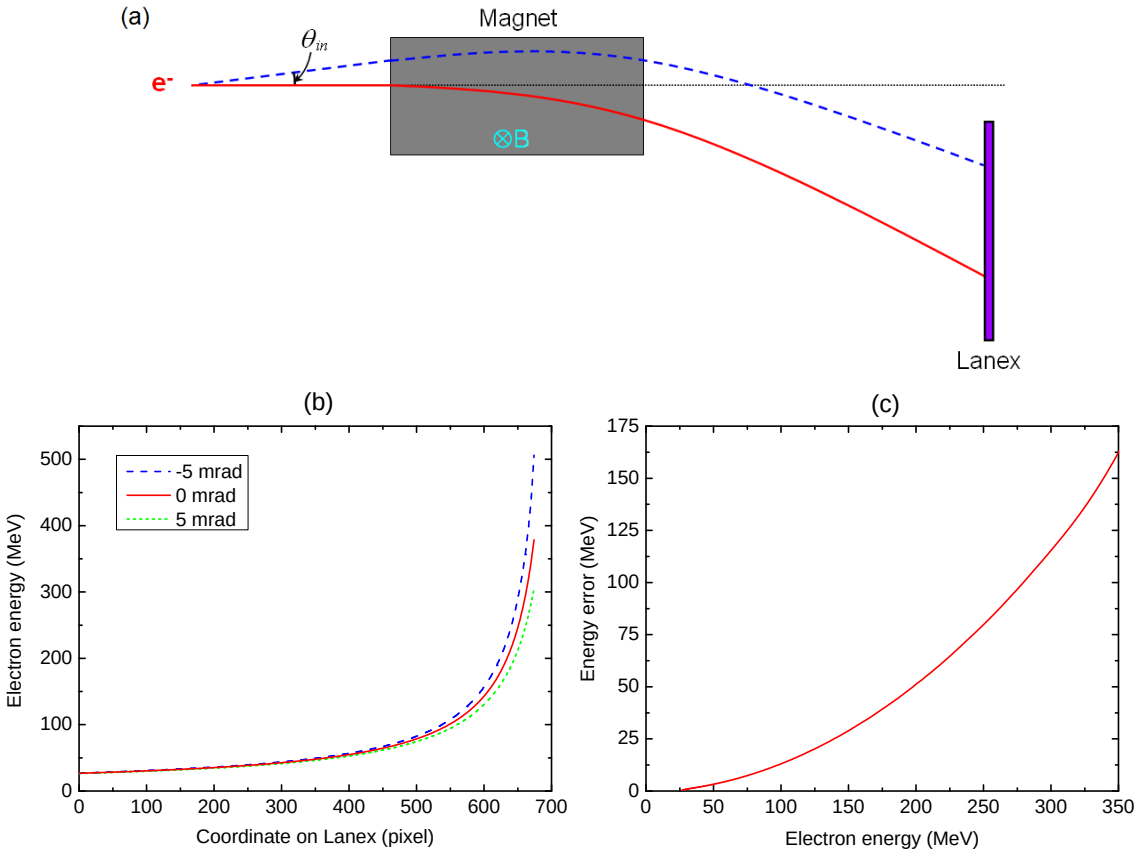

Figure 5.11: *(a) Schematic illustration of the trajectories of electrons entering perpendicularly to the magnetic field (red solid curve) or with an incident angle (blue dashed curve). (b) Dispersion curves of the spectrometer for different incident angles of the electrons. (c) Energy error for an electron bunch with full opening angle of 10 mrad.*

an energy of 250 MeV (resolution of 32%). The resolution of the spectrometer might be improved by cropping the electron beam with a collimator, or/and using a larger Lanex screen and putting it further away from the magnet.

5.4.3 Electron beam charge

Another important feature associated with an electron bunch is its beam charge. Two devices are used on conventional accelerators to measure the beam charge of an electron bunch: Faraday cup and integrating current transformer (ICT). In LWFA experiments, they have to be placed upstream of the magnet before electrons are dispersed, making the experimental arrangement difficult. Moreover, electromagnetic radiations, such as laser, X-ray, bremsstrahlung radiation and so forth, are present inside the vacuum chamber, making it a rather noisy environment. In order to measure the charge correctly, special attention has to paid to protect the ICT from ambient noise, as achieved by Nakamura *et al* [182].

In this context, a few groups have calibrated the fluorescence of Lanex for measuring beam charge [182, 183, 184], in order to be able to read-out the beam charge directly from an image if the optical transmission and CCD responsivity are calibrated as well. The photon number produced by an electron in the phosphor screen depends on the energy deposited by the electron in the screen. Previous study demonstrated that the deposited

energy is constant for a Kodak Lanex Fine screen as long as the incident electron energy is in excess of 1 MeV [183], so the total number of the emitted photons only depends on electron beam charge. The conversion efficiency from the deposited electron energy to the fluorescent light, is thus the only missing parameter for beam charge measurement. Ref. [184] calibrated several scintillating screens often used in LWFA experiments. This calibration was carried out on the ELBE linear accelerator at the Forschungszentrum Dresden-Rossendorf, which was capable of delivering single or multi electron bunches with charge from 1 pC up to 100 nC at an energy of 40 MeV. Figure 5.12(a) shows the calibration setup, where the beam charge was measured by an ICT, and the scintillating light was imaged onto a CCD camera. All the screens investigated exhibit a linear charge-to-photon dependency over the several order of magnitude of charge, as displayed in Figure 5.12(b). For the Kodak Lanex Regular screen used in our experiments, the absolute calibration from Ref. [184] is $(6.95 \pm 0.6) \times 10^9$ photons/sr/pC.

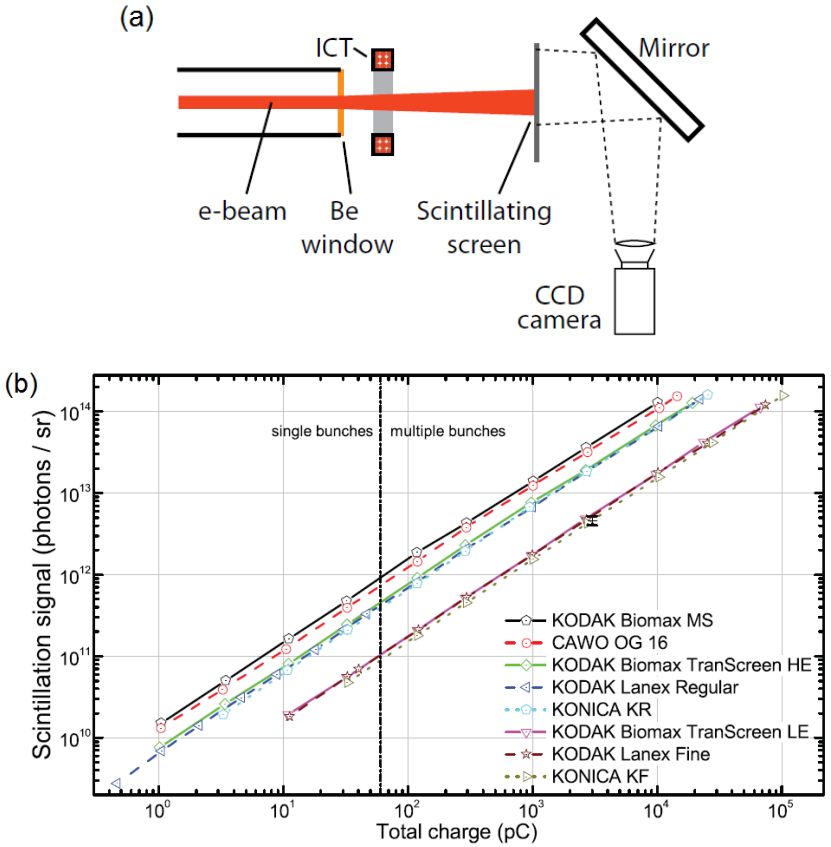

Figure 5.12: *(a) Setup of the scintillating screen and imaging system, and (b) the absolute charge calibration of scintillating screens given in Ref. [184].*

Figure 5.13 illustrates schematically the experimental setups for beam charge measurement in our two campaigns, and the corresponding parameters are given in Table 5.2. For a CCD-recorded image, the spectral charge can be obtained by the expression [183, 185]

$$\frac{dQ}{d\mathcal{E}}(\mathcal{E}_0) = \frac{C(\mathcal{E}_0)}{T_{op} q_{ccd} T_{IF} \Omega \cos(\theta_{ccd}) \eta_l \exp\left(-\frac{\tau_d}{\tau_l}\right)} \times \cos(\theta_{in}) \frac{\frac{ds}{d\mathcal{E}}(\mathcal{E}_0)}{\delta s_{pixel}}. \tag{5.2}$$

The left-hand side represents spectral charge in unit of pC/MeV at an electron energy of $\mathcal{E}_0$. On the right-hand side, the factor $C(\mathcal{E}_0)$ is the total CCD count measured for electron

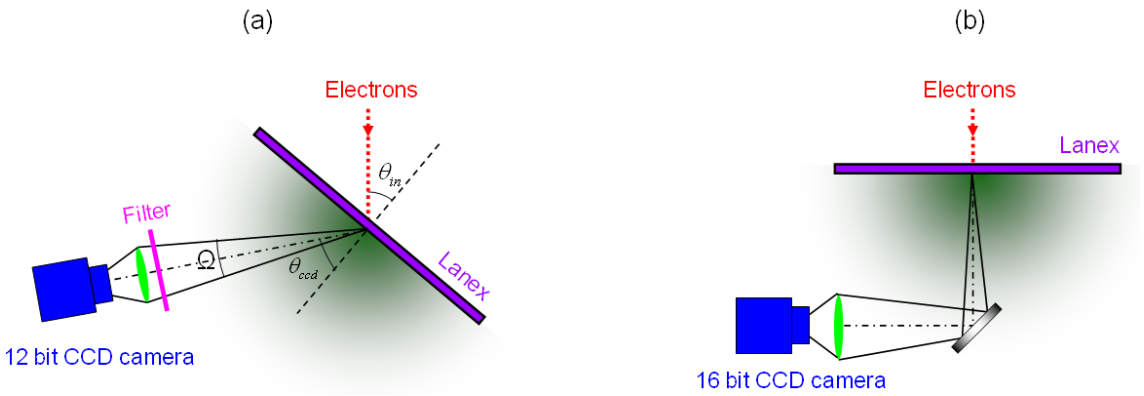

Figure 5.13: *Configurations of the beam charge measurement for (a) the first and (b) the second campaign at the LLC. The configuration in the second campaign was similar to that in Ref. [184] shown in Figure 5.12(a).*

Table 5.2: *Parameters for the beam charge measurement in the two campaigns.*

Campaign	$T_{op}q_{ccd}$ (count/photon)	T_{IF}	Ω (msr)	θ_{ccd} (°)	τ_d (μs)	θ_{in} (°)	δs_{pixel} (μm)
I	0.056	0.265	0.84	40	76.5	40	4.65
II	0.092	No filter	2	0	0	0	13

energy $\mathcal{E}_0$. T_{op} denotes the total transmission of the scintillating light through the optics except the filter placed in front of the CCD camera. q_{ccd} is the quantum efficiency of the CCD, namely CCD count per incident photon. T_{IF} represents the transmission through the interference filter. Ω indicates the solid collection angle, while θ_{ccd} is the viewing angle of the CCD camera with respect to the normal of Lanex screen, as shown in Figure 5.12(a). The factor $\cos(\theta_{ccd})$ arises from the fact that the emission of the angular distribution of the scintillating emission obeys a Lambertian (cosine) law [186]. $\eta_l = (6.95 \pm 0.6) \times 10^9$ photons/sr/pC is the absolute calibration of the Lanex screen [184]. The exponential term indicates how much the illumination is cut out if the camera is launched for data acquisition using a time delay τ_d, while the characteristic decay time is $\tau_l \simeq 660$ μs [181]. Using a time delay is favorable for reducing the noise level, whereas part of the signal will be lost, so one has to find a compromise value for τ_d. The factor $\cos(\theta_{in})$ accounts for the effective screen thickness for different electrons, and θ_{in} is the electron incident angle with respect to the screen normal. δs_{pixel} is the pixel size along the dispersion direction. The last term in Equation 5.2 yields the energy range corresponding to one pixel. Once the spectral charge is known, the total beam charge can be computed through $Q = \int \frac{dQ}{d\mathcal{E}} d\mathcal{E}$.

The spectrum of the scintillating light produced from the Kodak Lanex Regular screen, $S_L(\lambda)$, has a sharp peak at 546 nm [184]. Light transmission through the filter given in Table 5.2 is the value averaged over the spectrum range as $T_{IF} = \int S_L(\lambda) T_{if}(\lambda) d\lambda / \int S_L(\lambda) d\lambda$, where $T_{if}(\lambda)$ is the transmission as a function of wavelength. It should be mentioned that the emission spectrum of the Lanex screen was not known during our first campaign. The factor T_{IF} was thus determined to be 0.6 by measuring the transmission of a 543 nm green HeNe laser though the filter. This error in T_{IF} determination leads to an underestimation of beam charge by a factor of $0.6/0.265 \simeq 2.3$ in our publication [48].

5.4.4 Electron beam divergence

The last parameter we discuss here is beam divergence, which is of great interest for many applications of the electron beams. In our setup, one can shift the magnet out of the optical axis to directly measure electron beam distributions with the Lanex screen, and then it is straightforward to characterize the beam divergence. However in this case we do not have any information about electron energy or X-ray emission, as the X-ray detector has to be shifted off-axis to avoid damage by the electrons. Another way is to determine the beam divergence from the dispersed electron profile. Then we can get the divergence for a specific electron energy. In the following part, we present two examples to show how the beam divergences are determined accordingly in each case.

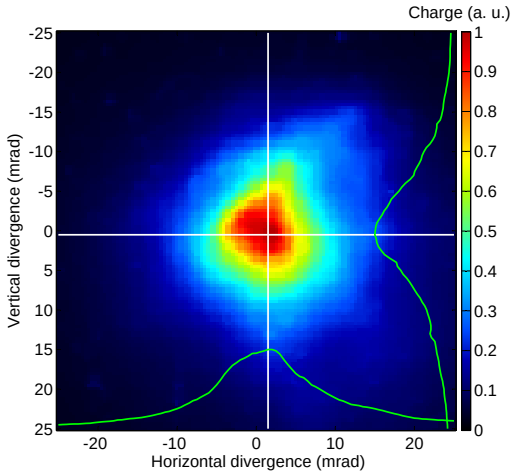

Figure 5.14: *An electron beam profile measured from a 10 mm long capillary tube with diameter of 178 μm for a plasma electron density* 8×10^{18} *cm*$^{-3}$*. The white cross indicates the position of the maximum of the charge distribution, while the green curves are line-outs of the charge distribution along the white lines.*

Shown in Figure 5.14 is an electron beam charge distribution measured from a 178 μm diameter, 10 mm long capillary tube at a plasma electron density 8×10^{18} cm^{-3}. We first of all find the position of the maximum of the charge distribution, and then the horizontal and vertical charge distributions through the maximum point (the green curves in Figure 5.14) are used to determine the beam size. The divergence is defined as the beam size over the distance from the capillary exit to the Lanex screen. For the beam shown in Figure 5.14, the horizontal and vertical FWHM beam divergences are determined to be 12.9 mrad and 13.8 mrad, respectively. Using Gaussian fits to the line-outs, the horizontal and vertical RMS beam divergences are found to be 8.4 mrad and 9.5 mrad, respectively. A detailed study of beam divergence will be presented in Chapter 6.

Figure 5.15 exhibits the energy distribution of a dispersed electron beam obtained on the Lanex screen after the magnet taken for the same parameters as those of Figure 5.14. The horizontal axis corresponds to dispersed electron energy. There is a negligible influence of the magnetic field on electron motion along the vertical axis, so the beam divergence can be evaluated using the beam size in this direction. As the electron are dispersed, one is able to determine the divergence for a specific energy. We chose the position corresponding to the maximum of vertically integrated intensity profile (the white line in Figure 5.15). In Figure 5.15, the size of the selected pixel corresponds to an electron energy range of [93, 93.5] MeV, which is determined by the dispersion of the spectrometer. The beam size

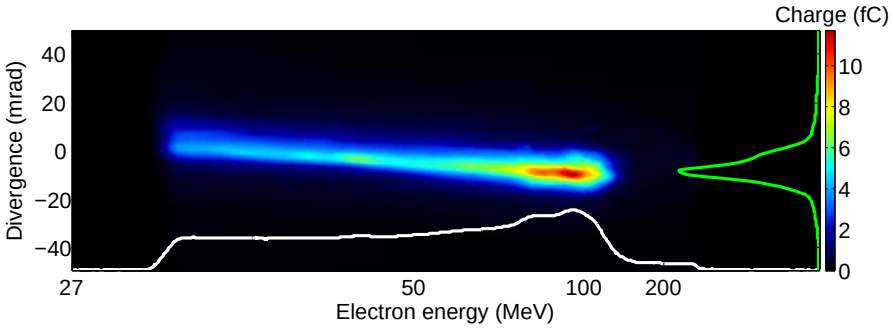

Figure 5.15: *Energy distribution of a dispersed electron beam. The conditions are the same as for Figure 5.14. The line along the horizontal axis is the vertically integrated intensity profile, while the line along the vertical axis is the line-out of intensity profile for electrons with energy from 93 to 93.5 MeV.*

is calculated using the vertical intensity profile for the chosen energy range (the vertical green line in Figure 5.15). The FWHM beam divergence of $93 - 93.5$ MeV electrons is found to be 12 mrad, and the RMS beam divergence using Gaussian fit is about 7 mrad.

It is noticeable that under the same conditions both the FWHM and RMS divergences are smaller when they are determined from the dispersed beam. This maybe because all the electrons are taken into account in the case of undispersed measurement, whereas lower energy electrons have larger divergences [10], which therefore give a larger overall beam divergence.

5.5 X-ray diagnostics

As demonstrated in Chapter 3, the electrons wiggling inside a plasma cavity generate X-ray radiation. Therefore beside electron diagnostics, X-ray characterization is the other important measurement in our experiments. We discuss in this section the devices and methods associated with X-ray diagnostics.

5.5.1 X-ray CCD cameras

Since the X-rays produced by betatron radiation are collimated and directional, the simplest measurement is to place an X-ray detector downstream to intercept and record the beam. During our experiments two X-ray sensitive CCD cameras were employed. The first one is a backilluminated Princeton instrument (model SXTE/CCD-512TKB1). The CCD chip is made by a 15 μm thick silicon layer, consisting of 512×512 pixels with a size of 24.8×24.8 μm^2. Each pixel is 16 bit, namely a dynamics count up to 2^{16}. This feature is very important to avoid CCD saturation, as the brightness of X-rays generated through betatron radiation could be as high as $\sim 10^{21} - 10^{23}$ photons/s/mm^2/mrad^2/0.1%BW [58, 59]. The chip lies 10 mm behind a 250 μm thick beryllium (Be) window in an evacuated, water cooled head. A detailed study of this camera features can be found in Ref. [187]. The second one that we used is an Andor X-ray CCD camera (iKon-L, model DO936N-MOW-BN). The CCD chip is composed by 2048×2048 pixels of 13.5×13.5 μm^2, providing a large field of view of 27.6×27.6 mm^2. The dynamics range of this camera is 16 bit as well. The camera was cooled down to -30 °C during our experiment to diminish the intrinsic electronic noise. This camera was particularly employed for X-ray source size measurement (see more details in Chapter 6) owing to its high spatial resolution.

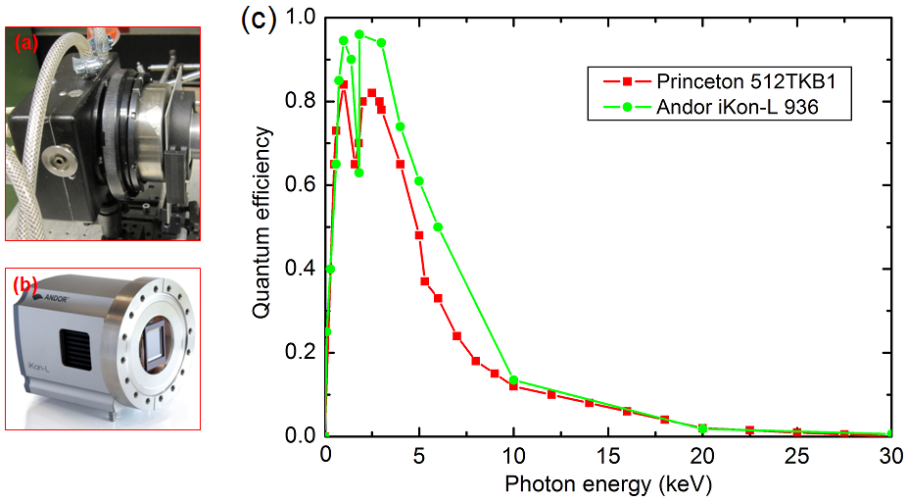

Figure 5.16: *(a) The Princeton X-ray CCD camera and (b) the Andor X-ray CCD camera used in our experiments. (c) Quantum efficiencies of these two cameras.*

The cameras respond to the incident photons according to the photoelectric effect. The photoelectrons that one photon can produce depend on the fraction of the energy it deposits in the chip, namely the quantum efficiency of the chip. The quantum efficiencies of the two X-ray cameras are given in Figure 5.16(c). As one can see, they are strongly dependant on photon energy. Both of them, specially the Andor one, possess high responsivity over the energy range of 1-10 keV, and are able to detect photons up to 20 keV. Furthermore there is a gain setting in each camera, which determines how many photoelectrons yields one count. This is also known as analogue-to-digital conversion. The gain setting of the Andor camera is 7 photoelectrons/count or 25.55 eV/count, while it is 20.2 eV/count for the Princeton camera.

Inside the chamber, apart from the betatron X-ray beam, there are other X-ray emissions generated by synchrotron radiation when the electrons are deflected by the magnet, and bremsstrahlung radiation when the electrons go through the target chamber. As we are mostly interested in betatron X-ray, the other radiations have to be filtered out. To do so, a 250 μm thick Be aperture was placed on the laser axis in front of the X-ray cameras. Since the cameras take in-line view of the target, synchrotron and bremsstrahlung radiations that do not propagate along the optical axis are thus drastically blocked.

5.5.2 Filter arrays

The betatron X-ray radiation produced in the wiggler regime has a broad spectrum, as examined in Chapter 3. The radiation spectrum was experimental demonstrated to be synchrotron-like using the single-hit method [122], however this measurement is intrinsically sensitive to noise and requires a large experimental space. So what we adopted is the method of Ross filter [188, 189] which contains an array of several metal pieces. Two filters with different metal patterns were used in our experiments. One was called “pizza” filter, and the other “square” filter, as shown in Figure 5.17. Both of the them consist of six metals of different thickness. The transmissions of X-ray photons in the range 1-30 keV through the materials of these filters strongly depend on their energies; this diagnostic is sensitive and suitable for photon energy determination. For a given X-ray beam, the spectrum critical energy is quantified using a least squares method [190]. The procedure

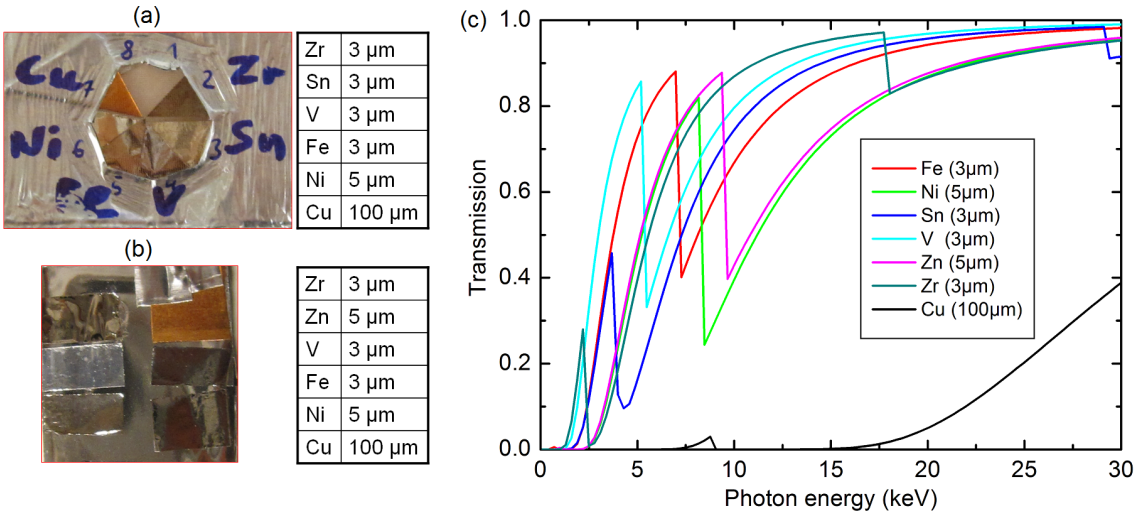

Figure 5.17: *(a) The "pizza" filter and (b) "square" filter employed in our experiments. (c) Transmissions of the metal pieces.*

can be described as follows.

We first of all assume the X-ray beam has a synchrotron spectrum described by Equation 3.21, whose shape is fully dominated by the parameter $\zeta = \mathcal{E}_{ph}/\mathcal{E}_c$. Photon number distribution is therefore given by

$$\frac{dN_{ph}}{d\mathcal{E}} = N_{ph}\frac{(\mathcal{E}/\mathcal{E}_c)^2\mathcal{K}_{2/3}^2(\mathcal{E}/\mathcal{E}_c)}{\int_0^\infty(\mathcal{E}/\mathcal{E}_c)^2\mathcal{K}_{2/3}^2(\mathcal{E}/\mathcal{E}_c)d\mathcal{E}}, \tag{5.3}$$

where N_{ph} is the total photon number of the radiation. One can calculate the theoretical CCD count in the area of metal m by

$$C_{ccd}^m = \int_0^\infty \frac{dN_{ph}}{d\mathcal{E}_{ph}}\frac{\mathcal{E}_{ph}T_{total}T_m q_{ccd}}{G_{ccd}}d\mathcal{E}_{ph}, \tag{5.4}$$

where G_{ccd} denotes the gain setting of the camera, and T_{total} indicates X-ray transmission before the filter. T_m represents the transmission through metal m. The second fraction in Equation 5.4 is the conversion factor from photon energy to CCD count, while the first one corresponds to the photon number for energy $\mathcal{E}_{ph}$. In reality, one only needs to integrate Equation 5.4 up to 30 keV, beyond which the quantum efficiency becomes less than 0.01, so the photon contribution can be neglected. Once the CCD count is known, we can compute the theoretical transmission of the X-ray beam via $T_{theory}^m = C_{ccd}^m/C_{ccd}^{wo}$. C_{ccd}^{wo} is the count without metal filter in front of the camera. It is easy to find that T_{theory}^m depends only on critical energy $\mathcal{E}_c$.

Figure 5.18(a) displays an X-ray beam produced using a 178 μm diameter, 20 mm long capillary tube at a plasma electron density 8.2×10^{18} cm^{-3}. In order to get the transmissions correctly, one needs to first properly process the noise. The mean CCD count obtained from the 100 μm thick copper covered area [lower-left part of Figure 5.18(a)] is viewed as noise level and subtracted from the whole image. As shown in Figure 5.17(c), the 100 μm copper blocks most of the photons below 20 keV. Next we select a significantly large area in each metal part to determine the local CCD count $C_{measure}^m$. The corresponding transmission is defined by $T_{measure}^m = C_{measure}^m/C_{ref}$. C_{ref} is the mean CCD count of a metal-free area just beside the metal, like, for example, the area labeled

as Zn and Ref in Figure 5.18(a). Finally we use a least squares method to determine the critical energy that leads to theoretical transmissions fitting best the experimental ones, namely when the residual

$$\chi^2 = \sum_m \left[T^m_{theory}(\mathcal{E}_c) - T^m_{measure} \right]^2 \tag{5.5}$$

reaches a minimum. In the case of Figure 5.18, the calculation quickly converges to a minimums value at 6.2 keV. Using this critical energy and the expression of synchrotron spectrum, the X-ray spectrum is found to peak at 2.6 keV and extend up to 20 keV, as shown in Figure 5.18(c).

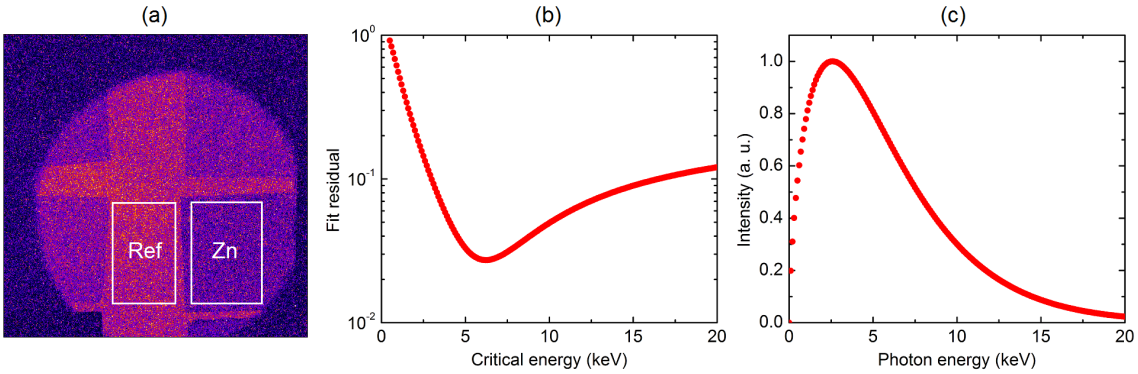

Figure 5.18: *(a) Far-field distribution of an X-ray beam with metal pieces of the filter in front of the camera. The shadow of the capillary tube is clearly visible. (b) Residual of the least squares fit of critical energy. A minimum is obtained at 6.2 keV. (c) X-ray spectrum corresponding to a critical energy of 6.2 keV.*

The other essential aspect associated to the X-ray beam is the photon number, which is often used to characterize beam flux and brightness. Once the critical energy is determined, we can calculate the incoming X-ray fluence using measured CCD counts. What we need is the conversion factor converting from CCD counts to photon number, which can be obtained through

$$\Lambda^{ph}_c = \frac{N_{ph}}{C^m_{ccd}} = \frac{\int_0^\infty (\mathcal{E}_{ph}/\mathcal{E}_c)^2 \mathcal{K}^2_{2/3}(\mathcal{E}_{ph}/\mathcal{E}_c) d\mathcal{E}_{ph}}{\int_0^\infty (\mathcal{E}_{ph}/\mathcal{E}_c)^2 \mathcal{K}^2_{2/3}(\mathcal{E}_{ph}/\mathcal{E}_c) T_{total} T_m q_{ccd} \frac{\mathcal{E}_{ph}}{G_{ccd}} d\mathcal{E}_{ph}}. \tag{5.6}$$

What we measure in experiments is the CCD counts $C^m_{measure}$, so the photon number per pixel is therefore given by $N_{ph}\,[\text{photon/pixel}] = C^m_{measure}\Lambda^{ph}_c$. If the pixel size and the distance between the X-ray source and the detector are known, we can further calculate the beam fluence in unit of photons/mrad^2. The total photon number is not possible to measure in our cases, as the beam is cropped by the exit wall of the capillary tube. Nevertheless the radiation divergence can be theoretically estimated to be $\Theta_\beta = K_\beta/\gamma$. If further assuming the transverse profile of the X-ray beam is Gaussian [57], one can evaluate the total photon number by counting all the photons in the divergence cone.

In principle, only one piece metal is sufficient to determine photon energy and X-ray fluence; however, more than three pieces should be used to most avoid misinterpretation that could be introduced by noise handling. That's also why two different pattern filter arrays were designed in our experiments. The shadow of long capillary tubes on the camera is smaller than the chip, so that the emission beam may illuminate only one metal piece

of the square filter. By contrast, all the sector-shaped pieces of the pizza filter are able to be illuminated as long as the filter is well centered on the optical path.

It is worth pointing out that the advantage of this diagnostic method using filter arrays is that one can acquire the X-ray spectrum, fluence, and profile for a single shot, and it is less noise sensitive than, for example, the single-photon counting method [187]. The essential drawback is one needs to assume the spectrum shape, and no spectrum detail, like $K\alpha$ emission from the chamber [191], can be resolved. However more and more recent single-photon counting measurements in different conditions demonstrate betatron radiation spectra are indeed synchrotron-like [192, 193], which justify the diagnostic method using filter array.

5.5.3 X-ray source size

Another aspect associated with the betatron X-ray radiation is its source size. It is of interest not only to estimate the emission brightness [58], but also to assess electron beam emittance [193], both of which are crucial parameters of the beams for their future applications. The upper limit of the X-ray source size can be evaluated by measuring the transmission of X-ray beam through microscopic objects. If the smallest feature of a micro-object is still able to be resolved in the image, one can conclude that the source size is smaller than the feature. To do so, micrometer size structures were laser-machined in 100 μm thick copper plates, as shown in Figure 5.19. The lines (diameters of the

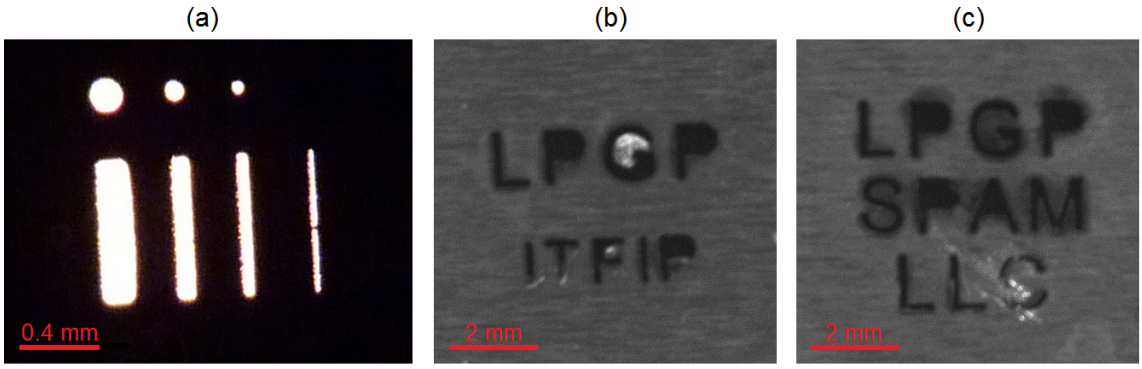

Figure 5.19: *Photographs of micro-objects used for X-ray imaging: (a) micro-structures as small as 10 μm; (b) logos of our laboratory and team names; (c) logos of the collaborators involved in our experiments. Machined by G. Bauville at LPGP.*

holes) in Figure 5.19(a) are separated by 500 μm with widths of 200, 100, 50, and 10 μm, respectively. Figure 5.19(b)-(c) are the logos of the collaborators involved in our experiments, which were machined with dimensions of the order of hundreds of microns. In order to achieve a high resolution, the camera has to be placed far away from the objects. Typically in our cases, the magnification, $\mathbb{M} = \frac{L_o+L_i}{L_0}$, was larger than five, which leads to resolutions of ~ 5 μm for the Princeton camera and 2.7 μm for the Andor camera. L_i and L_o represent the distances from the source to object and from the object to detector, respectively. In those setups, the narrowest 10 μm line was clearly resolved in the X-ray images (See more details in Chapter 6).

To achieve the determination of the X-ray source size with a high precision, knife-edge method was used. The knife-edge is provided by a commercially available (Gillette product) razor blade made of stainless steel, as displayed in Figure 5.20. The razor blade

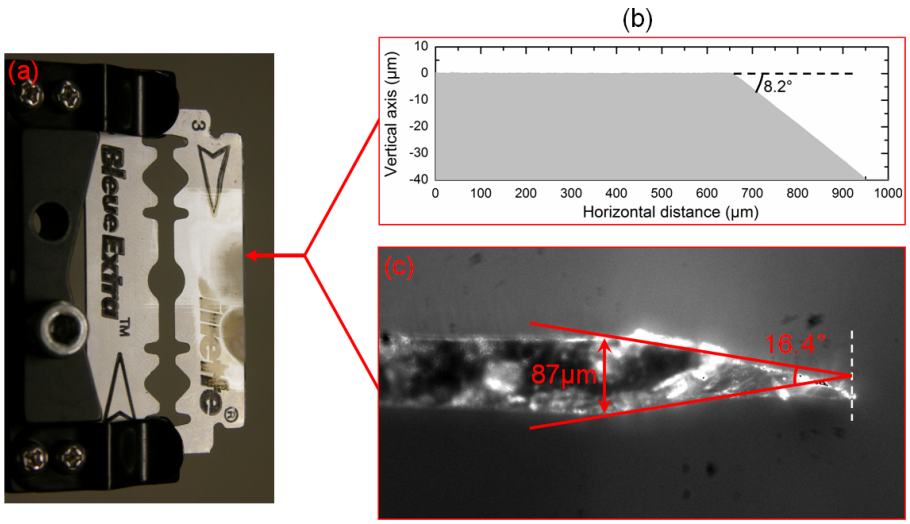

Figure 5.20: *(a) Photographic image of a razor blade after tens of shots; (b) taper angle of the blade measured using a profile meter; (c) the shape of a fresh razor blade measured with a CCD camera.*

was first measured with a profile meter[1] with resolution of ~ 0.2 μm. The tilt angle of the blade was found to be 8.2°. However, owing to technical problems, we were not able to measure the whole shape of the blade. It was further measured using a CCD camera with a 20× objective, as exhibited in Figure 5.20(c). The uniform part (razor body) has a thickness of approximately 87 μm, and the wedge has a symmetrical tapered angle of 16.4°, which is excellently consistent with the measurement of profile meter. Note that in Figure 5.20(c) the shape of the wedge part was slightly bent owing to shear stress when it was cut.

When X-ray radiation shines on the edge of the razor blade, an intensity transition is expected to be observed in the transmission pattern at the knife-edge, because on one hand the 87 μm thick razor would effectively stop all the photons below 20 keV, while on the other hand it is completely transparent outside the razor blade. The profile of the intensity transition depends on the source intensity distribution and the geometry, and can be fitted by an error function for a Gaussian source and an ideal step-like knife-edge

$$S_X(x) = \frac{1}{2}\left[1 + \mathrm{erf}\left(\frac{x}{\sqrt{2}\mathbb{M}\sigma}\right)\right], \tag{5.7}$$

where x is the position perpendicular to the projection of the razor blade on the camera and σ denotes the source waist.

A better evaluation of the source size can be achieved using the diffraction pattern induced by the razor blade. In the far-field, the diffraction pattern is known as the Fraunhofer diffraction, whereas it is described by the Fresnel diffraction in the near-field [146]. The two frameworks are distinguished by the Fresnel number

$$Fr = \frac{D_a^2}{L_i \lambda}, \tag{5.8}$$

where D_a is the characteristic X-ray beam size in the obstacle plane. In our experiments, $L_i = 2.32$ m, $\lambda \leq 1.24$ nm (for $\mathcal{E}_{ph} \geq 1$ keV), and L_o=0.26 m. A typical divergence of an

[1] With the help of Oliver Antonin at LPGP.

X-ray beam generated in a 20 mm long capillary tube could be $\sim$ 5 mrad (See Chapter 6), which yields $D_a \simeq 1.3$ mm. It yields $Fr \simeq 580 \gg 1$, which suggests theory of the Fresnel diffraction must be applied. The Fresnel diffraction pattern convolves the source information, aperture shape, locations of the aperture and the detector, as illustrated in Figure 5.21.

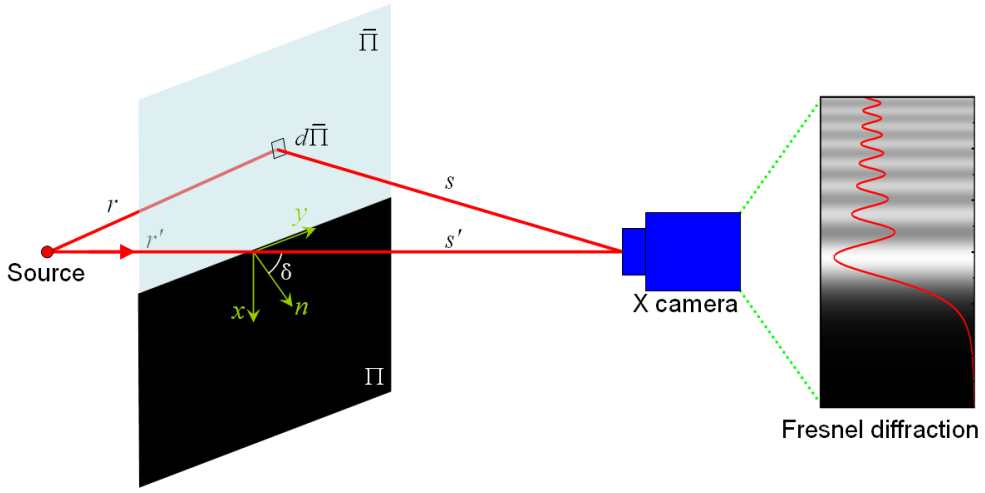

Figure 5.21: *Schematic illustration of the Fresnel diffraction from a half-plane, where* Π *represents the half-plane of obstacle.*

The general theory about Fresnel diffraction can be found in literature [146, 165]. The electric field at an observation point $P_0 = (x, y, z)$ after diffraction is given by

$$E(x,y,z) = -\frac{iU}{2\lambda}\iint_{\bar{\Pi}} \frac{e^{ik(r+s)}}{rs}[\cos(n,r) - \cos(n,s)]d\bar{\Pi}, \tag{5.9}$$

where U denotes the field amplitude, Π is the obstacle half-plane. r, s indicate the distances from the source and the observation point to the unit area $d\bar{\Pi}$, and n is the normal to the plane. Using the coordinate system shown in Figure 5.21, the obstacle half-plane can be defined as

$$\Pi = \{x > x_0, -\infty < y < \infty, z = 0\}. \tag{5.10}$$

Accordingly the other half-plane $\bar{\Pi}$ sits in vacuum, where the integral of Equation 5.9 is computed. To facilitate the calculation, especially the large parameter scan for least-squares fit, the razor blade is treated as an ideal step function, namely all the photons are absorbed by it. Equation 5.9 is then calculated to be

$$\begin{aligned} E(x,y,z) =& -\frac{iU}{2\lambda}\int_{-\infty}^{\infty}\int_{-\infty}^{x_0} \frac{e^{ik(r+s)}}{rs}[\cos(n,r) - \cos(n,s)]dxdy, \\ \simeq& -\frac{iU}{\lambda}\frac{\cos\delta}{r's'}\int_{-\infty}^{\infty}\int_{-\infty}^{x_0} e^{ik(r+s)}dxdy, \\ =& U'[C_F(w) + iS_F(w)], \end{aligned} \tag{5.11}$$

where r', s', and δ are defined in Figure 5.21. U', w, C_F, and S_F are given by

$$\begin{aligned} U' =& -\frac{iU\cos\delta}{\lambda}\frac{e^{ik(r'+s')}}{r's'}, \\ w =& \sqrt{\frac{2}{\lambda}\left(\frac{1}{r'}+\frac{1}{s'}\right)}x_0\cos\delta, \\ C_F =& \frac{\lambda}{2}\frac{1}{\left(\frac{1}{r'}+\frac{1}{s'}\right)\cos\delta}\left[\left(\frac{1}{2}+\mathcal{C}_F(w)\right)-\left(\frac{1}{2}+\mathcal{S}_F(w)\right)\right], \\ S_F =& \frac{\lambda}{2}\frac{1}{\left(\frac{1}{r'}+\frac{1}{s'}\right)\cos\delta}\left[\left(\frac{1}{2}+\mathcal{C}_F(w)\right)+\left(\frac{1}{2}+\mathcal{S}_F(w)\right)\right], \end{aligned} \tag{5.12}$$

where $\mathcal{C}_F(w) = \int_0^w \cos(t^2)dt$, $\mathcal{S}_F(w) = \int_0^w \sin(t^2)dt$ are the Fresnel integrals. Through Equation 5.11, one can finally obtain the diffraction intensity at P via

$$I = E\cdot E^* = \frac{I_0}{2}\left[\left(\frac{1}{2}+\mathcal{C}_F(w)\right)^2+\left(\frac{1}{2}+\mathcal{S}_F(w)\right)^2\right]. \tag{5.13}$$

The red line in Figure 5.22 is an example of the intensity profile produced by a monochromatic, 5 keV, point source. The half-plane and the detector are respectively 0.1 m and 1.1 m away from the source. The intensity overshoots, while the oscillation magnitude and period decrease with the distance from the knife-edge.

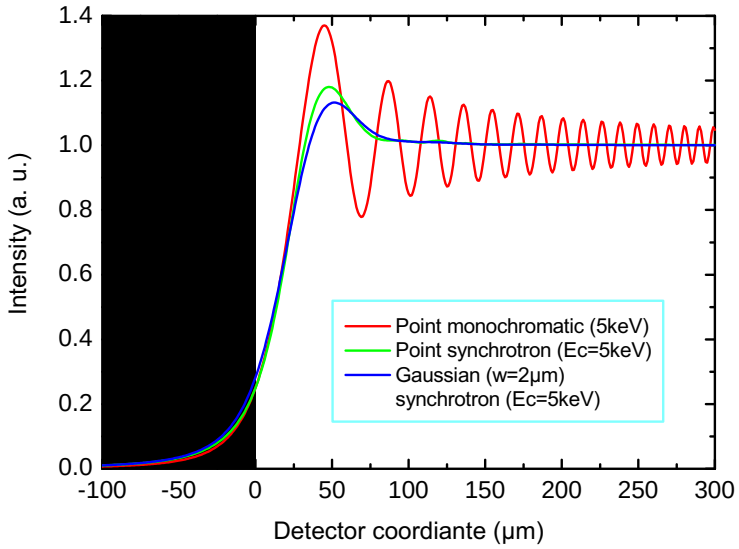

Figure 5.22: *Intensity profiles of Fresnel diffraction for fully incoherent source types. The spatial arrangements are $L_o = 0.1$ m and $L_i = 1$ m.*

In the case of our experiments, the X-ray has a finite source size, so the diffracted electric field has to be computed according to the spatial coherence of the source. As the phase distribution of the source is not known, here we examine two extreme cases of spatial coherence: fully incoherent and fully coherent [165]. If the source is fully incoherent, the diffraction pattern is given by

$$I_{inc}(x,y,z) = \int_\lambda \frac{dN_{ph}}{d\lambda}q_{ccd}(\lambda)\iint_\Xi f_I(x',y')I(x,y,z)dx'dy'd\lambda, \tag{5.14}$$

where $\Xi = [x', y']$ is the source plane, $f_I(x', y')$ represents the source intensity distribution, and $I(x, y, z)$ is calculated from Equation 5.13. The first integral in Equation 5.14 corresponds to the influences of X-ray spectrum and detector responsivity, while the second one relates to the effects of the source intensity distribution. If the source is fully coherent, the electric field at a observation point can be obtained through

$$E_{coh}(x, y, z) = \int_{\lambda} \frac{dN_{ph}}{d\lambda} q_{ccd}(\lambda) \iint_{\Xi} f_E(x', y') E(x, y, z) dx' dy' d\lambda, \tag{5.15}$$

where $E(x, y, z)$ is calculated from Equation 5.11, and $f_E(x', y')$ represents the source field distribution. The corresponding diffraction intensity distribution is therefore given by

$$I_{coh}(x, y, z) = E_{coh} \cdot E^*_{coh}. \tag{5.16}$$

Also shown in Figure 5.22 are two typical cases of fully incoherent source: a point source emits synchrotron radiation with critical energy of 5 keV, and another one has the same spectrum and moreover a Gaussian transverse profile with waist of 2 μm. It is seen that if the spectrum is broad, all the intensity oscillations except the first one are washed out even though the source is point-like. That's due to superposition of the diffraction fringes generated by photons with different energies. With a finite source size, the rising slope of the first overshot becomes even smoother. For a given fringe pattern measured in experiment, one can retrieve the critical energy and source size using a least-squares method. Such a fit could have a high precision, allowing to characterize an X-ray source size as small as 1 μm [58].

5.6 Summary

The multi-terawatt Ti:sapphire laser facility at the Lund Laser Centre in Sweden was employed for the two campaigns presented in this thesis, which delivered a laser pulse with FWHM duration of $\sim$ 40 fs and energy around 650 mJ on target. The phase abberations in the laser wavefront were compensated by a deformable mirror in order to achieve a symmetrical laser focal spot, while the laser pointing fluctuation was diminished by a stabilization system to merely 2.6 μrad in the focal plane.

Electrons and the X-rays were diagnosed simultaneously in the experiments. The high energy electrons were deflected by a magnet onto a scintillating (Kodak Lanex Regular) screen imaged by a CCD camera. For a recorded Lanex image, electron energy spectrum can be determined from the dispersion direction, while the undispersed direction yields the beam divergence, and the emitted photon number is proportional to electron beam charge. The X-ray photon energy was estimated using a Ross filter consisting of several metal pieces, and the CCD counts were used to determine the X-ray beam fluence. The X-ray source size can be deduced by imaging microscopic objects or through the intensity distribution of Fresnel diffraction induced by a razor blade.

Chapter 6

Experimental results and discussions

This chapter summarizes the most important results about high energy electrons and intense X-rays obtained in our experiments. The key features of the electrons and X-rays, and their dependences on plasma density and capillary parameters are first demonstrated. The second main part reports on the schematic study on electron and X-ray stabilities, and ends up with preliminary results of X-ray source size measurement. Results of numerical modelings are presented as well.

6.1 Introduction

The studies carried out in our group before this thesis include guiding intense laser pulses over long distance and generating linear plasma waves in capillary tubes [61]. The measurement of linear plasma wave amplitude was also performed during the thesis of Franck Wojda [62]. One way to use such a linear plasma wave is to inject an external electron bunch into the accelerating phase of the wave, which was not feasible with the accessible facilities when I started my PhD study. However, results on electron acceleration and X-ray generation using capillary guiding in the moderately nonlinear regime ($a_0 \simeq 0.7$) had already been obtained [46, 114, 115], where capillary tubes were found able to favor laser evolution and electron trapping. Due to operation around the threshold of self-injection, electrons were observed only in a narrow density regime, together with a photon critical energy ~ 1 keV and an X-ray fluence lower than 1×10^5 photons/mrad^2 [46].

During this thesis two campaigns were carried out at the LLC to explore capillary guided LWFA in the nonlinear regime, where simulations show that using long plasmas at relatively low density is promising to achieve multi-GeV range electrons [94]. To achieve low density plasmas and guide the intense laser over a long enough distance, capillary tubes [140] were used owing to the following considerations: the plasma density inside capillary tubes can be arbitrarily low, as the laser beam is guided by reflection from the tube walls and there is no density requirement for guiding, so that different plasma density ranges can be explored; the capillary tube is able to collect part of the laser energy in the wings around its central focal spot to assist laser guiding over a longer distance than in a gas jet or gas-cell [46, 47, 114]. The latter point is important from a practical point of view, as for present multi-terawatt laser facilities, the fraction of energy contained in the full width at half maximum (FWHM) focal spot is generally around or less than 50% [108, 194]. The laser energy outside the central focal spot is lost in the absence of guiding [107]. Hence this fraction of laser energy is not taken into account for the excitation

of plasma waves [98]. In the case of laser guiding by capillary tubes with radius larger than twice the waist of the focal spot, nearly all the laser energy can be collected by the interplay of self-focusing and reflection from the capillary wall, leading to a higher laser peak intensity and longer distance of self-focusing than in a medium without boundary.

The goal of the first campaign was to study the dependence of the electrons and X-rays on plasma density, and the role of capillary guiding on electron acceleration and X-ray production. Recently we performed a second campaign aiming at fully characterizing the stability of the electrons and X-rays, especially to investigate the correlations of the fluctuations between the laser and the produced beams. Moreover we attempted to test some interesting ideas in capillary tubes like gas mixture, plasma density ramp, and their effects on electron beam stability. Results of these two campaigns are presented in this chapter, together with the PIC and GEANT numerical modelings, to give the readers a full picture of our experimental conclusions.

The main parameters of the experiments and PIC simulations presented in this chapter are summarized as follows.

Table 6.1: *Summary of the parameters in the experiments and PIC simulations.*

Parameter	Experiment	PIC simulation
Laser wavelength (nm)	~ 800	800
Laser FWHM pulse duration (fs)	40 ± 5	40
Laser energy (mJ)	~ 650	650
a_0	~ 1.6	1.6
Offset of laser focus in capillary tube (mm)	~ 1	1, 2.5
Diameter of capillary tube (μm)	76-254	152
Length of capillary tube (mm)	8-30	10
Plasma electron density (10^{18} cm^{-3})	5-14	5, 7, 8, 12, 14

6.2 Properties of the electrons and X-rays

In this section, we present the results of the high energy electrons and X-rays obtained in our first campaign. Over the whole capillary parameter range explored, electron beams with charge[1] in the range of 1 to 100 pC and energy up to 300 MeV were observed. Meanwhile, X-rays in the range $1 - 10$ keV were observed with a peak brightness of the order of 10^{21} photons/s/mm^2/mrad^2/0.1%BW. One should always keep in mind that the beam charge determined experimentally accounts for electrons with an energy above the detector lower limit of 42 MeV.

6.2.1 Spectrally peaked electrons

It is always attractive to generate spectrally peaked electron beams, as they are required for many applications. As demonstrated in Chapter 2, spectrally peaked electron beams

[1]The beam charge was compensated for the underestimation induced by incorrect determination of the filter transmission discussed in Section 5.4, so the values of beam charge shown in this chapter are different from those in the publication [48].

can be obtained when the electrons are trapped very locally. The electron spectrum observed in experiment was found to sensitively depend on plasma density. For a given laser/capillary setup, we gradually decreased the plasma density towards the threshold of self-trapping [107, 108], where we were able to produce a spectrally peaked electron beam.

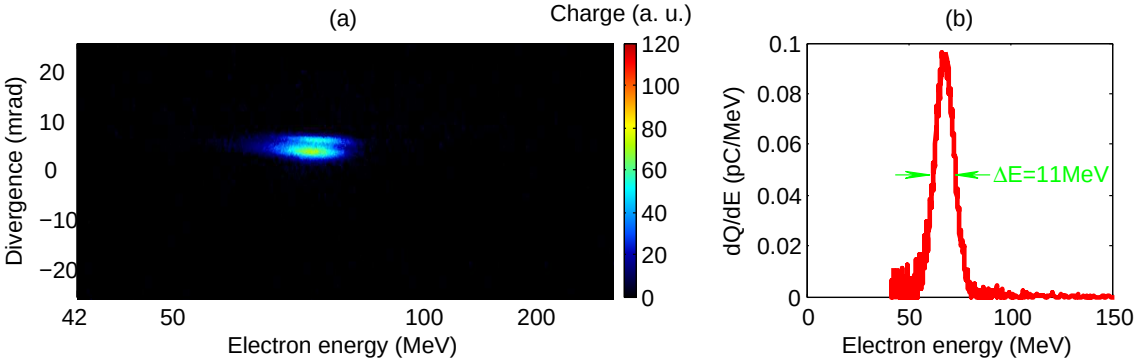

Figure 6.1: *(a) Raw Lanex image and (b) energy spectrum of a spectrally peaked electron bunch produced from a 20 mm long capillary tube with diameter of 152 μm at a plasma density* $\rho_e = (6 \pm 0.4) \times 10^{18}$ cm^{-3}. *The FWHM energy spread is 11 MeV.*

Figure 6.1 exhibits the spectrum of a typical spectrally peaked electron bunch obtained in experiment using a 20 mm long, 152 μm diameter capillary tube at a plasma density $\rho_e = (6 \pm 0.4) \times 10^{18}$ cm^{-3}. The electron beam peaks at 67 MeV with a total beam charge of approximately 2.8 pC. The FWHM energy spread is 11 MeV, corresponding to a relative spread of about 16%. This is the smallest energy spread achieved in the first campaign. It should be mentioned that the energy resolution of the spectrometer at 67 MeV is about 9.2 MeV owing to the beam divergence of 4.6 mrad FWHM, so the real electron energy spread should be smaller than the measured value of 11 MeV. At this plasma density, the critical power is $P_c \simeq 5$ TW, corresponding to $P_L/P_c \simeq 3.2$, which is very close to the threshold of laser power required for electron self-trapping found in Ref. [108] (See Section 2.5.3). However, owing to performing around the threshold of self-trapping, electron trapping is rather sensitive to laser or/and plasma fluctuation [37, 38, 39], so we just observed such a spectrally peaked electron beam occasionally. The fine structure of the electron beam in Figure 6.1(a) shows the bunch consists of two beamlets. It may be due to filament or/and hosing instabilities experienced by the electrons when they propagate in the plasma target beyond the laser pump depletion length $L_{pd}^{NL} \simeq 4.4$ mm [195].

6.2.2 Dependence of electrons and X-rays on plasma density

As laser-plasma interaction strongly depends on plasma density, it is of great interest to see how the produced electrons and X-rays are affected accordingly. The electrons are deflected onto the Lanex screen, and the X-ray camera is placed on-axis in the far-field, permitting us to record both the electrons and X-rays simultaneously. It is worth mentioning that X-rays were detected only for strong signals on the Lanex screen; in other words if there was no electron detected or the laser pulse was blocked, no X-ray was measured accordingly, which implies the X-rays indeed originate from the accelerated electrons.

To highlight the effects of plasma density, in this section we concentrate on one capillary tube of 10 mm in length and 178 μm in diameter, which was extensively studied in the first campaign. Two examples of energy spectra obtained for this tube are shown in

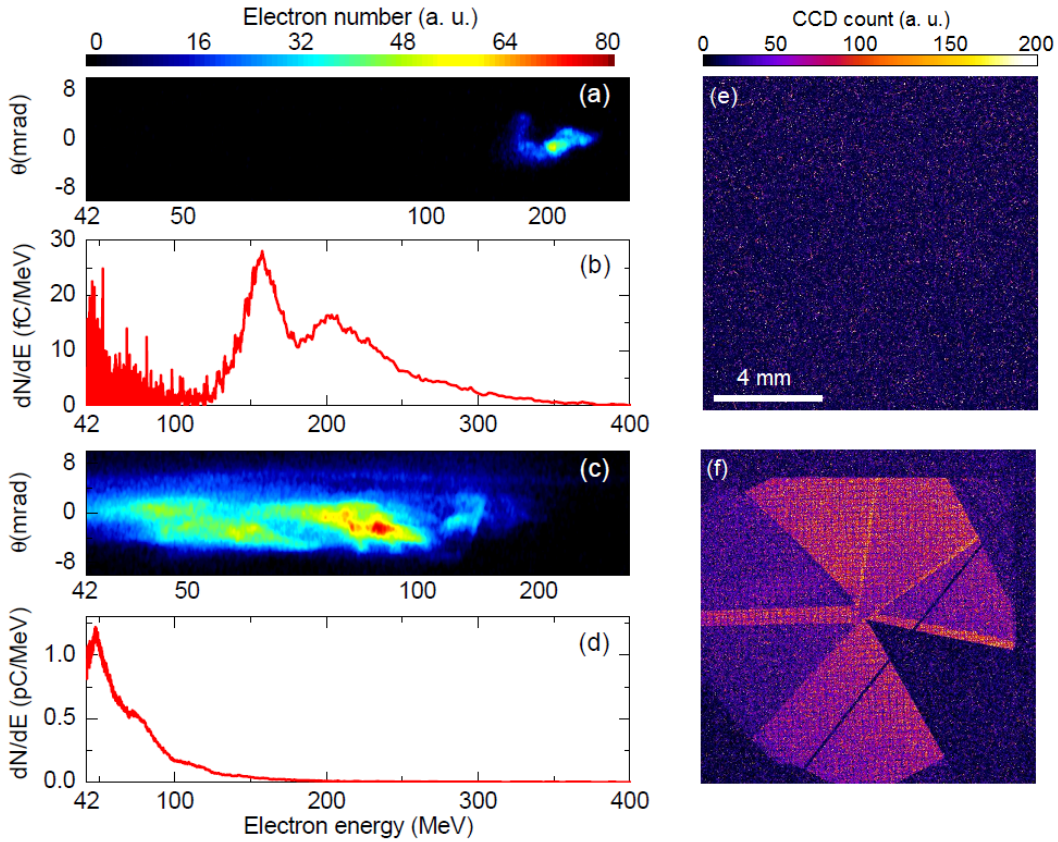

Figure 6.2: *Raw Lanex images and electron spectra obtained from a 10 mm long, 178 μm capillary tube at plasma densities: (a)-(b)* $(5.4 \pm 0.3) \times 10^{18}$ *cm*$^{-3}$*, and (c)-(d)* $(8.1 \pm 0.5) \times 10^{18}$ *cm*$^{-3}$*. (e)-(f) are the corresponding X-ray images.*

Figure 6.2 for two different values of the plasma electron density: $(5.4 \pm 0.3) \times 10^{18}$ cm^{-3} and $(8.1 \pm 0.5) \times 10^{18}$ cm^{-3}. The raw Lanex images are shown in panels (a) and (c), while the corresponding electron spectra are plotted in (b) and (d) after integrating in the transverse direction and rescaling in the horizontal direction to account for magnet dispersion. Accelerated electrons with a maximum energy of 300 MeV and a charge of $\sim$ 2 pC were obtained for the low plasma density case as seen in Figure 6.2(a)-(b). The maximum energy, $\mathcal{E}_{max}$, is defined when the energy spectrum decreases to 10% of its peak value. The electron beam FWHM divergence in the case of Figure 6.2(b) is around 5.2 mrad. It was found that at such a low plasma density, the electron beam properties exhibit large shot-to-shot fluctuations, due to the fact that LWFA operates just above the threshold of self-injection. When a higher plasma density, $\rho_e = (8.1 \pm 0.5) \times 10^{18}$ cm^{-3}, was used, electron beams with higher charges were produced, around 40 pC for the example in Figure 6.2(c)-(d). In this case, the maximum electron energy was limited to 120 MeV. Moreover, several structures are observed in the raw image of Figure 6.2(c), which can be interpreted as multiple electron trappings inside the bubble along the acceleration distance or/and electron emergences from different plasma buckets [196].

Exhibited in Figure 6.2(e)-(f) are the X-ray images corresponding to the two electron beams. Figure 6.2 (e) shows that no X-ray was detected for the low density case: although the electron energy is relatively high for this shot, the associated beam charge was too low to generate a detectable signal on the X-ray CCD. On the contrary, as seen in Figure

6.2(f), a strong X-ray signal was measured for the shot at higher plasma density owing to a higher beam charge. The different filters can be clearly seen, together with the copper grid substrate. The circular structure near the edges of the image is due to the filter holder blocking the edges of the beam. The photon energy was quantitatively determined using the transmissions of the X-ray beam through different metals, and a least squares method (See Section 5.5). For the case of Figure 6.2(f), the critical energy was evaluated to be 5.4 keV. Once the critical energy is known, one can furthermore quantify the X-ray fluence to be 5.7×10^5 photons/mrad^2.

In contrast to the narrow density range where self-electron trapping occurs at lower laser intensities [46, 115], of the order of 0.8×10^{18} W/cm^2 ($a_0 \simeq 0.6$), for the value of intensity used for the results presented in this chapter, electrons were detected in a broad range of plasma densities above the threshold for self-injection, as shown in Figure 6.3. In this figure, the maximum electron beam energy in (a), and the beam charge estimated for the corresponding shots in (b), are plotted as a function of the plasma electron density inside the capillary tube. The black squares are the experimental results, each point corresponding to one single laser shot and the error bars indicating the precision of the measurements.

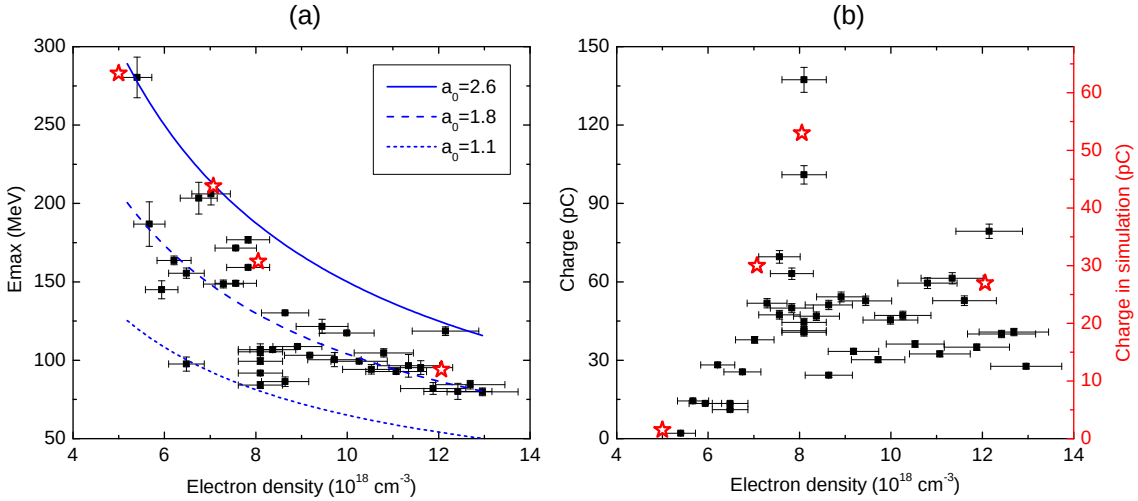

Figure 6.3: *(a) Maximum electron beam energy and (b) charge as a function of plasma electron density at the output of a 10 mm long, 178 µm diameter capillary tube. The black squares are experimental results, each point corresponding to one single laser shot. Red stars (the right-hand scale) are the results of PIC simulations. The curves in (a) show the predictions of scaling laws obtained for three different a_0 values.*

Figure 6.3(a) shows that the highest value of maximum beam energy is achieved for the lowest value of electron density where self-injection occurs, and that the beam maximum energy decreases as the plasma density is increased, in agreement with previous findings [37, 194]. The measured dependence of beam maximum energy behaves as $1/\rho_e$ and can be compared with the phenomenological scaling law developed for the 3D nonlinear regime [94] when the electron maximum energy is limited by dephasing: $\mathcal{E}_e\,[\mathrm{MeV}] = \frac{1}{3} a_0 \rho_c / \rho_e$. The experimental points are in a region of the graph limited by curves with values of a_0 in the range from 1.1 to 2.6, which can be interpreted as effective values of a_0 over the whole plasma length. The point of highest electron energy in Figure 6.3(a) corresponds to a curve with $a_0 = 2.6$. During the propagation in the plasma, the increase of laser intensity is linked to self-focusing and self-compressing (See Section 2.4) as the incident

laser power P_L is well above the critical power for self-focusing: $2.8P_c < P_L < 7.2P_c$. The maximum energy values measured agree well with 3D PIC simulation results (See Section 6.3), plotted as red stars in Figure 6.3(a).

The dephasing length L_{dp}, given by Equation 2.50, is calculated to be about 1.6 mm for $\rho_e = 5.4 \times 10^{18}$ cm^{-3}. L_{dp} becomes even shorter at higher plasma densities, and the capillary length, $L_{cap} = 10$ mm, was always longer than the dephasing length in this experiment. The electrons observed in this experiment were thus accelerated over the dephasing length and decelerated, so their output energies are in general lower than the prediction of the scaling law. The electron maximum energy obtained by PIC simulation at the output of the capillary tube agrees well with experimental observations. At low density the simulation data are consistent with the curve for $a_0 = 2.6$, while they start to deviate from it and approach the curve for $a_0 = 1.8$ as density increases, as the result of the shorter dephasing length and longer propagation distance inside the capillary beyond the dephasing length.

For plasma densities below 8×10^{18} cm^{-3}, the measured electron energy exhibits larger shot-to-shot fluctuations than in the larger density range. This might be attributed to electron injection just above the threshold of self-trapping, observed previously to be of the order of $P/P_c \simeq 3.3$ [114], corresponding here to a density of about 6×10^{18} cm^{-3}.

Figure 6.3(b) demonstrates that the beam charge reaches a maximum around the value of plasma density, $n_e = 8{\times}10^{18}$ cm^{-3} both in the experiment and the simulation. Here the characteristic pump depletion length is larger than the dephasing length in the range of electron density studied. Electron injection and acceleration occur above the threshold and the amount of accelerated charge increases with the density as the value of the ratio P_L/P_c becomes higher for a fixed incident laser power. The increase of accelerated charge above $\rho_e = 5{\times}10^{18}$ cm^{-3} can be explained by more efficient electron self-trapping occurring for a higher ratio of P_L/P_c, as observed in Ref. [108], and by the decrease of the phase velocity of the plasma wave. For densities in excess of $\rho_e = 8{\times}10^{18}$ cm^{-3}, beam charge does not increase due to the function of beam loading as previously observed in experiment [104] and simulation [114]. Moreover, the dephasing and pump depletion lengths being less than 1 mm and 2 mm respectively in this range of plasma density, some electrons are scattered during the propagation in the remaining part of the plasma [195], and do not reach the detector. The beam charges obtained in PIC simulation are about two times lower than the experimental ones, as shown in Figure 6.3(b). The main contribution to this difference is electrons going out from the simulation box. The simulation box moves forward with the group velocity of the laser in the plasma $v_g \simeq 0.998c$, while the accelerated electrons move in the first plasma bucket with speed of light c, so the electrons slip forward in the simulation box. Subsequently more and more of them overrun the front boundary of the simulation box and get lost with computation time increasing, resulting in the observed lower values of beam charge in the simulations.

Now let's examine the dependence of X-ray on plasma electron density. Figure 6.4 shows that betatron X-ray radiation can be tuned by varying the plasma density. In this case, the X-ray fluence peaks at $5.7{\times}10^5$ phtons/mrad^2 for $\rho_e \simeq 8{\times}10^{18}$ cm^{-3}, and behaves similarly as the beam charge given in Figure 6.3(b). The influences of the plasma electron density on the X-ray fluence can be understood as a result of the influences of the density on the laser propagation and the associated electron injection and acceleration. At lower plasma densities, the electron number decreases rapidly owing to inefficient self-trapping, so the photon number diminishes accordingly. If the beam charge is too low, the X-ray signal finally vanishes, as seen in Figure 6.2(e). Above the optimum density, trapping becomes more efficient and more charge can be accelerated, however the electron energy

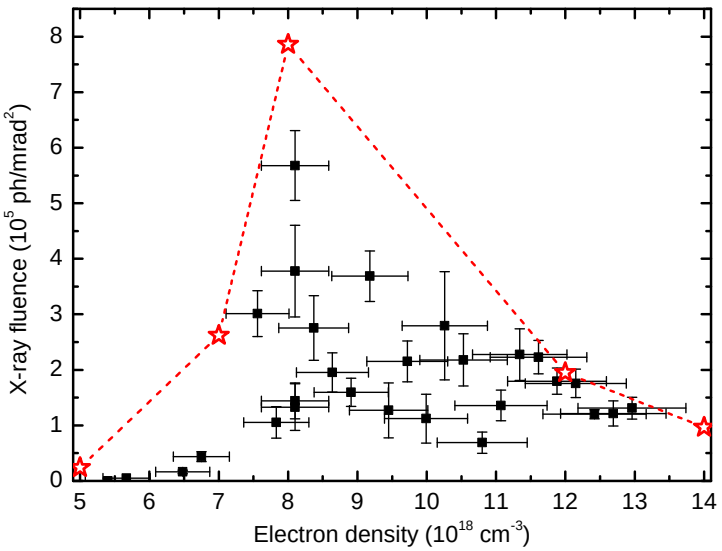

Figure 6.4: *X-ray fluence as a function of plasma electron density for the 10 mm long, 178 μm diameter capillary tube. Each black square corresponds to one laser shot, and the stars represent the results obtained in 3D PIC simulations.*

becomes lower due to shortening of both the electron dephasing length and laser pump depletion length, which consequently leads to a drop of X-ray signal. This dependence of X-ray fluence on plasma density is well reproduced by simulation results, plotted as red stars in Figure 6.4. More details of the simulations will be presented in Section 6.4.

6.2.3 Enhancement of X-ray by capillary guiding

To highlight the role of capillary guiding on electron acceleration and X-ray generation, we compare the results obtained from the 10 mm long, 178 μm capillary tube and a 2 mm long gas jet. The two targets were used during the same run with the same experimental parameters at the LLC. The laser was focused onto the front edge of a 2 mm gas jet which provides a plasma with a plateau of 1.8 ± 0.1 mm long. Electron trapping starts at a relatively low density in the case of capillary tube, and furthermore the peak X-ray brightness is enhanced by a factor of around 30 comparing with the result of the gas jet [48].

The enhancement of the X-ray fluence and the associated electron features are demonstrated in Figure 6.5 by comparison of the X-ray fluence measured from the two targets under the same experimental conditions. One can immediately find that the maximum X-ray fluence in the capillary is more than one order of magnitude higher than in the gas jet. This enhancement can be explained as follows.

Figure 6.5(c) shows that for the laser intensity used in this experiment, the use of a capillary tube allows electron self-injection to happen at lower density than in the gas jet. The capillary provides a long distance for laser evolution to the threshold required for self-trapping [46, 115], and helps collecting and refocusing the energy initially in the wings of the laser spot [114]; the excitation of multiple modes and their beating can also give rise locally to higher intensity than in vacuum, thus favoring an increase of a_0. In contrast, electron trapping starts around $\rho_e = 11 \times 10^{18}$ cm^{-3} for the gas jet, which results in lower energy electrons, as electron energy inversely depends on plasma density [94].

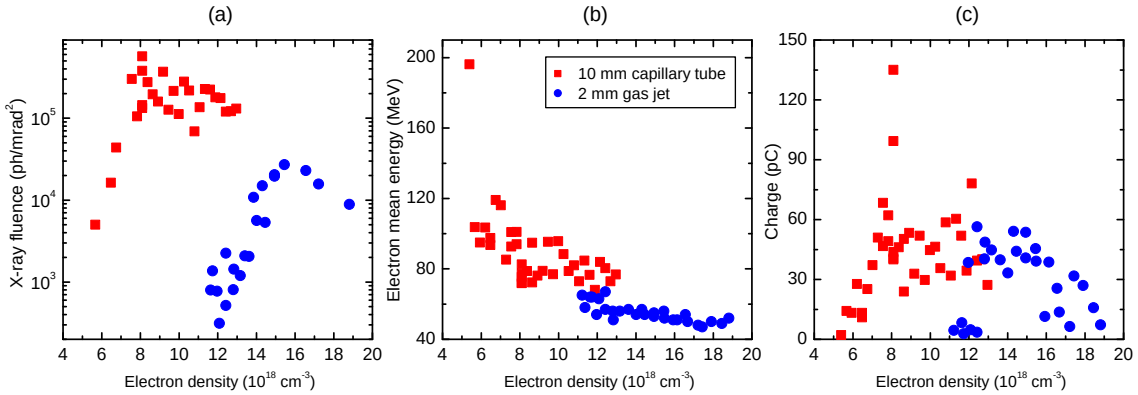

Figure 6.5: *(a) X-ray fluence in logarithmic scale, (b) electron mean energy and (c) beam charge as a function of plasma density for the 10 mm long capillary (red squares) and 2 mm gas jet (blue dots).*

In the density region where both plasma media produce accelerated electrons, namely $\rho_e = (11-13)\times10^{18}$ cm^{-3}, the increased electron energy in the capillary tube can be attributed to the more efficient use of laser energy by capillary collecting. In consequence, although similar beam charges in the range of 1 to 100 pC were observed for the two cases, much more intense X-rays were produced in the capillary tube as there is a strong nonlinear dependence of X-ray intensity on electron energy [116].

It is also interesting to assess the enhancement of X-ray peak brightness. The maximum X-ray fluence measured from the capillary tube is $(5.7 \pm 0.6) \times 10^5$ photons/mrad^2 for $\rho_e = 8 \times 10^{18}$ cm^{-3} [Figure 6.5(a)]. To estimate the peak brightness, the source size and pulse duration of X-ray are needed. The source size can be estimated from the expression of critical energy [120] as $r_\beta = \mathcal{E}_c c/3\hbar\gamma^3\omega_\beta^2$. The relativistic factor is determined using the mean energy of the electron spectra $\langle\mathcal{E}_e\rangle$, where $\langle\mathcal{E}_e\rangle$ is the average of electron energies weighted by their respective spectral intensities. For the shot plotted in Figure 6.2(d), $\langle\mathcal{E}_e\rangle$ is calculated to be 88±4 MeV. The source size is therefore estimated to be $r_\beta = 2 \pm 0.3$ μm. This estimation is also validated by 3D PIC simulation performed for input parameters close to the experimental ones (See Section 6.3). It shows that the laser pulse nonlinear evolution in the 178 μm diameter capillary tube leads to a maximum normalized vector potential in the range $3 < a_0 < 4$, and produces accelerated electrons with a mean energy of about 130 MeV. The transverse and longitudinal sizes of the electron bunch in the simulation are 1.3 μm and 10 μm (∼35 fs), respectively, in reasonable agreement with the estimation from the measurements. The peak brightness achieved in our experiment is conservatively estimated, using $r_\beta = 2$ μm, to be $\sim 1 \times 10^{21}$ photons/s/mm^2/mrad^2/0.1%BW. To the best of our knowledge, this is the brightest X-ray obtained with a 16 TW laser. On the other hand, the maximum X-ray fluence obtained with the gas jet is 2.7×10^4 photons/mrad^2 for $\rho_e = 15 \times 10^{18}$ cm^{-3}. Using the values obtained from experimental data, $\mathcal{E}_c = 4.6$ keV, $\langle\mathcal{E}_e\rangle = 56$ MeV, the source size is estimated to be 2.4 μm and the corresponding peak brightness is $\sim 3 \times 10^{19}$ photons/s/mm^2/mrad^2/0.1%BW, which is 30 times lower compared to the case of capillary guiding.

These results highlight the role of capillary guiding. It is consistent with the prediction of the scaling laws of betatron radiation in the blowout regime: lowering plasma density or/and increasing laser intensity are expected to improve X-ray brightness [106]. We would like to stress that using a longer gas jet or a gas-cell could also increase the X-ray

brightness, but the use of a capillary tube enhances this effect by collecting the unfocused laser energy and reflecting it back to the axis.

In the case of capillary tube, the wiggler strength parameter at the optimal density is computed to be $K_\beta \simeq 10$. Taking into account the divergence of the X-ray beam, $\Theta_\beta = K_\beta/\gamma$, the estimated total photon number over the whole spectrum is of the order of 10^9 per shot. Such a compact, bright, and ultrashort X-ray burst is of great interest for many applications such as phase-contrast imaging [123, 124].

6.2.4 Diagnostics of electron acceleration

As demonstrated in Section 3.6, betatron X-ray radiation is also a powerful tool to investigate the acceleration process because of its strong dependence on the electron properties [46, 60, 115]. The diagnostic of electron acceleration is very important for knowing how long the laser-plasma interaction extends inside the plasma in the nonlinear regime for matching the capillary length.

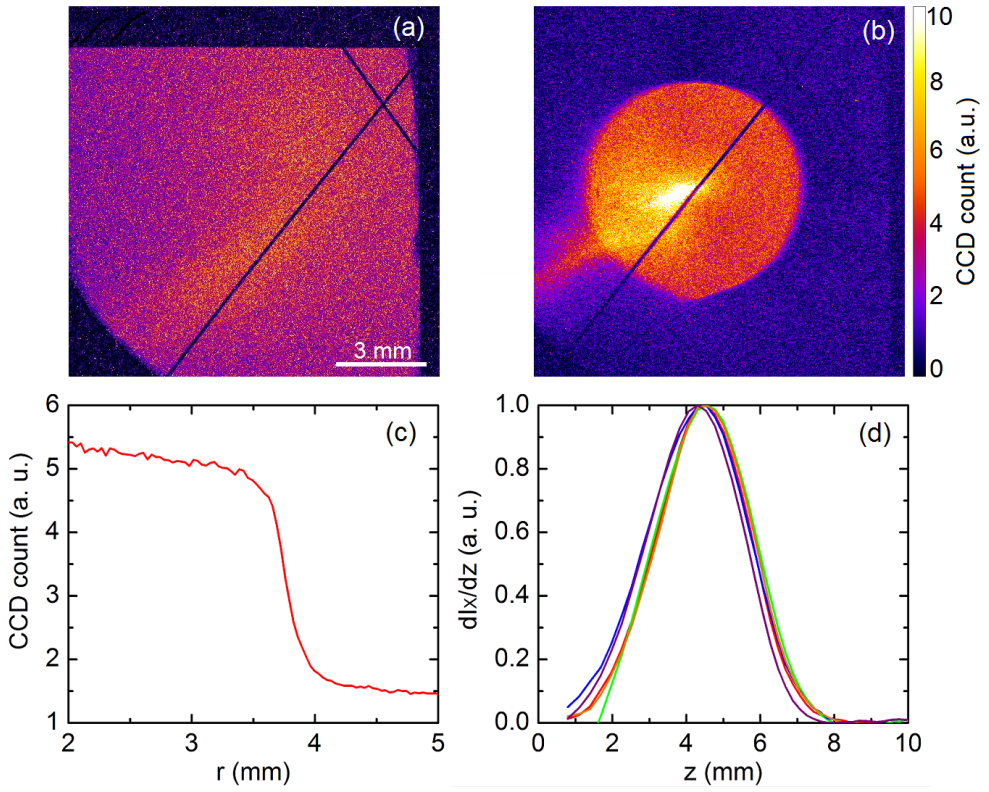

Figure 6.6: *X-ray beam distributions measured for* $\rho_e = (8.1 \pm 0.5) \times 10^{18}$ cm^{-3} *at the output of (a) the 10 mm long, 178 µm diameter capillary tube, (b) a 30.5 mm long, 178 µm diameter capillary tube; (c) averaged radial intensity profile of (b); (d) longitudinal profiles of X-ray emission for five consecutive shots under the same conditions. The curves are normalized to their respective maxima.*

The X-ray source is closer to the capillary exit when a short capillary tube is used, which geometrically produces a shadow with a larger diameter on the detector. For example, most of the shadow of the 10 mm long, 178 μm diameter capillary tube was beyond the X-ray detector size, as seen in Figure 6.6(a). Only roughly a quarter of the X-ray beam going through the capillary exit could be recorded. As the shortest capillary tube studied, $L_{cap} = 10$ mm, is still longer than the whole distance of laser evolution and

electron acceleration (See Figure 6.11), so that the X-ray emission due to electron trapping and acceleration is expected to be the same for a longer capillary tube. In order to determine the X-ray profile, a 30.5 mm long capillary tube was employed, for which the X-ray beam confined by the capillary exit could be recorded, like in Figure 6.6(b). In this shot, the X-ray beam is homogeneous expect for a bright feature in the bottom left region. This feature can be explained by the acceleration of some electrons along the direction of the feature extension [128]. To avoid this specific feature in the analysis, the bottom left region in Figure 6.6(b) is excluded in the following determination. The radial profile of the X-ray signal averaged over the azimuthal angle was calculated and plotted in Figure 6.6(c). In this plot, one can immediately find the transition zone between $r = 3.5 - 4$ mm. Substituting this profile into Equation 3.42, the longitudinal distribution of X-ray emission is obtained, and plotted in Figure 6.6(d). Also plotted are four other successive shots. In this calculation, $z = 0$ corresponds to the capillary entrance.

It shows that electrons start to generate detectable X-rays with photon energy above 2 keV around $z \simeq 2$ mm. The photons become detectable (> 2 keV) when the electron energy is higher than ~ 50 MeV for the plasma density 8×10^{18} cm^{-3} and oscillation amplitude $r_\beta = 2$ μm. After a distance corresponding to electron acceleration, the X-ray emission has a FWHM extension of about 3 mm, and peaks at $z \simeq 4.5$ mm, where the electrons reach their maximum energy (See Figure 6.11), because the radiated power scales with γ^4 [116]. Afterwards, the X-ray emission decreases and terminates at $z \simeq 7$ mm where the laser is fully depleted. The precision of the above analysis is limited by the beam transverse source size. For the position of emission peak at $z = 4.5$ mm, a beam size $r_\beta = 2$ μm will result in the same intensity gradient on the detector as does a longitudinal emission extending ~ 600 μm, which sets the resolution of the determination of the emission position. It should be also noted that this diagnostic scheme requires photon energy does not change significantly within the length scale of the intensity transition zone on the detector [$r \simeq 3.5 - 4$ mm in Figure 6.6(c)]. If not, the measured signal profile, $S_X(r)$, will be different from the real case, as the quantum efficiency or the CCD count of the detector (See Figure 5.16) sensitively depends on photon energy.

The emission profile determined in Figure 6.6(d) is confirmed by 3D PIC simulations shown in Section 6.3. They show that in the highly nonlinear regime electron acceleration terminates before $z = 10$ mm. This physical picture is quite different from the moderately nonlinear regime [46, 115], where several centimeter long capillary tubes are necessary to favor laser reaching the threshold of electron self-trapping.

6.2.5 Correlation of electrons and X-rays stability

One goal of the first campaign was examining the stability of the produced electrons and X-rays using capillary tubes. We were particularly intersected in finding the correlations between the fluctuations of electrons and X-rays, as there are some publications about the electron stability [41, 44, 45, 197], whereas none of them investigates the stability of betatron radiation. Considering its importance for the applications, we were therefore motivated to address this issue.

In previous section, we showed that the X-ray fluence exhibits large shot-to-shot fluctuations, as presented in Figure 6.4. These fluctuations could result from the process of electron injection that determines beam charge or/and the acceleration process which determines electron energy. These two effects together contribute to the X-ray intensity. The acceleration process has been characterized in Section 6.2.4 through the X-ray far-field profile. In Figure 6.6(d), the calculated longitudinal profiles of X-ray emission indicate a similar position and distance of X-ray emission for five consecutive shots, which implies

similar processes of electron acceleration. However the maximum amplitude of these emission curves [not shown in Figure 6.6(d) where they are normalized with their respective magnitudes], exhibits a fluctuation of the order of 20%. In this sense, it can be assumed that the origin of the fluctuations lies less in the acceleration process than in the trapping conditions, i.e. in the amount of injected charge. In order to get some insight on the origin of fluctuations, the stability of electrons and X-rays was examined.

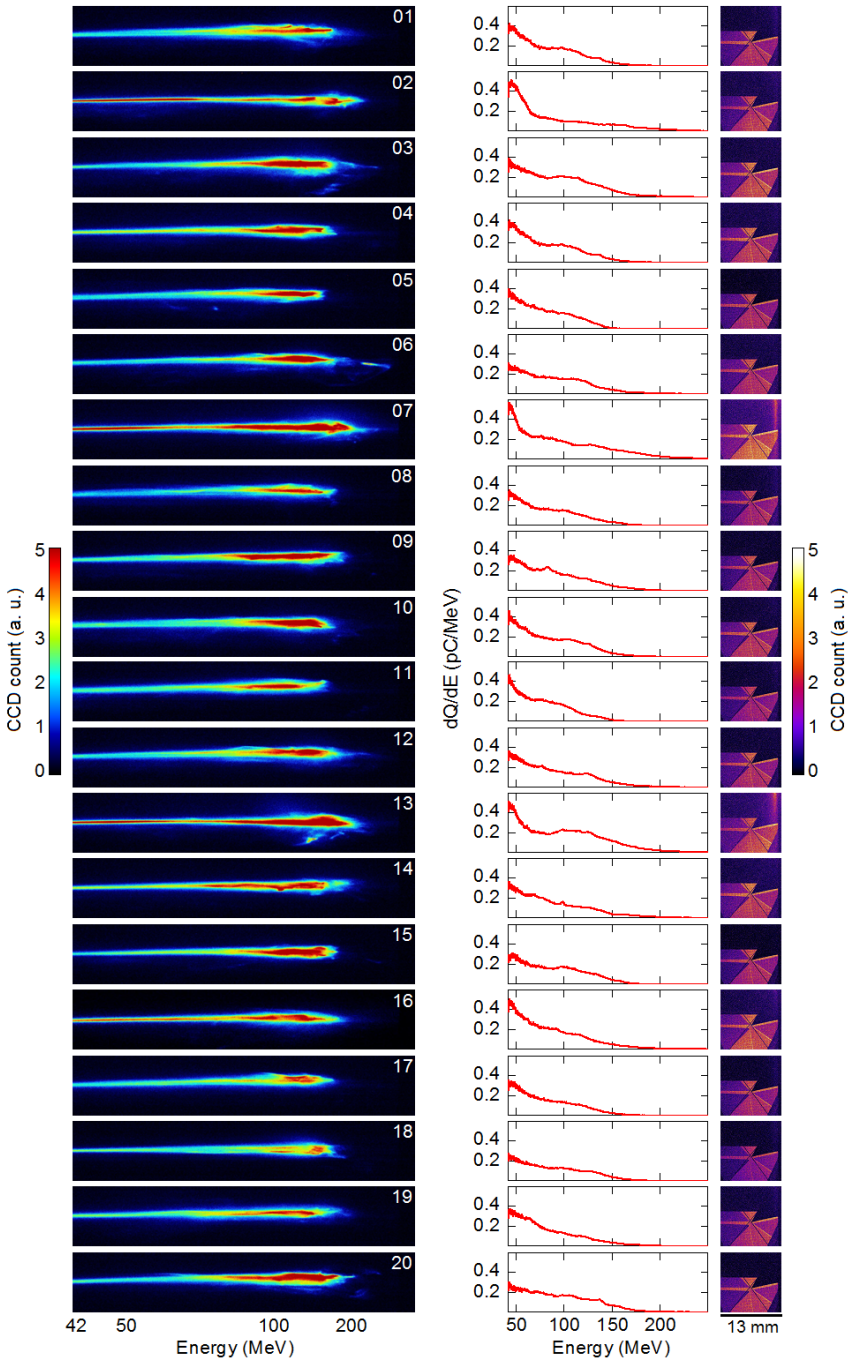

Figure 6.7: *Raw Lanex images (left panel), electron spectra(middle panel), and X-ray images (right panel) of 20 consecutive shots measured with a 10 mm long, 203 μm diameter capillary tube for a plasma density* $(7 \pm 0.4) \times 10^{18}$ cm^{-3}.

Figure 6.7 shows the electron and X-ray data recorded for 20 consecutive laser shots with a 10 mm long, 203 μm diameter capillary tube. The plasma density was chosen to be $\rho_e = (7 \pm 0.4) \times 10^{18}$ cm^{-3}, for which strong signals could be obtained for both electrons and X-rays. For these parameters, electron injection occurred for every shot. On average, $\sim$ 40 pC electrons were accelerated to a maximum energy of $\sim$150 MeV. The main

Table 6.2: *Summary of the main parameters of the electrons and X-rays associated with the shots in Figure 6.7.*

	$\mathcal{E}_{max}$ (MeV)	$\langle\mathcal{E}_e\rangle$ (MeV)	Q (pC)	$\mathcal{E}_c$ (keV)	S_X (photons/mrad^2)
Mean	147	91.4	46	3.3	2.5×10^5
Std	11.6	6.6	7.8	0.3	3×10^4
Std/Mean (%)	8	7	17	9	12

parameters of the electrons and the corresponding X-rays are summarized in Table 6.2. In terms of electron energy, both the maximum energy $\mathcal{E}_{max}$ (147$\pm$11.6 MeV) and the mean one $\langle\mathcal{E}_e\rangle$ (91.4$\pm$6.6 MeV) exhibit a relatively small instability with a relative standard deviation (std/mean) of $7-8\%$. The beam charge exhibits a shot-to-shot fluctuation of 17%. The critical energy of X-ray exhibits a fluctuation of about 9%, and the X-ray fluence fluctuation was measured to be 12%. Note that these X-rays in Figure 6.7 constitute the most intense on-axis part, measured by the detector with a small collecting angle, which may have smaller fluctuations than the the total X-ray beam.

Figure 6.8 shows the measured X-ray fluence as a function of the measured beam charge. As seen, the X-ray fluence and beam charge are linearly correlated. The extrapolation of the linear fit is close to zero when there is no charge. The residual value of the fluence may be due to the fact that electrons with energy less than 42 MeV which are beyond the detector limit, and are not taken into account for the calculation of beam charge. The slope of the linear fit is calculated to be 7.8×10^{-4} photons/mrad^2 per electron. The scaling developed for betatron radiation in ion channels [198] shows that the average number of photons emitted by an oscillating electron is given by $N_X \simeq 5.6 \times 10^{-3} N_\beta K$. The opening solid angle of the betatron radiation [116], $\Omega = K/\gamma^2$, can be used to evaluate the strength parameter. The number of photons per solid angle can therefore be theoretically estimated to be $N_X/\Omega \simeq 5.6 \times 10^{-9}\gamma^2 N_\beta$ in unit of photons/mrad^2 per electron. By measuring electron energy, γ was evaluated as the average value plus/minus three times the standard deviation to be $\gamma = 183 \pm 40$. Using the value of the slope of the linear fit in Figure 6.8, the number of oscillations performed by an electron in the plasma is calculated to be $N_\beta \simeq 4 \pm 2$. From this analysis of experimental results, we are thus able to estimate that the electron fulfills about four oscillations in the plasma. This finding is in reasonable agreement with the determination $N_\beta \simeq 5$ in PIC simulations for plasma density $\rho_e = 7 \times 10^{18}$ cm^{-3}.

The instability of beam charge is probably due to the process of electron self-injection. In the bubble regime, the dynamics of electron self-injection is a complex process dependent on the laser nonlinear evolution [108], the bubble dynamics [94], and beam loading [199]. As a result, a slight change to one of these processes, due for example to fluctuations of the laser energy distribution at the entrance of the plasma, would subsequently induce a large variation on beam charge, and consequently on the X-ray fluence. Stabilizing the electron beam charge would therefore be a reasonable way to reduce shot-to-shot fluctuations and

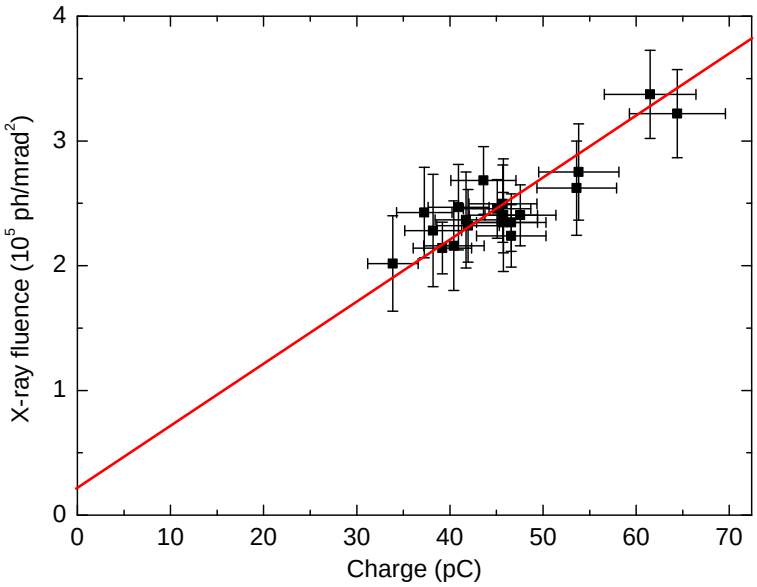

Figure 6.8: *X-ray fluence as a function of beam charge for the 20 shots shown in Figure 6.7, where the red line is a linear fit.*

improve X-ray stability. The beam charge has been observed to be the most unstable parameter of the electron bunches produced in LWFAs. Typically, the variation of beam charge is $> 50\%$ for commonly used gas jets [197], 16% for a gas-cell [45], $\sim 36\%$ for advanced optical injection techniques [41], and 45% for the recent staged acceleration with separated nozzle injector [44]. Although there is no corresponding study on X-ray stability in these publications, it is still reasonable to stress that controlling the beam charge would benefit X-ray stability.

6.2.6 Influence of capillary parameters

In this section, we discuss the influence of capillary diameter and length on the produced electron beams. As presented in Chapter 4, laser coupling and mode excitation sensitively depend on capillary diameter, and affect the structure of plasma wave generated inside capillary tubes. On the other hand, capillary length determines the plasma length which could furthermore affect the process of electron acceleration if the laser pump depletion length is long enough. The influence of capillary parameters were therefore explored in the first campaign.

Figure 6.9 displays the maximum electron energies and beam charges over the whole density range for three 20 mm long capillary tubes with 152, 178, and 203 μm diameters. The curves in (a) represents indicate the scaling law of electron energy $\mathcal{E}_e[\mathrm{MeV}] = \frac{a_0}{3}\rho_c/\rho_e$ developed in Ref. [94], and the a_o values agreeing best with the three cases are 1.9, 1.9, and 1.7, respectively. The curves in Figure 6.9(a) show higher electron energies (laser intensities) are achieved in the 152 and 178 μm tubes than in the 203 μm tube, but generally, the electron energy and beam charge are not significantly affected by capillary diameter within the explored parameter range. This finding can be elucidated as follows. As the laser power is well above the critical power, it is mainly guided by self-focusing and assisted by capillary collecting. Since the laser focal spot with 20 μm at the first minimum is relatively small compared to the capillary diameters ranging from 152 to 203 μm, higher eigenmodes are excited in the capillary tubes, as shown in Figure 5.6. In terms

of laser energy, the total coupling efficiency is above 95% for all the three diameters, so similar mechanisms of laser propagation and electron acceleration happen in the examined capillary tubes.

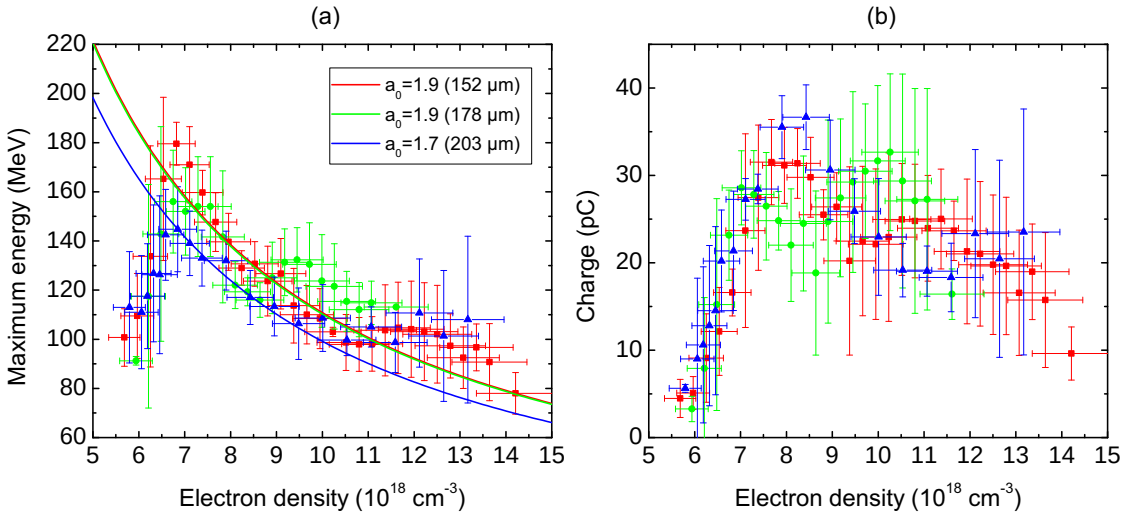

Figure 6.9: *(a) Electron maximum energy and (b) beam charge as a function of plasma density for 20 mm long capillary tubes with diameters of 152 μm (red squares), 178 μm (green circles), and 203 μm (blue triangles). Each point represents the average value of several shots for a given plasma density. The curves in (a) correspond to the scaling law for electron maximum energy* $\mathcal{E}_e = \frac{a_0}{3}\rho_c/\rho_e$.

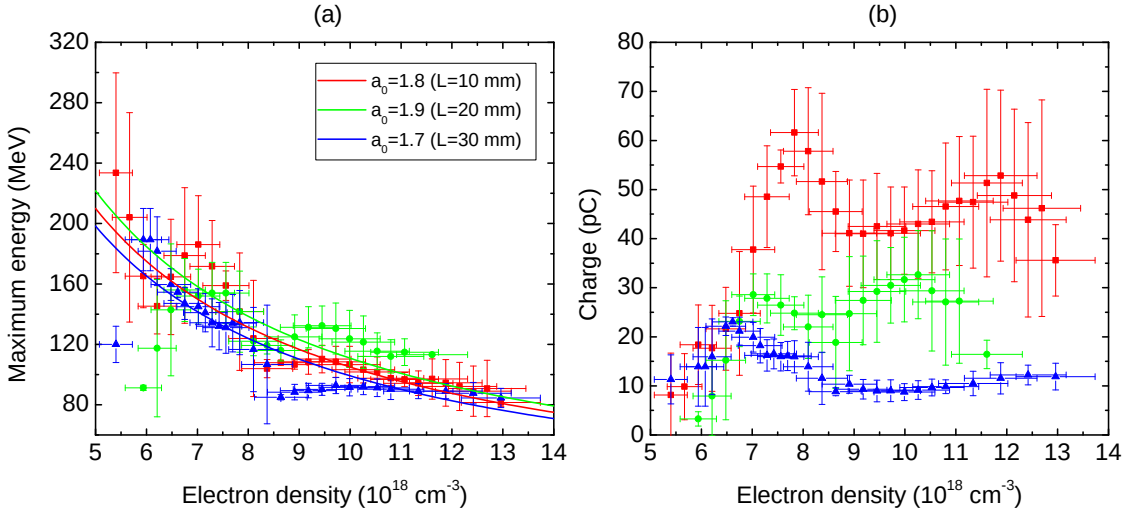

Figure 6.10: *(a) Electron maximum energy and (b) beam charge as a function of plasma density for 10 mm (red squares), 20 mm (green circles), and 30 mm (blue triangles) long capillary tubes with diameter of 178 μm. Each point represents the average value of several shots for a given plasma density. The curves in (a) correspond to the scaling law for electron maximum energy* $\mathcal{E}_e = \frac{a_0}{3}\rho_c/\rho_e$.

Figure 6.10 shows the influence of capillary length, where the electron maximum energy and beam charge are plotted as functions of plasma density for 10 mm, 20 mm, and 30 mm long capillary tubes with a given diameter of 178 μm. Likewise, the curves in (a) indicate

the scaling law of electron maximum energy $\mathcal{E}_e[\mathrm{MeV}] = \frac{a_0}{3}\rho_c/\rho_e$, and the corresponding a_0 values are 1.8, 1.9, and 1.7 for the three cases, respectively. In terms of electron energy, there is no substantial difference for the three cases. This observation agrees with the characterization of electron acceleration in the plasma demonstrated in Section 6.2.4, where the acceleration process is shown to terminate before the first 10 mm. Therefore the accelerated electrons can not gain energy as long as the plasma wave driven by the bunch itself is negligible. In Figure 6.10(b), it is noticeable that beam charge becomes lower in longer capillary tubes. This phenomenon can be explained by laser electron interaction. As will be seen in PIC simulation, the accelerated electrons finally catch up with and overrun the driving laser pulse, during which the electrons are transversely scattered by the laser ponderomotive force, resulting in a significant increase in the beam divergence. Subsequently, some of the scattered electrons enter the downstream part of the capillary wall. This process decreases the measured beam charge in two ways: (*i*) the electrons with divergence larger than the acceptable angle of the magnet in front of the Lanex screen ($\sim$ 30 mrad) are not measured; (*ii*) the electrons entering the capillary wall lose their energy therein. If their final energy is below the lower limit of the detection 42 MeV, they will not be recorded. Longer the capillary tube is, the more electrons are lost, and less beam charge is measured. When the scattered electrons go through the capillary wall, they generate bremsstrahlung radiation which casts a second illumination on the X-ray detector. This phenomenon will be presented in Section 6.4.

6.3 Results of PIC simulation

In order to obtain a deeper understanding of the underlying physics of LWFA in capillary tubes, simulations were performed with the 3D PIC code CALDER-CIRC [112]. Parameters were chosen close to the experimental ones: a FWHM 40 fs laser pulse was taken as input condition with a normalized intensity of $a_0 = 1.6$, and the transverse profile measured experimentally and shown in Figure 5.8. In experiments, the laser focus in vacuum was set inside the capillary at 1 mm from the capillary entrance. A similar condition was studied in the simulation and compared to focusing position at 2.5 mm from the entrance. The comparison of two PIC simulation cases with different focus positions presented in Figure 6.11 highlights the sensitivity of the laser propagation to the coupling conditions at the entrance of the plasma.

As demonstrated in Chapter 4, numerical simulations using the FLUENT code show that the gas density profile inside capillary tubes is constant over the length situated between the two slits, and decreases from the slits positions to the ends of the capillary tube. The gas distribution in the capillary tube and the density profile between the slit and the capillary exit was determined in Ref. [164]. For PIC simulations, the density profiles were simply assumed to be linearly increasing from 0 to a constant value of density, ρ_e, over a length of 3 mm, as shown in Figure 6.11(a) and (c); the capillary entrance is located at $z = 0$ mm and the density plateau is assumed to start at $z = 2.5$ mm. More details regarding the PIC simulation can be found in Ref. [115].

Simulations were carried out for different plasma electron densities and compared to experimental results. Whereas in the experiment the laser was focused 1 mm inside capillary tubes, it was found that simulation results are in good agreement with experiments for simulation results with focus at $z = 2.5$ mm, as can be shown in Figure 6.3 and Figure 6.4. This sensitivity to focusing position is linked to the density profile existing between the slit and the entrance of the capillary tube: it has not been measured experimentally, and can only be approximately calculated by fluid calculations. In the remaining part of

this section, the behaviour of the laser beam intensity, electron beam energy, and X-ray emission are examined along the capillary axis and the two cases of focus positions are compared for the plasma density $\rho_e = 8 \times 10^{18}$ cm^{-3}, at which both electrons and X-rays were systematically studied in experiment.

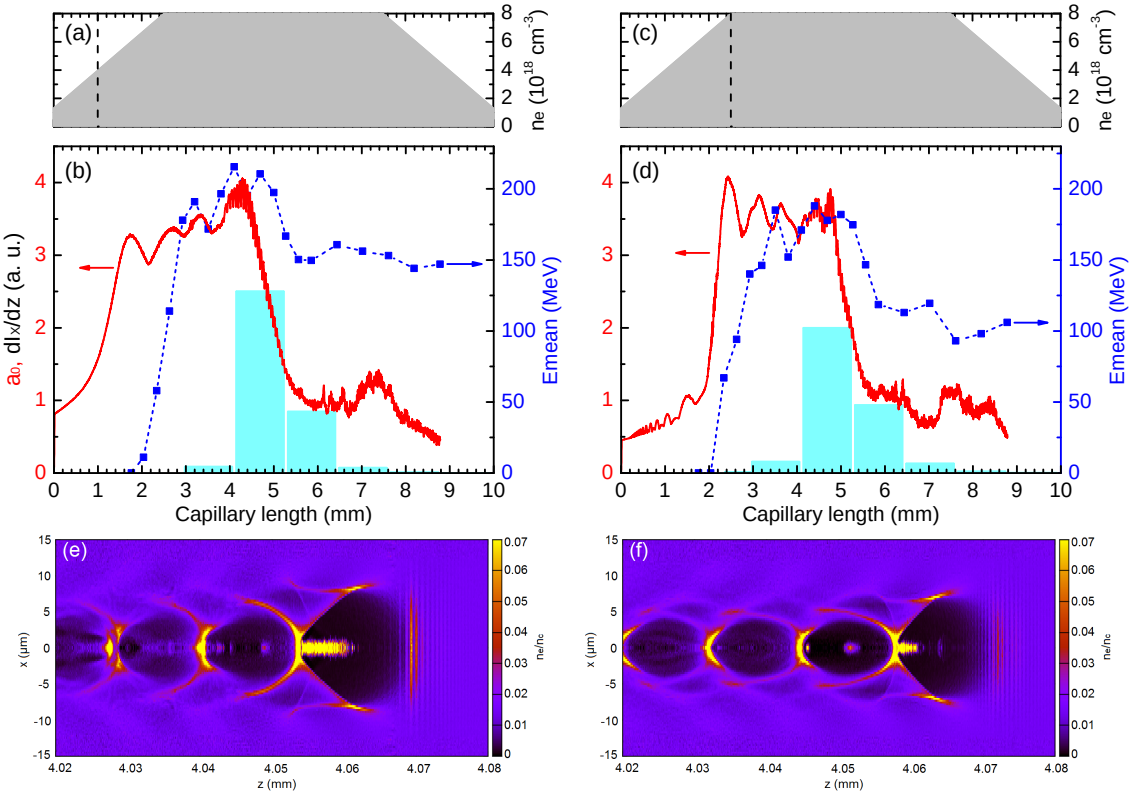

Figure 6.11: *Simulation results for $a_0 = 1.6$, and plasma density 8×10^{18} cm^{-3}. (a) Density profile used in 3D PIC simulation with laser focus position in vacuum at $z = 1$ mm, indicated by the vertical dashed line. (b) Evolution of the normalized laser intensity (red solid line) and the mean energy (dashed blue line) of the electron bunch accelerated in the first plasma bucket. The histogram corresponds to the amplitude of X-ray emission in arbitrary unit. (e) Snapshot of plasma density around the position $z = 4.07$ mm, where the laser propagates from left to right. The right column represents the corresponding results with laser focus position in vacuum at $z = 2.5$ mm.*

The left column in Figure 6.11 corresponds to the case of focus position of $z = 1$ mm. As seen in Figure 6.11, after entering the plasma the laser beam quickly self-focuses, and the normalized laser intensity increases to $a_0 \geq 3$ at $z \simeq 1.7$ mm. With the help of capillary guiding and self-focusing, the laser propagates with a stable amplitude until $z \simeq 4.2$ mm. When most of the laser energy is transferred to the plasma wave, the laser becomes subsequently too weak to maintain self-focusing. This simulation result agrees well with the theoretical prediction [94] of laser pump depletion length $L_{pd} \simeq 2.6$ mm. Closely following the laser pulse, a bubble with a radius of $\sim$7 μm is created, as illustrated in Figure 6.11(e). An appreciable number of electrons starts to be trapped by the bubble after the first maximum of laser normalized intensity $z \simeq 2$ mm in Figure 6.11(b), and the trapped electrons gain energy rapidly. The mean energy of the electron bunch produced in the first plasma bucket reaches a maximum of 220 MeV at $z \simeq 4$ mm and then gradually

decreases, because the electrons enter a decelerating phase. In addition, the laser intensity remains large enough ($a_0 > 3$) to trap electrons [197] over a few millimeters, so multiple electron injection occurs. The electron bunch formed in the first plasma bucket in Figure 6.11(e) has a transverse radius of $\sim 1\,\mu$m and a longitudinal length of approximately 6 μm, from which one can estimate the X-ray pulse duration to be ~ 20 fs. They confirm the calculation in Section 6.2.3 about X-ray peak brightness on the order of $\sim 1 \times 10^{21}$ photons/s/mm^2/mrad^2/0.1%BW.

The influence of the laser focus position can be evaluated by comparing the two columns in Figure 6.11. In the right column, the laser focus position is located at the beginning of the density plateau and this leads to a faster self-focusing with a higher peak amplitude than in the case of the left column. Then the laser amplitude oscillates with larger peak to peak amplitude. Electron injection occurs at about the same position $z \simeq 2$ mm, but the maximum value of the mean electron energy is higher in the case of the left column probably due to an increasing laser intensity from $z = 1.8$ to 4.5 mm. The X-ray emission in Figure 6.11(d) has a similar peak position around $z \simeq 4.7$ mm. It can also be noticed in Figure 6.11(f) that the number of electrons in the first bucket after the laser pulse is lower than that in Figure 6.11(e), which is linked to different laser evolutions in the two cases.

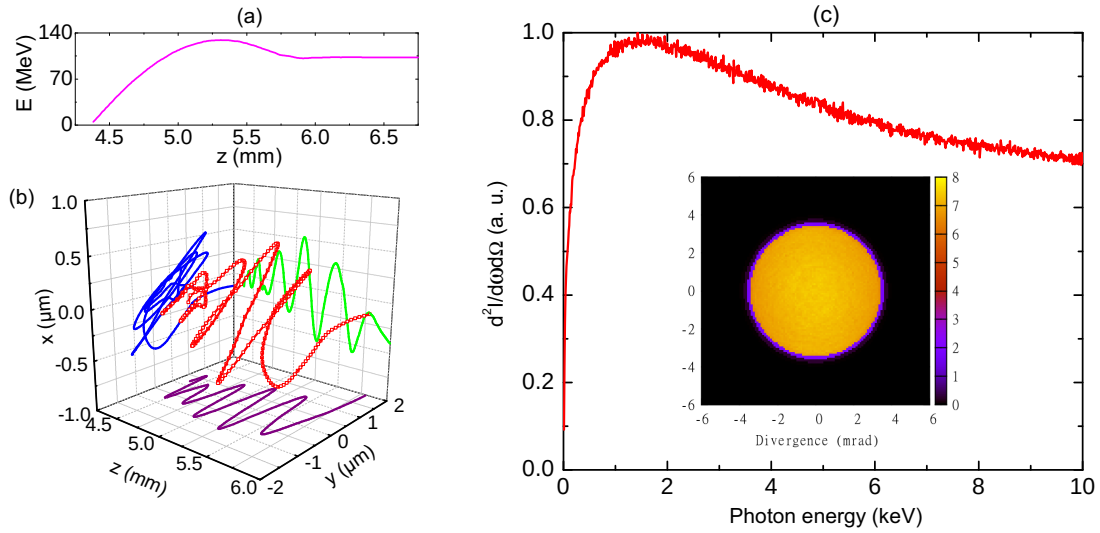

Figure 6.12: *(a) Energy evolution of an electron traced in PIC simulation and (b) its corresponding 3D trajectory, where the laser propagates along the z axis and is polarized along the y axis. (c) X-ray spectrum calculated in the simulation. The inset in (c) is the X-ray beam profile calculated in the exit plane of a 30 mm long, 178 μm diameter capillary tube. Other parameters are the same as for Figure 6.11(a) with focusing at $z = 1$ mm.*

The betatron radiation was calculated from Lineard-Wiechert potentials [116] by post-processing the trajectories of electrons with energies larger than 10 MeV. Figure 6.12(b) exhibits a typical electron trajectory obtained in simulation for the case of laser focus position at $z = 1$ mm (left column in Figure 6.11). As shown in Figure 6.12(a), the electron is trapped at around $z \simeq 4.4$ mm, and gets accelerated to 130 MeV at $z \simeq 5.3$ mm. Afterwards it enters the decelerating phase. The electron performs a spiral-like motion and fulfills four oscillations [Figure 6.12(b)]. The maximum oscillation amplitude along the y axis, the direction of laser polarization, is 1 μm, roughly equal to the transverse size of the electron bunch. The maximum oscillation amplitude along the direction (the

x axis) perpendicular to the laser polarization is 0.5 μm, smaller than that in the laser polarization direction. This kind of elliptical motion in the transverse plane is due to electron interacting with the laser tail in the first plasma bucket [200].

Figure 6.12(c) gives the spectrum of betatron radiation produced by the electron beam, which is synchrotron-like but differs from the standard synchrotron spectrum defined by Equation 3.21. That is because the accelerated electrons are widely-spread in energy and have different oscillation amplitudes. Fitting the simulated spectrum with a standard synchrotron spectrum yields a critical energy of 7.7 keV, however the simulated and the fitted spectra have a large difference in photon energy distribution. Therefore it is more significant to define the critical energy $\mathcal{E}_c$ as the energy below or above which half of the power is radiated [115]. Accordingly, $\mathcal{E}_c$ is 4.6 keV for this spectrum in Figure 6.12(c). The inset in Figure 6.12(c) shows the X-ray profile observed at the exit of a 30 mm long, 178 μm capillary tube in the simulation, where one can see the intensity transition due to X-ray cropping by the capillary exit border. The cropped X-ray beam has a divergence of 3.6 mrad which is close to the divergence of about 3.4 mrad deduced from the experimental measurement shown in Figure 6.6(b). Furthermore, the histogram in Figure 6.11(b) represents the X-ray intensity, obtained by integrating photons from 1 to 10 keV, emitted at different longitudinal positions calculated over each 1 mm. It is seen that the X-ray generation extends from about $z = 3$ mm to around $z = 7.5$ mm, and peaks at $z \simeq 4.6$ mm. This is in good agreement with the experimental observation presented in Figure 6.6(d). The agreement of the X-ray emission profile and location between simulation and experiment shows that the analysis of the X-ray emission is a powerful diagnostics, providing also information on the electron beam dynamics.

6.4 Bremsstrahlung radiation

6.4.1 Physical mechanism of secondary emission

In order to characterize the process of electron acceleration in plasma, a 30.5 mm long capillary tube was used in order to ensure the whole shadow of the capillary border lying within the chip of the X-ray CCD camera, as presented in Section 6.2.4. Beside achieving that diagnostics, another interesting phenomenon was observed in the X-ray images. A

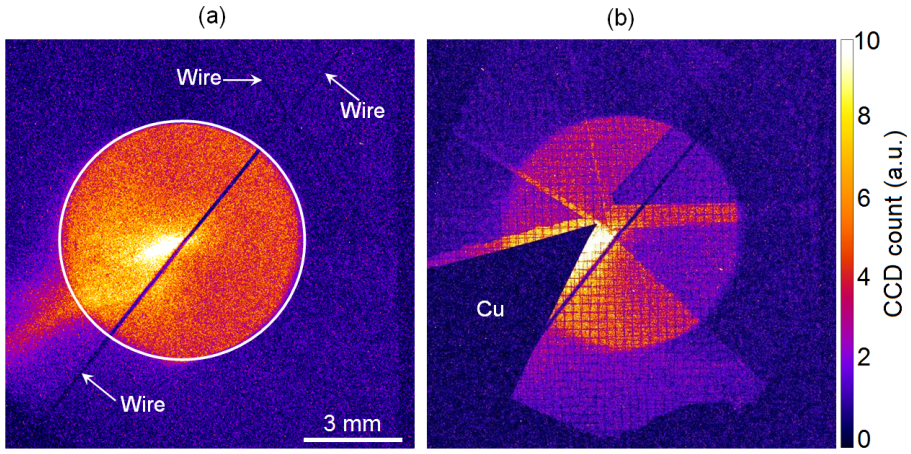

Figure 6.13: *X-ray beam profiles measured with the 30.5 mm long capillary tube (a) without or (b) with the filter metals. The wire cross outside the shadow of the capillary border, indicated by the white circle, is clearly visible in (a).*

cross made of stainless steel wire with diameter of 50 μm was placed in the optical path approximately 53 cm after the capillary tube and about 57 cm from the X-ray camera. The stainless steel wire was clearly resolved even outside the rim of the capillary tube, as exhibited in Figure 6.13(a). This region in principle should be completely dark unless there is another X-ray source illuminating the wire. This secondary emission can be better appreciated in the image with the filter metals [Figure 6.13(b)], where there is still a detectable signal on the CCD camera through the metal pieces outside the capillary shadow. Without a secondary emission, the local signals in those metals would be as low as in the copper part which blocks the secondary emission as well. This secondary emission was also detected occasionally with some 20 mm long capillary tubes, but not as strong as with the 30.5 mm long capillary tube, and never with the 10 mm long tubes, which means the secondary emission depends on the capillary length.

There are several possible explanations for the origin for such a secondary emission. We will examine them one by one in the following part.

X-ray reflection

To avoid ambiguity, we call the emission producing the capillary shadow in Figure 6.13(a) the main emission, as it produced a higher intensity inside the shadow [i.e. inside the white circle in Figure 6.13(a)]. Because the divergence of the main emission is larger than the cropping angle of the capillary exit, it could be envisaged that part of the beam is reflected by the capillary inner surface and goes out from the capillary tube as a second emission, as illustrated in Figure 6.14. However, this assumption can be easily ruled out. The capillary radius is 89 μm. Assuming an X-ray is produced at $z = 4.5$ mm, the emission peak position determined in Figure 6.6(d), the reflection just upstream the capillary exit has the smallest grazing angle $\theta_{in} \simeq 3.4$ mrad. Correspondingly, the reflectivity at the capillary surface with roughness of ~ 0.1 μm is of the order of $\sim 1 \times 10^{-3}$ for $1 - 10$ keV photons. The reflected beam is too weak to be detected in experiment, and it becomes even weaker for larger incident angles.

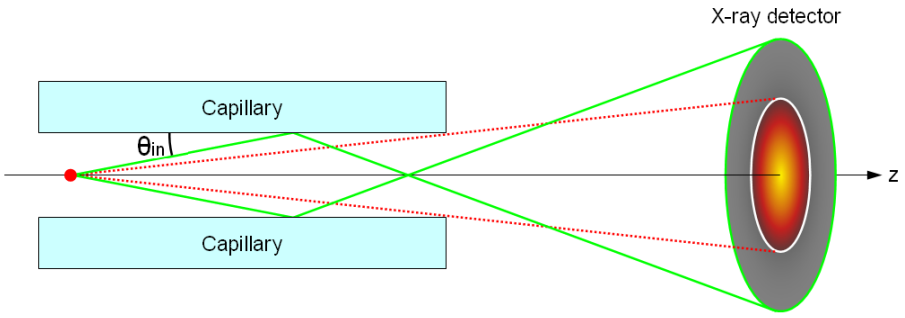

Figure 6.14: *Schematic illustration of X-rays cropped and reflected by a capillary tube. The cropped part confined within the two dotted lines is the main emission, and the the solid lines indicate the X-rays reflected by the capillary inner surface producing a secondary emission.*

Beam-driven betatron radiation

As seen both in experiment and simulation, after $z = 7$ mm the laser is depleted by transferring energy to the plasma wakefield. However, the accelerated electron bunch itself could excite a plasma wave beyond the pump depletion length [201], corresponding

to a transition to the plasma wakefield accelerator [15]. In this case, electrons can still perform betatron oscillations and generate X-rays at a later time owing to the transverse plasma field [60]. It is beyond our capacity to verify this in experiments, so we turned to PIC simulations.

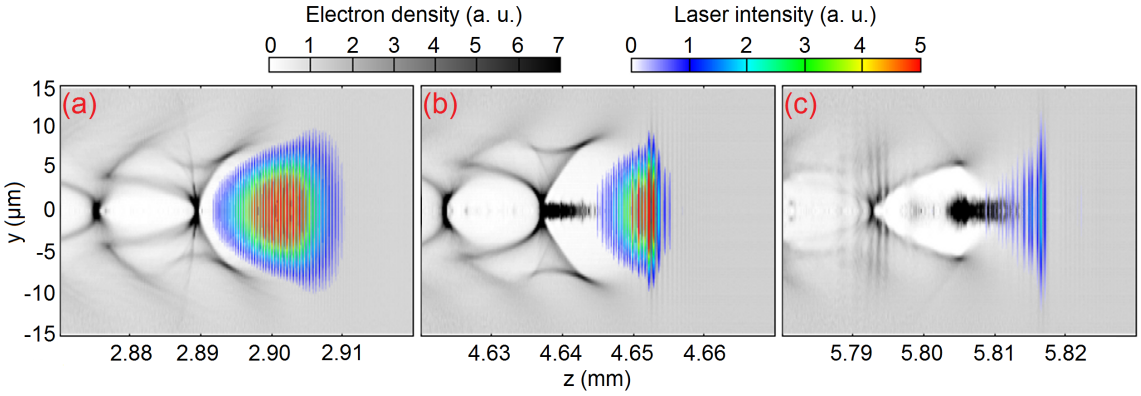

Figure 6.15: *Snapshots of plasma density (gray scale) and instantaneous laser intensity (color scale), in which the laser propagates from left to right at three different positions along the axis of capillary tube. Electron trapping starts at $z \simeq 2.895$ mm in (a), and at $z \simeq 4.645$ mm (b) a large amount of electrons are trapped and accelerated in the first plasma bubble, where the head of the electron bunch catches up with the laser. The electrons interact with the laser and get modulated at $z \simeq 5.805$ mm (c), where the transverse size of the electron bunch is appreciably increased.*

A simulation campaign was carried out to determine if we can generate the secondary emission by beam-driven betatron radiation in our parameter range. Different configurations of laser parameter and plasma density were examined, nevertheless no X-ray emission was found according to the aforementioned mechanism. Instead, we found that in most of the simulated cases the accelerated electrons gradually catch up with and overrun the driving laser pulse, while the electron bunch explodes owing to transverse expulsion by the laser ponderomotive force. Figure 6.15 shows one simulation case at plasma density of 7×10^{18} cm^{-3} with laser focus at 1 mm inside a 30 mm long capillary tube with diameter[2] of 152 μm. The laser parameters are the same as given in Section 6.3. In Figure 6.15(a), a plasma bubble is produced behind the laser and start trapping electrons at $z \simeq 2.895$ mm. Afterwards, the accelerated electrons catch up with the laser tail and get scattered by the laser ponderomotive force. The increase in transverse size of the electron bunch can be seen in Figure 6.15(c). The distance that it takes for a trapped electron (nearly moving at the speed of light) to catch up with the laser can be approximated by $L = R_b c/(c - v_g)$. The bubble radius in Figure 6.15(b) is $R_b \simeq 7$ μm, and the laser group velocity given by Equation 2.23 is $v_g \simeq 0.997c$, which yields $L \simeq 2.3$ mm. The laser pump depletion length is evaluated from Equation 2.52 as $L_{pd} \simeq 3$ mm. Since $L < L_{pd}$, some electrons can catch up with the laser before it is depleted.

Figure 6.16 shows the electron profiles at different longitudinal positions, namely $z = 5.3$, 7.6, and 8.8 mm. The simulation parameters are the same for Figure 6.15. A tiny bright spot is seen in Figure 6.16(a), corresponding to the typical electron profile before or just catching up with the driving laser. The bunch size is dramatically enlarged

[2]To reduce the time for parameter scan in 3D PIC simulation, a smaller capillary tube diameter 152 μm was used. It was verified in simulation that the laser-plasma interaction is nearly the same for capillary tubes with 152 and 178 μm diameters.

after interaction with the laser pulse [Figure 6.16(b)], and afterwards the outmost electrons start touching and entering into the capillary wall around $z = 8.8$ mm. The beam profile in Figure 6.16(c) consists of a central bright elliptical spot rounded by a big halo. The central part of the spot corresponds to the electrons that do not catch up with the laser before the laser depletes, so they are not modulated by the laser. Owing to a larger emittance along the laser polarization direction [200], electron explosion is more pronounced in that direction as shown in Figure 6.16(a)-(c). Some electron trajectories are given in Figure 6.16(d)-(e). Since the ponderomotive force does not depend on laser polarization (See Section 2.1.3), the electrons are expelled both along and perpendicular to the laser polarization direction. Especially the lower energy electrons are more scattered, because the transverse acceleration inversely depends on the relativistic electron mass γm_e.

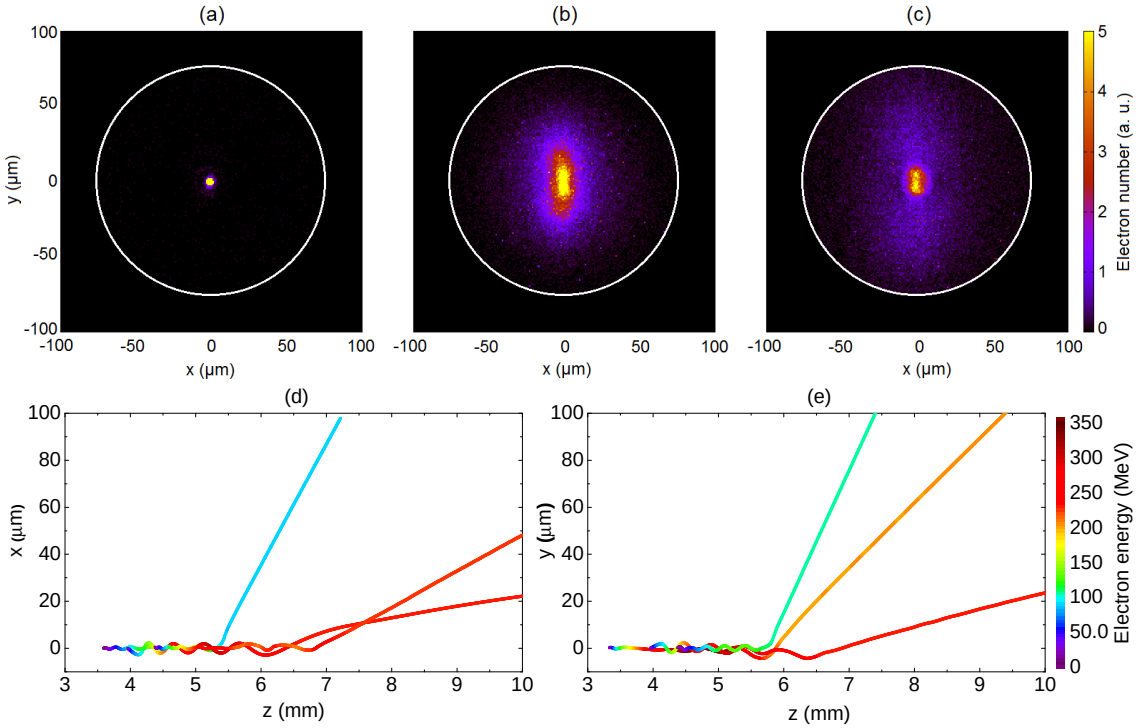

Figure 6.16: *Electron transverse profiles at different longitudinal positions (a) 5.3 mm, (b) 7.6 mm, and (c) 8.8 mm, where the circle indicates the capillary border of 152 μm. Increase in electron size is clearly visible. The laser is polarized along the y axis. Typical electron trajectories in the planes (d) perpendicular and (e) parallel with the laser polarization. The simulation parameters are the same as for Figure 6.15.*

In summary, the PIC simulations show that beam-driven betatron radiation does not occur in our experimental conditions, while the accelerated electrons are exploded when they overrun the driving laser pulse.

Estimation of bremsstrahlung radiation

When the electrons go through the capillary wall, they produce bremsstrahlung radiation. To verify the secondary emission is indeed resulted by the bremsstrahlung radiation, we need to check the spectrum and angular distribution of the bremsstrahlung radiation, as the detector that we used was sensitive to 1-20 keV photons and had a collecting angle of 12×12 mrad^2. Here we show a theoretical estimation about this.

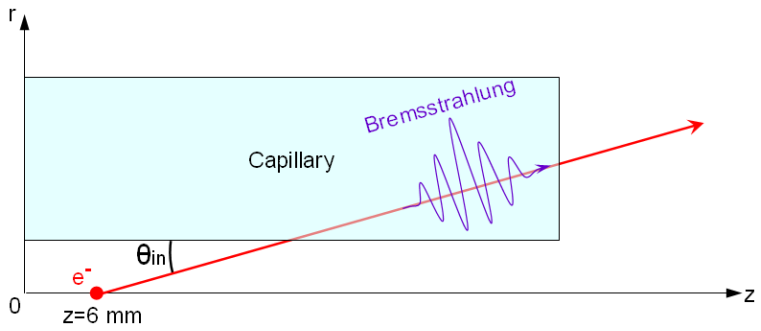

Figure 6.17: *Model for theoretical estimation of bremsstrahlung radiation generated in capillary wall.*

The model for the estimation is illustrated in Figure 6.17. We consider a 200 MeV electron expelled at $z = 6$ mm with an incident angle $\theta_{in} = 7.5$ mrad, a typical case in Figure 6.16. For a 30.5 mm long, 178 μm diameter capillary tube, the electron energy drops to 176 MeV at $z = 30.5$ mm owing to energy stopping[3] in the capillary wall, assumed to be pure SiO_2. When the incident electron is ultrarelativistic, the spectrum of bremsstrahlung radiation is given by [202]

$$\frac{dN_{ph}}{d\mathcal{E}_{ph}} = \frac{\mathcal{A}}{\mathcal{E}_{ph}} \left[1 + \left(\frac{\mathcal{E}_1}{\mathcal{E}_0} \right)^2 - \frac{2\mathcal{E}_1}{3\mathcal{E}_0} \right] \left[\ln \left(\frac{2\mathcal{E}_0 \mathcal{E}_1}{\mathcal{E}_{ph}} \right) - \frac{1}{2} \right], \tag{6.1}$$

where $\mathcal{A}$ is a coefficient associated with the material property. $\mathcal{E}_0 = 200$ MeV is the incident electron energy, and $\mathcal{E}_1 = 176$ MeV is the electron energy after going through the capillary wall. The calculated spectrum is shown in Figure 6.18(a). As seen, substantial

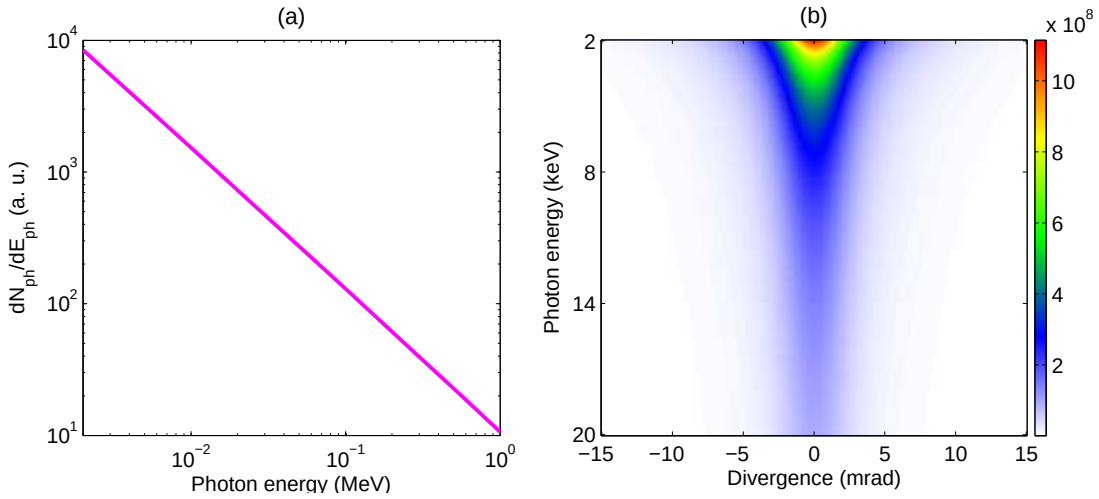

Figure 6.18: *(a) Spectrum and (b) angular distribution of bremsstrahlung radiation of an electron having incident and escaping energies of 200 MeV and 176 MeV.*

photons can be produced in the energy range of 2-20 keV. The angular distribution of

[3]Using the stopping energy rate in the database of ESTAR (stopping-power and range tables for electrons) provided by the National Institute of Standards and Technology.

bremsstrahlung radiation in the small angle approximation is given by [202]

$$\frac{d^2N_{ph}}{d\mathcal{E}_{ph}d\Omega} = \frac{\mathcal{A}}{\pi}\frac{1}{\mathcal{E}_{ph}}\frac{\mathcal{E}_1}{\mathcal{E}_0}\left\{\frac{16(\theta\mathcal{E}_0)^2\mathcal{E}_0^2}{(1+\theta^2\mathcal{E}_0^2)^4} - \frac{(\mathcal{E}_0+\mathcal{E}_1)^2\mathcal{E}_0}{\mathcal{E}_1(1+\theta^2\mathcal{E}_0^2)^2}\right. \\ \left. +2\ln\left(\frac{\mathcal{E}_0\mathcal{E}_1}{\mathcal{E}_{ph}}\right)\left[\frac{(\mathcal{E}_0^2+\mathcal{E}_1^2)\mathcal{E}_0}{\mathcal{E}_1(1+\theta^2\mathcal{E}_0^2)^2} - \frac{4\theta^2\mathcal{E}_0^4}{(1+\theta^2\mathcal{E}_0^2)^4}\right]\right\}, \tag{6.2}$$

where θ is the angle with respect to the electron propagation direction. For the case of incident and escaping energies of 200 and 176 MeV, the angular distribution of the bremsstrahlung radiation is shown in Figure 6.18(b). One can see that the emission distribution sensitively depends on the photon energy. The FWHM divergence is around 4.6 mrad for 2 keV photons. The emitted photons are very likely to be detected if they are created by electrons with a small divergence and close to the laser axis.

6.4.2 Modeling with GEANT4 and discussion

To more precisely calculate the bremsstrahlung radiation produced by an electron bunch, we performed a numerical modeling with the code GEANT4 [203]. GEANT4 is a toolkit specially designed for the simulation of the passage of particles through matter using the Monte Carlo method. The particle transport is described by the processes of bremsstrahlung, multiple scattering, and ionization, while the produced electromagnetic radiation experiences the processes of photoelectric effect, Compton scattering, and conversion into electron-positron pair.

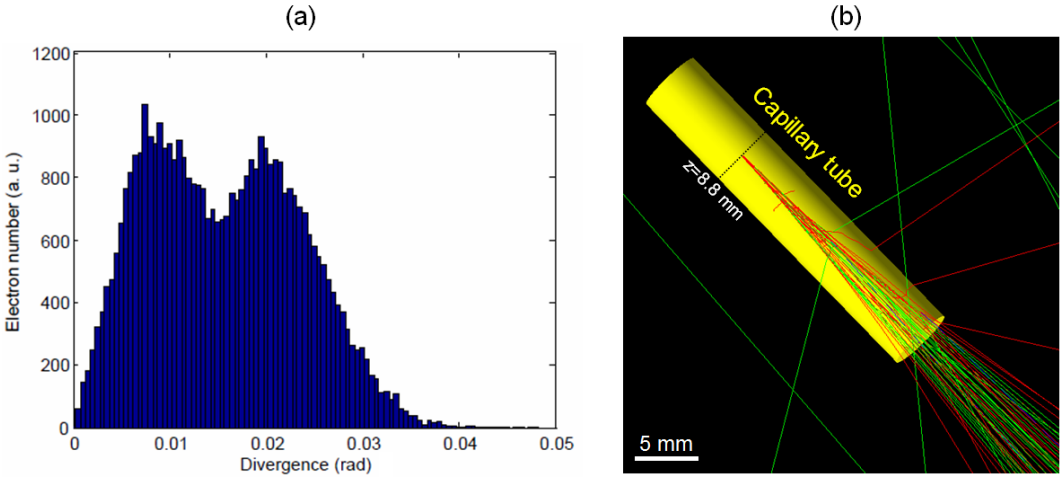

Figure 6.19: *(a) Angular distribution of the electron bunch obtained from PIC simulation at $z = 8.8$ mm. (b) Trajectories of the simulated particles in the capillary tube (yellow): photons (green), electrons (red), and positrons (blue).*

The bremsstrahlung modeling is initialized with the electron beam obtained from PIC simulation at $z \simeq 8.8$ mm, where the electrons have already been modulated after overrunning the laser pulse, but not yet reached the capillary wall. The electron beam is fully described using six parameters in phase space, namely (x, y, z, v_x, v_y, v_z). The electron beam transverse distribution used in the GEANT4 simulation is shown in Figure 6.16(c), and the corresponding beam divergence is shown in Figure 6.19(a). 4×10^4 macro-electrons are used in the GEANT4 calculation. The capillary tube, taken as pure SiO_2, is 30 mm

long with inner and outer radii of 89 μm and 2.75 mm, respectively. The two Be windows with total thickness of 300 μm and the 5 mm air gap (See setup in Figure 5.7) were included in the modeling as well.

Figure 6.19(b) shows the particle trajectories in the capillary wall, where the red, blue, and green lines represent the trajectories of electrons, positrons, and photons, respectively. As seen, numerous photons are produced by bremsstrahlung radiation when the electrons pass through the capillary wall. Most of the photons move forward very directionally. The spectrum of the emitted photons and their angular distribution are shown in Figure 6.20. The overall spectrum exponentially drops with only a few photons remaining around 100

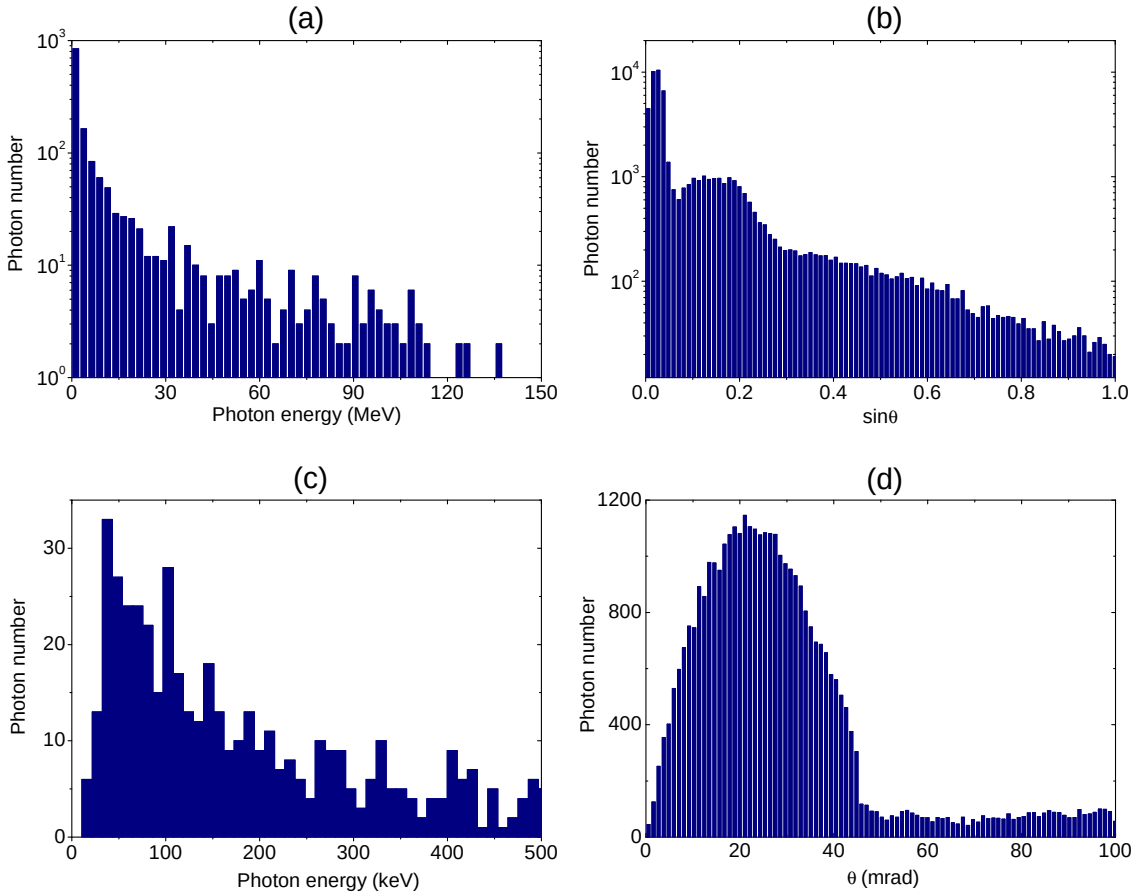

Figure 6.20: *(a) Spectrum and (b) angular distribution of the bremsstrahlung radiation. (c) Spectrum for 0-500 keV photons and (d) angular distribution for 0-100 mrad.*

MeV. Figure 6.20(c) shows the spectrum for photon energy below 500 keV, indicating the spectrum peaks around 40 keV, and diminishes when photon energy decreases towards zero. Furthermore, most of the photons are collimated within a divergence cone of 100 mrad as shown in Figure 6.20(b), where θ is defined as the angle with respect to the capillary central axis. Especially, a peak at $\theta \simeq 20$ mrad is observed in Figure 6.20(d). This peak perfectly coincides with the second divergence peak of the electron beam given in Figure 6.19(a), which implies the photons are indeed generated by the outer scattered electrons.

It is important to check whether this bremsstrahlung radiation could be detected by the X-ray camera and furthermore induce the X-ray halo observed in Figure 6.13. First the photon number generated by bremsstrahlung radiation needs to be estimated. Here

we particularly consider the photons with a divergence of $4 < \theta < 6$ mrad, corresponding to a ring consists of 1.1×10^5 pixels outside the capillary shadow (the white circle) in Figure 6.13(a), where the signal could be induced by the bremsstrahlung photons. The charge of the electron bunch obtained from PIC simulation is ~ 150 pC at $z \simeq 8.8$ mm, and the electron-to-photon ($4 < \theta < 6$ mrad) conversion efficiency is found to be 2% in the GEANT4 modeling, which yields 2×10^7 photons produced in the angle range of $4 - 6$ mrad. So the average fluence is approximately 200 photons per pixel. We shall furthermore estimate the resulting CCD counts. To do so, only the photons with energy less than 50 keV will be taken into account, because the detector responsivity for higher energy photons is negligible, as presented in Figure 5.16. Using the radiation spectrum obtained in the modeling and the quantum efficiency of the X-ray camera, we eventually get an average CCD count of around 500 for $4 < \theta < 6$ mrad. This numerical result is consistent with the experimental measurement. In Figure 6.13(a), we typically measured around 400 counts outside the shadow of the capillary border, which is nearly one order of magnitude lower than that inside the shadow, of ~ 3000 counts. We therefore can conclude that the X-ray halo is indeed generated by bremsstrahlung photons, while the relatively low CCD count is due to the poor detector responsivity for high energy photons but not a low fluence.

It is obvious that our detection system is not suitable for measuring the gamma-ray photons of bremsstrahlung radiation, as most of the photons are either out the detector view or beyond the detector energy range. Some special broad range detectors [204] could be employed for this purpose in future. As presented above, 10^9 photons per shot can be produced provided the beam charge is of the order of 100 pC. Such a gamma-ray is as intense as those generated by other schemes like Compton scattering [205], which could be applied for imaging the interior structure of dense object [206].

6.5 On the stability of electrons

In the first campaign, we examined the correlations between the instabilities of electrons and X-rays, as presented in Section 6.2.5. Nevertheless, the origins of the beam fluctuations were not explored. Some publications [197] stress that those fluctuations may result

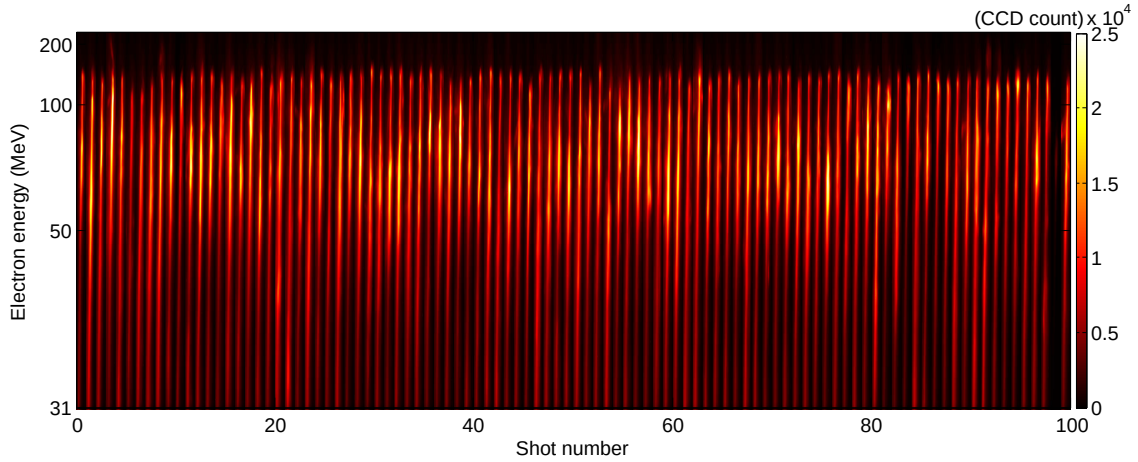

Figure 6.21: *Raw Lanex images of 100 consecutive electron beams obtained with a 10 mm long, 254 μm diameter capillary tube at* $\rho_e = (8.3 \pm 0.5) \times 10^{18}$ cm^{-3}.

from laser fluctuations. A second campaign was carried out at the LLC to study the cor-

relations between laser instabilities and those of the produced electron beams. It is worth mentioning that the supersonic gas flow provided by the gas jet in Ref. [197] can induce some fluctuations as well, however this issue of gas flow is greatly minimized when using capillary tube [164], which allows us to highlight the influence of laser fluctuations.

The laser parameters are nearly the same as for the first campaign presented in Section 5.3, while the differences about electron and X-ray diagnostics were discussed in Sections 5.4 and 5.5. Large capillary parameter ranges with diameter varying in $76 - 254$ μm and length ranging in $8 - 30$ mm were explored during this campaign. The experimental data are being analyzed. What we present here are the preliminary results. We typically discuss the stability study with a 10 mm long, 254 μm diameter capillary tube. Such a big capillary tube, working like a gas-cell [45], is chosen here to emphasize the relationship between laser and electron instabilities, because a smaller capillary tube may modify the influence of laser fluctuation through mode coupling.

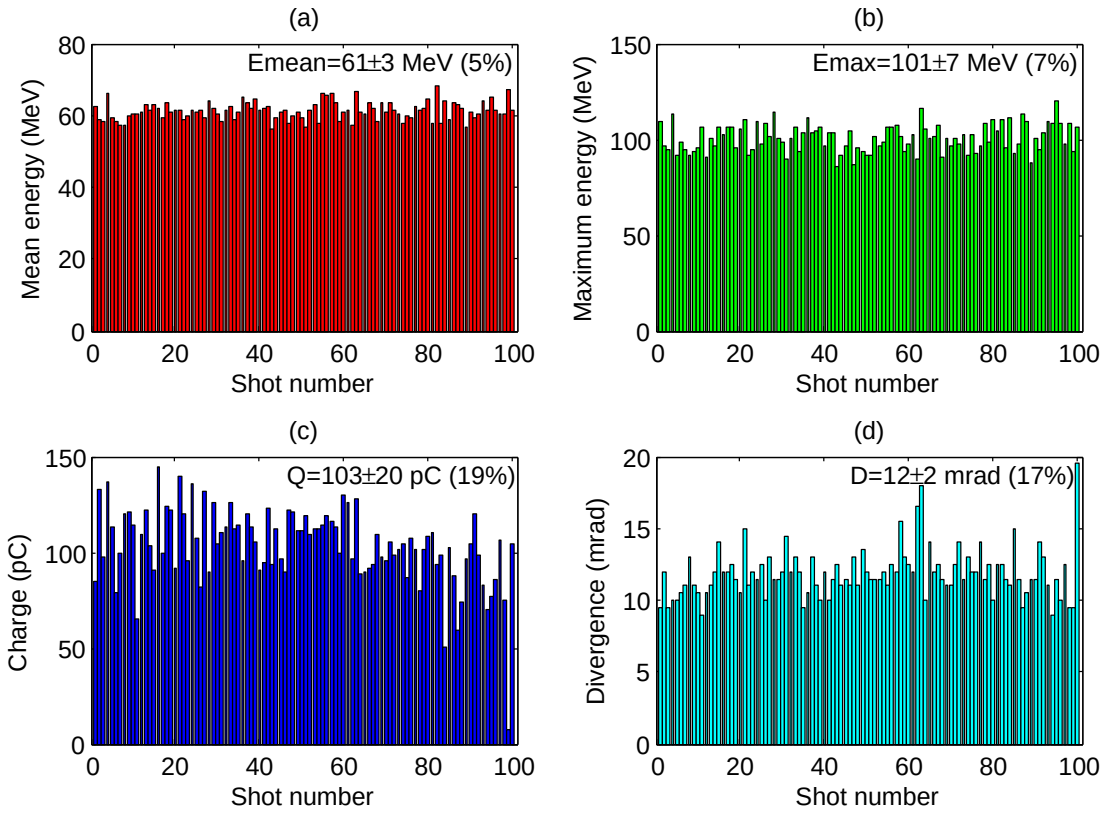

Figure 6.22: *(a) Mean energy, (b) maximum energy, (c) beam charge, and (d) beam divergence of the 100 consecutive electron beams shown in Figure 6.21.*

To perform a statistical stability study within a reasonable time schedule, we usually took hundred consecutive shots for a given set of parameters. Figure 6.21 exhibits 100 raw Lanex images of the electron beams obtained with a 10 mm long and 254 μm diameter capillary tube at a plasma density $\rho_e = (8.3 \pm 0.5) \times 10^{18}$ cm^{-3}. Electron injection was achieved for all the shots, even though the signal of the shot 99 was very weak. The electron spectra are generally Maxwellian-like with a cut-off energy around 130 MeV. The characteristic features associated with the 100 electron beams are presented in Figure 6.22, where the percentage values indicate standard deviation over mean. The electron energies correspond to instabilities of a few percents: 5% for mean energy and 7% for

maximum energy. The FWHM beam divergence shows an instability of 17%, while the largest fluctuation happens for beam charge as 19%. Those findings are both qualitatively and quantitatively similar to what we observed during the first campaign given in Table 6.2.

The laser parameters were recorded simultaneously for each single shot. To do so, about 1% laser energy was taken from the main beam and furthermore split into two beams. One was attenuated and imaged at the focus of a 1 m focal length by a 10 bit CCD camera outside the chamber, providing the information of laser energy and pointing, and the other was sent to an optical spectrometer to record the laser spectrum. Applying the Fourier transform to the recorded laser spectrum, we are able to obtain the temporal laser profile and the corresponding pulse duration. Without knowing the phase term of each frequency component, we assume a flat phase distribution for the Fourier transform. This assumption may lead to a pulse duration different from the real value, however this difference could be calibrated by comparing the calculated and experimentally measured (using an autocorrelator) durations.

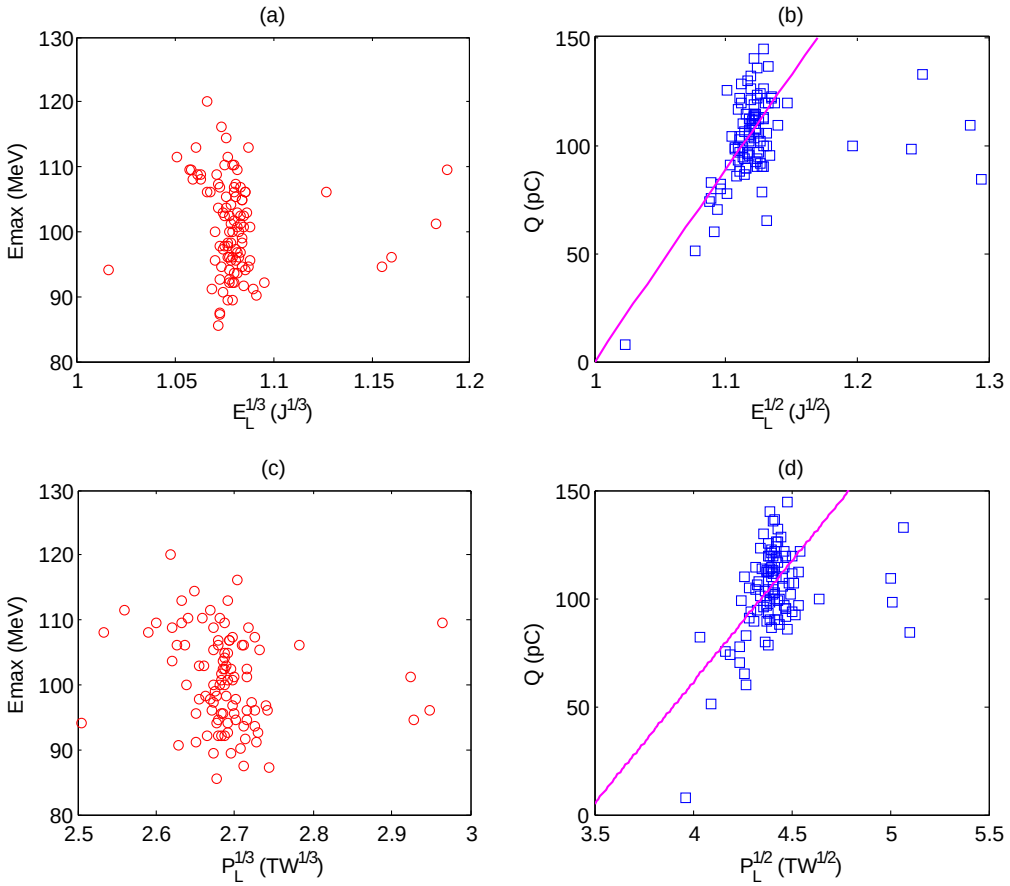

Figure 6.23: *Maximum electron energy and beam charge of the 100 shots shown in Figure 6.21 as functions of the corresponding (a) cube root (b) square root of laser energy before compressor, and (c) cube root (d) square root of laser power on target. The lines in (b) and (d) are linear fits.*

Figure 6.23 the dependences of electron maximum energy and beam charge on laser energy (before compressor) and laser power (on target) corresponding to the 100 shots in Figure 6.22. It seems that there is no clear correlations between electron maximum

energy and laser energy (power) as displayed in Figure 6.23(a)-(c). In order to interpret this observation, we recall the scaling law developed for electron energy gain in the bubble regime in Equation 2.54: $\mathcal{E}_e \propto P_L^{1/3} \propto \mathcal{E}_L^{1/3}$. Especially in Figure 6.23, the fluctuations (Std/Mean) of $P_L^{1/3}$ and $\mathcal{E}_L^{1/3}$ are around 2%. With such a small fluctuation, it is therefore not apparent to observe a clear correlation. Varying the laser energy purposefully in a larger range would perhaps give us a deeper understanding of this phenomenon. One should also keep in mind that the 10 mm long capillary tube is probably longer than the electron dephasing length of a few millimeters, so the accelerated electrons start rotating in the plasma potential well (See in Figure 2.7), which leads to electron energy different from the scaling law in Equation 2.54. By contrast, the beam charge strongly depends on laser energy (power). The scaling law in Equation 2.55 shows beam charge scales with laser energy and power as $Q_e \propto \sqrt{P_L} \propto \sqrt{\mathcal{E}_L}$. The line in Figure 6.23(b) corresponds to a linear fit $Q_e = 883(\sqrt{\mathcal{E}_L} - 1)$. The fluctuation of beam charge δQ_e therefore depends on the variation of laser energy $\delta\mathcal{E}_L$ by

$$\frac{\delta Q_e}{Q_e} = \frac{1}{2}\frac{1}{1-\frac{1}{\sqrt{\mathcal{E}_L}}}\frac{\delta\mathcal{E}_L}{\mathcal{E}_L}. \tag{6.3}$$

The coefficient on the right-hand side of Equation 6.3 is a function of laser energy $\mathcal{E}_L$. For example, the coefficient is calculated to be about 4 for a laser energy $\mathcal{E}_L = 1.3$ J, which means the fluctuation of beam charge is four times that of laser energy. The coefficient becomes even larger when the value of laser energy $\mathcal{E}_L \to 1$. The beam charge also exhibits a linear dependence on the square root of laser power as shown in Figure 6.23(d). The fit suggests that beam charge will decrease to zero when laser power $P_L \simeq 11.6 \pm 1.4$ TW. The critical power is $P_c \simeq 3.6$ TW for the plasma density 8.3×10^{18} cm^{-3} used in Figure 6.21. The fit in Figure 6.23(d) therefore suggests that the power ratio required for electron self-trapping is $P_L/P_c \simeq 3.2 \pm 0.4$, consistent with the ratio $P_L/P_c \simeq 3$ found by Froula *et al* in experiment [108].

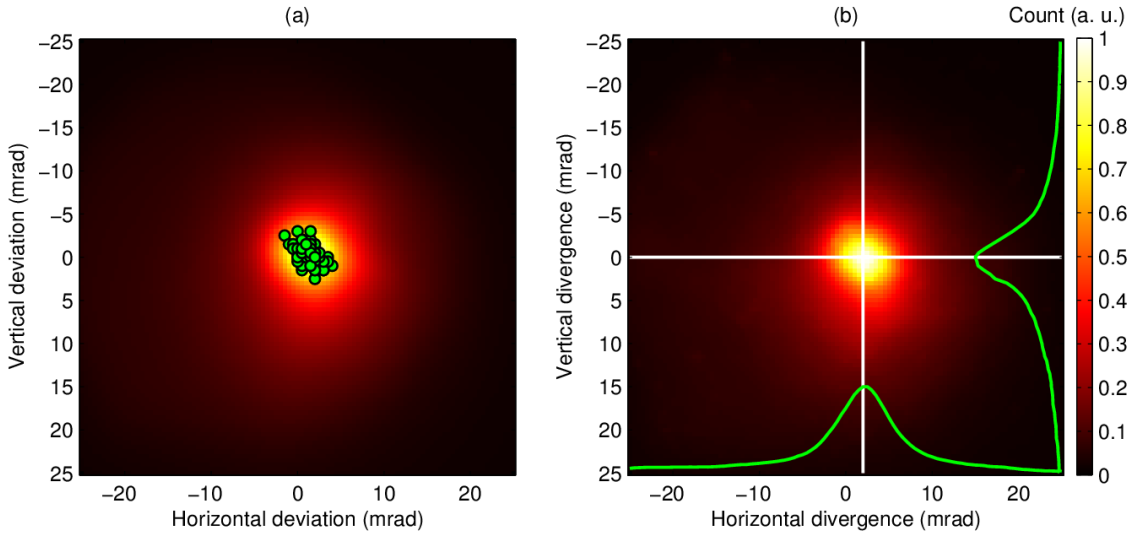

Figure 6.24: *(a) Sum of 100 electron beam profiles and the peak positions of the individual beam (green dots) obtained under the same condition as for Figure 6.21. (b) A typical single electron beam profile.*

Beside electron spectrum study, we examined the pointing of electron beam as well. Figure 6.24(a) shows the signal of 100 accumulated electron beams and their respective

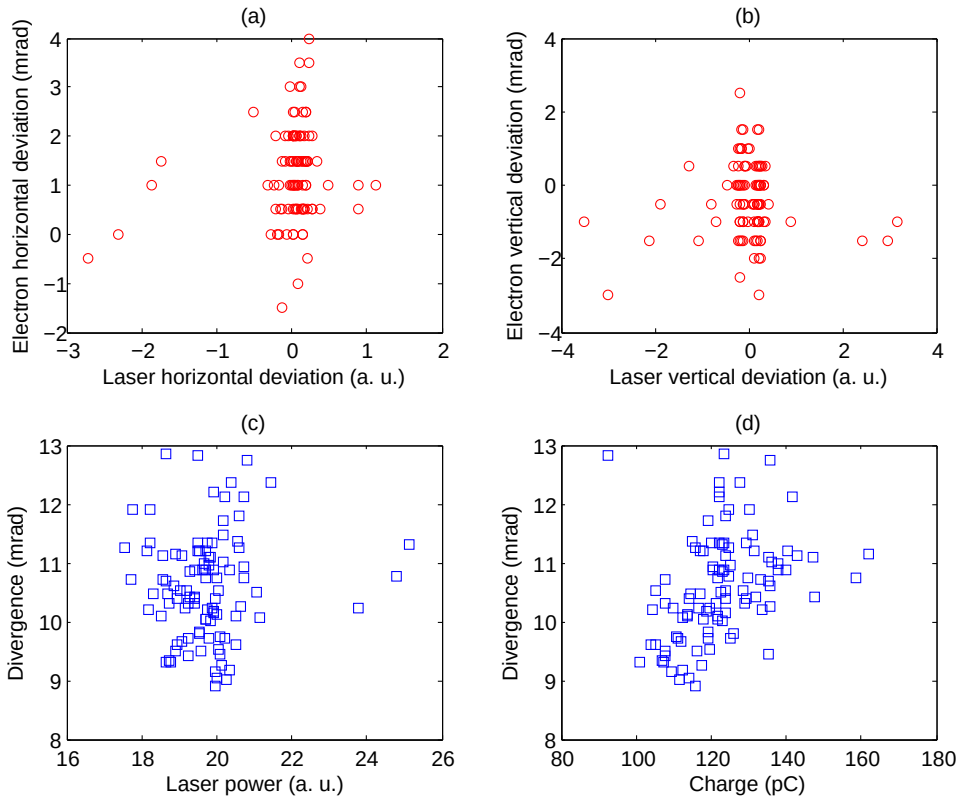

Figure 6.25: *(a)-(b) Correlations between laser and electron poingtings for the beams shown in Figure 6.24(a). (c)-(d) Dependences of the electron beam divergence on laser power and beam charge.*

peak positions, while Figure 6.24(b) displays a single electron beam profile with FWHM divergence of 7.4 mrad. No appreciable difference can be found between the two subfigures, suggesting the electron beams possess very good pointing stability. In Figure 6.24(a), the horizontal and vertical RMS pointing fluctuations are 1.23 and 1.0 mrad, respectively. Such an electron beam pointing is of great interest for multi-stage applications such as sending the electron beam to an undulator [56].

We furthermore attempted to correlate the electron beam divergence and pointing to the laser fluctuations, as presented in Figure 6.25. An intuitive presumption is laser pointing links to electron pointing. Figure 6.25(a)-(b) show the deviations of laser and electron pointings in the horizontal and vertical directions. The laser pointing was determined from the images recorded by the 10 bit CCD camera outside the chamber. The pointing deviation is defined as $(r_c - \langle r_c \rangle)/f_L$, where r_c is the position of the intensity maximum, $\langle r_c \rangle$ is the mean of r_c for the 100 shots, and $f_L = 1$ m is the focal length of the lens. As the laser pointing was stabilized, only a few laser shots exhibit large pointing deviations. Even though, we can still probably *observe* a correlation especially when the laser shifts towards the minus directions [bottom-left parts in Figure 6.25(a)-(b)]. Figure 6.25(c) shows that the electron beam divergence and laser power are independent. However, we found in Figure 6.25(d) that the beam divergence linearly increases with beam charge. This correlation can be understood as follows. On one hand, space charge effects become more pronounced for higher beam charge, which may increase the electron beam divergence. On the other hand, the electron spectrum is Maxwellian-like for the examined plasma density, which means it is the low energy electrons that dominate the population.

Increase in beam charge mainly contributes to increase the number of low energy electrons. Since low energy electrons are more divergent [10], larger divergence are measured for higher beam charge.

6.6 Characterization of X-ray source size

Another goal of the second campaign was the characterization of the source size of X-ray via Fresnel diffraction, since source size is crucial for evaluating X-ray brightness. It was obtained by theoretical estimation and PIC simulation but not experimentally measured in the first campaign [48]. Recently measurements of X-ray source size as small as 1 μm were reported by several groups [58, 118] using the method of Fresnel diffraction (See Section 5.5.3), so we were motivated to quantify the X-ray source size in our scheme employing capillary guiding.

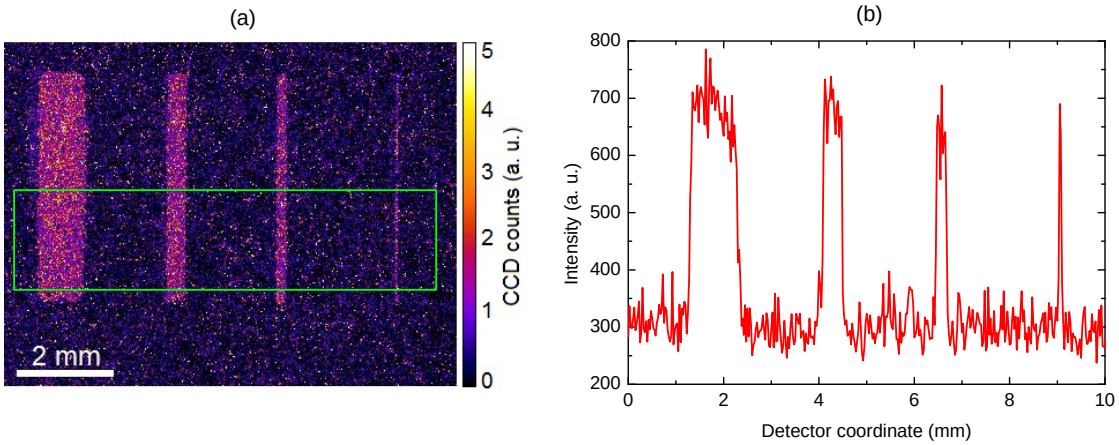

Figure 6.26: *(a) X-ray image of the microscopic object with the smallest feature of 10 μm. (b) Line-out of the intensity integrated along the vertical direction over the rectangle region in (a).*

We first attempted to assess the order of the X-ray source through imaging microstructures introduced in Figure 5.19. Figure 6.26(a) depicts the radiographic image of the microscopic slits backilluminated by an X-ray beam generated from a 10 mm long, 178 μm diameter capillary tube. The object and the X-ray CCD camera (Princeton) were respectively placed 25 and 130 cm away from the capillary exit, which corresponds to a magnification of $\mathbb{M} = \frac{L_o+L_i}{L_0} \simeq 5$. Given the detector pixel size of 24.8 μm, it yields a spatial resolution of about 5 μm. Figure 6.26(b) shows the line-out of vertically summed intensity over the rectangle region in Figure 6.26(a). An intensity peak is observed through the 10 μm slit and the signal contrast is as high as those for other big slits, implying the smallest feature is well resolved in this image. It indicates the X-ray source size must be smaller than 10 μm.

To ascertain the source size more precisely, we adopted the method of Fresnel diffraction. In order to achieve a high spatial resolution, an Andor X-ray CCD camera with a pixel size of 13.5 μm was employed. Figure 6.27 illustrates the spatial arrangement for this measurement. The razor blade was mounted onto a motorized translation stage just behind the magnet, and the razor blade was perpendicular to the laser path. The distance from capillary entrance to the razor was around 26 cm. In order to achieve a large magnification, the X-ray camera should be placed as far as possible away from the

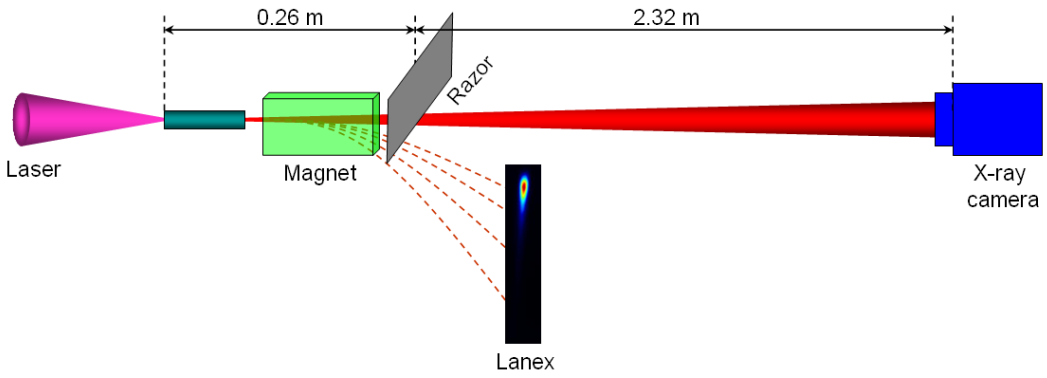

Figure 6.27: *Spatial arrangement for the source size measurement with razor blade.*

razor blade, however, on the other hand, the photon fluence per pixel will decrease, yielding a lower signal-to-noise ratio on the detector. Taking a compromise, in our setup the camera was placed 2.32 m away from the razor blade, corresponding to a magnification of $\mathbb{M} = \frac{L_o+L_i}{L_0} \simeq 10$ and a spatial resolution of approximately 1.35 μm.

The inset of Figure 6.28(a) shows an image of the razor blade casted by X-ray on the detector, where one can observe a pretty sharp shadow of the blade. Integrating the X-ray intensity along the direction of the razor edge gives the experimental data plotted in Figure 6.28, which is normalized to the X-ray intensity in a transparent area several millimeters away from the blade. We first notice that the normalized experimental data exhibit an overshoot peak with a value in excess of 1.4. Nevertheless, as discussed in Section 5.5.3,

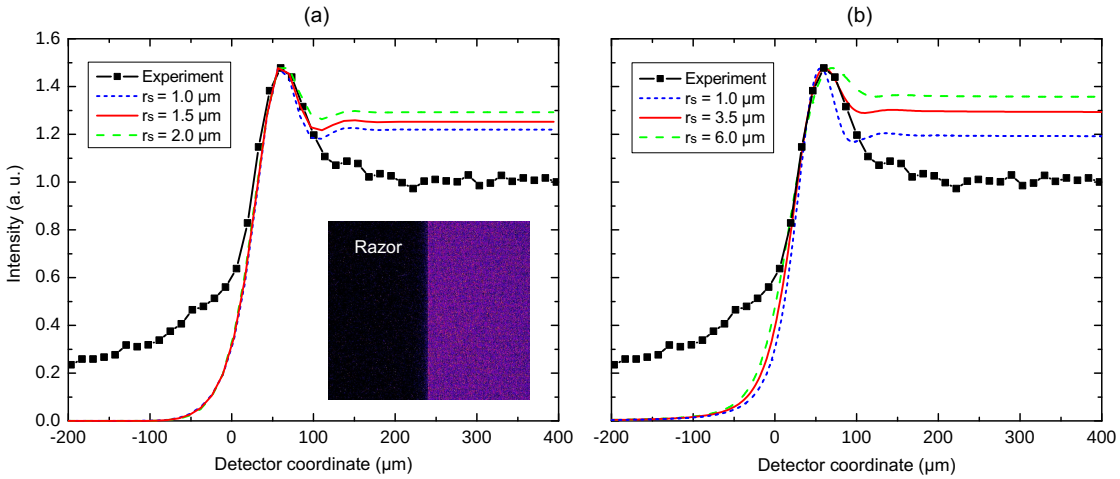

Figure 6.28: *The experimental data (black squares) are the X-ray intensity integrated along the direction of the razor blade edge, while other curves indicate numerical modelings for (a) fully coherent and (b) fully incoherent sources with different sizes. Inset in (a) is the X-ray image of the edge of a razor blade.*

the normalized intensity peak should not be that high even for a monochromatic point source. According to our understanding, the experimental overshoot could probably result from X-ray refraction in the razor blade part. As the blade has a tapered profile (See Figure 5.20) with several micron thick apex, some of the photons are able to penetrate the obstacle and are deflected towards the transparent area. The deflected photons overlap with the diffracted photons, producing the observed intensity overshoot. Since the model-

ing presented in Section 5.5.3 was designed for an ideal knife-edge with 100% absorption, we attempted to fit the profile but not the amplitude of the intensity overshoot observed in experiment. The source was assumed to have a Gaussian distribution $\exp(-2r^2/r_s^2)$ and synchrotron spectrum $\zeta^2\mathcal{K}_{2/3}^2(\zeta)$. Different combinations of source size r_s and critical energy $\mathcal{E}_c$ were calculated. As the spatial coherence of the source is not known, we examined two extreme cases: fully coherent and fully incoherent sources. To be clear and highlight the influence of source size, only the cases of 6 keV critical energy are displayed in Figure 6.28. All the fit magnitudes are adjusted to have the same maximum value as the experimental one. For the fully coherent sources shown in Figure 6.28(a), the curve for source size of $r_s = 1.5$ μm best predicts the tendencies of the intensity overshoot for both the rise and drop sides. 1 μm source size underestimates the drop slope, whereas 2 μm case overestimates it. All the fit curves are lower than the experimental one inside the razor region, as not all the photons are absorbed by the razor blade in the experimental case. For the modelings of fully incoherent sources, the curve corresponding to a Gaussian source with waist of 3.5 μm best reproduces the slopes of the experimental intensity overshoot. We can therefore tentatively conclude the X-ray source has a Gaussian distribution with $1/e^2$ intensity size between 1.5 and 3.5 μm.

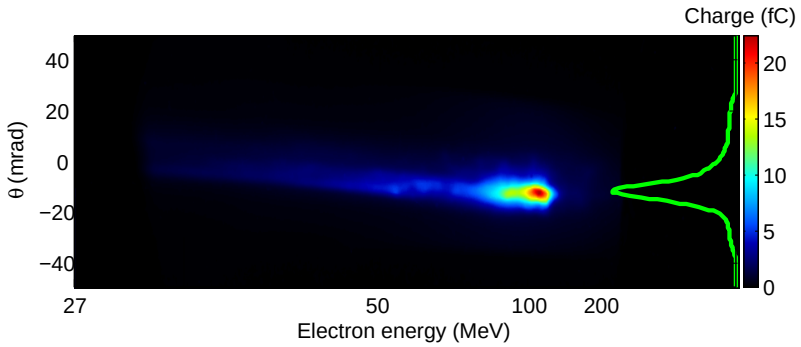

Figure 6.29: *Energy distribution of the dispersed electron beam corresponding to the X-ray beam in Figure 6.28.*

Once the source size is known, we can furthermore estimate the transverse emittance of electron beam. Beam emittance is a parameter describing the beam volume occupied by the particles in phase space, which is crucial for applications when the electron beam is needed to be transported or focused. The upper limit of normalized transverse emittance of an electron beam is defined as $\epsilon_n^\perp = \gamma\beta_z r_s \Theta_e$, where Θ_e represents electron beam divergence. The mean energy and RMS beam divergence of the electron beam in Figure 6.29 are 77 MeV and 6.7 mrad, respectively. The source size can be estimated by the mean value of the fully coherent and incoherent best fits to be 2.5 μm. It yields a RMS normalized transverse emittance $\epsilon_n^\perp < 0.83\pi$ mm mrad in our measurement, which is as low as reported for electron beams generated by LWFAs using other schemes [53, 54, 193, 207]. Such a low emittance electron bunch with beam charge as high as 90 pC is of great interest for future applications such as sending to an external undulator to generate X-ray free electron laser [56], or working as an injector for multi-stage acceleration [208].

6.7 Summary

This chapter presents the results of high energy electrons and intense X-rays obtained from the two campaigns at the Lund Laser Centre (LLC). The goal of the first campaign was

to characterize the influence of capillary tubes on the generation of electrons and X-rays, while the second campaign was devoted to investigating the stability of the electron beams and quantifying the X-ray source size.

Tens of pC electrons were found to be accelerated up to 300 MeV from 10 mm long capillary tubes. The electron spectrum, either spectrally peaked or Maxwellian-like, sensitively depends on the plasma electron density. The spectrally peaked electrons can only be obtained by decreasing the plasma density towards the threshold required for electron self trapping $P_L/P_c \simeq 3$. The electron energy and beam charge are not significantly affected by changing the capillary diameter from 152 μm to 203 μm, owing to a relatively small laser focal spot with a radius of around 20 μm at the first minimum of laser intensity distribution. The contribution of the capillary tube to laser guiding was highlighted by enhancing the X-ray brightness by 30 times, instead of using a 2 mm gas jet. The X-ray fluence was found to have a linear correlation with beam charge, which furthermore was used to deduce the number of electron betatron oscillations inside the plasma bubble.

The electron acceleration process inside the capillary tube was characterized using the far-field intensity profile of the X-ray beam cropped by the rim of capillary exit, which shows the laser-plasma acceleration terminates before the first 7 mm for a plasma density 8×10^{18} cm^{-3}. PIC simulations demonstrate that the accelerated electrons finally catch up with and overrun the driving laser pulse, where the electrons get scattered transversely by the laser ponderomotive force. The scattered electrons enter the downstream capillary wall and generate bremsstrahlung radiation, which casts a second illumination on the detector.

When the laser pointing is stabilized, the electrons exhibit typically a few percents fluctuation in electron energy, and around 20% for beam charge and divergence. Meanwhile, the RMS pointing fluctuation of the produced electron beams is found to be ~ 1 mrad. The X-ray source size ($1/e^2$ intensity waist) quantified by fitting the intensity distribution of X-ray diffraction induced by a razor blade is between $r_s = 1.5$ μm (assuming the source is fully coherent) and $r_s = 3.5$ μm (assuming the source is fully incoherent). Using the mean value of these two estimations $r_s = 2.5$ μm, the upper limit of the normalized RMS transverse emittance of the corresponding electron beam is evaluated to be $\epsilon_n^{\perp} \simeq 0.83\pi$ mm mrad.

Some new schemes of capillary-guided LWFA, like the use of plasma density ramp (See Section 4.7), gas mixture (99% H_2+1% N_2), and their influences on the beam stability were studied in the second campaign as well. The results will be reported in future publications.

Chapter 7

Conclusions

The objective of this thesis was to study laser-driven plasma-based electron acceleration and the associated betatron radiation in the nonlinear regime. In this work, we were particularly interested in understanding the physics of electron trapping and acceleration, and in generating bright X-rays by efficiently using a moderately intense laser. Capillary tubes were therefore employed to confine the gas over a long distance and to collect laser energy around its central focal spot to favor laser keeping self-focused over a longer distance comparing to a gas jet or gas-cell [46, 47, 140]. Two experimental campaigns were performed at the Lund Laser Centre (LLC) in Sweden by using the multi-terawatt laser pulse (40 fs FWHM duration, 16 TW on target) to explore electron acceleration and betatron X-ray radiation inside capillary tubes.

Significant efforts were dedicated to determining neutral gas density in capillary tubes. We investigated the temporal and spatial gas density evolution in capillary tube. Numerical fluid modeling was carried out in order to obtain the spatial distribution of gas along the central axis of capillary tube at the stationary state. The obtained results demonstrate a stable, uniformly distributed gas medium is established between the two capillary slits, outside which the gas density drops rapidly when the gas expands into vacuum background. Transient simulations reveal that the stationary state can be reached at $t > 40$ μs for a 2D capillary model, however it is beyond our computing capacity to calculate the gas evolution in a 3D model similar to the real gas filling system. Thus the temporal process of gas filling into capillary tube was determined using a self-developed scheme based on the Mach-Zehnder interferometer [164]. For a 30 mm long capillary tube with diameter of 178 μm, the gas inside capillary tube reaches the stationary state $\sim$ 34 ms after the opening of the valve, and then gas oscillating between the capillary holder and the valve induces a $\sim$ 6% fluctuation of gas density inside the tube. At the stationary state, there is a linear relationship between the gas density in tube and the reservoir pressure. Eventually, the large amount of gas in the filling pipe leaks into the vacuum chamber through the two small capillary exits, resulting in a second-scale characteristic decay time. It was also found that the filling process of hydrogen gas becomes saturated even for the shortest valve opening duration of 27 ms, which implies increasing the opening duration would just discharge more gas into the vacuum chamber but not benefit gas filling. In contrast, owing to a lower speed of propagation, the filled pressure of argon gas can be increased by lengthening the valve opting until 60 ms.

In order to study the nonlinear regime of capillary-guided LWFA, the laser at the LLC was focused to a peak intensity of 5.4×10^{18} W/cm^2 ($a_0 = 1.6$) in vacuum. The observed electrons could be either spectrally peaked with FWHM energy spread of 16% or broad-spread with a Maxwellian distribution. In a 10 mm long, 178 μm diameter capillary tube,

electrons with beam charge of tens of pC were typically accelerated with a maximum energy up to 300 MeV. The electron energy drops with increasing plasma density, consistent with the scaling law $\mathcal{E}_e \propto a_0/\rho_e$. Comparing the experimental data with the scaling law further indicates that the laser intensity is amplified by self-focusing and self-compression in the plasma to $a_0 \simeq 2.6$. Moreover, the produced electron beam charge reaches a maximum around the plasma density of 8×10^{18} cm^{-3}. That is because electron self-trapping is not efficient at lower densities, whereas the beam charge is limited by shortening of dephasing length and pump depletion length, and beam-loading when the plasma density increases. Meanwhile, betatron X-ray radiation consisting of 1-10 keV photons was measured with a peak fluence of 5.7×10^5 photons/mrad^2. The photon fluence is very sensitive to beam charge variance, and shows a peak at the same plasma density as the beam charge does. The relationship between beam charge and X-ray fluence furthermore allowed us to deduce the number of betatron oscillations fulfilled by an electron inside the plasma bubble to be $N_\beta = 4 \pm 2$. The X-ray peak brightness is estimated to be of the order of $\sim 10^{21}$ photons/s/mm^2/mrad^2/0.1%BW, which is around 30 times higher than that in the case of a 2 mm gas jet, highlighting the role of capillary guiding. The electron acceleration process, diagnosed using the far-field X-ray intensity profile, indicates that the laser-plasma interaction terminates when the pump laser is depleted at around $z \simeq 8$ mm for a plasma density $\rho_e = 8.1 \times 10^{18}$ cm^{-3}. Three dimensional PIC simulations reasonably reproduce the experimental findings. It shows that the laser intensity is amplified to $a_0 > 3$ at $\rho_e = 8 \times 10^{18}$ cm^{-3} and a significant number of electrons is trapped in the first plasma bubble, forming a bunch as short as ~ 10 fs. The calculated radiation spectrum deviates from the standard synchrotron case, but is similar to the spectrum corresponding to a distribution of accelerated electrons as discussed in Chapter 3. The PIC simulations also show the accelerated electrons finally overrun the driving laser pulse and get scattered by the laser ponderomotive force. The scattered electrons enter capillary wall if the capillary tube is long enough, generating bremsstrahlung radiation with photons extending to gamma-ray range. This radiation produces a broad secondary illumination on the X-ray detector.

The stability of the generated electron beam was examined. It exhibits a shot-to-shot reproducibility with fluctuations of a few percent in electron energy, and around 20% RMS in beam charge and divergence. Beam charge and divergence have a linear correlation, and the instability of beam charge is found to be sensitively linked to laser energy (power) fluctuation. It suggests laser energy must be carefully stabilized to diminish beam charge fluctuation. Meanwhile, the electron beams possess a pointing fluctuation of ~ 1 mrad when the laser pointing is stabilized, which is of great interest for further transporting and using the beam. Moreover, the X-ray source size was evaluated using Fresnel diffraction induced by a razor blade. Assuming a spatially coherent source with a synchrotron spectrum, the theoretically calculated curve with a source size ($1/e^2$ intensity waist of Gaussian distribution) of 1.5 μm and a critical energy of 6 keV best reproduces the experimental diffraction pattern. The difference between theoretical and experimental results probably result from a partial absorption of X-ray photons in the razor blade part. Consequently, some transmitted photons are deflected and overlap with the diffracted photons, inducing the observed X-ray intensity overshoot in experiments. Using the mean source size of $r_s = 2.5$ μm, we are able to compute the corresponding upper limit of the normalized RMS emittance of electron beam to be $\epsilon_n^\perp \simeq 0.83\pi$ mm mrad.

As presented in this thesis, even though LWFAs have made tremendous progress in the past decades, most of the generated electrons are still in the energy range from sub-GeV to ~ 1 GeV [40]. One of the promising perspectives is therefore to push the electron energy to multi-GeV or even further to TeV. One way to boost the output electron energy could be

the concept of proton-driven plasma walefield acceleration proposed by Caldwell *et al* [16], however a TeV-class proton beam has to be obtained first from a RF accelerator. Another attractive scheme is multi-stage laser-plasma acceleration [22, 209], which is being studied in our group and planned to be explored experimentally in the frame of the CILEX (Centre Interdisciplinaire Lumière Extrême) project in France.

List of Notations

α	:	Fraction of laser energy contained by the FWHM laser focal spot
α_p	:	Mean polarizability of molecule
A	:	Vector potential
A_m	:	Magnitude of the EH_{1m} mode in capillary tube
A_r	:	Molar refractivity
a	:	Normalized vector potential
β	:	Normalized velocity
β_z	:	Normalized longitudinal velocity
β_p	:	Normalized phase velocity of plasma wave
$\mathbf{B}$	:	Magnetic field
c	:	Speed of light in vacuum (3×10^8 m/s)
C_m	:	Efficiency of laser coupling to the EH_{1m} mode
C_{ccd}^m	:	CCD count in the region of filter metal m
C_{ph}	:	Contrast of photodiode signal
$\mathcal{C}_F$	:	Fresnel integral of cosine function
δ_{ij}	:	Kronecker delta function
d	:	Particle hard shell diameter
D_a	:	Characteristic size of aperture
D_{cap}	:	Capillary diameter
D_{ml}	:	Distance between magnet and Lanex screen
χ	:	Numerical difference of least squares
ϵ	:	Turbulent dissipation
ε_0	:	Permittivity of free space (8.85×10^{-12} F/m)
η_f	:	Efficiency of gas filling from reservoir into capillary tube
$-e$	:	Electron charge (-1.6×10^{-19} C)
$\mathbf{e}_\perp$	:	Unitary vector
$\mathcal{E}_e$	:	Electron energy
$\Delta\mathcal{E}_e$	:	Electron energy spread
$\mathcal{E}_c$	:	Critical energy
$\mathcal{E}_L$	:	Laser energy
$\mathcal{E}_{in}$	:	Internal energy per unit mass
$\mathcal{E}_{int}$	:	Initial electron energy of acceleration
$\mathcal{E}_{fin}$	:	Final electron energy of acceleration
$\mathcal{E}_{ph}$	:	Photon energy
$\mathbf{E}$	:	Electric field
E_0	:	Cold nonrelativistic wavebreaking field
E_L	:	Amplitude of electric field
E_{wb}	:	Relativistic wavebreaking field
E_r	:	Transverse electric field of plasma wave
E_z	:	Longitudinal electric field of plasma wave

$\mathbf{f}_b$: Body force per unit volume acting on fluid
$\mathcal{F}$: Normalized laser transverse flux at capillary wall
$\mathbf{F}_B$: Magnetic force
$\mathbf{F}_p$: Ponderomotive force
F_n : nth harmonic amplitude of betatron oscillation
F_r : Fresnel number
γ : Relativistic factor
$\gamma_\perp$: Transverse relativistic factor
γ_z : Longitudinal relativistic factor
γ_p : Relativistic factor of plasma wave
Γ : Keldysh parameter
G_{cdd} : Gain of CCD camera
$\mathcal{H}$: Hamiltonian
$\mathcal{H}_s$: Hamiltonian of the separatrix
H : Heaviside function
$\hbar$: Plank constant (1.055×10^{-34} J·s)
i : Imaginary unit ($i = \sqrt{-1}$)
I_0 : Laser peak intensity
I_b : X-ray intensity produced by electron bunch
I_f : Fringe intensity
I_X : X-ray intensity
$\mathcal{J}_n$: First kind Bessel function of the nth order
Φ : Scalar potential
Φ_{ion} : Ionization potential
ϕ : Normalized scalar potential
φ : Azimuthal angle
$\mathbf{j}$: Current density
K_β : Betatron strength parameter
Kn : Knudsen number
$\mathcal{K}$: Second kind modified Bessel function
k_0 : Laser wavenumber
k_β : Betatron wavenumber
k_p : Wavenumber of plasma wave
$\varkappa$: Energy in turbulence
κ : Dynamic viscosity
κ_B : Boltzmann constant (1.38×10^{-23} J/K)
κ_g : Heat capacity ratio of gas
λ_0 : Laser wavelength
λ_B : Period of magnetic field in an undulator/wiggler
λ_X : Wavelength of X-ray radiation
Λ_c^{ph} : Factor of photon per CCD count
ℓ_f : Molecular mean free path length
$L_\downarrow$: Characteristic length of density downramp
L_X : Distance between capillary exit and detector
L_{cap} : Length of capillary tube
L_d : Dephasing length
L_i : Distance from aperture to detector
L_o : Distance from X-ray source to aperture
L_{pd} : Pump depletion length
L_m^l : Attenuation length of the mth laser mode in capillary tube

μ_0 : Permeability of free space ($4\pi \times 10^{-7}$ N/A^2)
m_e : Electron mass (9.11×10^{-31} kg)
m_g : Mass of gas atom
M_a : Mach number
$\mathbb{M}$: Magnification
n : Index of refraction
$\mathbf{n}$: Unity vector from radiation source to observer
N_A : Avogadro constant (6.02×10^{23} mol^{-1})
N_β : Number of electron betatron oscillations
N_e : Total electron number
$\mathcal{N}_e$: Electron number for a specific electron energy
ω_β : Betatron frequency
ω_0 : Laser angular frequency
ω_c : Critical frequency
ω_c^{fit} : Best fit of critical frequency
ω_c^{max} : Critical frequency corresponding to maximum electron energy
ω_n : nth harmonic frequency of betatron radiation
ω_p : Plasma frequency
Ω : Solid angle
Ω_p : Surface of photodiode
$\mathcal{O}$: High-order small amount
$\Delta\psi$: Phase shift
ψ_g : Gouy phase term
ψ_{off} : Offset phase
Π : Half plane
$\mathbf{p}$: Momentum
P_L : Laser power
P_c : Critical power for self-focusing
P_s : Power radiated by a single electron
P : Pressure
q_{ccd} : Quantum efficiency of CCD chip
Q : Electron beam charge
ρ_e : Plasma electron density
ρ_c : Critical density
$\delta\rho_e$: Plasma electron density perturbation
ρ^* : Plateau gas density between two capillary slits
ϱ : Mass density
R : Radius of wavefront curvature
Re : Reynolds number
R_{X0} : Inner radius of X-ray transition zone
R_{X1} : Outer radius of X-ray transition zone
R_b : Bubble radius
R_{cap} : Radius of capillary tube
R_g : Gas constant (8.31 J/K/mol)
R_n : Spectrum function of betatron radiation
$\mathbf{S}$: Poynting's vector
S_p : Photodiode signal
S_N : Normalized photodiode signal
S_X : X-ray signal
$\mathcal{S}_F$: Fresnel integral of sine function

τ_0	:	FWHM pulse duration
ϑ	:	Normalized gas density profile
θ	:	Angle
θ_{ccd}	:	Viewing angle of CCD camera
θ_{in}	:	Incident angle
θ_L	:	Laser diffraction angle
Θ_0	:	Opening angle of betatron radiation at a give time
Θ_β	:	Opening angle of betatron radiation
Θ_{cap}	:	Cropping angle of capillary tube
Θ_e	:	Divergence of electron beam
t	:	Time
τ_d	:	Time delay
τ_l	:	Characteristic decay time of Lanex fluorescence
T	:	Temperature
T	:	Stress tensor
u	:	Normalized momentum
u_m	:	mth root of $\mathcal{J}_0(x) = 0$
U	:	Magnitude constant of electric field
v_g	:	Group velocity of electromagnetic wave in plasma
v_{ph}	:	Phase velocity of electromagnetic wave in plasma
v_p	:	Phase velocity of plasma wave
W_s	:	Energy radiated by a single electron
w_0	:	Waist of laser spot in focal plane
ξ	:	Coordinate in the co-moving frame
Ξ	:	Source plane
$\mathcal{Y}$	:	Bessel function of the second kind
Δz	:	Longitudinal extension of betatron radiation
z_0	:	Center of capillary tube
z_R	:	Rayleigh length
Z_n^m	:	Zernike polynomial
ζ	:	Frequency normalized by critical frequency (ω/ω_c)

List of Figures

List of Tables

Appendix A

Theoretical derivations

A.1 Maxwell's equations

Maxwell's equations contains four equations to describe the static electric and magnetic fields are generated by charge and current, and how the time varying electric and magnetic fields depend on each other. For some cases, the problem can be simplified by using the Maxwell's equations in Gaussian units.

Table A.1: *Maxwell's equations*

Name	SI units	Gaussian units
Gauss's law	$\nabla \cdot \mathbf{E} = \frac{\rho}{\varepsilon_0}$	$\nabla \cdot \mathbf{E} = 4\pi\rho$
Gauss's law for magnetism	$\nabla \cdot \mathbf{B} = 0$	$\nabla \cdot \mathbf{B} = 0$
Maxwell-Faraday equation	$\nabla \times \mathbf{E} = -\frac{\partial \mathbf{B}}{\partial t}$	$\nabla \times \mathbf{E} = -\frac{1}{c}\frac{\partial \mathbf{B}}{\partial t}$
Ampère-Maxwell equation	$\nabla \times \mathbf{B} = \mu_0\mathbf{j} + \frac{1}{c^2}\frac{\partial \mathbf{E}}{\partial t}$	$\nabla \times \mathbf{B} = \frac{4\pi}{c}\mathbf{j} + \frac{1}{c}\frac{\partial \mathbf{B}}{\partial t}$

where ∇ is the gradient operator:

$$\nabla = \begin{cases} \mathbf{e}_x \frac{\partial}{\partial x} + \mathbf{e}_y \frac{\partial}{\partial y} + \mathbf{e}_z \frac{\partial}{\partial z}, & \text{in cartesian coordinate} \\ \mathbf{e}_r \frac{\partial}{\partial r} + \mathbf{e}_\theta \frac{1}{r}\frac{\partial}{\partial \theta} + \mathbf{e}_z \frac{\partial}{\partial z}, & \text{in cylindrical coordinate} \\ \mathbf{e}_r \frac{\partial}{\partial r} + \mathbf{e}_\theta \frac{1}{r}\frac{\partial}{\partial \theta} + \mathbf{e}_\varphi \frac{1}{r\sin\theta}\frac{\partial}{\partial \varphi}, & \text{in spherical coordinate} \end{cases} \tag{A.1}$$

A.2 The laser frame

The laser frame is a reference frame moving at the speed of the laser group velocity (the phase velocity of plasma wave) v_p. It is a Galilean transform from (z, t) to (ξ, τ), where $\xi = z - v_p t$ and $\tau = t$. The derivatives change accordingly

$$\begin{aligned} \frac{\partial}{\partial t} =& \frac{\partial \tau}{\partial t}\frac{\partial}{\partial \tau} + \frac{\partial \xi}{\partial t}\frac{\partial}{\partial \xi} = \frac{\partial}{\partial \tau} - v_p \frac{\partial}{\partial \xi}, \\ \frac{\partial}{\partial z} =& \frac{\partial \tau}{\partial z}\frac{\partial}{\partial \tau} + \frac{\partial \xi}{\partial z}\frac{\partial}{\partial \xi} = \frac{\partial}{\partial \xi}, \\ \frac{\partial^2}{\partial t^2} =& \frac{\partial^2}{\partial \tau^2} + v_p^2 \frac{\partial^2}{\partial \xi^2} - 2v_p \frac{\partial^2}{\partial \xi \partial \tau}, \\ \frac{\partial^2}{\partial z^2} =& \frac{\partial^2}{\partial \xi^2}. \end{aligned} \tag{A.2}$$

A.3 Equations of plasma wave

A.3.1 Linear plasma wave

Assuming the plasma is initially uniform with a density of ρ_0 and the density perturbation is relatively small, $|\rho_e - \rho_0|/\rho_0 \ll 1$, the continuity equation $\partial\rho_e/\partial t + \nabla\cdot(\rho_e\mathbf{v}) = 0$ can be linearized and averaged to

$$\frac{\partial\delta\rho_e}{\partial t} + \rho_0\nabla\cdot\langle\mathbf{v}\rangle = 0, \tag{A.3}$$

where $\delta\rho_e = \rho_e - \rho_0$ denotes the plasma electron density variation. Differentiating Equation A.3 with respect to t yields

$$\frac{\partial^2}{\partial t^2}\left(\frac{\delta\rho_e}{\rho_0}\right) + \nabla\cdot\frac{\partial\langle\mathbf{v}\rangle}{\partial t} = 0. \tag{A.4}$$

The term $\partial\langle\mathbf{v}\rangle/\partial t$ can be found from the Lorentz equation 2.7 to be

$$\begin{aligned}\frac{\partial\langle\mathbf{v}\rangle}{\partial t} &= \left\langle -\frac{e}{m_e}\mathbf{E} - (\mathbf{v}\cdot\nabla)\mathbf{v} - \frac{e}{m_e}\mathbf{v}\times\mathbf{B}\right\rangle, \\ &= -\frac{e}{m_e}\langle\mathbf{E}\rangle - c^2\nabla\frac{\langle a^2\rangle}{2}, \\ &= -\frac{e}{m_e}\langle\mathbf{E}\rangle - c^2\nabla\frac{a_0^2}{4}.\end{aligned} \tag{A.5}$$

Substituting Equation A.5 together with Gauss's law

$$\nabla\cdot\langle\mathbf{E}\rangle = -\frac{e}{\varepsilon_0}(\rho_e - \rho_0) = -\frac{e}{\varepsilon_0}\delta\rho_e, \tag{A.6}$$

into Equation A.4, one will get the governing equation for plasma wave generation

$$\left(\frac{\partial^2}{\partial t^2} + \omega_p^2\right)\frac{\delta\rho_e}{\rho_0} = c^2\nabla^2\frac{a_0^2}{4}. \tag{A.7}$$

The left-hand side of Equation A.7 represents the density oscillation of the plasma wave, while the right-hand side corresponds to the wave driver: the ponderomotive force. The Green's function solution of Equation A.7 is [21]

$$\begin{aligned}\frac{\delta\rho_e}{\rho_0} &= \frac{c^2}{\omega_p^2}\int_0^t \nabla^2\frac{a_0^2(\mathbf{r},t')}{4}\sin[\omega_p(t-t')]dt', \\ \frac{\langle\mathbf{E}\rangle}{E_0} &= -c\int_0^t \nabla^2\frac{a_0^2(\mathbf{r},t')}{4}\sin[\omega_p(t-t')]dt',\end{aligned} \tag{A.8}$$

where $E_0 = m_e c\omega_p/e$ is the cold wavebreaking field.

A.3.2 Nonlinear plasma wave

Following the mathematical approach in Refs. [79, 210], we will derive the governing equation of nonlinear plasma wave in the laser co-moving frame (ξ, τ). The Hamiltonian describing the motion of an electron in 1D plasma is given by [79]

$$\mathcal{H}(\gamma,\xi) = \gamma(1-\beta_z\beta_p) - \phi(\xi) = \gamma - u_z\beta_p - \phi(\xi), \tag{A.9}$$

where $\phi = -e\Phi/m_e c^2$ is the normalized plasma potential. The Hamiltonian does not explicitly depends on time, so at any time $\mathcal{H}(t) = \mathcal{H}(t = 0)$. Initially, there is no plasma wave, so $\gamma(t = 0) = 1$, $\beta_z(t = 0) = 0$, and $\phi(t = 0) = 0$, leading to $\mathcal{H}(t = 0) = 1$. Substituting the initial Hamiltonian into Equation A.9 yields

$$\gamma - u_z\beta_p - \phi(\xi) - 1 = 0. \tag{A.10}$$

The electron energy and momentum are related by $\gamma^2 = 1 + u^2$, where $u = p/m_e c$ is the normalized momentum. Furthermore, u can be written as $u^2 = u_\perp^2 + u_z^2 = a^2 + u_z^2$. Thus the relativistic factor becomes

$$\gamma = \sqrt{1 + a^2 + u_z^2}. \tag{A.11}$$

On the other hand, transforming the continuity equation into the laser frame gives

$$-ev_p\frac{\partial\rho_e(\xi)}{\partial\xi} - \frac{\partial j(\xi)}{\partial\xi} = 0, \tag{A.12}$$

where v_p is the phase velocity of the plasma wave. Integrating this equation yields $e\rho_e v_p + j = e\rho_0 v_p$. Recalling the current is given by $j = -e\rho_e v_z$, one can obtain

$$\rho_e(v_p - v_z) - \rho_0 v_p = 0. \tag{A.13}$$

Treating β_p, ϕ, and a as variables, Equations A.10, A.11, A.13 constitute a closed equation system. Solving them leads to [21]

$$\frac{\rho_e}{\rho_0} = \gamma_p^2\beta_p\left[\left(1 - \frac{1 + a^2}{\gamma_p^2(1 + \phi)^2}\right)^{-1/2} - \beta_p\right]. \tag{A.14}$$

Besides, in the co-moving frame Poisson equation is written as

$$\frac{\partial^2\phi}{\partial\xi^2} = k_p^2\left(\frac{\rho_e}{\rho_0} - 1\right). \tag{A.15}$$

Inserting Equation A.14 into Equation A.15, one will finally obtain the equation describing nonlinear plasma wave generation

$$\frac{\partial^2\phi}{\partial\xi^2} = k_p^2\gamma_p^2\left\{\beta_p\left[1 - \frac{1 + a^2}{\gamma_p^2(1 + \phi)^2}\right]^{-1/2} - 1\right\}. \tag{A.16}$$

Likewise, the term a^2 on the right-hand side of Equation A.16 indicates the origin of plasma wave excitation is the laser ponderomotive force. This equation can be solved numerically, and the associated electric field is obtained through $E_z = -E_0\partial\phi/\partial\xi$.

A.4 Derivation from Equation 4.34 to Equation 4.36

Figure A.1 schematically shows laser beam propagation around the second cube of the interferometer. The wavefront of beam 2 is titled by a tiny angle θ with respect to the z axis. Beam 1 is the reference beam which propagates along the z axis. Beam 2 is the one coming from the capillary tube. $P' = (x_0, 0, 0)$ is the virtual source of beam 2 with respect

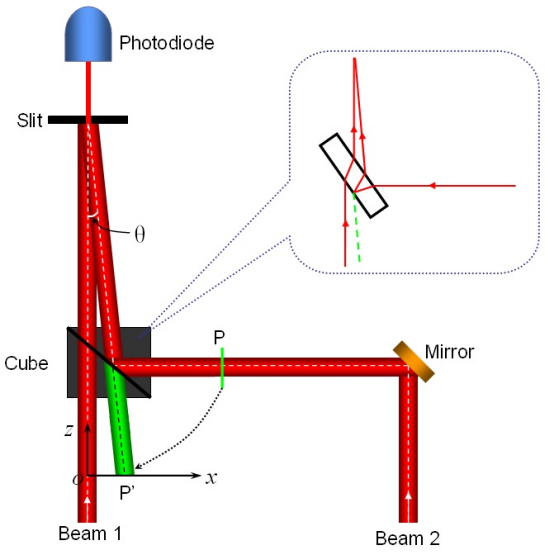

Figure A.1: Schematic illustration of laser beam propagation in the interferometer.

to the cube. Both of the optical beams are assumed to be Gaussian, so the superposed wave is

$$\begin{aligned} E(x,y,t) &= E_1 \exp\left(-\frac{x^2+y^2}{w_1^2}\right)\cos(kz-\omega t) \\ &+ E_2 \exp\left[-\frac{(x-x_0)^2+y^2}{w_2^2}\right]\cos\left[kz\cos\theta + k(x_0-x)\sin\theta + \Delta\psi(t) - \omega t\right], \end{aligned} \tag{A.17}$$

where w_1, w_2 are the waists of beam 1 and 2, respectively. We can further have

$$\begin{aligned} E^2(x,y,t) &= E_1^2 \exp\left(-2\frac{x^2+y^2}{w_1^2}\right)\cos^2(kz-\omega t) \\ &+ E_2^2 \exp\left[-2\frac{(x-x_0)^2+y^2}{w_2^2}\right]\cos^2\left[kz\cos\theta + k(x_0-x)\sin\theta + \Delta\psi(t) - \omega t\right] \\ &+ 2E_1E_2 \exp\left[-\frac{x^2+y^2}{w_1^2} - \frac{(x-x_0)^2+y^2}{w_2^2}\right]\cos(kz-\omega t)\cos\left[kz\cos\theta + k(x_0-x)\sin\theta + \Delta\psi(t) - \omega t\right]. \end{aligned} \tag{A.18}$$

Averaging Equation A.18 in time leads to

$$\begin{aligned} \langle E^2(x,y,t)\rangle &= \frac{E_1^2}{2}\exp\left(-2\frac{x^2+y^2}{w_1^2}\right) + \frac{E_2^2}{2}\exp\left[-2\frac{(x-x_0)^2+y^2}{w_2^2}\right] \\ &+ E_1E_2 \exp\left[-\frac{x^2+y^2}{w_1^2} - \frac{(x-x_0)^2+y^2}{w_2^2}\right]\cos\left[\underbrace{kz\cos\theta - kz + k(x_0-x)\sin\theta}_{\psi_0} + \Delta\psi(t)\right]. \end{aligned} \tag{A.19}$$

The intensity of fringe at position (x, y) can be calculated through

$$I_f(x,y,t) = \frac{c\varepsilon_0}{2}\langle E^2(x,y,t)\rangle. \tag{A.20}$$

On the other hand, the photodiode signal is given by

$$\begin{aligned} S_p(t) &= \alpha_{ph} \iint_{\Omega_p} I_f(x,y,t) H(x,y)\, dx\, dy = \alpha_{ph} \iint_{\Omega'} I_f(x,y,t)\, dx\, dy \\ &= \alpha_{ph} \int_{-\Delta y}^{\Delta y} \int_{-\Delta x}^{\Delta x} I_f(x,y,t)\, dx\, dy = \frac{\alpha_{ph} c \varepsilon_0}{2} \int_{-\Delta y}^{\Delta y} \int_{-\Delta x}^{\Delta x} \langle E^2(x,y,t) \rangle\, dx\, dy, \end{aligned} \tag{A.21}$$

where $\Omega' = [-\Delta x, \Delta x] \times [-\Delta y, \Delta y]$ indicates the slit region. Substituting Equation A.19 into Equation A.21, one can obtain

$$\begin{aligned} S_p(t) &= \frac{\alpha_{ph} c \varepsilon_0}{2} \int_{-\Delta y}^{\Delta y} \int_{-\Delta x}^{\Delta x} \langle E^2(x,y,t) \rangle\, dx\, dy \\ &= \underbrace{\frac{\alpha_{ph} c \varepsilon_0}{2} \int_{-\Delta y}^{\Delta y} \int_{-\Delta x}^{\Delta x} \left\{ \frac{E_1^2}{2} \exp\left(-2 \frac{x^2+y^2}{w_1^2} \right) + \frac{E_2^2}{2} \exp\left[-2 \frac{(x-x_0)^2+y^2}{w_2^2} \right] \right\} dx\, dy}_{\mathcal{A}} \\ &+ \underbrace{\frac{\alpha_{ph} c \varepsilon_0}{2} \int_{-\Delta y}^{\Delta y} \int_{-\Delta x}^{\Delta x} \left\{ E_1 E_2 \exp\left[-\frac{x^2+y^2}{w_1^2} - \frac{(x-x_0)^2+y^2}{w_2^2} \right] \cos[\psi_0 + \Delta\psi(t)] \right\} dx\, dy}_{\mathcal{W}}. \end{aligned} \tag{A.22}$$

The second term $\mathcal{W}$ in Equation A.22 can be further simplified as

$$\begin{aligned} \mathcal{W} =& \frac{\alpha_{ph} c \varepsilon_0}{2} E_1 E_2 \int_{-\Delta y}^{\Delta y} \int_{-\Delta x}^{\Delta x} \left\{ \exp\left[-\frac{x^2+y^2}{w_1^2} - \frac{(x-x_0)^2+y^2}{w_2^2} \right] \cos[\psi_0 + \Delta\psi(t)] \right\} dx\, dy \\ =& \frac{\alpha_{ph} c \varepsilon_0}{2} E_1 E_2 \int_{-\Delta y}^{\Delta y} \int_{-\Delta x}^{\Delta x} \left\{ \exp\left[-\frac{x^2+y^2}{w_1^2} - \frac{(x-x_0)^2+y^2}{w_2^2} \right] \right. \\ & \left. \times [\cos\psi_0 \cos\Delta\psi(t) - \sin\psi_0 \sin\Delta\psi(t)] \right\} dx\, dy \\ =& \underbrace{\frac{\alpha_{ph} c \varepsilon_0}{2} E_1 E_2 \int_{-\Delta y}^{\Delta y} \int_{-\Delta x}^{\Delta x} \left\{ \exp\left[-\frac{x^2+y^2}{w_1^2} - \frac{(x-x_0)^2+y^2}{w_2^2} \right] \cos\psi_0 \right\} dx\, dy}_{\mathcal{P}} \cos\Delta\psi(t) \\ & \underbrace{- \frac{\alpha_{ph} c \varepsilon_0}{2} E_1 E_2 \int_{-\Delta y}^{\Delta y} \int_{-\Delta x}^{\Delta x} \left\{ \exp\left[-\frac{x^2+y^2}{w_1^2} - \frac{(x-x_0)^2+y^2}{w_2^2} \right] \sin\psi_0 \right\} dx\, dy}_{\mathcal{Q}} \sin\Delta\psi(t) \\ =& \mathcal{P} \cos\Delta\psi(t) - \mathcal{Q} \sin\Delta\psi(t). \end{aligned} \tag{A.23}$$

We then introduce an angle variable θ_0 satisfying

$$\begin{aligned} \cos\theta_0 &= \frac{\mathcal{P}}{\sqrt{\mathcal{P}^2+\mathcal{Q}^2}}, \\ \sin\theta_0 &= \frac{\mathcal{Q}}{\sqrt{\mathcal{P}^2+\mathcal{Q}^2}}. \end{aligned} \tag{A.24}$$

Substituting Equation A.24 into Equation A.23, $\mathcal{W}$ can be reformed as

$$\begin{aligned} \mathcal{W} =& \sqrt{\mathcal{P}^2+\mathcal{Q}^2} [\cos\theta_0 \cos\Delta\psi(t) - \sin\theta_0 \sin\Delta\psi(t)] \\ =& \sqrt{\mathcal{P}^2+\mathcal{Q}^2} \cos[\theta_0 + \Delta\psi(t)]. \end{aligned} \tag{A.25}$$

Using Equation A.25 into Equation A.22, the photodiode signal becomes

$$S_p(t) = \mathcal{A} + \mathcal{W} = \mathcal{A} + \mathcal{B}\cos[\theta_0 + \Delta\psi(t)], \tag{A.26}$$

where $\mathcal{B} = \sqrt{\mathcal{P}^2 + \mathcal{Q}^2}$. For a given experimental setup, the constants $\mathcal{A}$, $\mathcal{B}$ can be calculated numerically.

A.5 Zernike polynomials

The Zernike polynomials are a sequence of polynomials which are orthogonal on the unit disk. It is defined as

$$\begin{aligned} Z_n^m(\rho,\varphi) &= R_n^m(\rho)\cos(m\varphi), \\ Z_n^{-m}(\rho,\varphi) &= R_n^m(\rho)\sin(m\varphi), \end{aligned} \tag{A.27}$$

where $\rho \in [0,1]$; n and m are integrals with $n \geq m$. If $n-m$ is odd, $R_n^m = 0$. Otherwise it is given by

$$R_n^m(\rho) = \sum_{k=0}^{(n-m)/2} \frac{(-1)^k\,(n-k)!}{k!\,((n+m)/2-k)!\,((n-m)/2-k)!}\,\rho^{n-2\,k}. \tag{A.28}$$

The first 15 Zernike polynomials are plotted in Figure A.2. The first ten low-order modes describes the most common aberrations seen in optics such as tilt, coma, and astigmatism. The fourth order modes correspond to spherical aberrations.

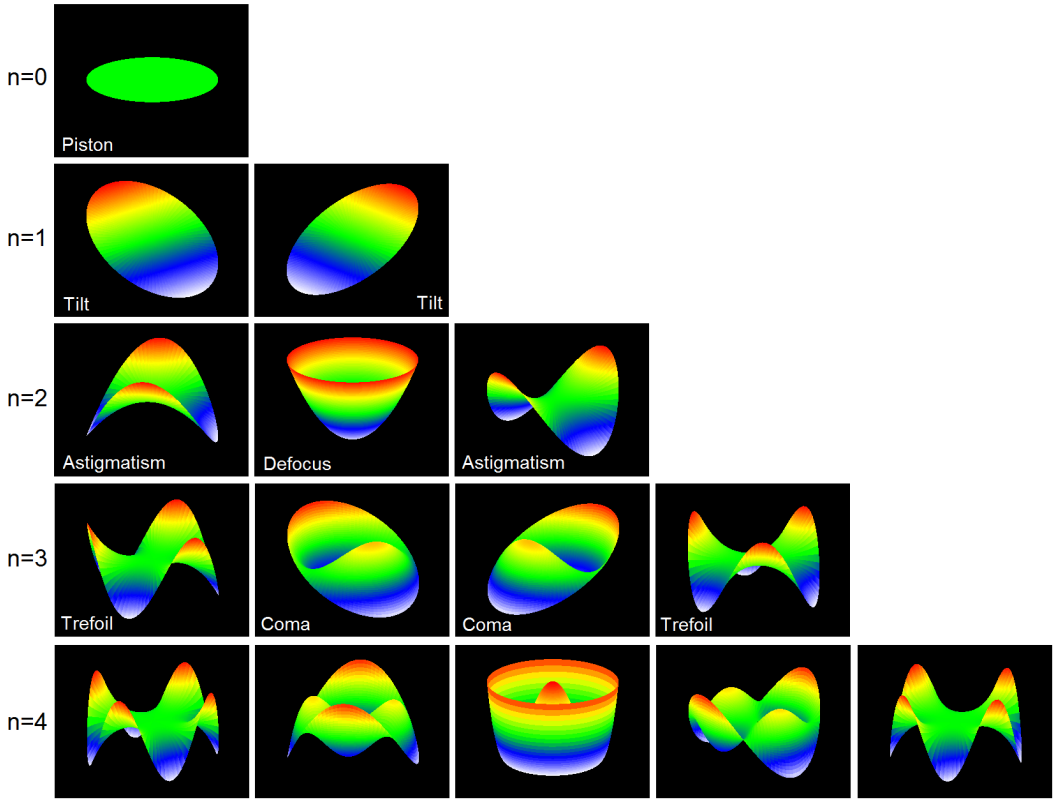

Figure A.2: *The first 15 Zernike polynomials on the unit disk and the corresponding most common laser beam aberrations.*

Appendix B

Results of 2D transient simulations with FLUENT

B.1 Influence of capillary length on gas filling process

In this section, Figures B.1-B.3 present the results of 2D transient simulations for capillary tubes with lengths ranging from 15 to 60 mm while the slit is kept 300 μm wide. The simulation setup parameters can be found in Section 4.5.5.

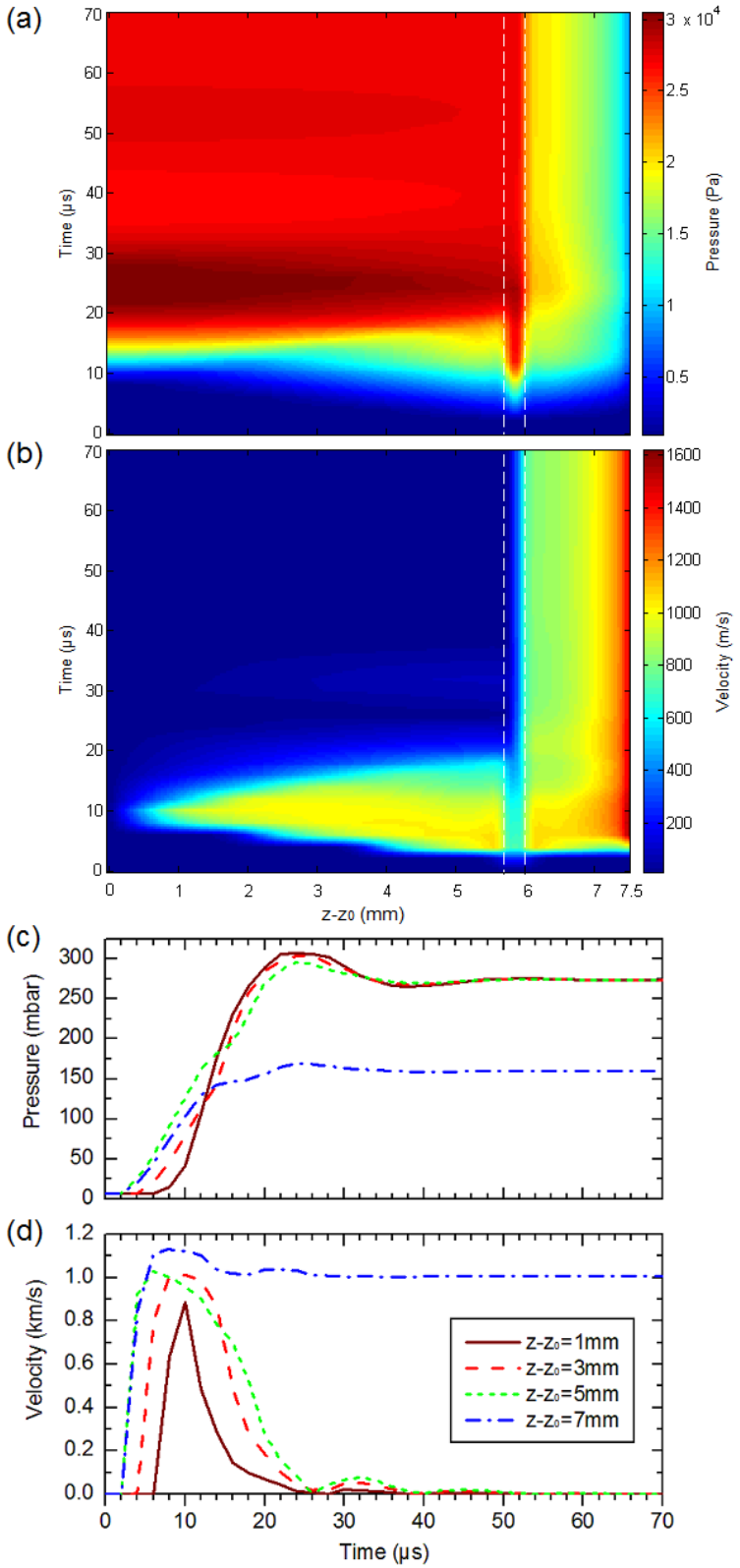

Figure B.1: *Time evolutions of the on-axis (a) gas static pressure and (b) velocity in a 15 mm long, 200 µm diameter capillary tube, where the two dashed lines indicate the slit of 300 µm wide. Evolutions of (c) gas static pressure and (d) velocity at four different locations along the capillary axis.*

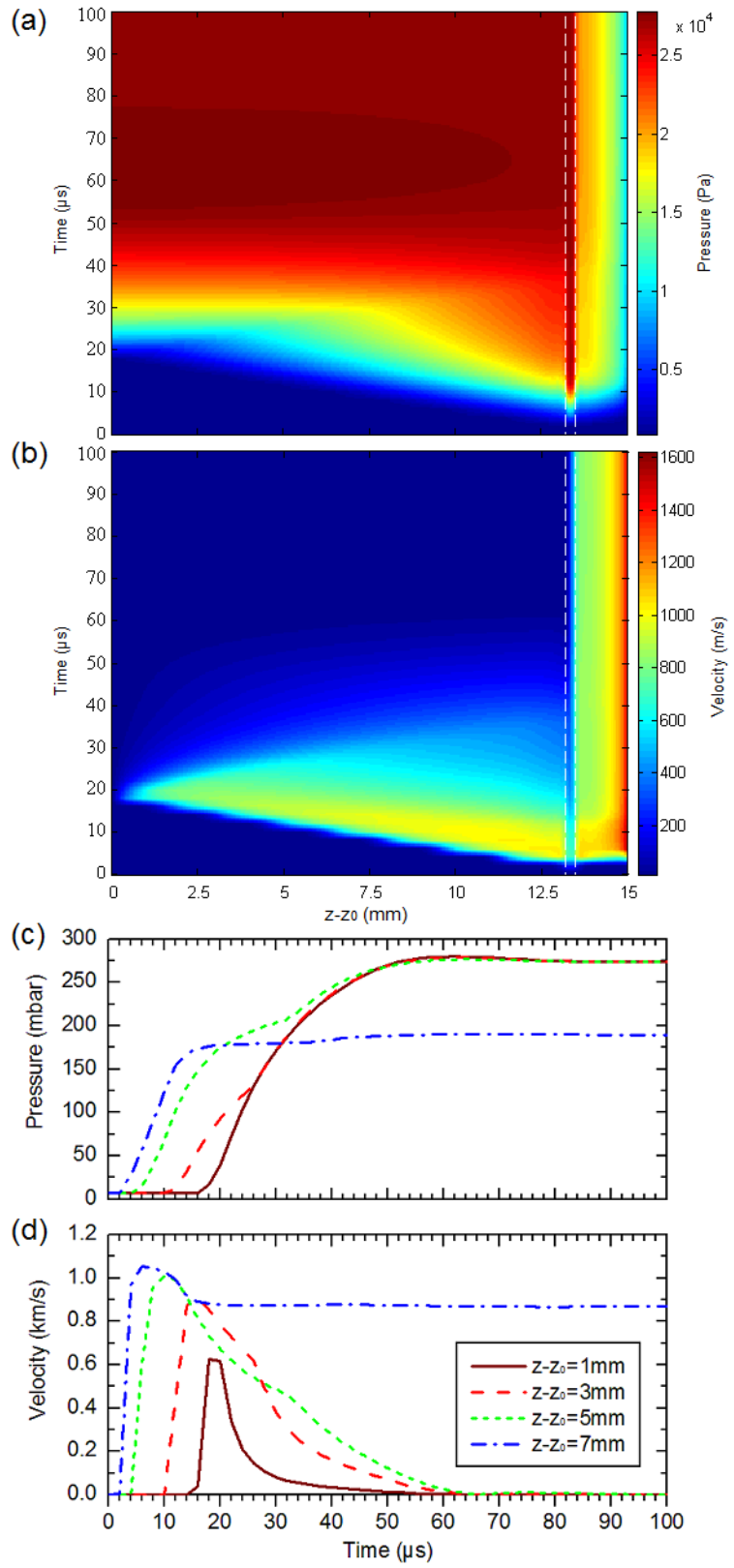

Figure B.2: *Time evolutions of the on-axis (a) gas static pressure and (b) velocity in a 30 mm long, 200 µm diameter capillary tube, where the two dashed lines indicate the slit of 300 µm wide. Evolutions of (c) gas static pressure and (d) velocity at four different locations along the capillary axis.*

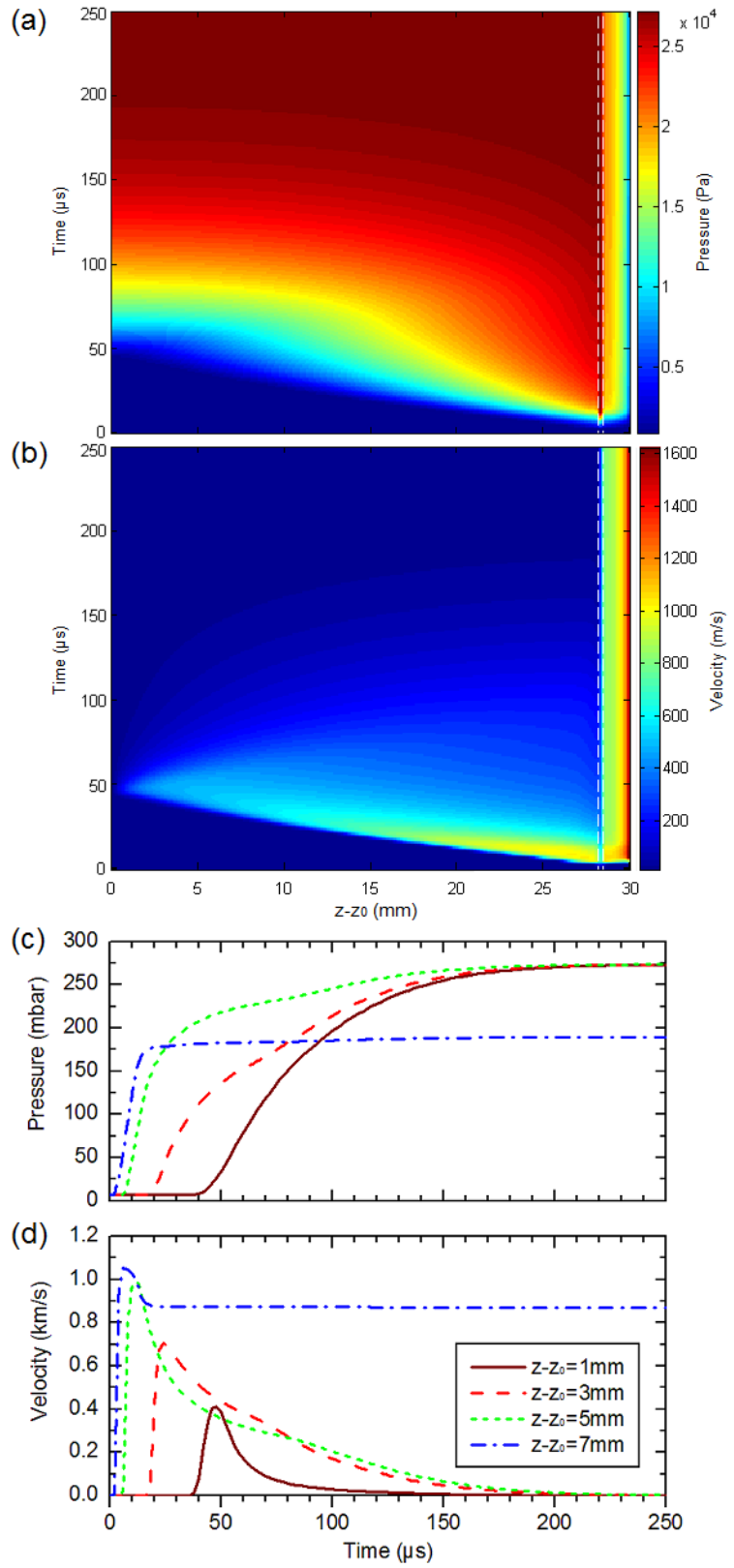

Figure B.3: *Time evolutions of the on-axis (a) gas static pressure and (b) velocity in a 60 mm long, 200 µm diameter capillary tube, where the two dashed lines indicate the slit of 300 µm wide. Evolutions of (c) gas static pressure and (d) velocity at four different locations along the capillary axis.*

Publications and Presentations

I. Publications on the work presented in this thesis:

1. J. Ju, K. Svensson, A. Döpp, H. E. Ferrari, K. Cassou, O. Neveu, G. Genoud, F. Wojda, M. Burza, A. Persson, O. Lundh, C.-G. Wahlström, and B. Cros. Enhancement of X-rays generated by a guided laser wakefield accelerator inside capillary tubes. *Appl. Phys. Lett.*, **100**:191106, 2012.

2. B. Cros, J. Ju, A. Döpp, K. Cassou, H. E. Ferrari, G. Maynard, G. Genoud, F. Wojda, K. Svensson, M. Burza, O. Lundh, A. Persson, and C.-G. Wahlström. Electron beams and X-ray radiation generated by laser wakefield in capillary tubes. *AIP Conf. Proc.*, **1507**:267-272, 2012.

3. J. Ju and B. Cros. Characterization of temporal and spatial distribution of hydrogen gas density in capillary tubes for laser-plasma experiments. *J. Appl. Phys.*, **112**:113102, 2012.

4. J. Ju, K. Svensson, H. E. Ferrari, A. Döpp, G. Genoud, F. Wojda, M. Burza, A. Persson, O. Lundh, C.-G. Wahlström, and B. Cros. Study of electron acceleration and X-ray radiation as a function of plasma density in capillary-guided laser wakefield accelerators. *To be published in Phys. Plasmas.*

5. J. Ju, *et al.* Electron bunch interaction with the driving laser pulse in a long capillary-guided laser wakefield accelerator. *Manuscript.*

Several papers are being prepared to report on the results obtained in the second campaign, for which the author was mainly involved.

II. Publications on the work that the author did during the first year of his PhD study in China:

1. J. Ju, Y. W. Fan, H. H. Zhong, and T. Shu. An improved X-band magnetically insulated transmission line oscillator. *Phys. Plasmas*, **16**:073103, 2009.

2. J. Ju, Y. W. Fan, H. H. Zhong, and T. Shu. A novel dual-frequency magnetically insulated transmission line oscillator. *IEEE Trans. Plasma Sci.*, **37**:2041-2047, 2009.

3. J. Ju, X. J. Ge, H. H. Zhong, and T. Shu. Coupling impedance of 1.6 GHz coaxial relativistic backward wave oscillator. *High Power Laser Part. Beams*, **22**:94-98, 2010.

III. Presentations given by the author during the PhD study:

1. J. Ju, K. Svensson, A. Döpp, H. E. Ferrari, K. Cassou, G. Genoud, F. Wojda, M. Burza, A. Persson, O. Lundh, C.-G. Wahlström, and B. Cros. Rayonnement X et accélération d'électrons par sillage laser dans des tubes capillaires (Poster in French). *19ème Colloque de Jeunes Chercheurs en Physique*, 2011, France.

2. J. Ju, K. Svensson, A. Döpp, H. E. Ferrari, K. Cassou, G. Genoud, F. Wojda, M. Burza, A. Persson, O. Lundh, C.-G. Wahlström, and B. Cros. Rayonnement X et électrons générés par un accélérateur laser plasma dans des tubes capillaires (Oral in French). *Journées Accélérateurs de la SFP*, 2011, France.

3. J. Ju, K. Svensson, A. Döpp, H. E. Ferrari, K. Cassou, G. Genoud, F. Wojda, M. Burza, A. Persson, O. Lundh, C.-G. Wahlström, and B. Cros. Electron beam and X-ray generated by laser wakefield in dielectric capillary tubes (Oral in English). *LaserLab Europe Meeting*, 2012, Hungary.

4. J. Ju, K. Svensson, A. Döpp, H. E. Ferrari, K. Cassou, G. Genoud, F. Wojda, M. Burza, A. Persson, O. Lundh, C.-G. Wahlström, and B. Cros. Capillary-guided laser plasma acceleration and betatron X-ray radiation (Oral in English). *32nd European Conference on Laser Interaction with Matter*, 2012, Poland.

5. J. Ju, K. Svensson, H. E. Ferrari, G. Genoud, F. Wojda, M. Burza, A. Persson, O. Lundh, C.-G. Wahlström, and B. Cros. Study of electron acceleration and betatron X-ray radiation in capillary-guided laser wakefield accelerators (Poster in English). *1st European Advanced Accelerator Concepts Workshop*, 2013, Italy.

Bibliography

[1] T. Feder. Accelerator school travels university circuit. *Phys. Today*, 63:20–22, 2010.

[2] R. J. Van De Graaff. A 1,5000,000 volt electrostatic generator. *Rhys. Rev.*, 38:1919, 1931.

[3] Jr. S. Humphries. *Principles of charged particle acceleration.* John Wiley and Sons, 1999.

[4] D. H. Bilderback, P. Elleaume, and E. Weckert. Review of third and next generation synchrotron light sources. *J. Phys. B: At. Mol. Opt. Phys.*, 38:S733–S797, 2005.

[5] B. W. J. McNeil and N. R. Thompson. X-ray free-electron lasers. *Nat. Photon.*, 4:814–821, 2010.

[6] J. M. J. Madey. Spontaneous emission of bremsstrahlung in a periodic magnetic field. *J. Appl. Phys.*, 42:1906–1913, 1971.

[7] P. Emma, R. Akre, J. Arthur, R. Bionta, C. Bostedt, J. Bozek, A. Brachmann, P. Bucksbaum, R. Coffee, F.-J. Decker, Y. Ding, D. Dowell, S. Edstrom, A. Fisher, J. Frisch, S. Gilevich, J. Hastings, G. Hays, Ph. Hering, Z. Huang, R. Iverson, H. Loos, M. Messerschmidt, A. Miahnahri, S. Moeller, H.-D. Nuhn, G. Pile, D. Ratner, J. Rzepiela, D. Schultz, T. Smith, P. Stefan, H. Tompkins, J. Turner, J. Welch, W. White, J. Wu, G. Yocky, and J. Galayda. First lasing and operation of an ångstrom-wavelength free-electron laser. *Nat. Photon.*, 4:641–647, 2010.

[8] E. Hand. X-ray free-electron lasers fire up. *Nature*, 461:708–709, 2009.

[9] T. Tajima and J. M. Dawson. Laser electron accelerator. *Phys. Rev. Lett.*, 43(4):267–270, 1979.

[10] V. Malka, S. Fritzler, E. Lefebvre, M.-M. Aleonard, F. Burgy, J.-P. Chambaret, J.-F. Chemin, K. Krushelnick, G. Malka, S. P. D. Mangles, Z. Najmudin, M. Pittman, J.-P. Rousseau, J.-N. Scheurer, B. Walton, and A. E. Dangor. Electron acceleration by a wake field forced by an intense ultrashort laser pulse. *Science*, 298(5598):1596–1600, 2002.

[11] P. Chen, J. M. Dawson, R. W. Huff, and T. Katsouleas. Acceleration of electrons by the interaction of a bunched electron beam with a plasma. *Phys. Rev. Lett.*, 54(7):693–696, 1985.

[12] J. B. Rosenzweig, D. B. Cline, B. Cole, H. Figueroa, W. Gai, R. Konecny, J. Norem, P. Schoessow, and J. Simpson. Experimental observation of plasma wake-field acceleration. *Phys. Rev. Lett.*, 61(1):98–101, 1988.

[13] J. B. Rosenzweig, B. Breizman, T. Katsouleas, and J. J. Su. Acceleration and focusing of electrons in two-dimensional nonlinear plasma wake fields. *Phys. Rev. A*, 44(10):R6189–R6192, 1991.

[14] B. E. Blue, C. E. Clayton, C. L. O'Connell, F.-J. Decker, M. J. Hogan, C. Huang, R. Iverson, C. Joshi, T. C. Katsouleas, W. Lu, K. A. Marsh, W. B. Mori, P. Muggli, R. Siemann, and D. Walz. Plasma-wakefield acceleration of an intense positron beam. *Phys. Rev. Lett.*, 90(21):214801, 2003.

[15] I. Blumenfeld, C. E. Clayton, F.-J. Decker, M. J. Hogan, C. Huang, R. Ischebeck, R. Iverson, C. Joshi, T. Katsouleas, N. Kirby, W. Lu, K. A. Marsh, W. B. Mori, P. Muggli, E. Oz, R. H. Siemann, D. Walz, and M. Zhou. Energy doubling of 42 GeV electrons in a metre-scale plasma wakefield accelerator. *Nature*, 445(7129):741–744, 2007.

[16] A. Caldwell, K. Lotov, A. Pukhov, and F. Simon. Proton-driven plasma-wakefield acceleration. *Nat. Phys.*, 5(5):363–367, 2009.

[17] P. Muggli and M. J. Hogan. Review of high-energy plasma wakefield experiments. *C. R. Physique*, 10:116–129, 2009.

[18] E. Esarey, P. Sprangle, J. Krall, and A. Ting. Overview of plasma-based accelerator concept. *IEEE Trans. Plasma Science*, 24(2):252, 1996.

[19] K. Krushelnick, Z. Najmudin, and A. E. Dangor. Particle acceleration using intense laser produced plasmas. *Laser Phys. Lett.*, 4(12):847–862, 2007.

[20] V. Malka, J. Faure, Y. A. Gauduel, E. Lefebvre, A. Rousse, and K. Ta Phuoc. Principles and applications of compact laser-plasma accelerators. *Nat. Phys.*, 4(6):447–453, 2008.

[21] E. Esarey, C. B. Schroeder, and W. P. Leemans. Physics of laser-driven plasma-based electron accelerators. *Rev. Mod. Phys.*, 81(3):1229–1285, 2009.

[22] W. Leemans and E. Esarey. Laser-driven plasma-wave electron accelerators. *Phys. Today*, 62(3):44–49, 2009.

[23] K. V. Lotov. Simulation of proton driven plasma wakefield acceleration. *Phys. Rev. ST Accel. Beams*, 13(4):041301, 2010.

[24] C. Joshi and T. Katsouleas. Plasma accelerators at the energy frontier and on tabletops. *Phys. Today*, 56(6):47–53, 2003.

[25] W. L. Kruer. *The physics of laser plasma interactions.* Westview Press, 2003.

[26] Y. Kitagawa, T. Matsumoto, T. Minamihata, K. Sawai, K. Matsuo, K. Mima, K. Nishihara, H. Azechi, K. A. Tanaka, H. Takabe, and S. Nakai. Beat-wave excitation of plasma wave and observation of accelerated electrons. *Phys. Rev. Lett.*, 68(1):48–51, 1992.

[27] C. E. Clayton, K. A. Marsh, A. Dyson, M. Everett, A. Lal, W. P. Leemans, R. Williams, and C. Joshi. Ultrahigh-gradient acceleration of injected electrons by laser-excited relativistic electron plasma waves. *Phys. Rev. Lett.*, 70(1):37–40, 1993.

[28] M. Everett, A. Lal, D. Gordon, C. E. Clayton, K. A. Marsh, and C. Joshi. Trapped electron acceleration by a laser-driven relativistic plasma wave. *Nature*, 368(6471):527–529, 1994.

[29] F. Amiranoff, D. Bernard, B. Cros, F. Jacquet, G. Matthieussent, P. Miné, P. Mora, J. Morillo, F. Moulin, A. E. Specka, and C. Stenz. Electron acceleration in nd-laser plasma beat-wave experiments. *Phys. Rev. Lett.*, 74(26):5220–5223, 1995.

[30] P. Maine, D. Strickland, P. Bado, M. Pessot, and G. Mourou. Generation of ultrahigh peak power pulses by chirped pulse amplification. *IEEE Journal of Quantum Electronics*, 24(2):398–403, 1988.

[31] N. E. Andreev, L. M. Gorbunov, V. I. Kirsanov, A. A. Pogosova, and R. R. Ramazashvili. Resonant excitation of wakefields by a laser pulse in a plasma. *JETP Lett.*, 55(10), 1992.

[32] A. Modena, Z. Najmudin, A. Dangor, C. Clayton, K. A. Marsh, C. Joshi, V. Malka, C. Darrow, C. Danson, D. Neely, and F. Walsh. Electron acceleration from the breaking of relativistic plasma waves. *Nature*, 377(6550):606–608, 1995.

[33] D. Umstadter, S.-Y. Chen, A. Maksimchuk, G. Mourou, and R. Wagner. Nonlinear optics in relativistic plasmas and laser wake field acceleration of electrons. *Science*, 273(5274):472–475, 1996.

[34] K. Nakajima, D. Fisher, T. Kawakubo, H. Nakanishi, A. Ogata, Y. Kato, Y. Kitagawa, R. Kodama, K. Mima, H. Shiraga, K. Suzuki, K. Yamakawa, T. Zhang, Y. Sakawa, T. Shoji, Y. Nishida, N. Yugami, M. Downer, and T. Tajima. Observation of ultrahigh gradient electron acceleration by a self-modulated intense short laser pulse. *Phys. Rev. Lett.*, 74(22):4428–4431, 1995.

[35] S. Backus, C. G. Durfee, M. M. Murnane, and H. C. Kapteyn. High power ultrafast lasers. *Rev. Sci. Instrum.*, 69(3):1207–1223, 1998.

[36] A. Pukhov and J. Meyer-ter Vehn. Laser wake field acceleration: the highly nonlinear broken-wave regime. *Appl. Phys. B*, 74:355–361, 2002.

[37] S. P. D. Mangles, C. D. Murphy, Z. Najmudin, A. G. R. Thomas, J. L. Collier, A. E. Dangor, E. J. Divall, P. S. Foster, J. G. Gallacher, C. J. Hooker, D. A. Jaroszynski, A. J. Langley, W. B. Mori, P. A. Norreys, F. S. Tsung, R. Viskup, B. R. Walton, and K. Krushelnick. Monoenergetic beams of relativistic electrons from intense laser-plasma interactions. *Nature*, 431(7008):535–538, 2004.

[38] C. G. R. Geddes, Cs. Toth, J. van Tilborg, E. Esarey, C. B. Schroeder, D. Bruhwiler, C. Nieter, J. Cary, and W. P. Leemans. High-quality electron beams from a laser wakefield accelerator using plasma-channel guiding. *Nature*, 431(7008):538–541, 2004.

[39] J. Faure, Y. Glinec, A. Pukhov, S. Kiselev, S. Gordienko, E. Lefebvre, J.-P. Rousseau, F. Burgy, and V. Malka. A laser-plasma accelerator producing monoenergetic electron beams. *Nature*, 431(7008):541–544, 2004.

[40] W. P. Leemans, B. Nagler, A. J. Gonsalves, Cs. Toth, K. Nakamura, C. G. R. Geddes, E. Esarey, C. B. Schroeder, and S. M. Hooker. Gev electron beams from a centimetre-scale accelerator. *Nat. Phys.*, 2(10):696–699, 2006.

[41] J. Faure, C. Rechatin, A. Norlin, A. Lifschitz, Y. Glinec, and V. Malka. Controlled injection and acceleration of electrons in plasma wakefields by colliding laser pulses. *Nature*, 444(7120):737–739, 2006.

[42] J. S. Liu, C. Q. Xia, W. T. Wang, H. Y. Lu, Ch. Wang, A. H. Deng, W. T. Li, H. Zhang, X. Y. Liang, Y. X. Leng, X. M. Lu, C. Wang, J. Z. Wang, K. Nakajima, R. X. Li, and Z. Z. Xu. All-optical cascaded laser wakefield accelerator using ionization-induced injection. *Phys. Rev. Lett.*, 107(3):035001, 2011.

[43] B. B. Pollock, C. E. Clayton, J. E. Ralph, F. Albert, A. Davidson, L. Divol, C. Filip, S. H. Glenzer, K. Herpoldt, W. Lu, K. A. Marsh, J. Meinecke, W. B. Mori, A. Pak, T. C. Rensink, J. S. Ross, J. Shaw, G. R. Tynan, C. Joshi, and D. H. Froula. Demonstration of a narrow energy spread, 0.5 Gev electron beam from a two-stage laser wakefield accelerator. *Phys. Rev. Lett.*, 107(4):045001, 2011.

[44] A. J. Gonsalves, K. Nakamura, C. Lin, D. Panasenko, S. Shiraishi, T. Sokollik, C. Benedetti, C. B. Schroeder, C. G. R. Geddes, J. van Tilborg, J. Osterhoff, E. Esarey, C. Toth, and W. P. Leemans. Tunable laser plasma accelerator based on longitudinal density tailoring. *Nat. Phys.*, 7(11):862–866, 2011.

[45] J. Osterhoff, A. Popp, Zs. Major, B. Marx, T. P. Rowlands-Rees, M. Fuchs, M. Geissler, R. Horlein, B. Hidding, S. Becker, E. A. Peralta, U. Schramm, F. Gruner, D. Habs, F. Krausz, S. M. Hooker, and S. Karsch. Generation of stable, low-divergence electron beams by laser-wakefield acceleration in a steady-state-flow gas cell. *Phys. Rev. Lett.*, 101(8):085002, 2008.

[46] G. Genoud, K. Cassou, F. Wojda, H. Ferrari, C. Kamperidis, M. Burza, A. Persson, J. Uhlig, S. Kneip, S. Mangles, A. Lifschitz, B. Cros, and C.-G. Wahlstrom. Laser-plasma electron acceleration in dielectric capillary tubes. *Appl. Phys. B: Lasers and Optics*, 105:309–316, 2011.

[47] D. P. Umstadter. Laser-wakefield accelerators: Glass-guiding benefits. *Nat. Photon.*, 5(10):576–577, 2011.

[48] J. Ju, K. Svensson, A. Dopp, H. E. Ferrari, K. Cassou, O. Neveu, G. Genoud, F. Wojda, M. Burza, A. Persson, O. Lundh, C.-G. Wahlstrom, and B. Cros. Enhancement of x-rays generated by a guided laser wakefield accelerator inside capillary tubes. *Appl. Phys. Lett.*, 100(19):191106, 2012.

[49] N. H. Matlis, S. Reed, S. S. Bulanov, V. Chvykov, G. Kalintchenko, T. Matsuoka, P. Rousseau, V. Yanovsky, A. Maksimchuk, S. Kalmykov, G. Shvets, and M. C. Downer. Snapshots of laser wakefields. *Nat. Phys.*, 2(11):749–753, 2006.

[50] P. Dong, S. A. Reed, S. A. Yi, S. Kalmykov, Z. Y. Li, G. Shvets, N. H. Matlis, C. McGuffey, S. S. Bulanov, V. Chvykov, G. Kalintchenko, K. Krushelnick, A. Maksimchuk, T. Matsuoka, A. G. R. Thomas, V. Yanovsky, and M. C. Downer. Holographic visualization of laser wakefields. *New J. Phys.*, 12(4):045016, 2010.

[51] A. Buck, M. Nicolai, K. Schmid, C. M. S. Sears, A. Savert, J. M. Mikhailova, F. Krausz, M. C. Kaluza, and L. Veisz. Real-time observation of laser-driven electron acceleration. *Nat. Phys.*, 7(7):543–548, 2011.

[52] O. Lundh, J. Lim, C. Rechatin, L. Ammoura, A. Ben-Ismail, X. Davoine, G. Gallot, J-P. Goddet, E. Lefebvre, V. Malka, and J. Faure. Few femtosecond, few kiloampere electron bunch produced by a laser-plasma accelerator. *Nat. Phys.*, 7(3):219–222, 2011.

[53] E. Brunetti, R. P. Shanks, G. G. Manahan, M. R. Islam, B. Ersfeld, M. P. Anania, S. Cipiccia, R. C. Issac, G. Raj, G. Vieux, G. H. Welsh, S. M. Wiggins, and D. A. Jaroszynski. Low emittance, high brilliance relativistic electron beams from a laser-plasma accelerator. *Phys. Rev. Lett.*, 105(21):215007, 2010.

[54] S. Kneip, C. McGuffey, J. L. Martins, M. S. Bloom, V. Chvykov, F. Dollar, R. Fonseca, S. Jolly, G. Kalintchenko, K. Krushelnick, A. Maksimchuk, S. P. D. Mangles, Z. Najmudin, C. A. J. Palmer, K. Ta Phuoc, W. Schumaker, L. O. Silva, J. Vieira, V. Yanovsky, and A. G. R. Thomas. Characterization of transverse beam emittance of electrons from a laser-plasma wakefield accelerator in the bubble regime using betatron x-ray radiation. *Phys. Rev. ST Accel. Beams*, 15(2):021302, 2012.

[55] H.-P. Schlenvoigt, K. Haupt, A. Debus, F. Budde, O. Jackel, S. Pfotenhauer, H. Schwoerer, E. Rohwer, J. G. Gallacher, E. Brunetti, R. P. Shanks, S. M. Wiggins, and D. A. Jaroszynski. A compact synchrotron radiation source driven by a laser-plasma wakefield accelerator. *Nat. Phys.*, 4(2):130–133, 2008.

[56] M. Fuchs, R. Weingartner, A. Popp, Z. Major, S. Becker, J. Osterhoff, I. Cortrie, B. Zeitler, R. Horlein, G. D. Tsakiris, U. Schramm, T. P. Rowlands-Rees, S. M. Hooker, D. Habs, F. Krausz, S. Karsch, and F. Gruner. Laser-driven soft-x-ray undulator source. *Nat. Phys.*, 5(11):826–829, 2009.

[57] A. Rousse, K.-Ta Phuoc, R. Shah, A. Pukhov, E. Lefebvre, V. Malka, S. Kiselev, F. Burgy, J.-P. Rousseau, D. Umstadter, and D. Hulin. Production of a kev x-ray beam from synchrotron radiation in relativistic laser-plasma interaction. *Phys. Rev. Lett.*, 93(13):135005, 2004.

[58] S. Kneip, C. McGuffey, J. L. Martins, S. F. Martins, C. Bellei, V. Chvykov, F. Dollar, R. Fonseca, C. Huntington, G. Kalintchenko, A. Maksimchuk, S. P. D. Mangles, T. Matsuoka, S. R. Nagel, C. A. J. Palmer, J. Schreiber, K. Ta Phuoc, A. G. R. Thomas, V. Yanovsky, L. O. Silva, K. Krushelnick, and Z. Najmudin. Bright spatially coherent synchrotron x-rays from a table-top source. *Nat. Phys.*, 6(12):980–983, 2010.

[59] S. Cipiccia, M. R. Islam, B. Ersfeld, R. P. Shanks, E. Brunetti, G. Vieux, X. Yang, R. C. Issac, S. M. Wiggins, G. H. Welsh, M.-P. Anania, D. Maneuski, R. Montgomery, G. Smith, M. Hoek, D. J. Hamilton, N. R. C. Lemos, D. Symes, P. P. Rajeev, V. O. Shea, J. M. Dias, and D. A. Jaroszynski. Gamma-rays from harmonically resonant betatron oscillations in a plasma wake. *Nat. Phys.*, 7(11):867–871, 2011.

[60] S. Corde, C. Thaury, K. Ta Phuoc, A. Lifschitz, G. Lambert, J. Faure, O. Lundh, E. Benveniste, A. Ben-Ismail, L. Arantchuk, A. Marciniak, A. Stordeur, P. Brijesh, A. Rousse, A. Specka, and V. Malka. Mapping the x-ray emission region in a laser-plasma accelerator. *Phys. Rev. Lett.*, 107(21):215004, 2011.

[61] C. Courtois. *Propagation d'impulsions laser de haute intensité dans des tubes capillaires*. PhD thesis, Université de Paris-Sud 11, Orsay, FRANCE, 2001.

[62] F. Wojda. *Measure de l'amplitude d'une onde de plasma créée par sillage laser guidé.* PhD thesis, Université de Paris-Sud 11, Orsay, FRANCE, 2010.

[63] P. Gibbon. *Short Pulse Laser Interactions with Matter.* Imperial College Press, 2005.

[64] E. A. Startsev and C. J. McKinstrie. Multiple scale derivation of the relativistic ponderomotive force. *Phys. Rev. E*, 55(6):7527–7535, 1997.

[65] F. F. Chen. *Introduction to plasma physics and controlled fusion.* Plenum press, 2nd edition, 1983.

[66] D. A. Gurnett and A. Bhattacharjee. *Introduction to Plasma Physics: With Space and Laboratory Applications.* Cambridge University Press, 2005.

[67] D.J. Spence, A. Butler, and S. M. Hooker. First demonstration of guiding of high-intensity laser pulses in a hydrogen-filled capillary discharge waveguide. *Journal of Physics B: Atomic, Molecular and Optical Physics*, 34(21):4103–4112, 2001.

[68] L. V. Keldysh. Ionization in the field of a strong electromagnetic wave. *Soviet Phys. JETP*, 20(5):1307–1314, 1965.

[69] M. V. Ammosov, N. B. Delone, and V. P. Krainov. Tunnel ionization of complex atoms and of atomic ions in an alternating electromagnetic field. *Soviet Phys. JETP*, 64(6):1191–1194, 1986.

[70] S. P. D. Mangles, A. G. R. Thomas, M. C. Kaluza, O. Lundh, F. Lindau, A. Persson, Z. Najmudin, C.-G. Wahlstrom, C. D. Murphy, C. Kamperidis, K. L. Lancaster, E. Divall, and K. Krushelnick. Effect of laser contrast ratio on electron beam stability in laser wakefield acceleration experiments. *Plasma Physics and Controlled Fusion*, 48(12B):B83–B90, 2006.

[71] A. Pak, K. A. Marsh, S. F. Martins, W. Lu, W. B. Mori, and C. Joshi. Injection and trapping of tunnel-ionized electrons into laser-produced wakes. *Phys. Rev. Lett.*, 104(2):025003, 2010.

[72] C. McGuffey, A. G. R. Thomas, W. Schumaker, T. Matsuoka, V. Chvykov, F. J. Dollar, G. Kalintchenko, V. Yanovsky, A. Maksimchuk, K. Krushelnick, V. Yu. Bychenkov, I. V. Glazyrin, and A. V. Karpeev. Ionization induced trapping in a laser wakefield accelerator. *Phys. Rev. Lett.*, 104(2):025004, 2010.

[73] C. E. Clayton, J. E. Ralph, F. Albert, R. A. Fonseca, S. H. Glenzer, C. Joshi, W. Lu, K. A. Marsh, S. F. Martins, W. B. Mori, A. Pak, F. S. Tsung, B. B. Pollock, J. S. Ross, L. O. Silva, and D. H. Froula. Self-guided laser wakefield acceleration beyond 1 Gev using ionization-induced injection. *Phys. Rev. Lett.*, 105(10):105003, 2010.

[74] H. Ihee, V. A. Lobastov, U. M. Gomez, B. M. Goodson, R. Srinivasan, C.-Y. Ruan, and A. H. Zewail. Direct imaging of transient molecular structures with ultrafast diffraction. *Science*, 291(5503):458–462, 2001.

[75] A. H. Zewail. Femtochemistry: Atomic-scale dynamics of the chemical bond. *J. Phys. Chem. A*, 104(24):5660–5694, 2000.

[76] G. Genoud. *Laser-driven plasma waves for particle acceleration and* X*-ray production.* PhD thesis, Lund University, Sweden, 2011.

[77] S. F. Martins, R. A. Fonseca, W. Lu, W. B. Mori, and L. O. Silva. Exploring laser-wakefield-accelerator regimes for near-term lasers using particle-in-cell simulation in lorentz-boosted frames. *Nat. Phys.*, 6(4):311–316, 2010.

[78] F. S. Tsung, W. Lu, M. Tzoufras, W. B. Mori, C. Joshi, J. M. Vieira, L. O. Silva, and R. A. Fonseca. Simulation of monoenergetic electron generation via laser wakefield accelerators for 5–25 tw lasers. *Phys. Plasmas*, 13(5):056708, 2006.

[79] E. Esarey and M. Pilloff. Trapping and acceleration in nonlinear plasma waves. *Phys. Plasmas*, 2(5):1432–1436, 1995.

[80] J. B. Rosenzweig. Trapping, thermal effects, and wave breaking in the nonlinear plasma wake-field accelerator. *Phys. Rev. A*, 38(7):3634–3642, 1988.

[81] T. Katsouleas and W. B. Mori. Wave-breaking amplitude of relativistic oscillations in a thermal plasma. *Phys. Rev. Lett.*, 61(1):90–93, 1988.

[82] F. Amiranoff, S. Baton, D. Bernard, B. Cros, D. Descamps, F. Dorchies, F. Jacquet, V. Malka, J. R. Marquès, G. Matthieussent, P. Miné, A. Modena, P. Mora, J. Morillo, and Z. Najmudin. Observation of laser wakefield acceleration of electrons. *Phys. Rev. Lett.*, 81(5):995–998, 1998.

[83] C. B. Schroeder, E. Esarey, B. A. Shadwick, and W. P. Leemans. Trapping, dark current, and wave breaking in nonlinear plasma waves. *Phys. Plasmas*, 13(3):033103–9, 2006.

[84] S. V. Bulanov, F. Pegoraro, A. M. Pukhov, and A. S. Sakharov. Transverse-wake wave breaking. *Phys. Rev. Lett.*, 78(22):4205–4208, 1997.

[85] S. Kalmykov, S. A. Yi, V. Khudik, and G. Shvets. Electron self-injection and trapping into an evolving plasma bubble. *Phys. Rev. Lett.*, 103(13):135004, 2009.

[86] S. Y. Kalmykov, A. Beck, S. A. Yi, V. N. Khudik, M. C. Downer, E. Lefebvre, B. A. Shadwick, and D. P. Umstadter. Electron self-injection into an evolving plasma bubble: Quasi-monoenergetic laser-plasma acceleration in the blowout regime. *Phys. Plasmas*, 18(5):056704, 2011.

[87] W. B. Mori. The physics of the nonlinear optics of plasmas at relativistic intensities for short-pulse lasers. *IEEE J. Quant. Elec.*, 33(11):1942–1953, 1997.

[88] G.-Z. Sun, E. Ott, Y. C. Lee, and P.s Guzdar. Self-focusing of short intense pulses in plasmas. *Phys. Fluids*, 30(2):526–532, 1987.

[89] P. Sprangle, E. Esarey, A. Ting, and G. Joyce. Laser wakefield acceleration and relativistic optical guiding. *Appl. Phys. Lett.*, 53(22):2146–2148, 1988.

[90] E. Esarey, P. Sprangle, J. Krall, A. Ting, and G. Joyce. Optically guided laser wake-field acceleration. *Phys. Fluids B*, 5(7):2690–2697, 1993.

[91] J. Faure, V. Malka, J.-R. Marques, P.-G. David, F. Amiranoff, K. Ta Phuoc, and A. Rousse. Effects of pulse duration on self-focusing of ultra-short lasers in underdense plasmas. *Phys. Plasmas*, 9(3):756–759, 2002.

[92] C. Delfin, V. Lokhnygin, J. Mauritsson, A. Sjogren, C.-G. Wahlstrom, A. Pukhov, and G. D. Tsakiris. Influence of laser pulse duration on relativistic channels. *Phys. Plasmas*, 9(3):937–940, 2002.

[93] C. D. Decker, W. B. Mori, K.-C. Tzeng, and T. Katsouleas. The evolution of ultra-intense, short-pulse lasers in underdense plasmas. *Phys. Plasmas*, 3(5):2047–2056, 1996.

[94] W. Lu, M. Tzoufras, C. Joshi, F. S. Tsung, W. B. Mori, J. Vieira, R. A. Fonseca, and L. O. Silva. Generating multi-gev electron bunches using single stage laser wakefield acceleration in a 3d nonlinear regime. *Phys. Rev. ST Accel. Beams*, 10(6):061301, 2007.

[95] J. E. Ralph, K. A. Marsh, A. E. Pak, W. Lu, C. E. Clayton, F. Fang, W. B. Mori, and C. Joshi. Self-guiding of ultrashort, relativistically intense laser pulses through underdense plasmas in the blowout regime. *Phys. Rev. Lett.*, 102(17):175003, 2009.

[96] W. Lu, C. Huang, M. Zhou, M. Tzoufras, F. S. Tsung, W. B. Mori, and T. Katsouleas. A nonlinear theory for multidimensional relativistic plasma wave wakefields. *Phys. Plasmas*, 13(5):056709, 2006.

[97] J. Faure, Y. Glinec, J. J. Santos, F. Ewald, J.-P. Rousseau, S. Kiselev, A. Pukhov, T. Hosokai, and V. Malka. Observation of laser-pulse shortening in nonlinear plasma waves. *Phys. Rev. Lett.*, 95(20):205003, 2005.

[98] J. Schreiber, C. Bellei, S. P. D. Mangles, C. Kamperidis, S. Kneip, S. R. Nagel, C. A. J. Palmer, P. P. Rajeev, M. J. V. Streeter, and Z. Najmudin. Complete temporal characterization of asymmetric pulse compression in a laser wakefield. *Phys. Rev. Lett.*, 105(23):235003, 2010.

[99] F. Wojda, K. Cassou, G. Genoud, M. Burza, Y. Glinec, O. Lundh, A. Persson, G. Vieux, E. Brunetti, R. P. Shanks, D. Jaroszynski, N. E. Andreev, C.-G. Wahlstrom, and B. Cros. Laser-driven plasma waves in capillary tubes. *Phys. Rev. E*, 80(6):066403, 2009.

[100] W. Lu, C. Huang, M. Zhou, W. B. Mori, and T. Katsouleas. Nonlinear theory for relativistic plasma wakefields in the blowout regime. *Phys. Rev. Lett.*, 96(16):165002, 2006.

[101] A. G. R. Thomas, Z. Najmudin, S. P. D. Mangles, C. D. Murphy, A. E. Dangor, C. Kamperidis, K. L. Lancaster, W. B. Mori, P. A. Norreys, W. Rozmus, and K. Krushelnick. Effect of laser-focusing conditions on propagation and monoenergetic electron production in laser-wakefield accelerators. *Phys. Rev. Lett.*, 98(9):095004, 2007.

[102] T. Katsouleas, S. Wilks, P. Chen, J. M. Dawson, and J. J. Su. Beam loading in plasma accelerators. *Part. Accel.*, 22:81–99, 1987.

[103] M. Tzoufras, W. Lu, F. S. Tsung, C. Huang, W. B. Mori, T. Katsouleas, J. Vieira, R. A. Fonseca, and L. O. Silva. Beam loading in the nonlinear regime of plasma-based acceleration. *Phys. Rev. Lett.*, 101(14):145002, 2008.

[104] C. Rechatin, X. Davoine, A. Lifschitz, A. Ben Ismail, J. Lim, E. Lefebvre, J. Faure, and V. Malka. Observation of beam loading in a laser-plasma accelerator. *Phys. Rev. Lett.*, 103(19):194804, 2009.

[105] C. G. R. Geddes, Cs. Toth, J. van Tilborg, E. Esarey, C. B. Schroeder, D. Bruhwiler, C. Nieter, J. Cary, and W. P. Leemans. Production of high-quality electron bunches by dephasing and beam loading in channeled and unchanneled laser plasma accelerators. *Phys. Plasmas*, 12(5):056709, 2005.

[106] A. G. R. Thomas. Scalings for radiation from plasma bubbles. *Phys. Plasmas*, 17(5):056708, 2010.

[107] S. P. D. Mangles, G. Genoud, M. S. Bloom, M. Burza, Z. Najmudin, A. Persson, K. Svensson, A. G. R. Thomas, and C.-G. Wahlstrom. Self-injection threshold in self-guided laser wakefield accelerators. *Phys. Rev. ST Accel. Beams*, 15(1):011302, 2012.

[108] D. H. Froula, C. E. Clayton, T. Doppner, K. A. Marsh, C. P. J. Barty, L. Divol, R. A. Fonseca, S. H. Glenzer, C. Joshi, W. Lu, S. F. Martins, P. Michel, W. B. Mori, J. P. Palastro, B. B. Pollock, A. Pak, J. E. Ralph, J. S. Ross, C. W. Siders, L. O. Silva, and T. Wang. Measurements of the critical power for self-injection of electrons in a laser wakefield accelerator. *Phys. Rev. Lett.*, 103(21):215006, 2009.

[109] S. P. D. Mangles, A. G. R. Thomas, C. Bellei, A. E. Dangor, C. Kamperidis, S. Kneip, S. R. Nagel, L. Willingale, and Z. Najmudin. Self-guided wakefield experiments driven by petawatt-class ultrashort laser pulses. *IEEE Trans. Plasma Science*, 36(4):1715–1721, 2008.

[110] B. A. Shadwick, C. B. Schroeder, and E. Esarey. Nonlinear laser energy depletion in laser-plasma accelerators. *Phys. Plasmas*, 16(5):056704, 2009.

[111] J. M. Dawson. Particle simulation of plasmas. *Rev. Mod. Phys.*, 55(2):403–447, 1983.

[112] A. F. Lifschitz, X. Davoine, E. Lefebvre, J. Faure, C. Rechatin, and V. Malka. Particle-in-cell modelling of laser-plasma interaction using fourier decomposition. *J. Comp. Phys.*, 228(5):1803–1814, 2009.

[113] X. Davoine, E. Lefebvre, J. Faure, C. Rechatin, A. Lifschitz, and V. Malka. Simulation of quasimonoenergetic electron beams produced by colliding pulse wakefield acceleration. *Phys. Plasmas*, 15(11):113102, 2008.

[114] H. E. Ferrari, A. F. Lifschitz, and B. Cros. Modelling of laser-plasma electron acceleration in capillary tubes. *Plasma Physics and Controlled Fusion*, 53(1):014005, 2011.

[115] H. E. Ferrari, A. F. Lifschitz, G. Maynard, and B. Cros. Electron acceleration by laser wakefield and x-ray emission at moderate intensity and density in long plasmas. *Phys. Plasmas*, 18(8):083108, 2011.

[116] E. Esarey, B. A. Shadwick, P. Catravas, and W. P. Leemans. Synchrotron radiation from electron beams in plasma-focusing channels. *Phys. Rev. E*, 65(5):056505, 2002.

[117] K. Ta Phuoc, F. Burgy, J.-P. Rousseau, V. Malka, A. Rousse, R. Shah, D. Umstadter, A. Pukhov, and S. Kiselev. Laser based synchrotron radiation. *Phys. Plasmas*, 12(2):023101, 2005.

[118] R. C. Shah, F. Albert, K. Ta Phuoc, O. Shevchenko, D. Boschetto, A. Pukhov, S. Kiselev, F. Burgy, J.-P. Rousseau, and A. Rousse. Coherence-based transverse measurement of synchrotron x-ray radiation from relativistic laser-plasma interaction and laser-accelerated electrons. *Phys. Rev. E*, 74(4):045401, 2006.

[119] F. Albert, K. Ta Phuoc, R. Shah, S. Corde, R. Fitour, A. Tafzi, F. Burgy, D. Douillet, T. Lefrou, and A. Rousse. Full characterization of a laser-produced kev x-ray betatron source. *Plasma Physics and Controlled Fusion*, 50(12):124008, 2008.

[120] F. Albert, R. Shah, K. Ta Phuoc, R. Fitour, F. Burgy, J.-P. Rousseau, A. Tafzi, D. Douillet, T. Lefrou, and A. Rousse. Betatron oscillations of electrons accelerated in laser wakefields characterized by spectral x-ray analysis. *Phys. Rev. E*, 77(5):056402, 2008.

[121] K. Ta Phuoc, R. Fitour, A. Tafzi, T. Garl, N. Artemiev, R. Shah, F. Albert, D. Boschetto, A. Rousse, D-E. Kim, A. Pukhov, V. Seredov, and I. Kostyukov. Demonstration of the ultrafast nature of laser produced betatron radiation. *Phys. Plasmas*, 14(8):080701, 2007.

[122] S. Fourmaux, S. Corde, K. Ta Phuoc, P. M. Leguay, S. Payeur, P. Lassonde, S. Gnedyuk, G. Lebrun, C. Fourment, V. Malka, S. Sebban, A. Rousse, and J. C. Kieffer. Demonstration of the synchrotron-type spectrum of laser-produced betatron radiation. *New J. Phys.*, 13(3):033017, 2011.

[123] S. Fourmaux, S. Corde, K. Ta Phuoc, P. Lassonde, G. Lebrun, S. Payeur, F. Martin, S. Sebban, V. Malka, A. Rousse, and J. C. Kieffer. Single shot phase contrast imaging using laser-produced betatron x-ray beams. *Opt. Lett.*, 36(13):2426–2428, 2011.

[124] S. Kneip, C. McGuffey, F. Dollar, M. S. Bloom, V. Chvykov, G. Kalintchenko, K. Krushelnick, A. Maksimchuk, S. P. D. Mangles, T. Matsuoka, Z. Najmudin, C. A. J. Palmer, J. Schreiber, W. Schumaker, A. G. R. Thomas, and V. Yanovsky. X-ray phase contrast imaging of biological specimens with femtosecond pulses of betatron radiation from a compact laser plasma wakefield accelerator. *Appl. Phys. Lett.*, 99(9):093701, 2011.

[125] S. Dusterer, P. Radcliffe, C. Bostedt, J. Bozek, A. L. Cavalieri, R. Coffee, J. T. Costello, D. Cubaynes, L. F. DiMauro, Y. Ding, G. Doumy, F. Gruner, W. Helml, W. Schweinberger, R. Kienberger, A. R. Maier, M. Messerschmidt, V. Richardson, C. Roedig, T. Tschentscher, and M. Meyer. Femtosecond x-ray pulse length characterization at the linac coherent light source free-electron laser. *New J. Phys.*, 13(9):093024, 2011.

[126] W. D. Jackson. *Classical Electrodynamics*. John Wiley and Sons Press, 2nd edition, 1975.

[127] A. G. R. Thomas. Algorithm for calculating spectral intensity due to charged particles in arbitrary motion. *Phys. Rev. ST Accel. Beams*, 13(2):020702, 2010.

[128] K. Ta Phuoc, S. Corde, R. Shah, F. Albert, R. Fitour, J.-P. Rousseau, F. Burgy, B. Mercier, and A. Rousse. Imaging electron trajectories in a laser-wakefield cavity using betatron x-ray radiation. *Phys. Rev. Lett.*, 97(22):225002, 2006.

[129] K. Ta Phuoc, S. Corde, R. Fitour, R. Shah, F. Albert, J.-P. Rousseau, F. Burgy, A. Rousse, V. Seredov, and A. Pukhov. Analysis of wakefield electron orbits in plasma wiggler. *Phys. Plasmas*, 15(7):073106, 2008.

[130] Y. Glinec. *Propagation d'une impulsion laser ultra-intense dans un plasma sous-dense : Génération de faisceaux d'électrons quasi-monoénergétiques et développement d'applications*. PhD thesis, Ecole Polytechnique, FRANCE, 2006.

[131] S. P. D. Mangles, G. Genoud, S. Kneip, M. Burza, K. Cassou, B. Cros, N. P. Dover, C. Kamperidis, Z. Najmudin, A. Persson, J. Schreiber, F. Wojda, and C.-G. Wahlstrom. Controlling the spectrum of x-rays generated in a laser-plasma accelerator by tailoring the laser wavefront. *Appl. Phys. Lett.*, 95(18):181106, 2009.

[132] A. Popp, J. Vieira, J. Osterhoff, Zs. Major, R. Horlein, M. Fuchs, R. Weingartner, T. P. Rowlands-Rees, M. Marti, R. A. Fonseca, S. F. Martins, L. O. Silva, S. M. Hooker, F. Krausz, F. Gruner, and S. Karsch. All-optical steering of laser-wakefield-accelerated electron beams. *Phys. Rev. Lett.*, 105(21):215001, 2010.

[133] D. J. Spence and S. M. Hooker. Investigation of a hydrogen plasma waveguide. *Phys. Rev. E*, 63(1):015401, 2000.

[134] D. J. Spence, A. Butler, and S. M. Hooker. Gas-filled capillary discharge waveguides. *J. Opt. Soc. Am. B*, 20(1):138, 2003.

[135] C. G. R. Geddes, Cs. Toth, J. van Tilborg, E. Esarey, C. B. Schroeder, J. Cary, and W. P. Leemans. Guiding of relativistic laser pulses by preformed plasma channels. *Phys. Rev. Lett.*, 95(14):145002, 2005.

[136] W. Leemans, E. Esarey, C. Geddes, C. Schroeder, and C. Toth. Laser guiding for gev laser-plasma accelerators. *Phil. Trans. R. Soc. A: Mathematical, Physical and Engineering Sciences*, 364(1840):585, 2006.

[137] A. Butler, D. J. Spence, and S. M. Hooker. Guiding of high-intensity laser pulses with a hydrogen-filled capillary discharge waveguide. *Phys. Rev. Lett.*, 89(18):185003, 2002.

[138] R. F. Hubbard, D. Kaganovich, B. Hafizi, C. I. Moore, P. Sprangle, A. Ting, and A. Zigler. Simulation and design of stable channel-guided laser wakefield accelerators. *Phys. Rev. E*, 63(3):036502, 2001.

[139] D. H. Froula, L. Divol, P. Davis, J. P. Palastro, P. Michel, V. Leurent, S. H. Glenzer, B. B. Pollock, and G. Tynan. Magnetically controlled plasma waveguide for laser wakefield acceleration. *Plasma Physics and Controlled Fusion*, 51(2):024009, 2009.

[140] B. Cros, C. Courtois, G. Matthieussent, A. Di Bernardo, D. Batani, N. Andreev, and S. Kuznetsov. Eigenmodes for capillary tubes with dielectric walls and ultraintense laser pulse guiding. *Phys. Rev. E*, 65(2):026405, 2002.

[141] F. Dorchies, J. R. Marques, B. Cros, G. Matthieussent, C. Courtois, T. Velikoroussov, P. Audebert, J. P. Geindre, S. Rebibo, G. Hamoniaux, and F. Amiranoff. Monomode guiding of $10\hat{1}6$ w/cm$\hat{2}$ laser pulses over 100 rayleigh lengths in hollow capillary dielectric tubes. *Phys. Rev. Lett.*, 82(23):4655, 1999.

[142] C. Courtois, B. Cros, G. Malka, G. Matthieussent, J. R. Marques, N. Blanchot, and J. L. Miquel. Experimental study of short high-intensity laser-pulse monomode propagation in centimeter-long capillary tubes. *J. Opt. Soc. Am. B*, 17(5):864, 2000.

[143] B. Cros, C. Courtois, G. Malka, G. Matthieussent, J. R. Marques, F. Dorchies, F. Amiranoff, S. Rebibo, G. Hamoniaux, N. Blanchot, and J. L. Miquel. Extending plasma accelerators: guiding with capillary tubes. *IEEE Trans. Plasma Science*, 28(4):1071, 2000.

[144] N. E. Andreev, K. Cassou, F. Wojda, G. Genoud, M. Burza, O. Lundh, A. Persson, B. Cros, V. E. Fortov, and C.-G. Wahlstrom. Analysis of laser wakefield dynamics in capillary tubes. *New J. Phys.*, 12(4):045024, 2010.

[145] D. Du, X. Liu, G. Korn, J. Squier, and G. Mourou. Laser-induced breakdown by impact ionization in sio2 with pulse widths from 7 ns to 150 fs. *Appl. Phys. Lett.*, 64(23):3071, 1994.

[146] E. Hecht. *Optics*. Addison Wesley, 4th edition, 2002.

[147] M. Veysman, N. E. Andreev, K. Cassou, Y. Ayoul, G. Maynard, and B. Cros. Theoretical and experimental study of laser beam propagation in capillary tubes for non-symmetrical coupling conditions. *J. Opt. Soc. Am. B*, 27(7):1400, 2010.

[148] P. Mora and Jr. Antonsen, T. M. Electron cavitation and acceleration in the wake of an ultraintense, self-focused laser pulse. *Phys. Rev. E*, 53(3):R2068–R2071, 1996.

[149] A. Behjat, G. J. Tallents, and D. Neely. The characterization of a high-density gas jet. *Journal of Physics D: Applied Physics*, 30(20):2872, 1997.

[150] V. Malka, C. Coulaud, J. P. Geindre, V. Lopez, Z. Najmudin, D. Neely, and F. Amiranoff. Characterization of neutral density profile in a wide range of pressure of cylindrical pulsed gas jets. *Rev. Sci. Instrum.*, 71(6):2329, 2000.

[151] A. J. Gonsalves, T. P. Rowlands-Rees, B. H. P. Broks, J. J. A. M. van der Mullen, and S. M. Hooker. Transverse interferometry of a hydrogen-filled capillary discharge waveguide. *Phys. Rev. Lett.*, 98(2):025002, 2007.

[152] G. A. Bird. *Molecular Gas Dynamics and the Direct Simulation of Gas Flows*. Oxford University Press, 2nd edition, 1994.

[153] I. A. Graur, M. S. Ivanov, G. N. Markelov, Y. Burtschell, E. Valerio, and D. Zeitoun. Comparison of kinetic and continuum approaches for simulation of shock wave/boundary layer interaction. *Shock Waves*, 12:343, 2003.

[154] P. S. Prasanth and J. K. Kakkassery. Direct simulation monte carlo (dsmc): A numerical method for transition-regime flows-a review. *J. Indian Inst. Sci.*, 83(3):169, 2006.

[155] L. D. Landau and E. M. Lifshitz. *Fluid mechanics*. Pergamon Press, 2nd edition, 1987.

[156] K. R. Sreenivasan. Fluid turbulence. *Rev. Mod. Phys.*, 71(2):S383, 1999.

[157] K. V. Sharp and R. J. Adrian. Transition from laminar to turbulent flow in liquid filled microtubes. *Experiments in Fluids*, 36(5):741, 2004.

[158] T. Cebeci. *Analysis of Turbulent Flows.* Elsevier, 2003.

[159] D. C. Wilcox. *Turbulence Modeling for CFD.* DCW Industries, 3rd edition, 2006.

[160] B. E. Launder and B. I. Sharma. Application of the energy-dissipation model of turbulence to the calculation of flow near a spinning disc. *Letters in Heat and Mass Transfer*, 1:131, 1974.

[161] http://www.ansys.com/products/simulation+technology/fluid+dynamics/ansys+fluent.

[162] A. J. Smits and J.-P. Dussauge. *Turbulent Shear Layers in Supersonic Flow.* Springer, 2nd edition, 2005.

[163] C. G. R. Geddes. *Plasma Channel Guided Laser Wakefield Accelerator.* PhD thesis, University of California, Berkeley, 2005.

[164] J. Ju and B. Cros. Characterization of temporal and spatial distribution of hydrogen gas density in capillary tubes for laser-plasma experiments. *J. Appl. Phys.*, 112(11):113102, 2012.

[165] M. Born and E. Wolf. *Principles of Optics.* Pergamon, 6th edition, 1980.

[166] R. C. Weast, editor. *Handbook of Chemistry and Physics.* Chemical Rubber Company, 54th edition, 1973.

[167] M. Takeda, H. Ina, and S. Kobayashi. Fourier-transform method of fringe-pattern analysis for computer-based topography and interferometry. *J. Opt. Soc. Am.*, 72(1):156–160, 1982.

[168] H. Suk, N. Barov, J. B. Rosenzweig, and E. Esarey. Plasma electron trapping and acceleration in a plasma wake field using a density transition. *Phys. Rev. Lett.*, 86(6):1011–1014, 2001.

[169] C. G. R. Geddes, K. Nakamura, G. R. Plateau, Cs. Toth, E. Cormier-Michel, E. Esarey, C. B. Schroeder, J. R. Cary, and W. P. Leemans. Plasma-density-gradient injection of low absolute-momentum-spread electron bunches. *Phys. Rev. Lett.*, 100(21):215004, 2008.

[170] K. Schmid, A. Buck, C. M. S. Sears, J. M. Mikhailova, R. Tautz, D. Herrmann, M. Geissler, F. Krausz, and L. Veisz. Density-transition based electron injector for laser driven wakefield accelerators. *Phys. Rev. ST Accel. Beams*, 13(9):091301, 2010.

[171] W. Rittershofer, C. B. Schroeder, E. Esarey, F. J. Gruner, and W. P. Leemans. Tapered plasma channels to phase-lock accelerating and focusing forces in laser-plasma accelerators. *Phys. Plasmas*, 17(6):063104, 2010.

[172] Meng Wen, Baifei Shen, Xiaomei Zhang, Fengchao Wang, Zhangying Jin, Liangliang Ji, Wenpeng Wang, Jiancai Xu, and Kazuhisa Nakajima. Controlled electron acceleration in the bubble regime by optimizing plasma density. *New Journal of Physics*, 12(4):045010, 2010.

[173] D. Strickland and G. Mourou. Compression of amplified chirped optical pulses. *Opt. Commun.*, 56(3):219–221, 1985.

[174] D. E. Spence, J. M. Evans, W. E. Sleat, and W. Sibbett. Regeneratively initiated self-mode-locked ti:sapphire laser. *Opt. Lett.*, 16(22):1762–1764, 1991.

[175] P. F. Moulton. Spectroscopic and laser characteristics of ti:al2o3. *J. Opt. Soc. Am. B*, 3(1):125–133, 1986.

[176] J. E. Murray and W. H. Lowdermilk. Nd : Yag regenerative amplifier. *J. Appl. Phys.*, 51(7):3548–3556, 1980.

[177] W. H. Lowdermilk and J. E. Murray. The multipass amplifier: Theory and numerical analysis. *J. Appl. Phys.*, 51(5):2436–2444, 1980.

[178] G. Genoud, F. Wojda, M. Burza, A. Persson, and C.-G. Wahlstrom. Active control of the pointing of a multi-terawatt laser. *Rev. Sci. Instrum.*, 82(3):033102, 2011.

[179] C. E. Clayton, J. E. Ralph, F. Albert, R. A. Fonseca, S. H. Glenzer, C. Joshi, W. Lu, K. A. Marsh, S. F. Martins, W. B. Mori, A. Pak, F. S. Tsung, B. B. Pollock, J. S. Ross, L. O. Silva, and D. H. Froula. Self-guided laser wakefield acceleration beyond 1 Gev using ionization-induced injection. *Phys. Rev. Lett.*, 105(10):105003, 2010.

[180] K. A. Tanaka, T. Yabuuchi, T. Sato, R. Kodama, Y. Kitagawa, T. Takahashi, T. Ikeda, Y. Honda, and S. Okuda. Calibration of imaging plate for high energy electron spectrometer. *Rev. Sci. Instrum.*, 76(1):013507, 2005.

[181] R. Nowotny and A. Taubeck. A method for the production of composite scintillators for dosimetry in diagnostic radiology. *Physics in Medicine and Biology*, 54(6):1457, 2009.

[182] K. Nakamura, A. J. Gonsalves, C. Lin, A. Smith, D. Rodgers, R. Donahue, W. Byrne, and W. P. Leemans. Electron beam charge diagnostics for laser plasma accelerators. *Phys. Rev. ST Accel. Beams*, 14(6):062801, 2011.

[183] Y. Glinec, J. Faure, A. Guemnie-Tafo, V. Malka, H. Monard, J. P. Larbre, V. De Waele, J. L. Marignier, and M. Mostafavi. Absolute calibration for a broad range single shot electron spectrometer. *Rev. Sci. Instrum.*, 77(10):103301, 2006.

[184] A. Buck, K. Zeil, A. Popp, K. Schmid, A. Jochmann, S. D. Kraft, B. Hidding, T. Kudyakov, C. M. S. Sears, L. Veisz, S. Karsch, J. Pawelke, R. Sauerbrey, T. Cowan, F. Krausz, and U. Schramm. Absolute charge calibration of scintillating screens for relativistic electron detection. *Rev. Sci. Instrum.*, 81(3):033301, 2010.

[185] K. Svensson. *Laser-produced plasmas for particle acceleration.* PhD thesis, Lund University, Sweden, 2012.

[186] G. E. Giakoumakis and D. M. Miliotis. Light angular distribution of fluorescent screens excited by x-rays. *Physics in Medicine and Biology*, 30(1):21, 1985.

[187] W. Fullagar, J. Uhlig, M. Walczak, S. Canton, and V. Sundstrom. The use and characterization of a backilluminated charge-coupled device in investigations of pulsed x-ray and radiation sources. *Rev. Sci. Instrum.*, 79(10):103302, 2008.

[188] P. Kirkpatrick. On the theory and use of ross filters. *Rev. Sci. Instrum.*, 10(6):186–191, 1939.

[189] P. Kirkpatrick. Theory and use of ross filters. ii. *Rev. Sci. Instrum.*, 15(9):223–229, 1944.

[190] S. Kneip, S. R. Nagel, C. Bellei, N. Bourgeois, A. E. Dangor, A. Gopal, R. Heathcote, S. P. D. Mangles, J. R. Marquès, A. Maksimchuk, P. M. Nilson, K. Ta Phuoc, S. Reed, M. Tzoufras, F. S. Tsung, L. Willingale, W. B. Mori, A. Rousse, K. Krushelnick, and Z. Najmudin. Observation of synchrotron radiation from electrons accelerated in a petawatt-laser-generated plasma cavity. *Phys. Rev. Lett.*, 100(10):105006, 2008.

[191] D. B. Thorn, C. G. R. Geddes, N. H. Matlis, G. R. Plateau, E. H. Esarey, M. Battaglia, C. B. Schroeder, S. Shiraishi, Th. Stohlker, C. Toth, and W. P. Leemans. Spectroscopy of betatron radiation emitted from laser-produced wakefield accelerated electrons. *Rev. Sci. Instrum.*, 81(10):10E325, 2010.

[192] M. Schnell, A. Savert, B. Landgraf, M. Reuter, M. Nicolai, O. Jackel, C. Peth, T. Thiele, O. Jansen, A. Pukhov, O. Willi, M. C. Kaluza, and C. Spielmann. Deducing the electron-beam diameter in a laser-plasma accelerator using x-ray betatron radiation. *Phys. Rev. Lett.*, 108(7):075001, 2012.

[193] G. R. Plateau, C. G. R. Geddes, D. B. Thorn, M. Chen, C. Benedetti, E. Esarey, A. J. Gonsalves, N. H. Matlis, K. Nakamura, C. B. Schroeder, S. Shiraishi, T. Sokollik, J. van Tilborg, Cs. Toth, S. Trotsenko, T. S. Kim, M. Battaglia, Th. Stohlker, T.lker, and W. P. Leemans. Low-emittance electron bunches from a laser-plasma accelerator measured using single-shot x-ray spectroscopy. *Phys. Rev. Lett.*, 109(6):064802, 2012.

[194] S. Kneip, S. R. Nagel, S. F. Martins, S. P. D. Mangles, C. Bellei, O. Chekhlov, R. J. Clarke, N. Delerue, E. J. Divall, G. Doucas, K. Ertel, F. Fiuza, R. Fonseca, P. Foster, S. J. Hawkes, C. J. Hooker, K. Krushelnick, W. B. Mori, C. A. J. Palmer, K. Ta Phuoc, P. P. Rajeev, J. Schreiber, M. J. V. Streeter, D. Urner, J. Vieira, L. O. Silva, and Z. Najmudin. Near-Gev acceleration of electrons by a nonlinear plasma wave driven by a self-guided laser pulse. *Phys. Rev. Lett.*, 103(3):035002, 2009.

[195] C. M. Huntington, A. G. R. Thomas, C. McGuffey, T. Matsuoka, V. Chvykov, G. Kalintchenko, S. Kneip, Z. Najmudin, C. Palmer, V. Yanovsky, A. Maksimchuk, R. P. Drake, T. Katsouleas, and K. Krushelnick. Current filamentation instability in laser wakefield accelerators. *Phys. Rev. Lett.*, 106(10):105001, 2011.

[196] O. Lundh, C. Rechatin, J. Lim, V. Malka, and J. Faure. Experimental measurements of electron-bunch trains in a laser-plasma accelerator. *Phys. Rev. Lett.*, 110(6):065005, 2013.

[197] S. P. D. Mangles, A. G. R. Thomas, O. Lundh, F. Lindau, M. C. Kaluza, A. Persson, C.-G. Wahlstrom, K. Krushelnick, and Z. Najmudin. On the stability of laser wakefield electron accelerators in the monoenergetic regime. *Phys. Plasmas*, 14(5):056702, 2007.

[198] I. Kostyukov, S. Kiselev, and A. Pukhov. X-ray generation in an ion channel. *Phys. Plasmas*, 10(12):4818–4828, 2003.

[199] C. Rechatin, J. Faure, X. Davoine, O. Lundh, J. Lim, A. Ben-Ismail, F. Burgy, A. Tafzi, A. Lifschitz, E Lefebvre, and V. Malka. Characterization of the beam loading effects in a laser plasma accelerator. *New J. Phys.*, 12(4):045023, 2010.

[200] S. P. D. Mangles, A. G. R. Thomas, M. C. Kaluza, O. Lundh, F. Lindau, A. Persson, F. S. Tsung, Z. Najmudin, W. B. Mori, C.-G. Wahlstrom, and K. Krushelnick. Laser-wakefield acceleration of monoenergetic electron beams in the first plasma-wave period. *Phys. Rev. Lett.*, 96(21):215001, 2006.

[201] K. H. Pae, I. W. Choi, and J. Lee. Self-mode-transition from laser wakefield accelerator to plasma wakefield accelerator of laser-driven plasma-based electron acceleration. *Phys. Plasmas*, 17(12):123104, 2010.

[202] H. W. Koch and J. W. Motz. Bremsstrahlung cross-section formulas and related data. *Rev. Mod. Phys.*, 31(4):920–955, 1959.

[203] S. Agostinelli *et al.* Geant4-a simulation toolkit. *Nuclear Instruments and Methods in Physics Research Section A: Accelerators, Spectrometers, Detectors and Associated Equipment*, 506(3):250–303, 2003.

[204] D. M. Smith. Hard x-ray and gamma-ray detectors. *arXiv:1010.4069v1*, 2010.

[205] K. Ta Phuoc, S. Corde, C. Thaury, V. Malka, A. Tafzi, J. P. Goddet, R. C. Shah, S. Sebban, and A. Rousse. All-optical compton gamma-ray source. *Nat Photon*, 6(5):308–311, 2012.

[206] A. Ben-Ismail, O. Lundh, C. Rechatin, J. K. Lim, J. Faure, S. Corde, and V. Malka. Compact and high-quality gamma-ray source applied to 10 um-range resolution radiography. *Appl. Phys. Lett.*, 98(26):264101, 2011.

[207] R. Weingartner, S. Raith, A. Popp, S. Chou, J. Wenz, K. Khrennikov, M. Heigoldt, A. R. Maier, N. Kajumba, M. Fuchs, B. Zeitler, F. Krausz, S. Karsch, and F. Gruner. Ultralow emittance electron beams from a laser-wakefield accelerator. *Phys. Rev. ST Accel. Beams*, 15(11):111302, 2012.

[208] N. E. Andreev, V. E. Baranov, B. Cros, V. E. Fortov, S. V. Kuznetsov, G. Maynard, and P. Mora. Electron bunch compression and acceleration in the laser wakefield. *Nuclear Instruments and Methods in Physics Research Section A: Accelerators, Spectrometers, Detectors and Associated Equipment*, 653(1):66–71, 2011.

[209] V. Malka, A. Lifschitz, J. Faure, and Y. Glinec. Staged concept of laser-plasma acceleration toward multi-gev electron beams. *Phys. Rev. ST Accel. Beams*, 9(9):091301, 2006.

[210] P. Sprangle, E. Esarey, and A. Ting. Nonlinear theory of intense laser-plasma interactions. *Phys. Rev. Lett.*, 64(17):2011–2014, 1990.